Integrated AVO Analysis, Seismic Inversion and Machine Learning for De-risking New Prospects in The Hutton Sandstone Formation, Onshore Australia

by
Mohamed Ahmed Mahmoud Gad

A thesis submitted to the Department of Earth and Atmospheric Sciences,
College of Natural Sciences and Mathematics
in partial fulfillment of the requirements for the degree of

Master of Science

in Geophysics

Chair of Committee: Professor. John Castagna

Committee Member: Professor. Evgeni Chesnokov

Committee Member: Dr. Yasser Metwally

University of Houston
Dec 2019

Acknowledgements

No words can describe countless blesses that God has gifted me. All thanks to **Allah** who always supports me, gifts me my mind for thinking and has inspired me by ideas and has helped me to achieve accomplishments including this master thesis.

I would like to thank my advisor, Professor John Castagna, for his continuous guidance to me in this research study and for providing me a research assistantship. It has been a great opportunity to me to pursue my research under the supervision of a great scientist like him. I would like to thank Professor Fred Hilterman, for providing excellent data and JTIPS software package license, and for his continuous friendly support to my research. Thanks for Professor Chesnkov for being a co-advisor in my committee.

Special thanks to Dr. Mohamed Eissa for his continuous friendly guidance and support not only to my research, but also at personal level. Special thanks to Dr. Yasser Metwally for his guidance to me in this research study.

I would like to thank Department of State, Fulbright and Amideast for their financial support and to be given the opportunity to carry out this research in one of the many reputable institutes in the USA, the University of Houston.

I would like to acknowledge faculty members of Earth and Atmospheric Sciences for their outstanding education. Thanks for staff members Jim, Karen and Jay for their guidance. In addition, special thanks to SAExploration for providing excellent data. I would like also to thank Lumina Geophysical and SAExploration for conducting bandwidth extension to data and special thanks to Gabriel Gil for his help in improving data resolution. Furthermore, thanks to IHS, CGG, SAExploration, Schlumberger, Geophysical Insights and Ikon science for providing licenses used in this research study.

I would like to thank faculty members in my home institution, Tanta University, especially my supervisor, Professor Abdelaziz, for his continuous support and help.

Finally, thanks to my beloved parents, Ahmed and Laila for their continuous praises and support. And, my beloved sisters, Mariam and Sara, for their encourage to me. And, my beloved wife and son, Zahra and Omar, for being with me in my journey to USA and for their motivation to me during hardship moments. And, my beloved family members for their continuous praises especially my uncle Hamdy.

ABSTRACT

Identifying lithofacies and pore fluids is still a problematic issue in the Hutton Formation, Queensland field, onshore Australia. The target reservoir is usually a one-well prospect since it is of limited size and most wells drilled on basement influenced highs are dry amidst similar structures that are hydrocarbon charged. On the same anticlinal closure, two wells encountered different pore fluids, oil and brine, though both were high on structure, suggesting stratigraphic complexity. Because of ambiguous facies distribution, quantitative seismic analysis is badly needed to predict facies changes between wells.

In this research study, different quantitative analysis methods and datasets were used for facies prediction. These included: AVO analysis, post-stack inversion, pre-stack simultaneous inversion, sparse-layer inversion, probabilistic facies prediction by Bayes classification, supervised machine learning using neural network and unsupervised machine learning using Self-Organizing Maps (SOM). To address methods and data performance for lithology and pore-fluids prediction, blind validation wells were used. In addition, a confusion matrix was constructed to compare methods.

Post-stack inversion on bandwidth-extended seismic data, accomplished with sparse-layer inversion, has the highest pore-fluid prediction accuracy (94.5%). Although supervised and unsupervised machine learning shows good lateral facies distribution along wells, insufficient validation wells prevented statistically meaningful evaluation. High acoustic impedance and compressional-to-shear-wave velocity ratio correlate with meandering stratigraphic features identified from curvedeness and dip of maximum similarity seismic attributes. After co-rendering

these attributes with facies distribution horizon slices, shale and brine-sand facies are distributed along these meandering features. These facies are probably the low stand systems tract of the overlaying Birkhead Formation deposited in incised paleo valley system formed after falling base level. This incision removed the whole, or the upper part of the, Hutton Formation at some locations. In addition, an observed braided channel has anomalous Class 4 AVO response and is characterized by low acoustic impedance. After using a rock-physics template and Bayesian classification, high-probability oil sand facies with high porosity are distributed along the channel feature.

List of Tables

List of Figures

Chapter 1

Introduction

The aim of quantitative seismic interpretation is pore-fluid and lithology discrimination away from existing wells (Avseth et al., 2005). Many scientific approaches have been used to achieve these ends including: AVO attributes, post-stack and pre-stack simultaneous inversion. Amplitude-variation-with-offset (AVO) has widely been used for hydrocarbon detection (e.g., Chopra and Castagna, 2014). Russell (1988) integrated seismic data and well logs to build a complete model of subsurface elastic properties. Hampson et al., (2005) conducted pre-stack simultaneous inversion for simultaneously extracting rock-physical properties such as P-impedance, S-impedance, density and compressional-to-shear-wave velocity ratio which are linked to different pore fluids and facies. Interpretation can be based on statistical relations such as statistical rock physics (Mukerji et al., 2001). Multiattribute analysis and probabilistic neural networks are also commonly used (Hampson et al., 2001). Mukerji et al., (2001) developed statistical rock physics using Bayesian classification for identifying pore-fluids and lithology from seismic data. Ødegaard and Avseth (2004) introduced the idea of a rock physics template (RPT) which uses petrophysical properties estimated at wells for classifying seismic-inversion data. Trappe and Hellmich, (2000) used neural networks for lithofacies prediction. Hampson et al., (2001) derived multiple attributes from seismic data using stepwise regression for well-log predictions and introduced probabilistic neural networks for enhancing resolution of multiattribute analysis. Roden et al., (2015) used the Self-Organizing Map (SOM) algorithm for identifying geologic variations.

My study area is located in the Eromanga Basin, Onshore Australia, and the target reservoir is the Hutton Sandstone Formation. In this area, mixed drilling results suggest that quantitative seismic analysis may result in better exploration success rates. The purpose of this thesis is to attempt to use advanced seismic analysis to explain unusual drilling results in the Queensland field, with the hope of generalizing any learning to other localities in the Eromanga Basin. Because all the above-mentioned approaches have non-unique solutions, a comparison of methods may allow increased confidence in the estimation of pore fluids and lithology distribution in the Hutton Sandstone.

1.1. Problem

Identifying facies and pore fluids is problematic in the Hutton Sandstone Formation. The target is usually a one-well prospect of limited size. Most wells have been drilled on basement influenced highs. Numerous positive structures are dry (exploration failures) amidst similar structures that are hydrocarbon charged. In my dataset, two wells were drilled in the same anticlinal closure; the up-dip well has 100% brine saturation in the Hutton Sandstone while the well mid-dip has lower density oil in the same interval at a greater depth; firm evidence of reservoir compartmentalization. Stratigraphic interference on the anticlinal closure could potentially be the reason for this apparently gravity defying distribution of pore fluids.

1.2. Objectives

My research objective is focused on seismic reservoir characterization of the target reservoir. Seismic reservoir characterization means identifying reservoir properties and hence, discriminating different lithology and pore fluids. Rock-property analysis provides the link between reservoir properties at wells and the seismic response, which is sensitive to changes in reservoir properties such as porosity, lithology and pore fluids. By using available data such as well logs and 3D seismic volumes, rock properties away from the well bore can be estimated. Thus, facies and pore fluids may be discriminated and their distribution over the study area can be reasonably addressed. This could potentially lead to the delineation of new prospects and the avoidance of dry holes in the area. In addition to the lithology and pore-fluid discrimination objective, a comparison between different approaches such as AVO analysis, post-stack seismic inversion, pre-stack simultaneous inversion and multiattribute analysis using machine learning applied to conventional and high-frequency seismic data is another goal. Results will be validated at blind out-of-sample wells. It is hoped that this comparison will reveal the best approach for deciphering the available data and may improve future exploration in the vicinity.

1.3. Methodology

The workflow proposed for quantitative seismic reservoir characterization consists of the following steps: (1) Petrophysical and rock property analyses are performed around and through the target formation in the existing wells. (2) Fluid substitution is conducted to address rock property change to water saturation change and to monitor hydrocarbon pore-fluid detectability from seismic data. In addition, sensitivity and seismic-resolution analyses provide expected seismic-amplitude changes to petrophysical-property changes. (3) AVO analysis was conducted to address pore-fluid discrimination by AVO attributes. (4) Inversion of three offset-limited seismic volumes for Extended Elastic Inversion (EEI) to yield bandlimited P-wave velocity (Vp), S-wave velocity (Vs), and density volumes. Rock properties estimated from inversion are used to characterize reservoir heterogeneity. (5) Rock-property crossplots are tied to the petrophysical properties for discriminating different pore fluids and lithology and for establishing facies cubes. (6) To reduce exploration risk and address uncertainty, Bayesian classification is conducted. (7) Supervised and unsupervised machine learning are used to estimate rock properties and then accuracy of predicted results. (8) Evaluation of these results using the F-test and confusion matrix. and (9) Investigation of blind validation wells. (10) For a more robust rock-physical property estimate, sparse-layer inversion is conducted to create high-frequency seismic data. Then, quantitative seismic interpretation is repeated with the high-resolution seismic data. A workflow for the methodology is shown in Figure 1.1. Methodology will be discussed in detail in the following chapters.

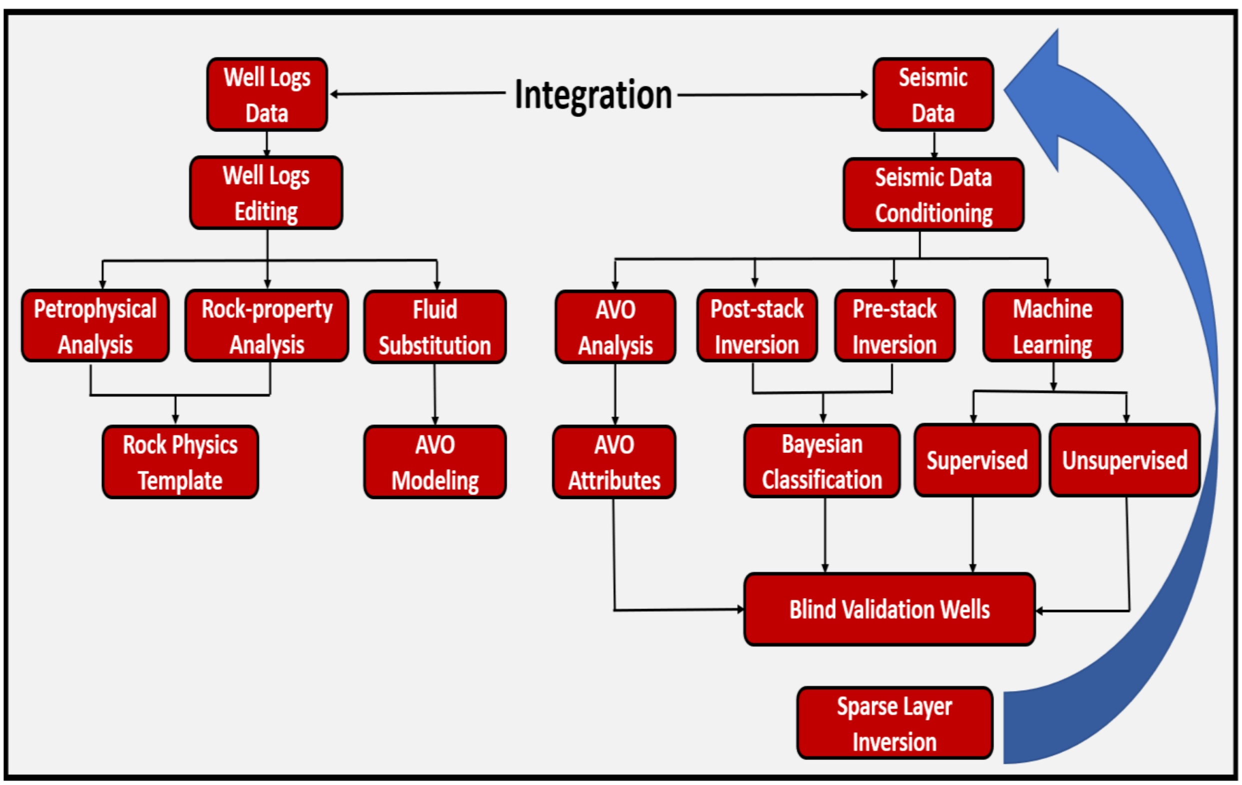

Figure 1.1: Methodology workflow chart for seismic reservoir characterization.

1.4. Data

The available data include recently acquired 3D seismic data over the study area, which is 7860 m by 8440 m. The 3D seismic stack volumes are (1) full, (2) 0-600 m, (3) 600-1200 m, (4) 1200-1800 m, and (5) 1800-2400 m. Four suites of conventional well-log curves from the four wells (A, B, C and D) in the study area include three wells (A, B and C) that have oil production in the upper Hutton formation and one dry hole (Well D). Available logs at the four wells are shown in Table 1.1. All wells have caliper log, resistivity log, SP log, gamma-ray log, sonic log, density log and neutron log. Well A has a measured shear log. In Figure 1.2, the map of the study area shows the four well locations and the area covered by the seismic survey. Software packages used for analyzing data are Hampson-Russell, SMT Kingdom, Petrel, PetroSeismic (JTIPS), RockDoc, Techlog and Excel Microsoft Office.

Table 1.1: Available logs in the four wells.

Logs	Well A	Well B	Well C	Well D
Caliper log	✓	✓	✓	✓
Resistivity log	✓	✓	✓	✓
SP log	✓	✓	✓	✓
Gamma Ray log	✓	✓	✓	✓
Sonic log	✓	✓	✓	✓
Shear log	✓	X	X	X
Density log	✓	✓	✓	✓
Neutron log	✓	✓	✓	✓

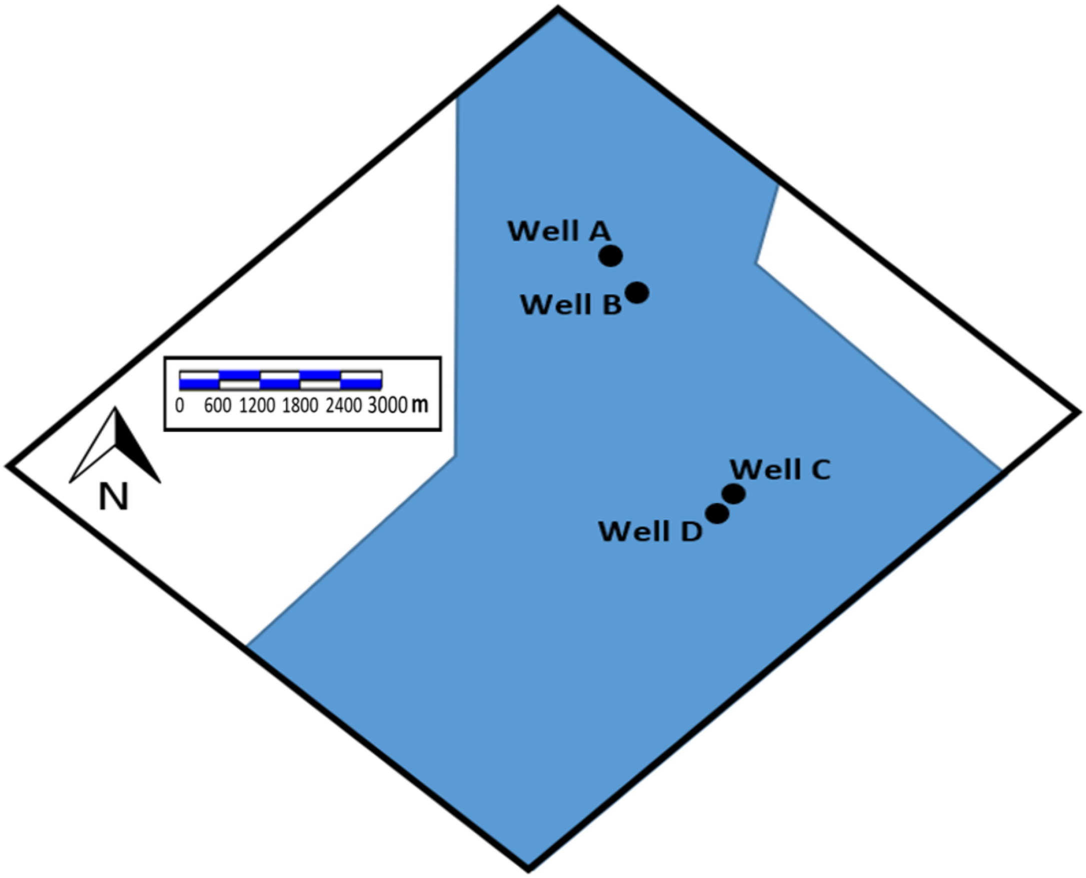

Figure 1.2: Map of the study area shows four wells and the extent of the 3D seismic survey represented by blue area.

1.5. Geological background of study area

The study area is in the Queensland Field, Eromanga Basin, Onshore Australia as shown in Figure 1.3. Most of the oilfields are in the Eromanga Basin sequence where the target pay zone is the Hutton Sandstone Formation.

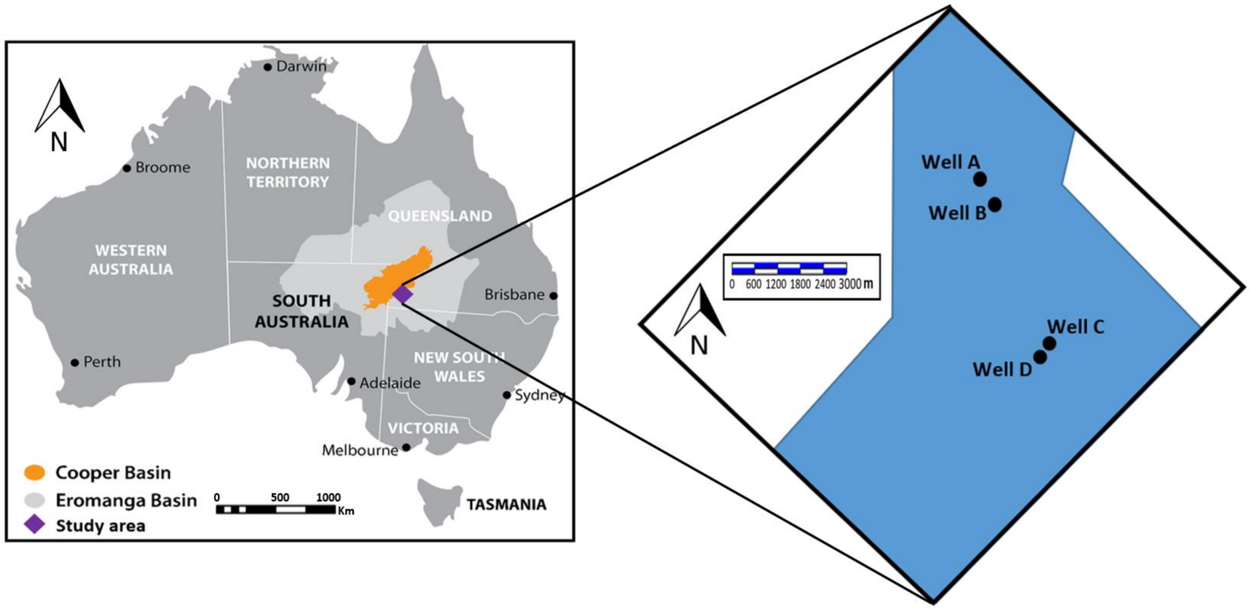

Figure 1.3: Study area, Onshore Australia (modified from GSA, 2019).

1.5.1. Cooper-Eromanga Basin petroleum system

The depositional setting of the Eromanga Basin is a non-marine sequence with high hydrocarbon productivity overlain by two non-productive sequences of marine and non-marine sediments. Permian rocks of the underlying Cooper Basin are regarded as the source rocks for productive reservoirs formed by braided and meandering fluvial, shoreface and lacustrine turbidity sandstones. These Permian source rocks have average TOC and S2 pyrolysis yields of 3.9 % and 6.9 kg/t, respectively. Lacustrine and floodplain shales cover the productive reservoirs to form seals (Radke, 2009).

When it comes to thermal history, as mentioned by (Radke, 2009), hydrocarbons were generated as a result of four heat flow events: Late Permian (250 Ma), late Early Cretaceous (105 Ma), Late Cretaceous (90-85 Ma), and Late Neogene – present (5-2 Ma).

The Eromanga Basin is an intracratonic basin and it dips gently toward the north-west, plunging toward the underlying depocenters of the Cooper Basin at the Nappamerri Trough. In some areas, the Eromanga Basin sequences are thinning toward the east and onlapping the basement highs of the Thargomindah Shelf. Early basement induced faults appear to have undergone limited activity throughout the Jurassic – Cretaceous and rarely extend into the Eromanga section.

The regional structural framework of the Eromanga Basin is represented by four-way dip closed anticlinal trends in a regional sag basin. These anticlinal closures with stratigraphic interferences form the trapping systems such as occur in the Queensland Field, in the Hutton–Birkhead transition (Radke, 2009).

The stratigraphic column of the basin is illustrated in Figure 1.4. There are two key formations of interest. The Cadna–Owie formation produces a regional seismic marker at about 1200 m depth in the study area and the Hutton formations at approximately 1600 m depth is the main reservoir target.

Oil migrated from Cooper Basin source rocks into the upper Eromanga Basin reservoirs. The schematic diagram in Figure 1.5 shows oil migration from Cooper Basin source rocks to overlaying Eromanga Basin reservoirs. Due to poor sealing, net oil columns have small height compared with the height of the closures (from PIRSA, 2000).

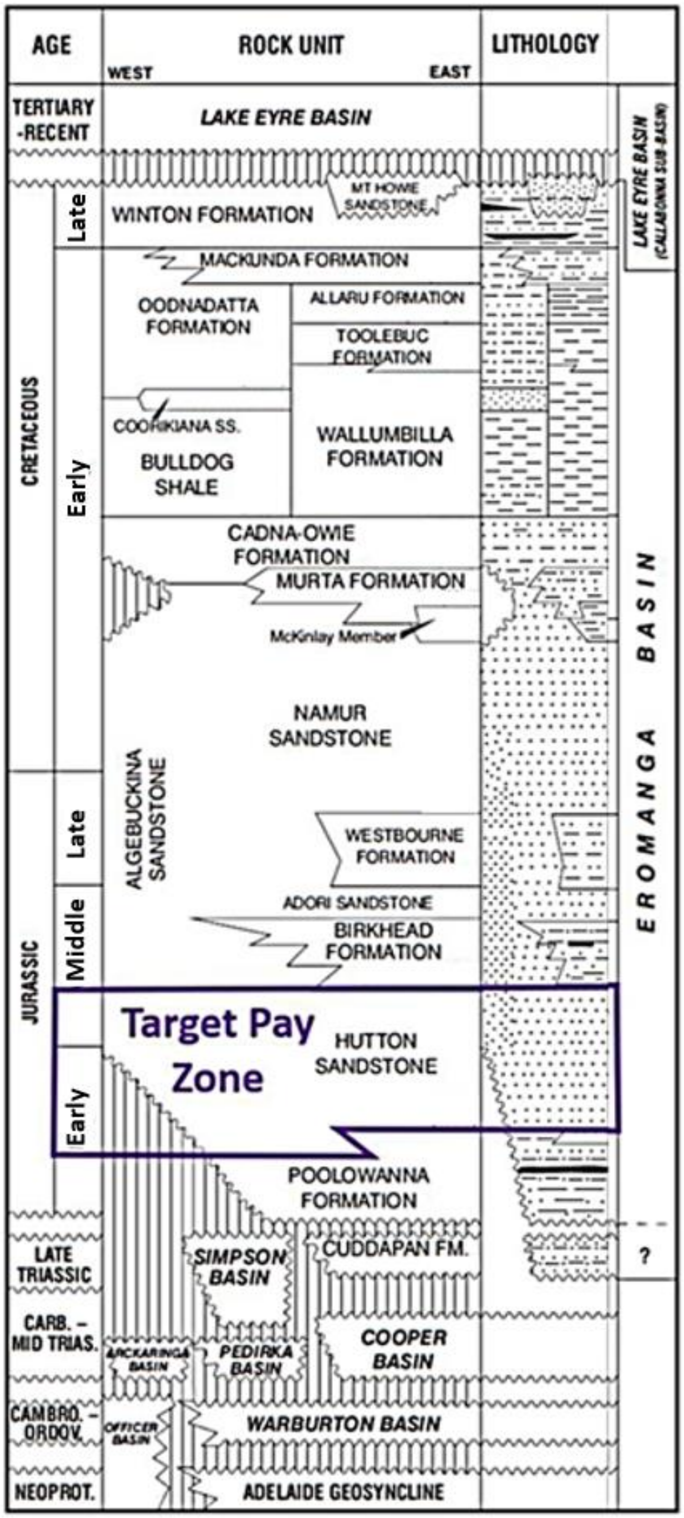

Figure 1.4: Stratigraphic Column of Eromanga Basin in the Cooper region. (modified from DEM, 2018).

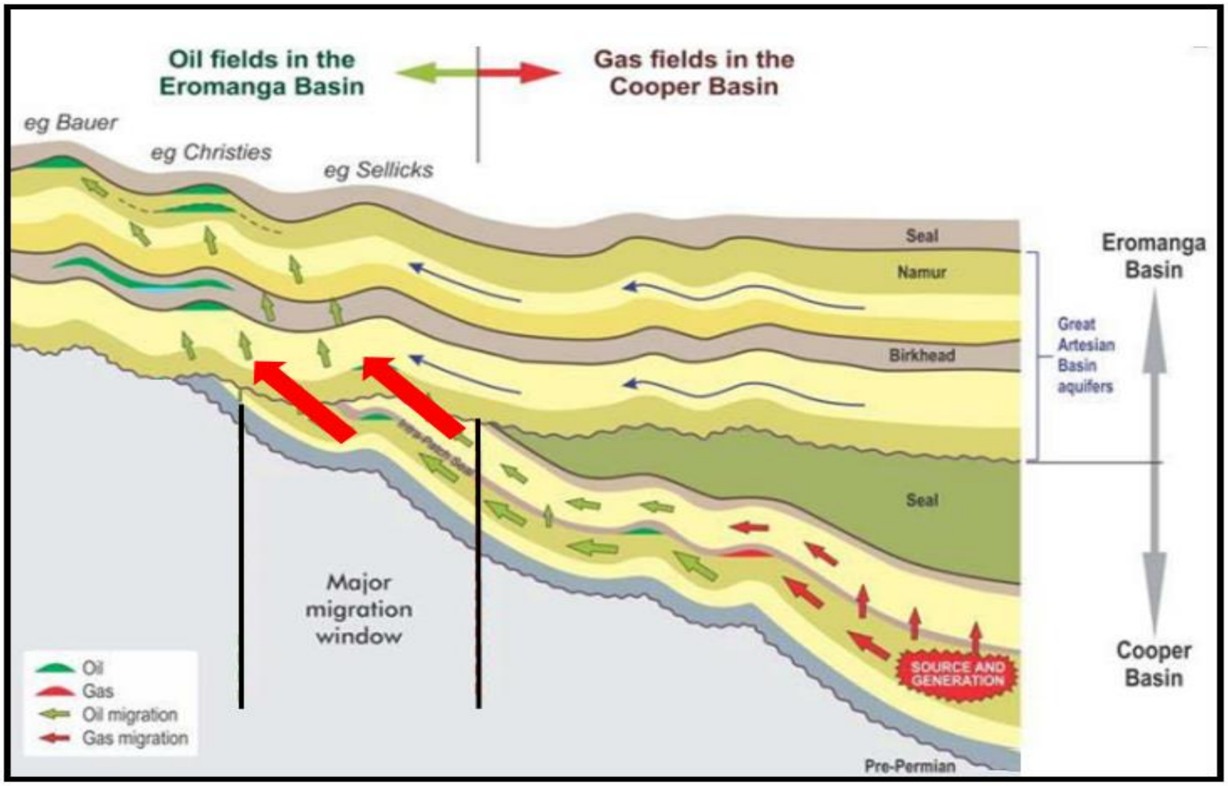

Figure 1.5: Schematic diagram shows oil migration from the Cooper Basin to the Eromanga Basin (modified from Buick, 2015).

1.5.2. Hutton Formation

Dodman and Rodrigues (1989) reported the characteristics of the Hutton Sandstone in the Jackson Oil Field. They described the Hutton reservoir as a largely anticlinal structure overlain by the Birkhead Formation as a top seal. The Hutton Sandstone was deposited in a braided fluvial environment of high energy and consists of fine to coarse grained light brown quartzose sandstones represented by fining upward cycles. Beneath the Hutton oil column, there is a thick aquifer that provides the main drive mechanism. Hamilton et al., (1998) identified Hutton stratigraphy as a sandy sequence consisting of amalgamated, blocky channel fills with few intercalated shales.

The Hutton Formation is overlain by the Birkhead Formation, which scours into the thick, partially consolidated succession of the Hutton sand. This introduces compartmentalization in the upper part of the Hutton Formation. Lateral change in facies produce reservoir heterogeneity that can restrict pore-fluid flow through the reservoir and, hence, prevent hydrocarbon migration into isolated compartments. Reservoir heterogeneity is enhanced by diagenetic processes that create permeability differences among facies (Hamilton et al., 1998). The overlaying Birkhead Formation is composed of interbedded mudstone, siltstone and medium to coarse channel sandstones. These mixed facies were deposited in a meandering fluvial environment. Birkhead Formation deposition is controlled by the Hutton Sandstone paleo-structure (Lanzilli, 1999). A schematic diagram (Figure 1.6) shows sediment provinces and paleogeography during early deposition of Birkhead Formation seal overlaying the target pay zone.

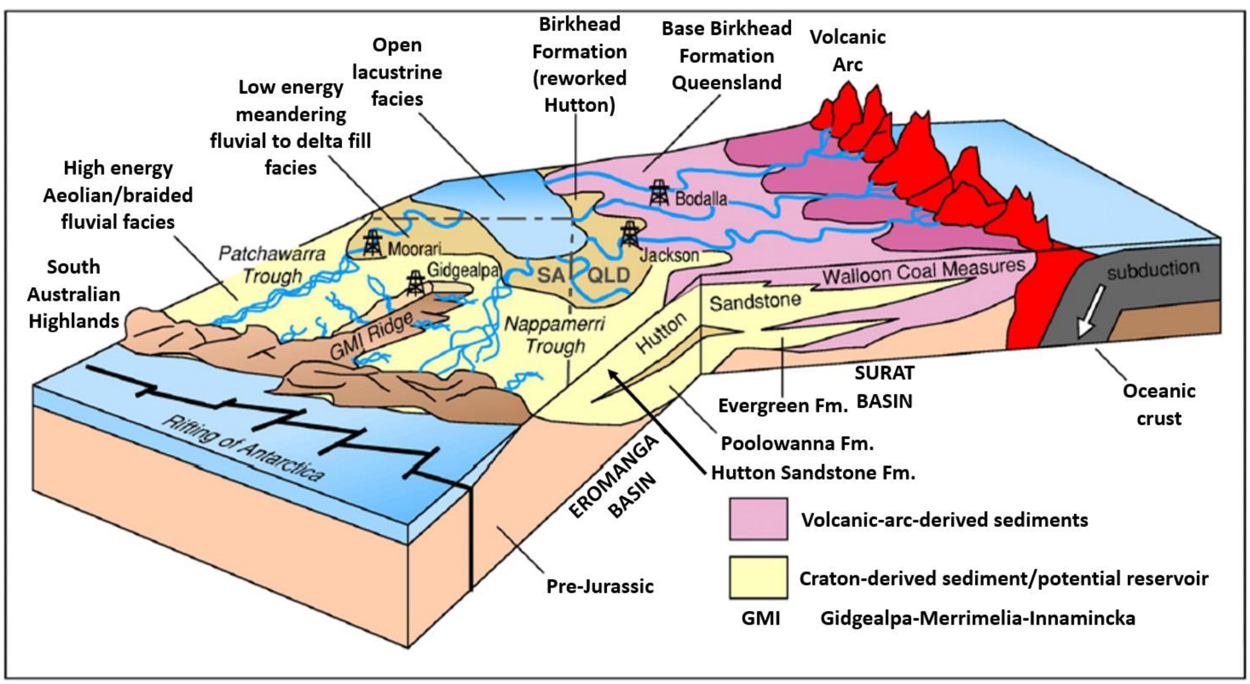

Figure 1.6: Schematic diagram shows sediment provinces and paleogeography during early deposition of seal rock overlaying the target pay zone (modified from Boult et al., 1998).

According to XRD and QEMSCAN analyses of samples taken from the Hutton Sandstone, the main framework mineral is quartz while minor minerals exist including feldspars, clay minerals and other minerals such as K-silicate–quartz interfaces, sulphates, TiO_2 phases and iron oxides as described by Dillinger et al., (2014). In addition, petrographic analysis indicates that sandstone is influenced by diagenetic processes (compaction, cementation, recrystallization, dissolution, authigenesis) which have a significant effect on porosity and permeability and hence, decreasing flow rate of pore fluids within the reservoir. Furthermore, grain contact type varies with facies change from line contacts to suture contacts (Dillinger et al., 2014).

According to core analysis of the Hutton Sandstone samples, porosity ranges from 16% to 25%, and permeability ranges from 10 mD to 1000 mD which indicates good reservoir quality (Hamilton et al., 1998).

Chapter 2

Petrophysical and Rock-property Analyses

2.1. Petrophysical analysis

Petrophysical analysis plays an important role in formation evaluation. It includes lithology (mineral volumetrics), water saturation and porosity estimation through and around the Hutton Formation. The lithology discrimination is basically a sand/shale ratio determination where the volume of shale was estimated by the Stieber method (1970). The shale index was first estimated and then the volume of shale was calculated as shown in following equations:

$$I_{GR} = \frac{GR_{log} - GR_{min}}{GR_{max} - GR_{min}} \text{ , and} \tag{2-1}$$

$$V_{sh} = \frac{\mathrm{GR_{min}}}{3 - 2 * \mathrm{I_{GR}}} \text{ ,} \tag{2-2}$$

where, I_{GR} is shaliness indicator, GR_{max} is maximum gamma ray reading, GR_{min} is minimum gamma ray reading, GR_{log} is gamma log reading and V_{sh} is volume of shale.

Moreover, the SP logs were used to discriminate permeable zones from impermeable ones, and thus, help in lithologic discrimination in conjunction with gamma-ray logs.

Hydrocarbon zones were detected using resistivity logs that are regarded as pore-fluid indicator logs. The average resistivity (R_o) of the brine saturated zone of the Hutton formation was calculated. Archie's equation (1942) was used to calculate the water saturation (Sw):

$$Sw = \sqrt{Ro/Rt} \text{ ,} \tag{2-3a}$$

where, Sw is water saturation, Rt is deep resistivity and Ro is brine-saturated zone resistivity.

When Ro was not readily available, the resistivity of the connate water, R_W was estimated and the second Archie equation used:

$$Sw = c\,(Rw/Rt)^{1/2} / \Phi\ , \tag{2-3b}$$

where, porosity (Φ) is calculated with the mass-balance equation where ρ_b is the measured bulk density, ρ_g is grain density and ρ_{fl} is fluid density:

$$\rho_b = \rho_g\,(1-\Phi) + \rho_{fl}\Phi\ , \text{ and} \tag{2-4}$$

$$\Phi = (\rho_g - \rho_b)/\,(\rho_g - \rho_{fl})\ , \tag{2-5}$$

The fluid density is a function of the water saturation (Sw) and is expressed as:

$$\rho_{fl} = \rho_{HYD}(1-Sw) + \rho_{BR}Sw\ , \tag{2-6}$$

where the density of the hydrocarbons (ρ_{HYD}) and the density of brine (ρ_{BR}) were estimated using equations published by Batzle and Wang (1992). Before calculating porosity, especially in the hydrocarbon zones, the density logs were corrected in zones of irregular values of the caliper log.

Water saturation, volume of shale and porosity curves were calculated for the zone of interest around the Hutton Formation at the four wells as shown in Figures 2.1, 2.2, 2.3 and 2.4. Water saturations for the upper part of the Hutton Formation are 30% in Well A and Well B, which is an indication of hydrocarbon pore-fluid occurrence and 60% in Well C. Although high water saturation occurs at Well C, a drill stem test tested oil from 1523 m to 1525 m depth. At Well D, water saturation is 100%. Calculated volume of shale shows some intercalations of shale within the Hutton Formation which are highest at Wells A, B and D and least at Well C. Porosity ranges from 10% to 21% within the Hutton Formation at Wells A, B and C and from 10% to 15% at Well D.

The density and neutron logs were crossplotted to address lithology and porosity variations in the brine-saturated interval of the Hutton Formation in the four wells as illustrated in Figures 2.5 to 2.8. The plotted data are colored by shale volume (*Vsh*). Most of data plots along the sandstone line. As volume of shale increases, data is shifted toward limestone and dolomite lines. In addition, porosity ranges from 14% to 22% at Well A and Well B as illustrated in Figure 2.5 and Figure 2.6. At Well C, porosity ranges from 17% to 23%. The porosity range decreases to between 14% and 18% at Well D as shown in Figures 2.7 and 2.8.

Porosity reduction along the Hutton Formation at Well D may be attributed to compaction and cementation increasing as a result of diagenetic processes. Sandstone facies change due to increasing volume of shale and/or porosity reduction will lead, in turn, to rock-physical property change.

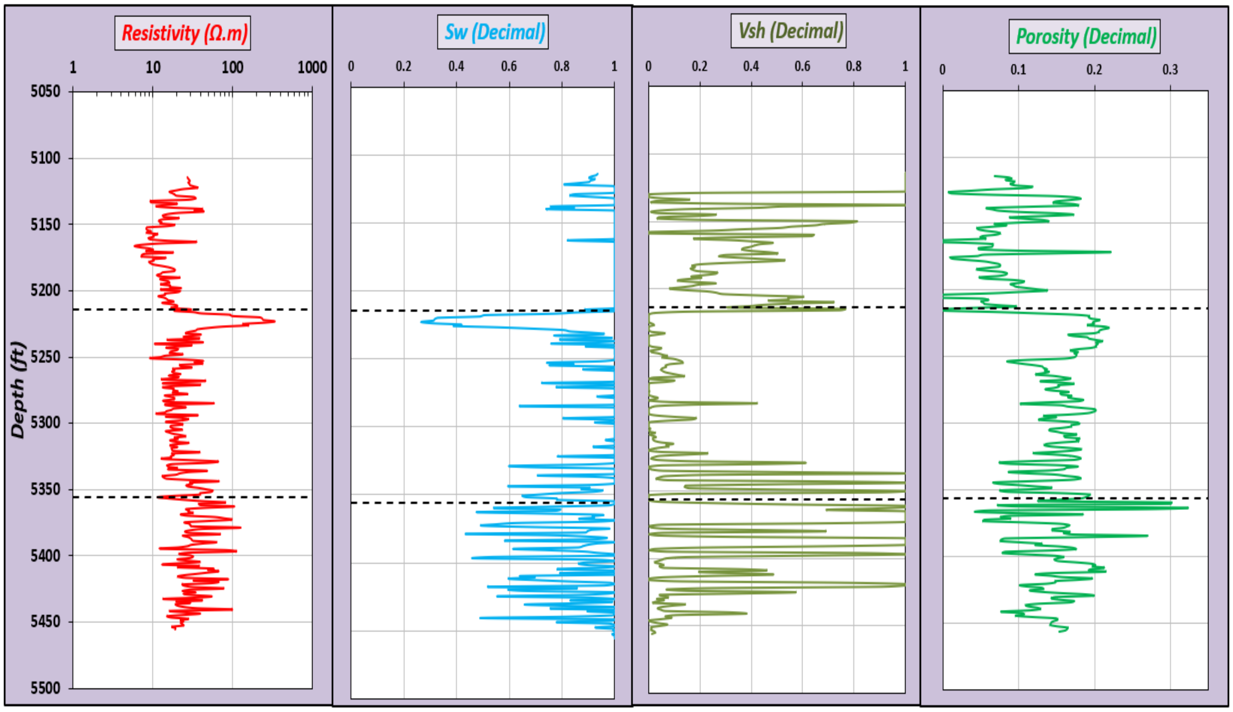

Figure 2.1: Petrophysical analysis of Well A. Dashed lines represent top and base of Hutton Formation.

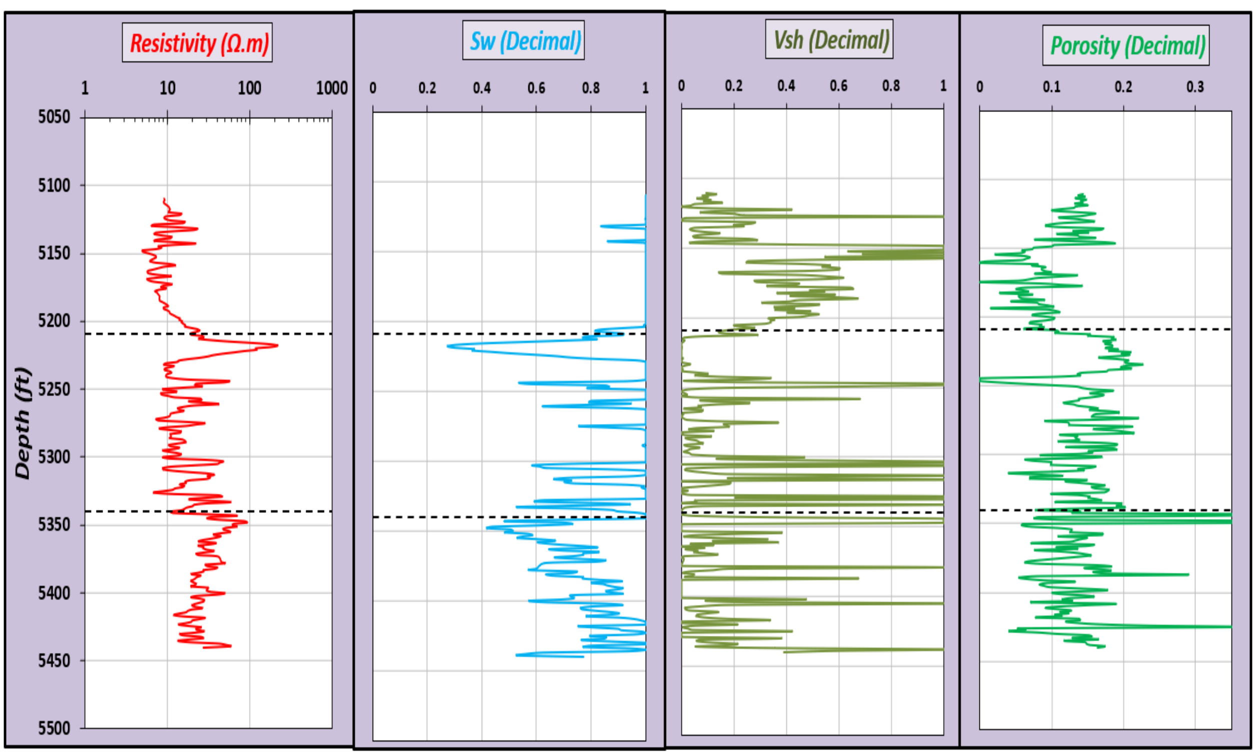

Figure 2.2: Petrophysical analysis of Well B. Dashed lines represent upper and lower Hutton Formation.

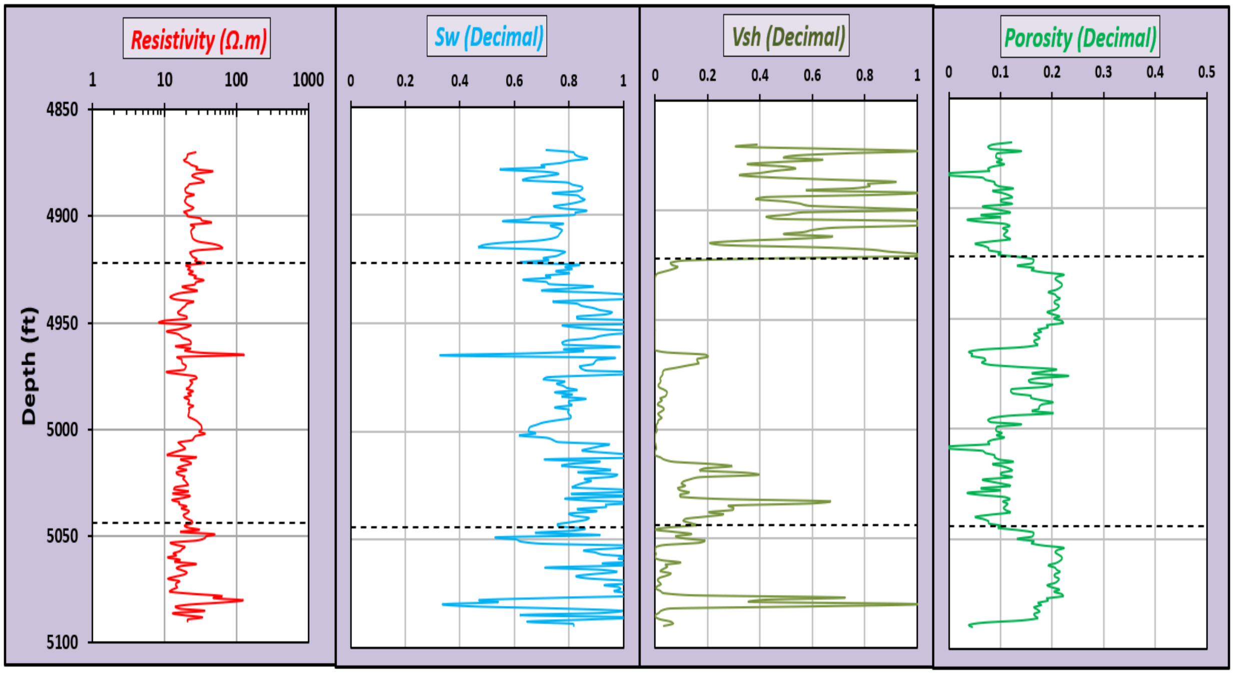

Figure 2.3: Petrophysical analysis of Well C. Dashed lines represent upper and lower Hutton Formation.

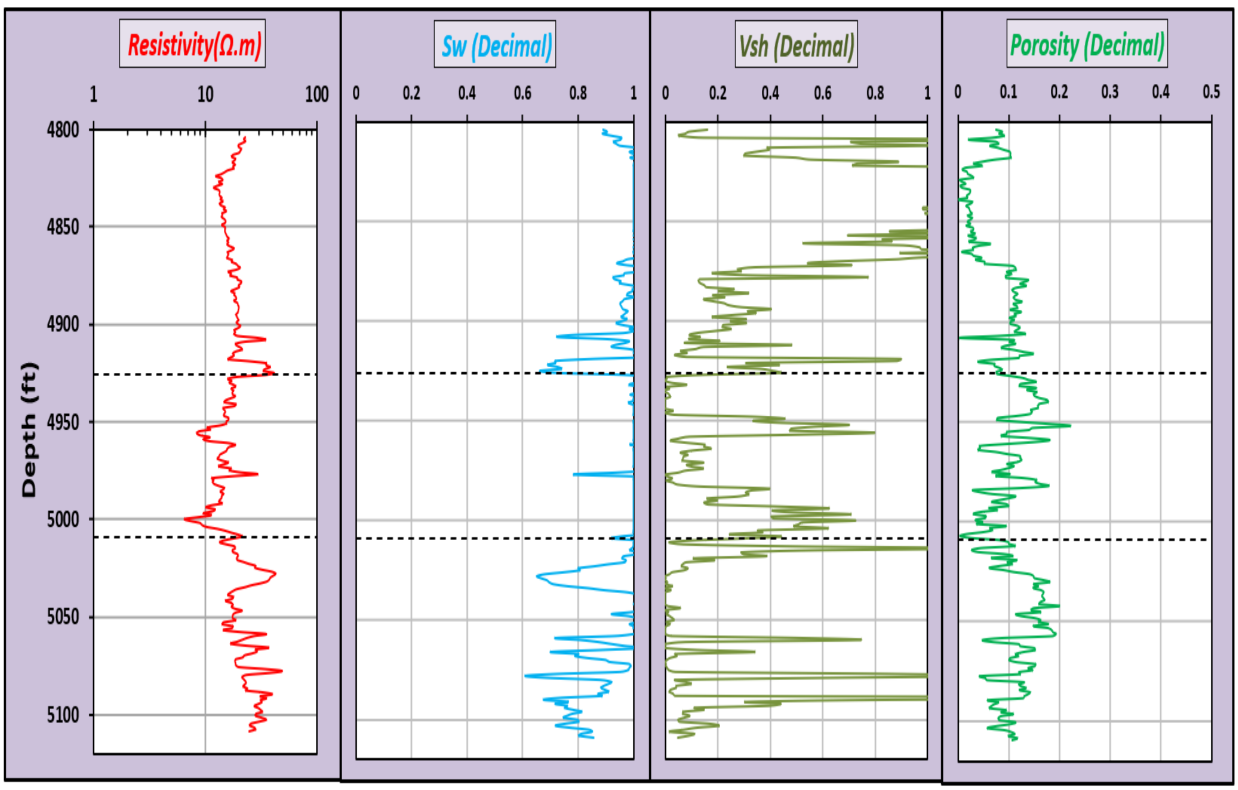

Figure 2.4: Petrophysical analysis of Well D. Dashed lines represent upper and lower Hutton Formation.

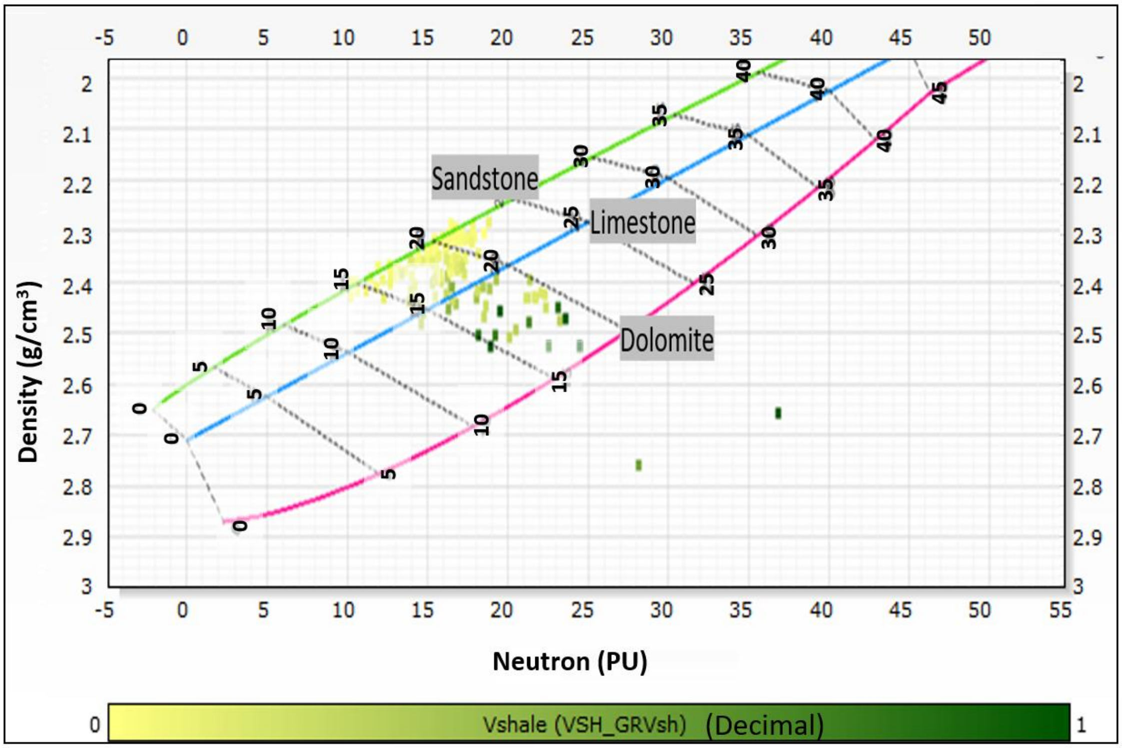

Figure 2.5: Brine-saturated zone of the Hutton Formation at Well A is plotted on density log versus neutron log Schlumberger chart.

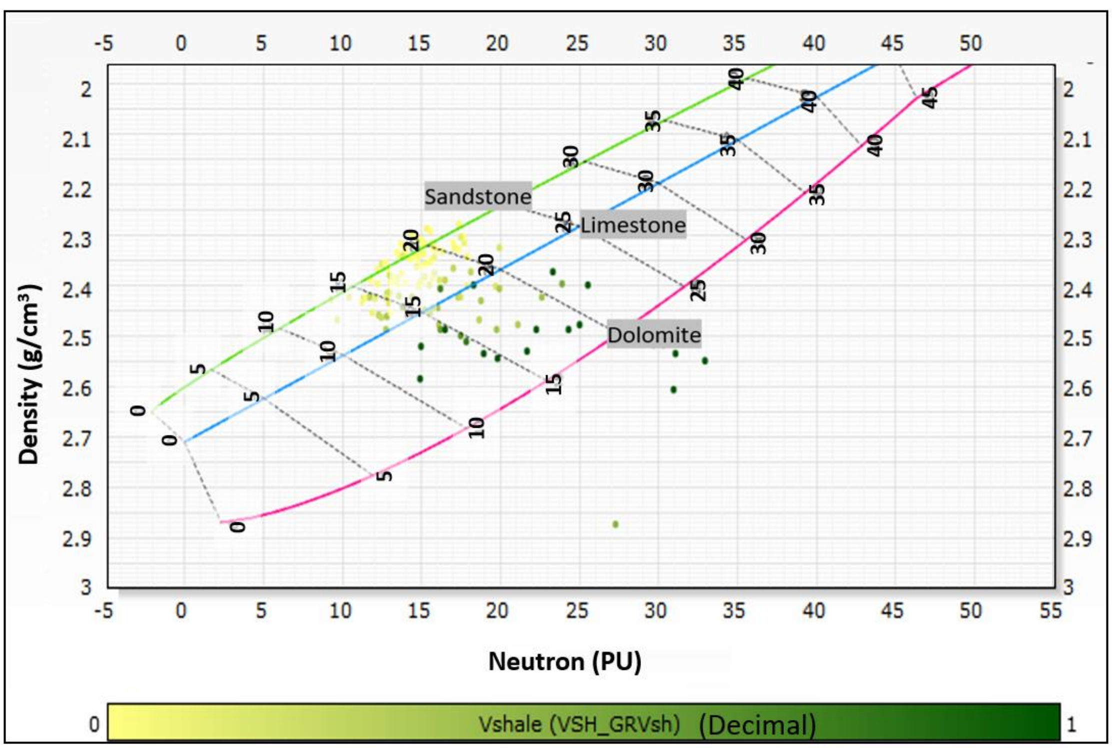

Figure 2.6: Brine-saturated zone of the Hutton Formation at Well B is plotted on density log versus neutron log Schlumberger chart.

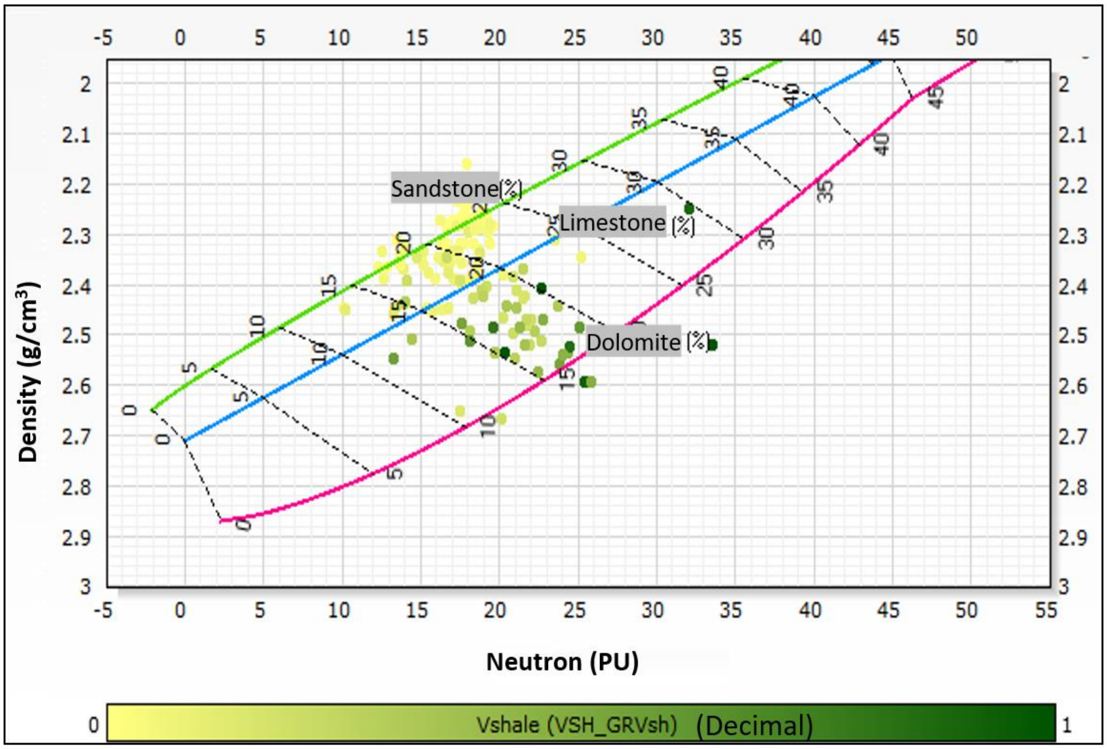

Figure 2.7: Brine-saturated zone of the Hutton Formation at Well C is plotted on density log versus neutron log Schlumberger chart.

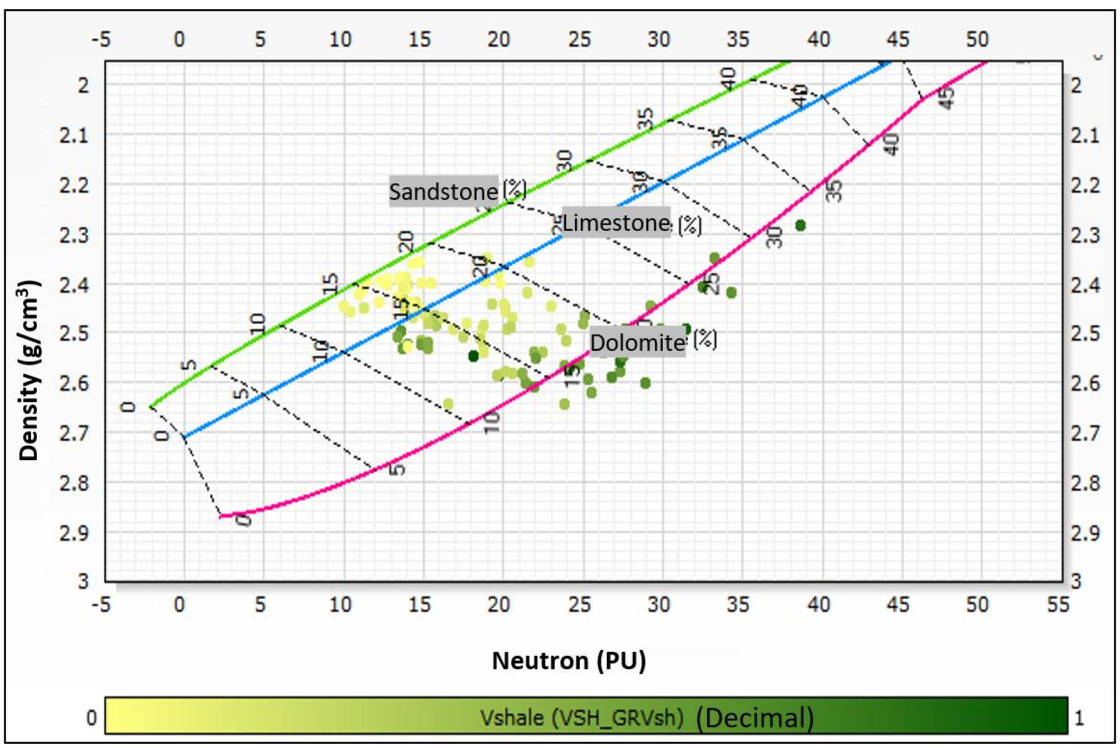

Figure 2.8: Brine-saturated zone of the Hutton Formation at Well D is plotted on density log versus neutron log Schlumberger chart.

After identifying lithology from petrophysical analysis, well log correlation was generated at the four wells to adjust formation tops at their correct positions. Well log correlation between Well A and Well B is illustrated in Figure 2.9.

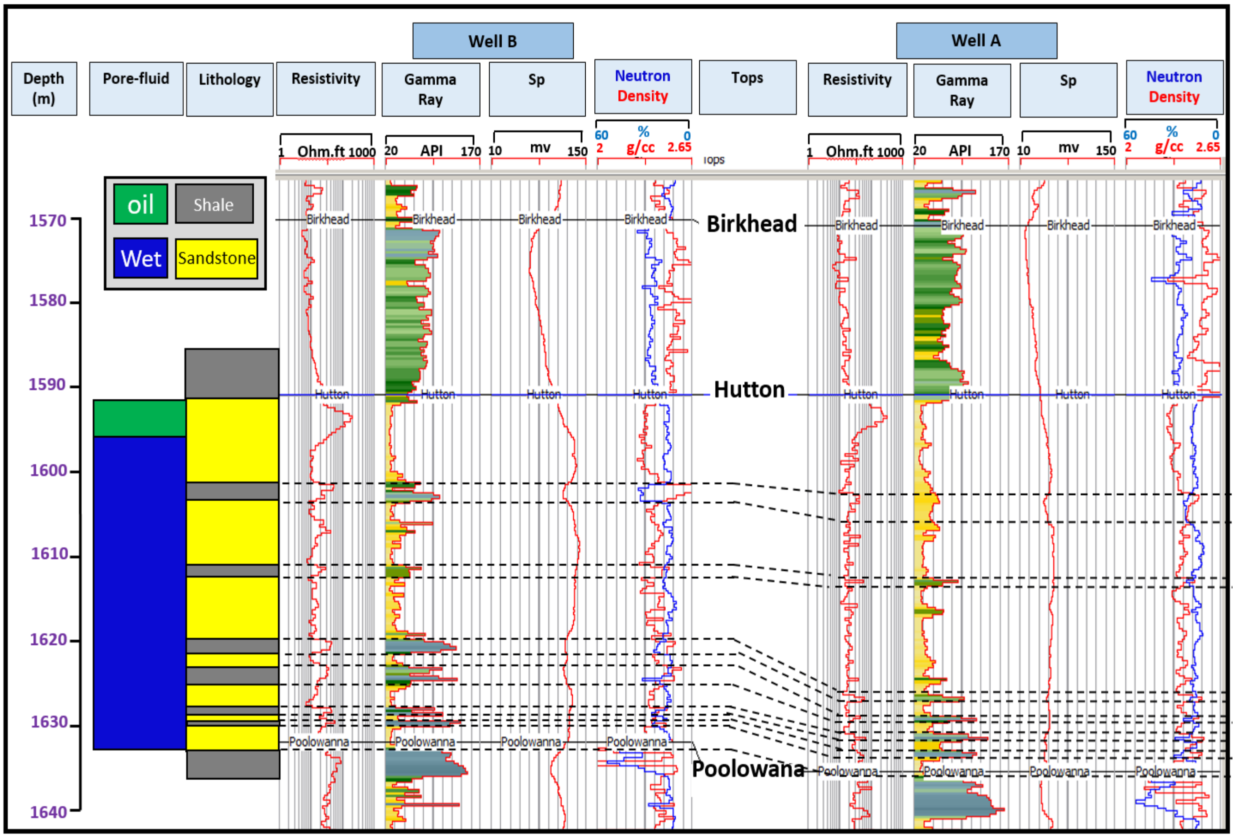

Figure 2.9: Well log correlation between Well B and Well A at the Hutton Formation.

Because these two wells are close to each other and there is no complex structure through and around them, there is a consistency in well correlation. In addition, a well log correlation was performed at the Hutton Formation between one of these two wells (Well B) and other wells (Well C and Well D) as shown in Figure 2.10. The correlation indicates decreasing in the Hutton Formation unit and increasing shale facies toward Well D. This implies lateral change not only in the Hutton Formation thickness but also in its facies toward well D.

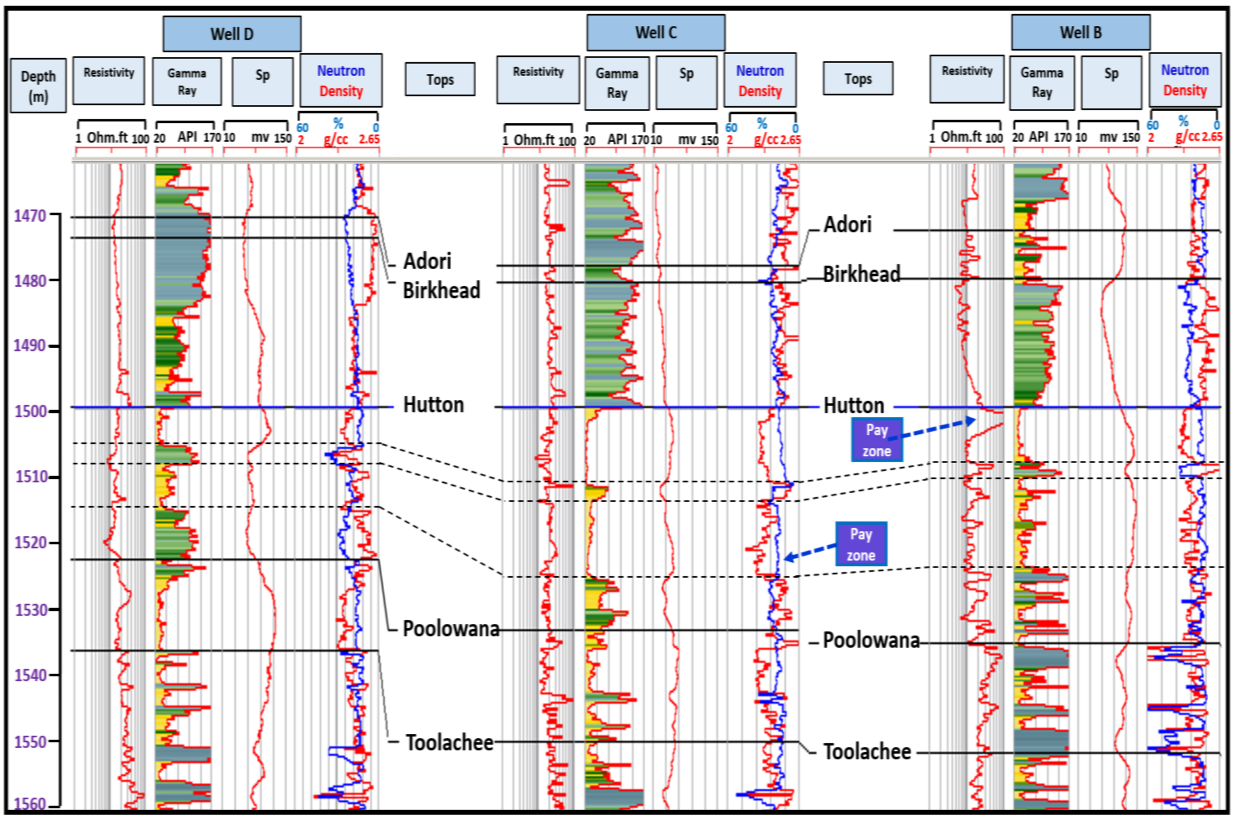

Figure 2.10: Well log correlation between Well B, Well C and Well D at the Hutton Formation. The Hutton Formation top was used as a datum plane.

The pay zone proven by the drill stem test at Well C is distributed along the second upper unit of the Hutton Formation and has crossover between neutron and density logs that are not obvious along the same unit in Well B and Well D. This implies that a seal within the Hutton Formation prevented upward hydrocarbon migration to the top of the sandstone. A layer is observed between the lower pay in Well C and the pay in Well B which is interpreted to be carboniferous siltstone because of its high density and resistivity as well as siltstone and carbonaceous claystone occurrence in the formation described in the literature (Dodman and Rodrigues (1998).

From well correlation, it is also noticed that the upper part of the Hutton Formation is destroyed by the lower part of the Brikhead Formation. This matches with Birkhead Formation fluvial system incision described by Hamilton et al., (1998) as shown in Figure 2.11.

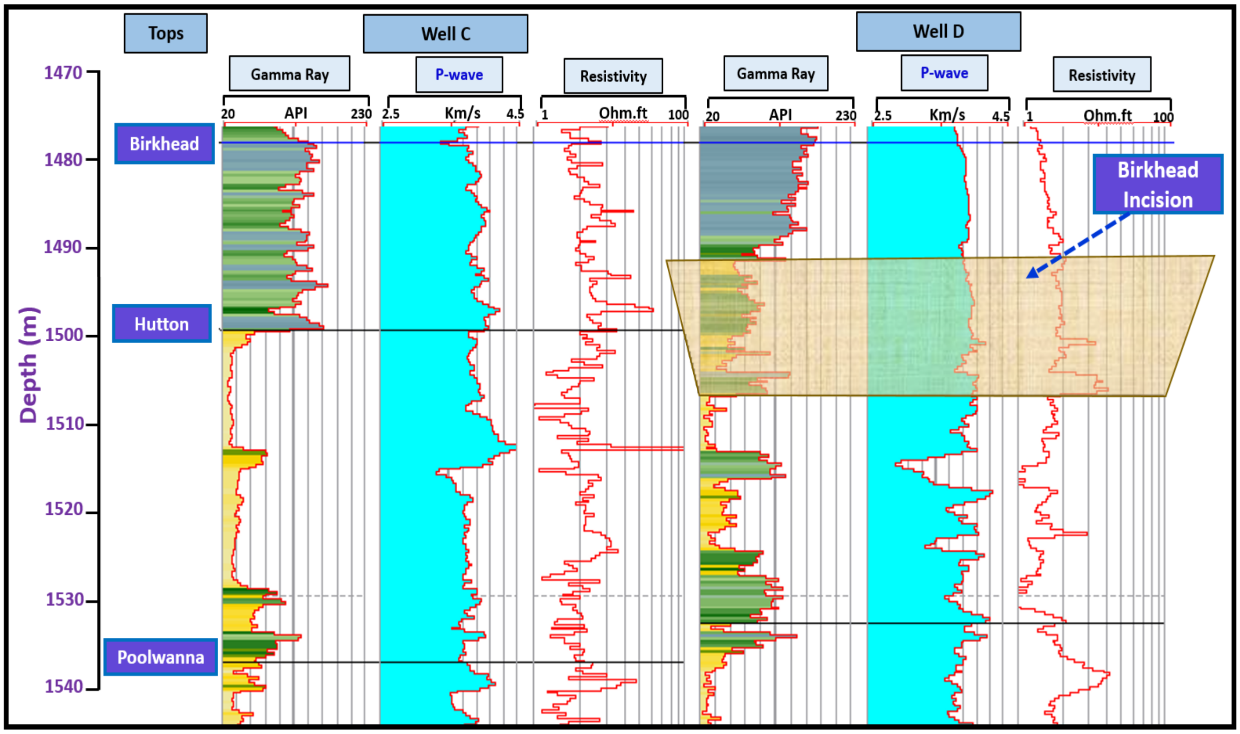

Figure 2.11: Lower part of Birkhead Formation is incised in the upper part of the Hutton Formation.

2.2. Rock-property analysis

In this research, the ultimate goal is to obtain estimates of the petrophysical properties for away from wells using the seismic data, inversions and rock-property analysis from petrophysical crossplots and trends. The 3D seismic volumes available for the 3D petrophysical volume estimates include, though are not necessarily limited to: P-wave velocity (Vp), S-wave velocity (Vs), Acoustic Impedance (AI), Shear Impedance (SI), Vp/Vs ratio, Poisson’s ratio and Pseudo-Lambda-Rho.

P-wave and S-wave velocity are theoretically calculated for an isotropic medium by the following equations:

$$Vp = \sqrt{\frac{K + \frac{4}{3}\mu}{\rho}} \text{ and } Vs = \sqrt{\frac{\mu}{\rho}}\ , \qquad (2\text{-}7)$$

where K is bulk modulus, μ is shear modulus and ρ is density.

Using well-log inversion for grain moduli as describe by (Chaveste and Hilterman, 2007), the saturated moduli K and μ are expressed in terms of grain moduli, porosity and *Sw*, which is the starting point for sensitivity analyses using appropriate empirical and/or theoretical rock-property relationships.

One well in the study area, Well A, has sonic and shear dipole logs. Oil saturation, *Vp* and *Vs* curves are available in Well A. However, Wells B, C, and D only have sonic logs. A *Vp* versus *Vs* regression relationship was established at Well A. The resultant *Vp* versus *Vs* relationship is compared with the other empirical and theoretical *Vp* versus *Vs* relationships, such as the mudrock line (Castagna, 1985). The *Vp* versus *Vs* relationship at Well A is close to the mudrock line trend in all formations as well as the brine-saturated interval of the Hutton formation. The regression coefficients are shown in Figures 2.12 and 2.13 where Well A results are compared to the mudrock line.

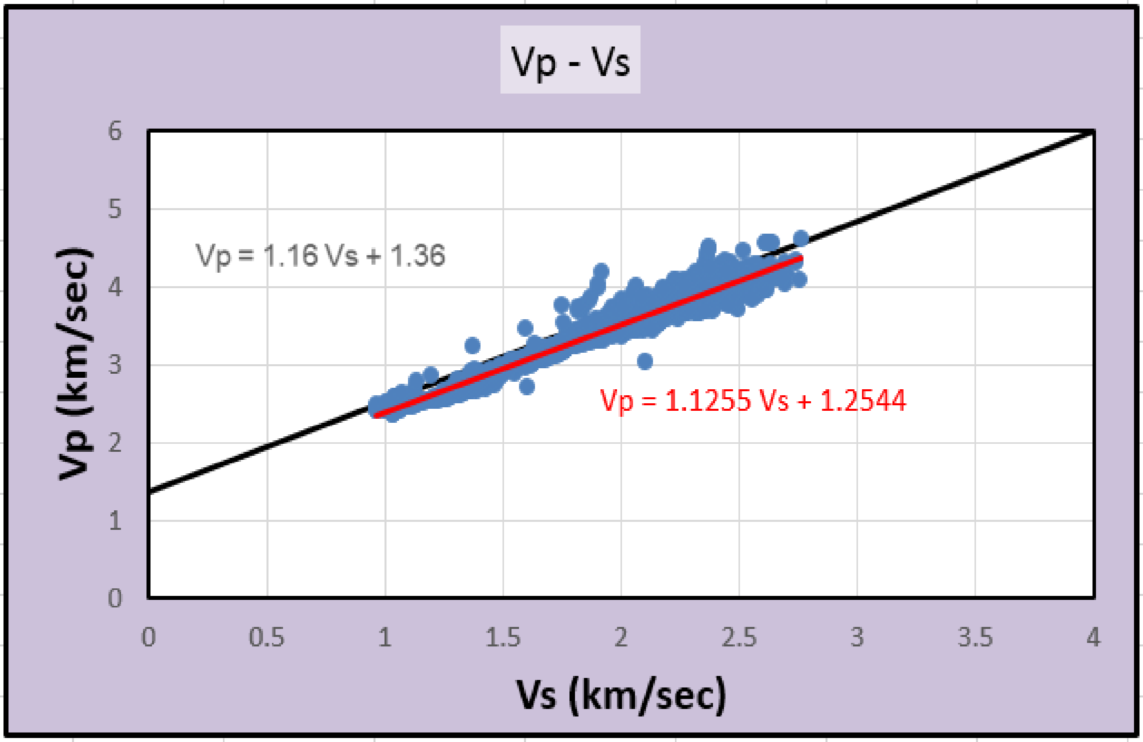

Figure 2.12: *Vp* versus *Vs* relationship for depth interval 3608 ft – 5512 ft at Well A.

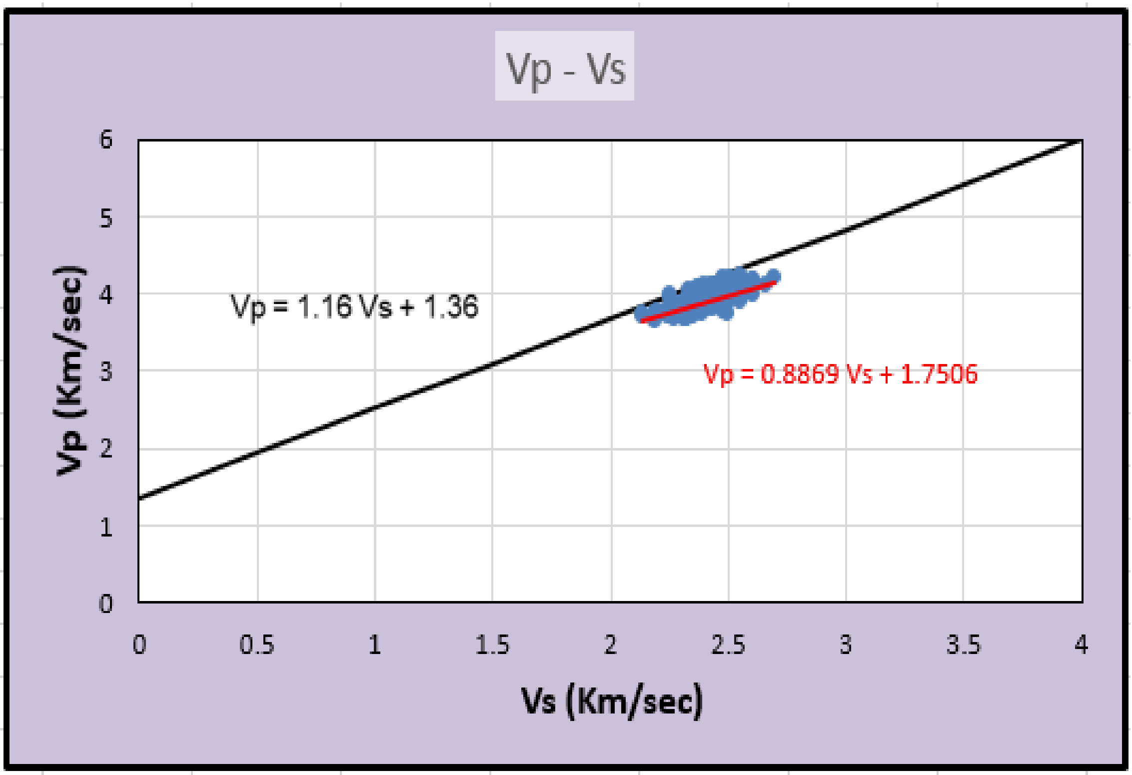

Figure 2.13: *Vp* versus *Vs* relationship for brine-saturated zone of Hutton Formation at Well A.

Measured shear-wave velocity at Well A is compared with shear-wave velocity predicted by the Greenberg and Castagna (1992) equation. Because there is a small shift between measured and predicted shear-wave velocity, regression coefficients of the Greenberg and Castagna equation for sandstone were modified and velocity was calculated linearly by the following equation:

$$Vs = ((0.7019*Vp - 0.3134)*Vsand) + ((0.76969*Vp - 0.86735)*Vsh), \qquad (2\text{-}8)$$

where $Vsand$ is volume fraction of quartz and Vsh is volume fraction of clay and $Vsand + Vsh = 1$.

The modified regression coefficients were calculated at Well A from trend lines of clean sand and shale zones. Because Vp and Vs change with depth, clean sand and shale zones were chosen to be quite close to the target reservoir zone. Figure 2.14 and 2.15 show comparison between measured and predicted shear-wave velocity by the Greenberg and Castagna (1992) equation and predicted shear-wave velocity by modified regression coefficients at Well A. Predicted shear-wave velocity by the modified regression coefficients is very close to the measured shear-wave velocity at Well A. Thus, Vs was calculated at Well B, Well C and Well D by using modified regression coefficients in equation (2-8).

Only the parameters of sandstone were modified in the Greenberg and Castagna (1992) equation. Because the Greenberg and Castagna equation parameters were estimated well for clean sandstone, the modified parameters for sandstone indicate mineralogy deviation of the Hutton formation from pure quartz. This would be expected for immature sandstones with feldspars, clays, and lithic fragments.

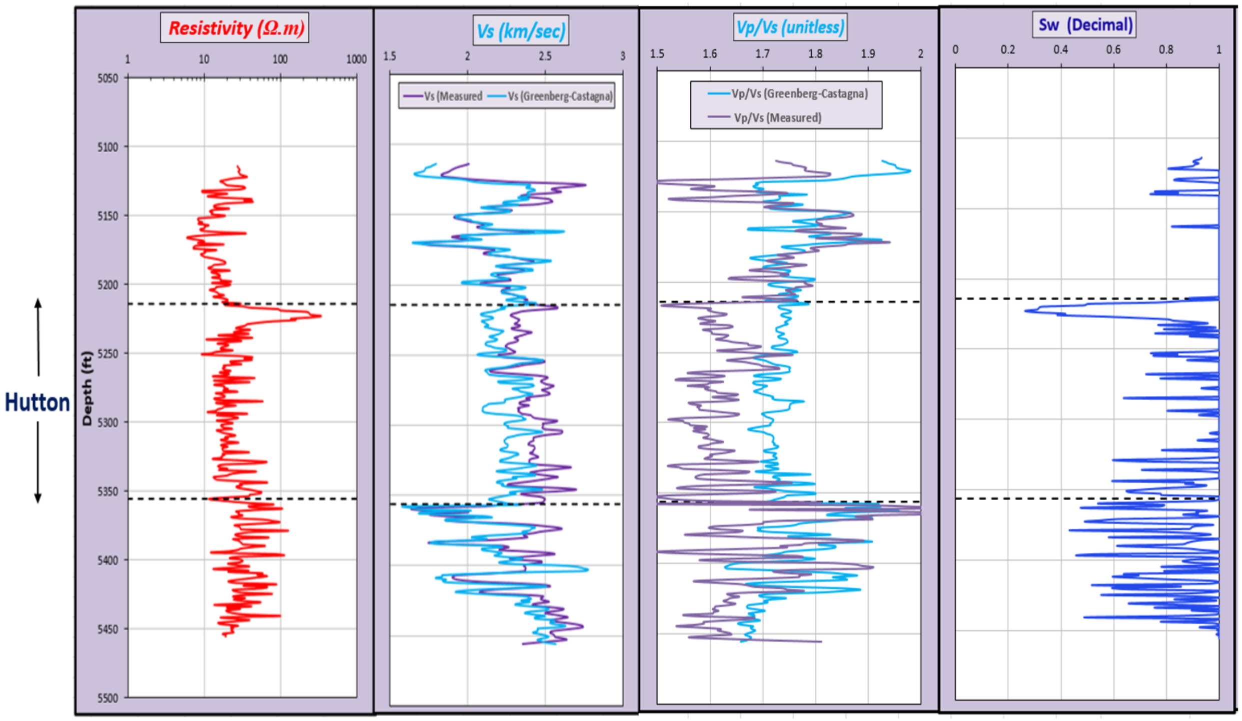

Figure 2.14: Comparison between measured and predicted shear-wave velocity by the Greenberg and Castagna (1992) equation.

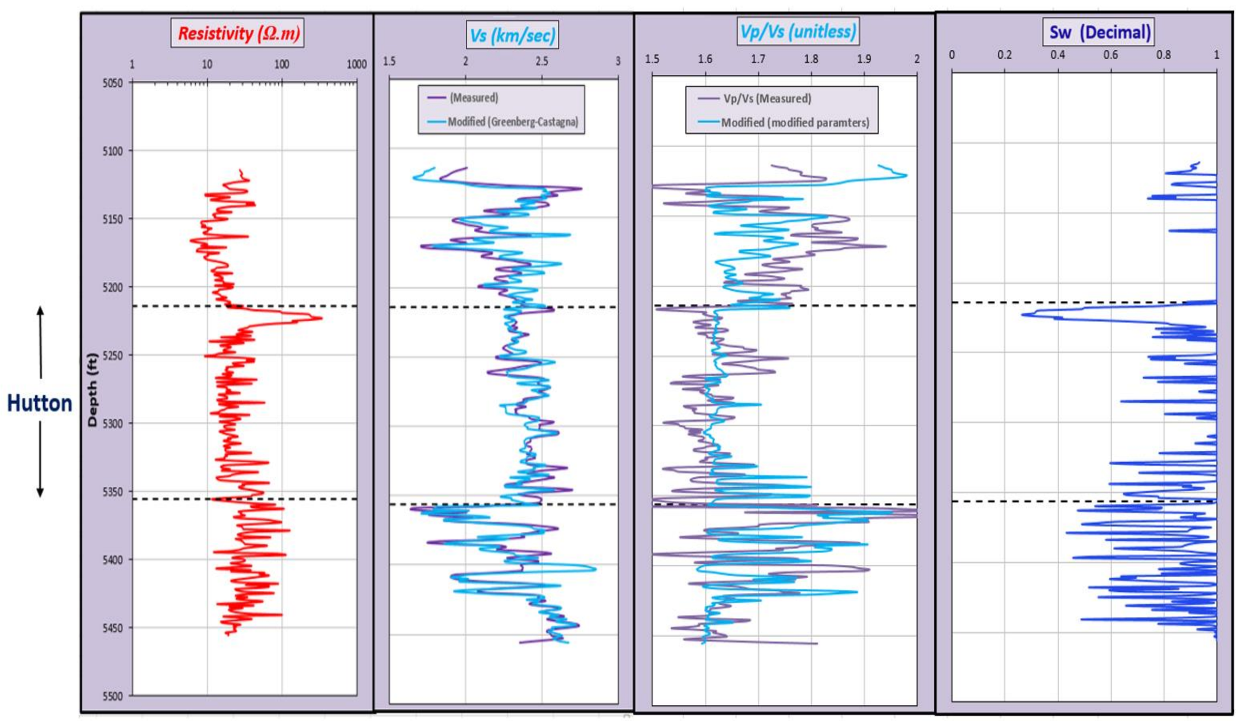

Figure 2.15: Comparison between measured and predicted shear-wave velocity by modifying regression coefficients.

Acoustic Impedance (*AI*), Shear Impedance (*SI*), Poisson ratio and Lambda-Rho ($\lambda\rho$) are calculated using the following equations:

$$AI = \rho * Vp \ , \tag{2-9}$$

$$SI = \rho * Vs \ , \tag{2-10}$$

$$\sigma = \frac{0.5-\left(\frac{VS}{VP}\right)^2}{1-\left(\frac{VS}{VP}\right)^2}, \text{ and} \tag{2-11}$$

$$\lambda\rho = (AI)^2 - c(SI)^2 \ . \tag{2-12}$$

As shown in Figure 2.16, there are no abrupt differences in the velocity-depth trends between the A, B, C and D wells. Most of the velocity variations with depth are attributed to lithology variations and not attributed to overpressure.

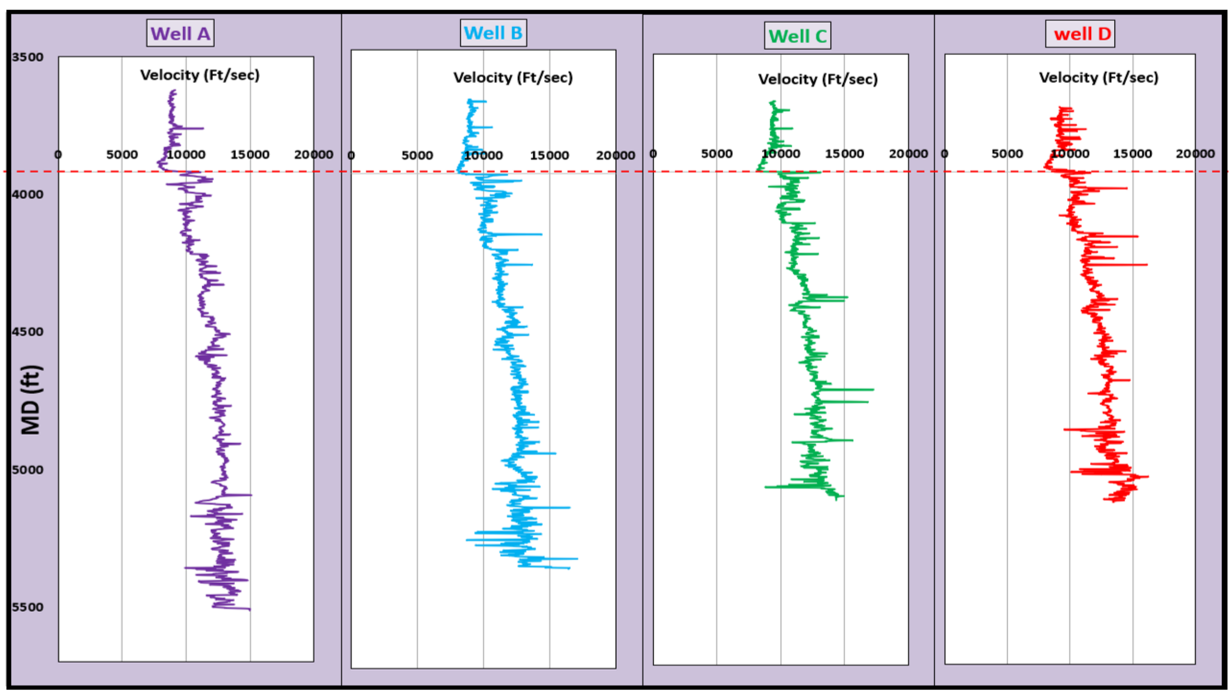

Figure 2.16: Velocity-Depth trend at A, B, C and D Wells. Red dashed line represents the Cadna-Owie, C, seismic marker.

Figure 2.17 focuses on velocity variations at wells within the Hutton sandstone depth range. There is a significant change in velocity at Well D. At the upper part of the Hutton formation, there is an increase in velocity at Well D compared with other wells which is attributed to facies change. Furthermore, there is a large decrease in velocity in the middle part of the Hutton Formation at Well D. Because this low-velocity zone corresponds to high gamma ray and Well D has no significant hydrocarbons, the velocity decrease is attributed to facies changes. In addition, there is an increase in velocity at the middle of the pay zone at Well C. This increase is also attributed to facies change.

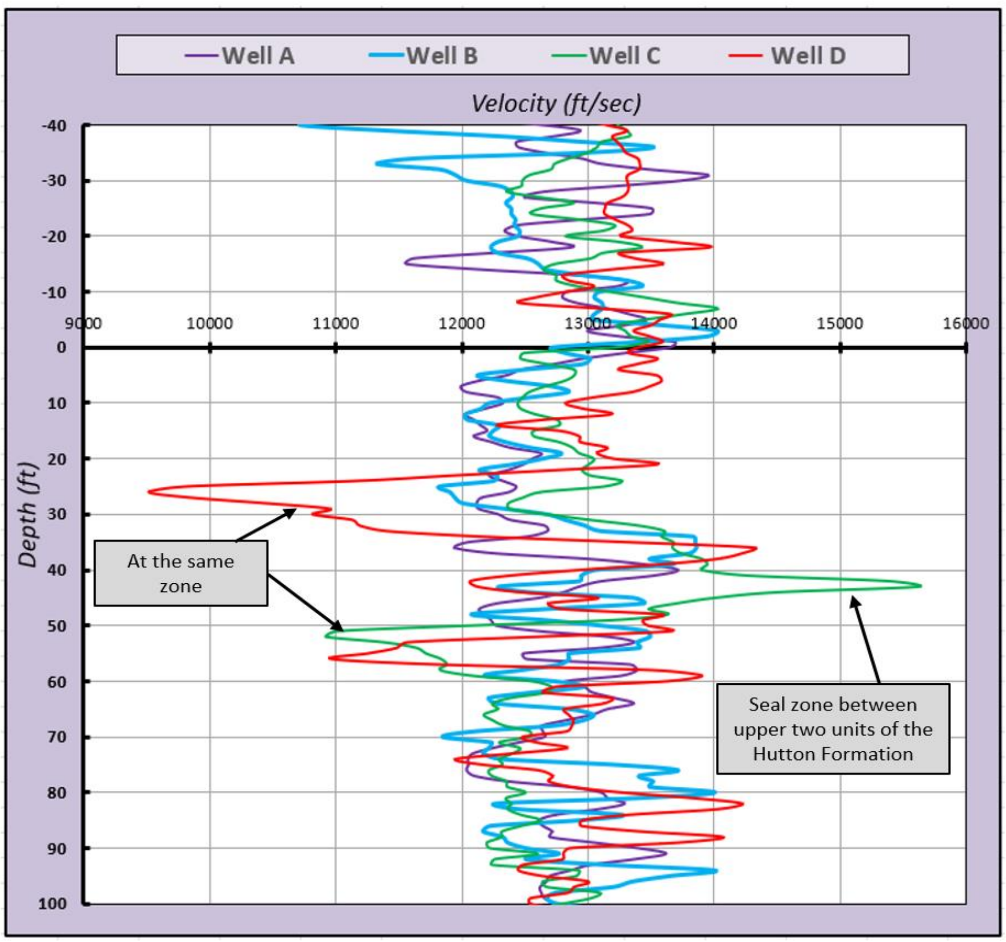

Figure 2.17: Velocity-Depth trend at A, B, C and D Wells. Black horizontal line represents the Hutton Formation top.

To address density variation with depth, Figure 2.18 shows that there is no abrupt change in the density-depth trends at the four wells (A, B, C and D). Most of the density variations with depth are attributed to lithology variations and not attributed to overpressure. Figure 2.19 focuses on density variation with depth within the Hutton formation at the four wells. At the upper and lower parts of the Hutton Formation, there is an increase in density at Well D compared with other wells. This increase may be attributed to facies change.

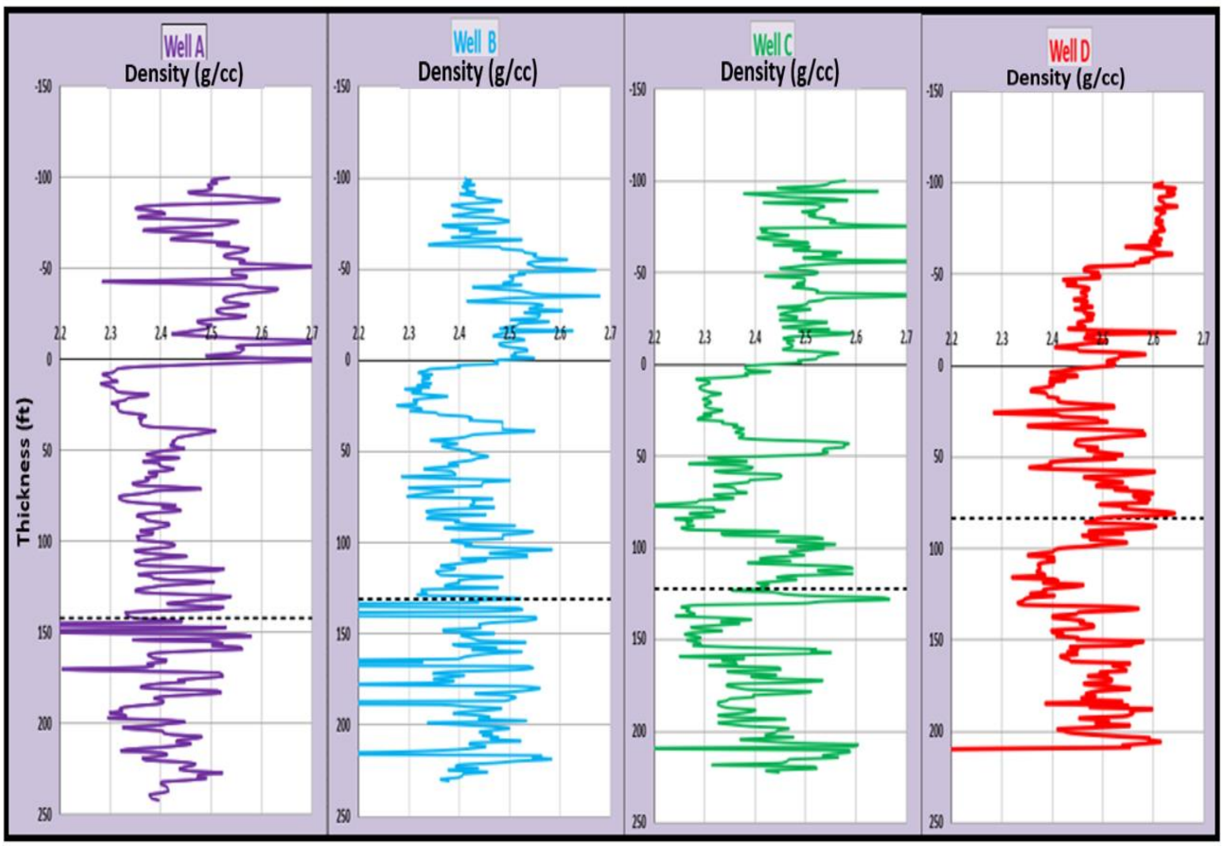

Figure 2.18: Density-Depth trend at A, B, C and D Wells. Datum at zero level represents the Hutton Top and dashed lines represents the Hutton bottom.

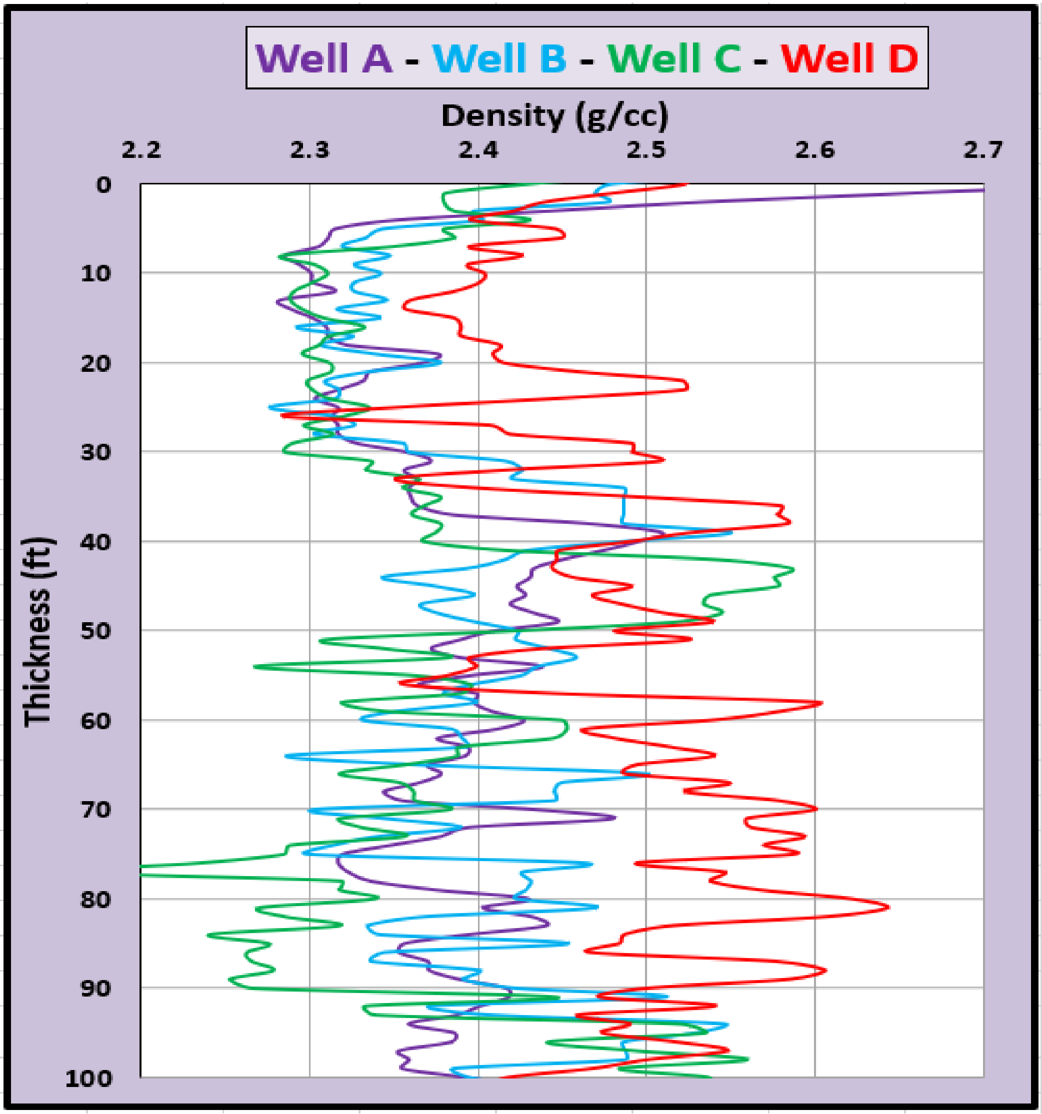

Figure 2.19: Density-Depth trend at A, B, C and D Wells for 100 m below the Hutton Formation Top.

2.3. Rock-property crossplots

After extracting petrophysical and rock properties from well logs, crossplots of various rock properties versus petrophysical properties were generated. From these crossplots, different lithologies and pore fluids were discriminated. In addition, these petrophysical properties will assist in evaluating depositional trends and the degree of lithification of the Hutton Formation.

Velocity-Density and Velocity-Porosity crossplots are theoretically and empirically generated by many authors. Gardner (1974) proposed an empirical relationship between velocity and density for all sedimentary rocks:

$$\rho = 1.741\ V^{0.25}\ , \qquad (2\text{-}13)$$

where ρ is density (g/cc) and V is velocity (km/sec). Castagna (1993) extended Gardner's work by developing velocity-density transforms that were a function of rock type.

Wyllie's (1956) time-average equation is an empirical estimate of slowness for well lithified brine porous rocks:

$$1/V = (1\text{-}\Phi)/V_{ma} + \Phi/V_{fl}\ , \qquad (2\text{-}14)$$

where V is rock velocity, V_{ma} is matrix velocity and V_{fl} is fluid velocity.

Raymer, Hunt and Gardner (RHG) (1981) provided an updated empirical time-average equation by proposing the following expressions:

$$V = (1\text{-}\Phi)^2 Vma + \Phi Vfl \qquad (2\text{-}15)$$

for $\Phi < 37\%$, and

$$1/\rho V^2 = (1\text{-}\Phi)/\ \rho_{ma} V_{ma}{}^2 + \Phi/\ \rho_{fl} V_{fl}{}^2 \qquad (2\text{-}16)$$

for $\Phi > 47\%$.

where ρ is bulk density, V is rock velocity, ρ_{ma} is matrix density, V_{ma} is matrix velocity, ρ_{fl} is fluid density, V_{fl} is fluid velocity, and Φ is porosity.

The RHG trend represents the upper bound for the velocity-density crossplot. While the lower bound is represented by an equation similar to Wood's equation (1955). Han (1986) provides a velocity-porosity relationship that includes the effect of clay content on velocity at 40 MPa. For clean sandstone:

$$Vp = 6.08 - 8.06\Phi, \tag{2-17a}$$

and,

$$Vs = 4.06 - 6.28\Phi. \tag{2-17b}$$

For shaly sandstone:

$$Vp = 5.59 - 6.93\Phi - 2.18C, \tag{2-18a}$$

and,

$$Vs = 3.52 - 4.91\Phi - 1.89C, \tag{2-18b}$$

where *Vp* is P-wave velocity, *Vs* is the S-wave velocity, *Φ* is porosity, and *C* is clay fraction.

Voigt (1928) proposed a theoretical model that estimates the upper limit for effective moduli:

$$M_V = \sum_{i=1}^{n} f_i M_i \ . \tag{2-19}$$

Reuss (1929) proposed another theoretical model that estimates the lower limit for effective moduli:

$$1/M_R = \sum_{i=1}^{n} f_i / M_i \ , \tag{2-20}$$

where, M, is grain bulk or shear modulus.

Both models have been used in velocity-porosity crossplots to limit the upper and lower bounds. Hill (1952) took the average between Voigt and Ruess bounds:

$$M = 0.5(M_V + M_R)\ . \qquad (2\text{-}21)$$

Velocity-porosity crossplots were generated to compare data with theoretical and empirical trends in an aim to detect the depositional trend. Figure 2.20 shows Well A and Well B data colored by shale volume (*Vsh*). It exhibits a depositional sorting trend rather than a diagenetic trend. In addition, trends of brine-saturated data of the Hutton Formation at the four wells are crossplotted separately as shown in Figures 2.21, 2.22, 2.23 and 2.24. Brine data also have a depositional sorting trend and not a diagenetic trend.

In addition to identifying the depositional trend, velocity-density crossplots were generated to identify the degree of lithification. Most brine-saturated data of the Hutton Formation at the four wells plot below the RHG line and around the Gardner line but with a different trend as shown in Figure 2.25, 2.26, 2.27 and 2.28. Thus, the Hutton Sandstone is not highly lithified.

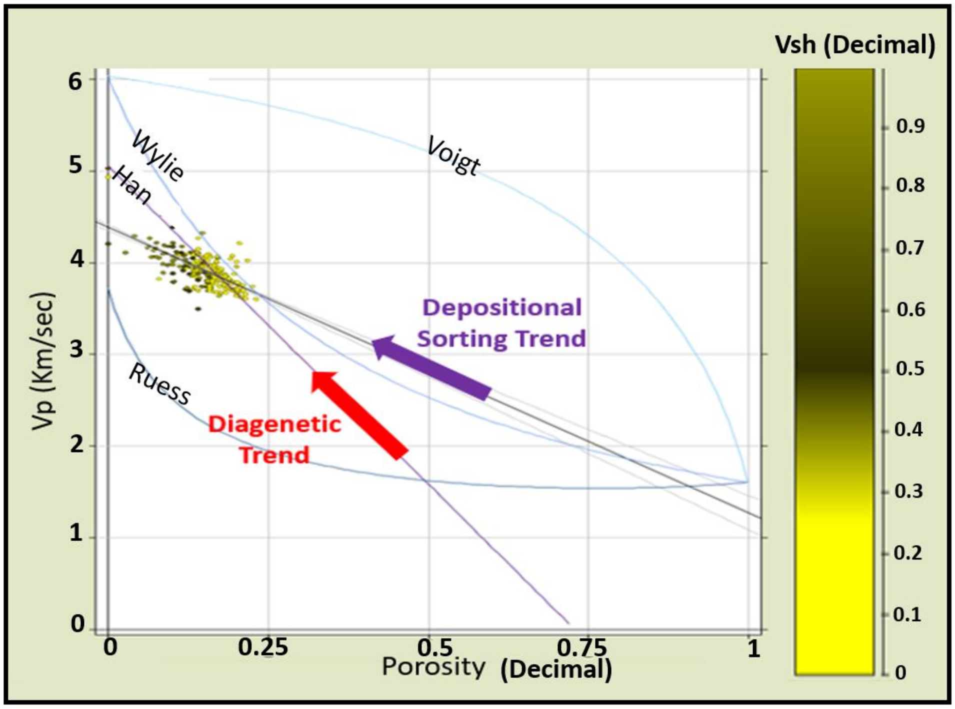

Figure 2.20: Velocity-Density relationship at Well A and Well B colored by Vsh.

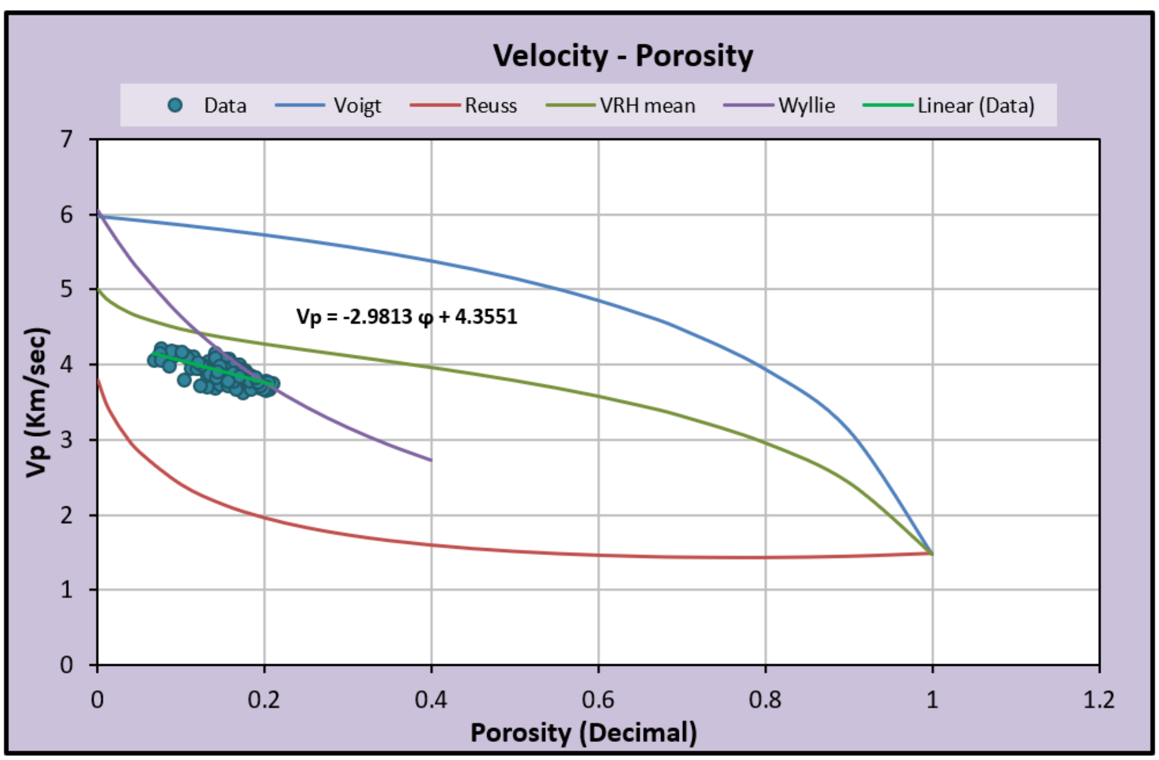

Figure 2.21: Velocity-Porosity relationship at Well A.

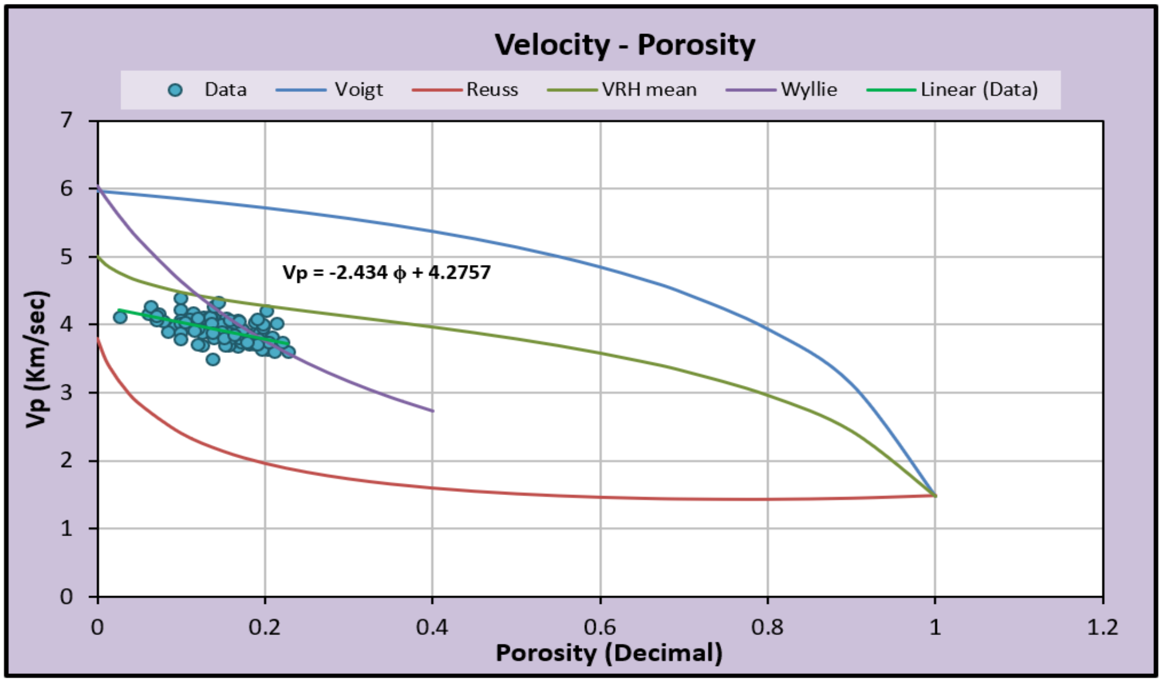

Figure 2.22: Velocity-Porosity relationship at Well B.

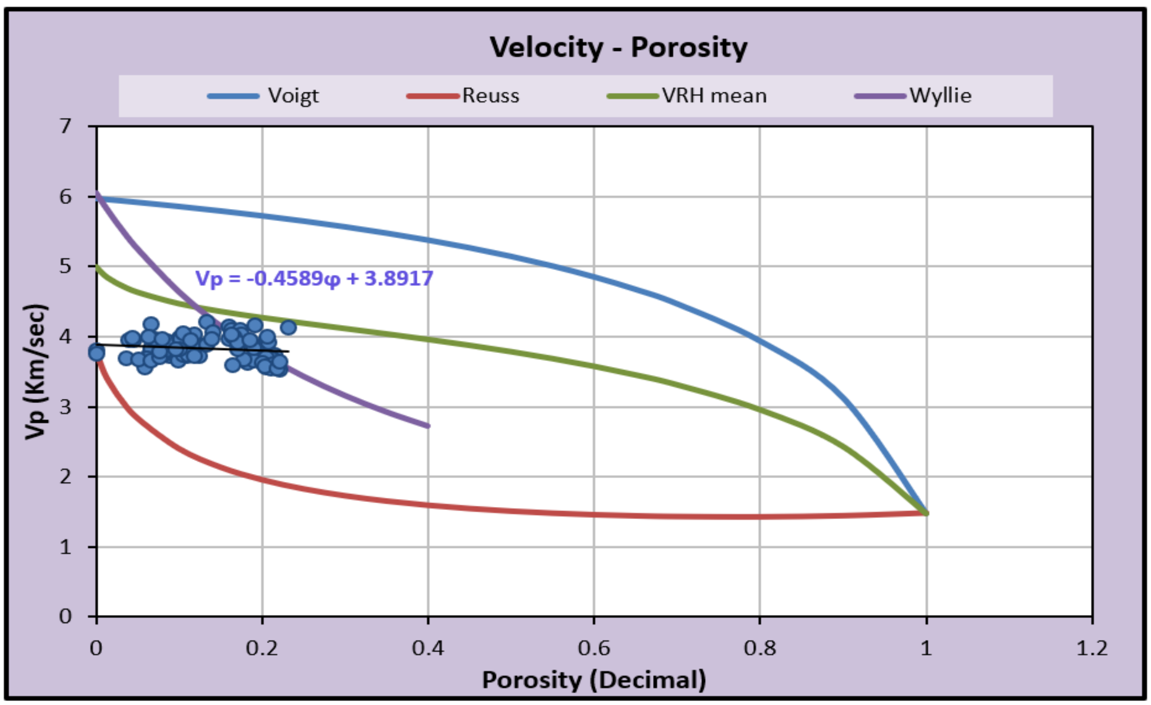

Figure 2.23: Velocity-Porosity relationship at Well C.

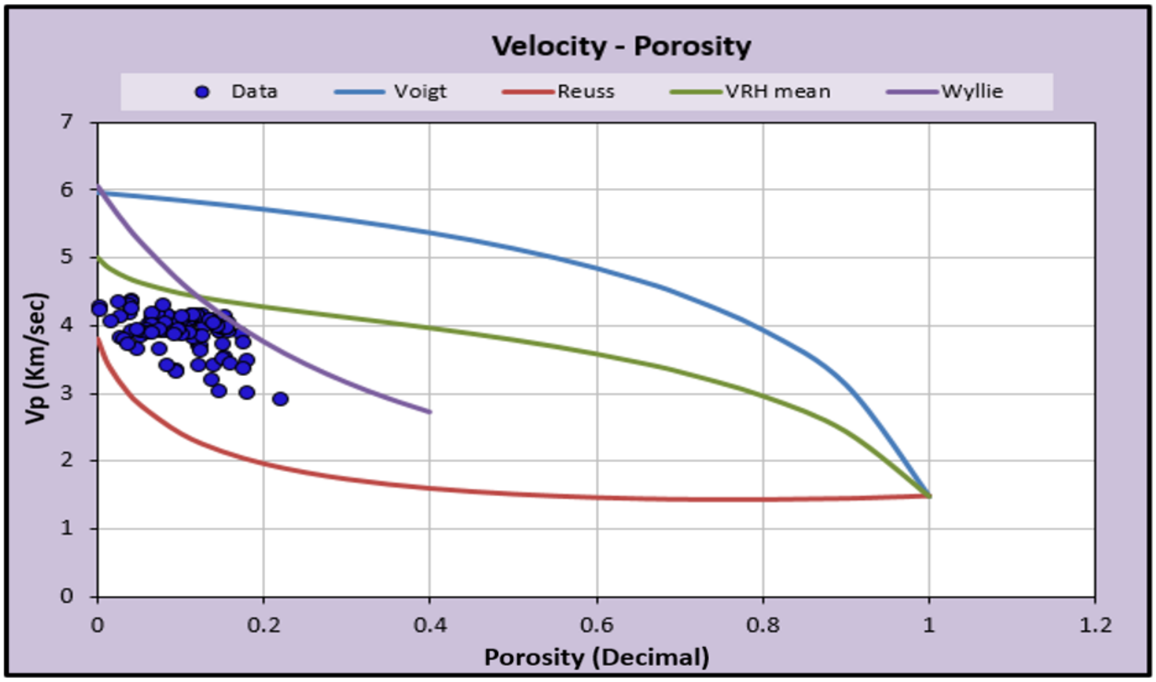

Figure 2.24: Velocity-Porosity relationship at Well D.

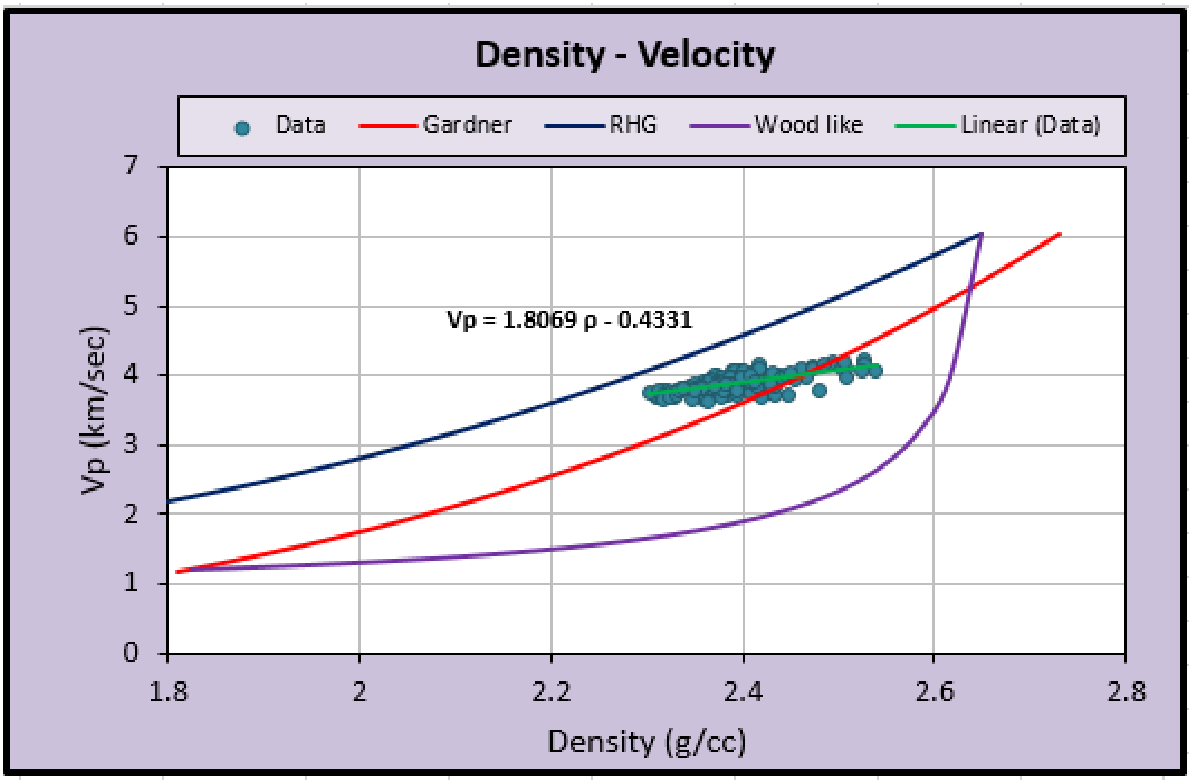

Figure 2.25: Velocity-Density relationship at Well A.

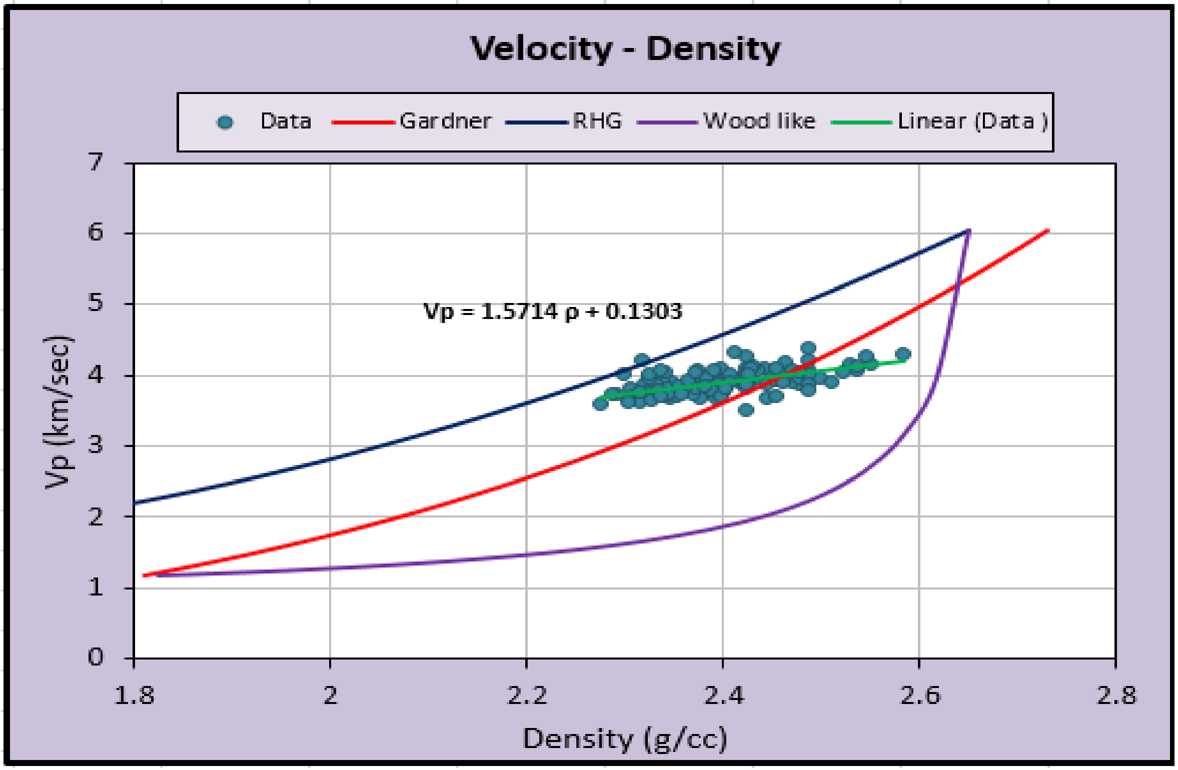

Figure 2.26: Velocity-Density relationship at Well B.

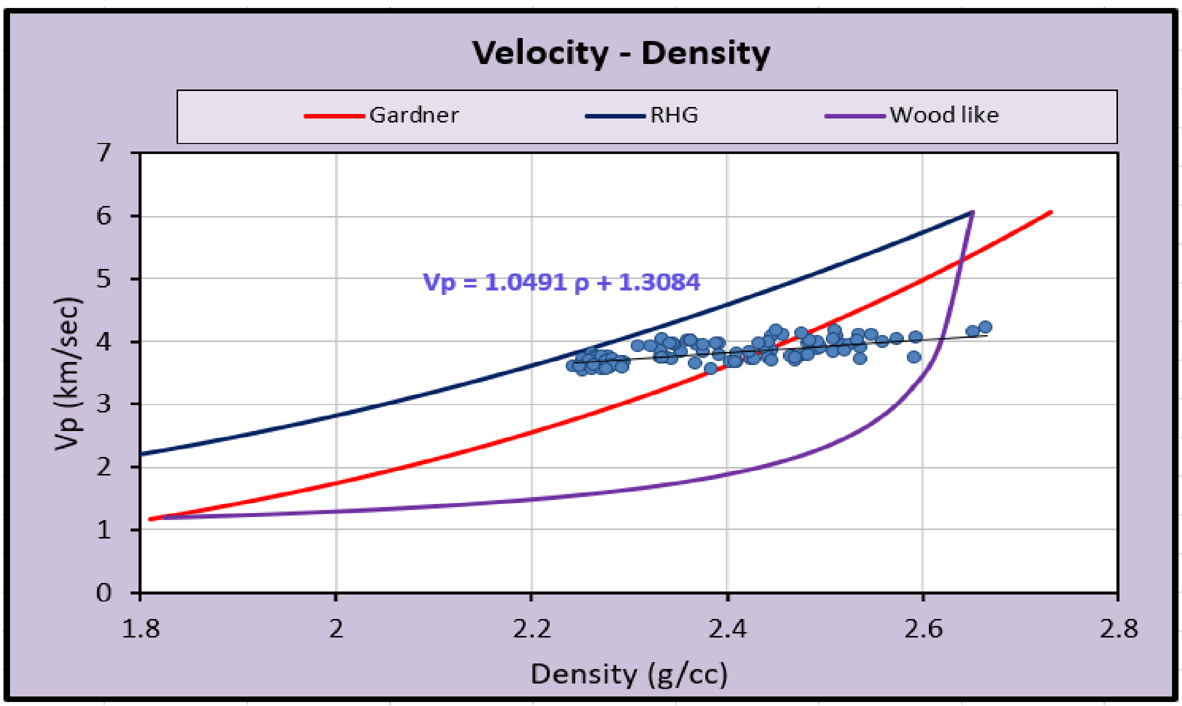

Figure 2.27: Velocity-Density relationship at Well C.

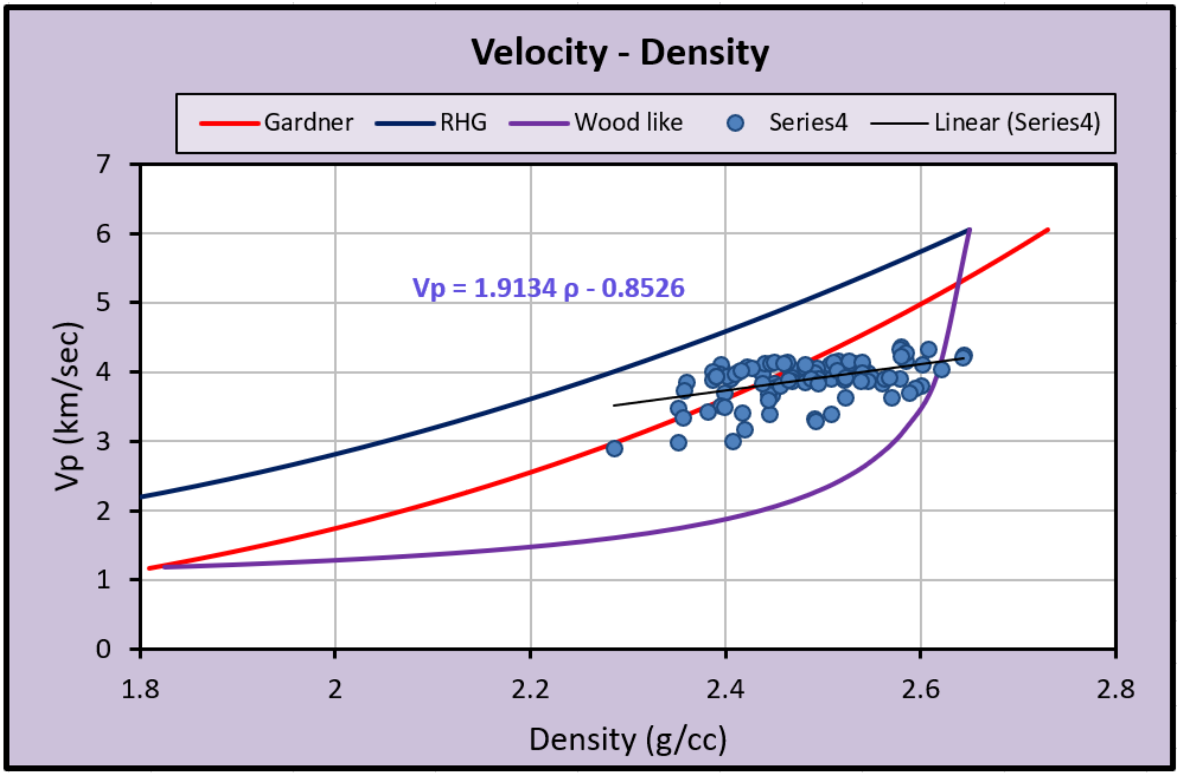

Figure 2.28: Velocity-Density relationship at Well D.

Multiple regressions were established at the four wells using only measured logs to address volume of shale and porosity effect on compressional-wave and shear-wave velocities. The calculated regression coefficients are shown in Figure 2.29. All of the regression coefficients basically indicate decreasing velocity with increasing porosity and/or volume of shale except for the oil zone of Well A and B and the brine zone of Well C. Volume of shale at these zones has positive signs which means that velocity increases with increasing shale volume. This may be attributed to shale deficiency at these zones that affects regression coefficient calculations. Rock templates were established using regression coefficients to show shale volume percentage change along data points of brine-saturated zones at the four wells as illustrated in Figure 2.30. The multiple regression equation for all the brine zones combined is *Vp*= 4.21275 -2.04512 Ø - 0.32307 *Vsh.*

Well A (P-wave)

Oil zone

$V_p = 4.19 - 2.452\,\Phi - 0.0628\,V_{sh}$

Brine zone

$V_p = 4.435 - 3.429\,\Phi - 0.104\,V_{sh}$

Well A (S-wave)

Oil zone

$V_s = 2.76 - 2.24\,\Phi + 0.59\,V_{sh}$

Brine zone

$V_s = 2.66 - 1.54\,\Phi - 0.101\,V_{sh}$

Well B (P-wave)

Oil zone

$V_p = 3.983 - 1.26\,\Phi + 0.582\,V_{sh}$

Brine zone

$V_p = 4.539 - 3.932\,\Phi - 0.188\,V_{sh}$

Well C (P-wave)

Oil zone

$V_p = 3.840 - 1.84\,\Phi - 0.644\,V_{sh}$

Brine zone

$V_p = 3.859 - 0.3824\,\Phi + 0.185\,V_{sh}$

All wells (P-wave)

Brine zones

$V_p = 4.212 - 2.045\,\Phi - 0.323\,V_{sh}$

Well D (P-wave)

Brine zone

$V_p = 4.614 - 5.175\,\Phi - 0.815\,V_{sh}$

Figure 2.29: Multiple regression coefficients calculated for pore-fluid zones at the four wells.

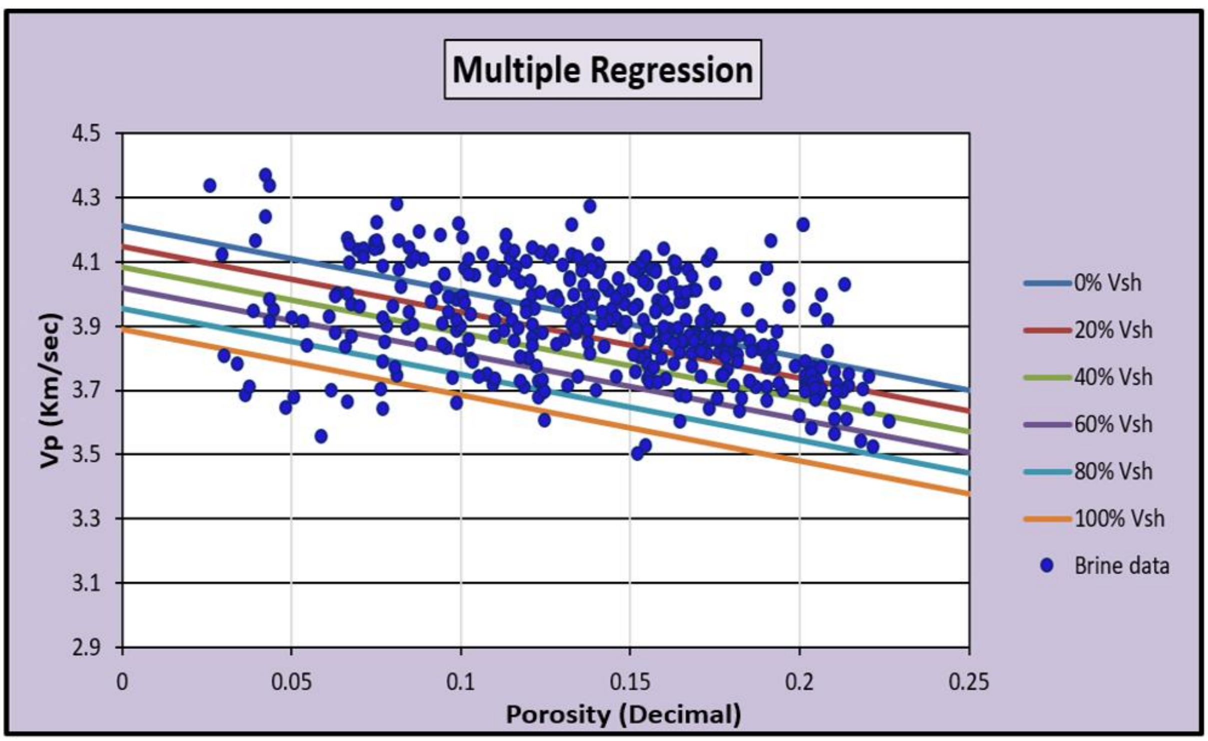

Figure 2.30: Velocity-Porosity relationship shows shale volume lines along brine-saturated zones of four wells.

In addition to identifying depositional trends and the degree of lithification of the Hutton Formation, rock-property crossplots are also used for lithology and pore-fluid discrimination. In fact, Pickett, as early as 1963, suggested using *Vp/Vs* as a lithologic discriminator. Likewise, Castagna et al., (1985) investigated *Vp/Vs* as a lithologic indicator and suggested using this ratio as pore-fluid discriminator. The rock-property lambda-rho ($\lambda\rho$) is a pore-fluid indicator suggested by Goodway et al. (1997)., This attribute is related to the pore-fluid term of Gassmann (1951) as suggested by Hilterman (2001). Russell et al., (2003) modified it to a pseudo-lambda-rho attribute for achieving a better pore-fluid discrimination by rotating the wet-trend axis in the AI^2 versus SI^2 crossplot. This rotation enhances pore-fluid projection as suggested by Hendrickson (1999) and Whitcombe and Fletcher (2001).

Because Well A has measured logs, it was preferable for conducting rock property crossplots. Lithology is discriminated using the Picket (1963) chart as shown in Figure 2.31. Most data points are plotted around *Vp/Vs* = 1.6, which is a characteristic *Vp/Vs* ratio for sandstone. Some data points are shifted from this trend as volume of shale increases. The *Vp/Vs* to *Vp* relationship of Castagna et al., (1985) and *Vp/Vs* versus AI crossplot were used to discriminate pore fluids, but there is no separation between hydrocarbon and brine-saturated samples at the Hutton Formation as shown in Figure 2.32 and 2.33. Difficult discrimination may be attributed either to reservoir rock that possibly is more lithified or to pore fluid that probably approaches dead oil characteristics. In Figure 2.34, a crossplot of AI^2 versus SI^2 was generated where ($AI_{wet}^2 = 2.0625\ SI_{wet}^2 + 18.018$) is the trend of the brine-saturated zone of the Hutton Formation at well A. To discriminate pore fluids, a crossplot of SI^2 versus pseudo-lambda-rho was generated in Figure 2.35 where (pseudo-lambda-rho = $AI_{wet}^2 - 2.0625\ SI_{wet}^2 - 18.018$). There is a poor discrimination between oil- and brine-saturated samples. Oil pore-fluid is 32 API gravity with low gas-oil ratio. Therefore, oil properties similar to those of brine provide a possible reason for little discrimination between pore fluids at the wells.

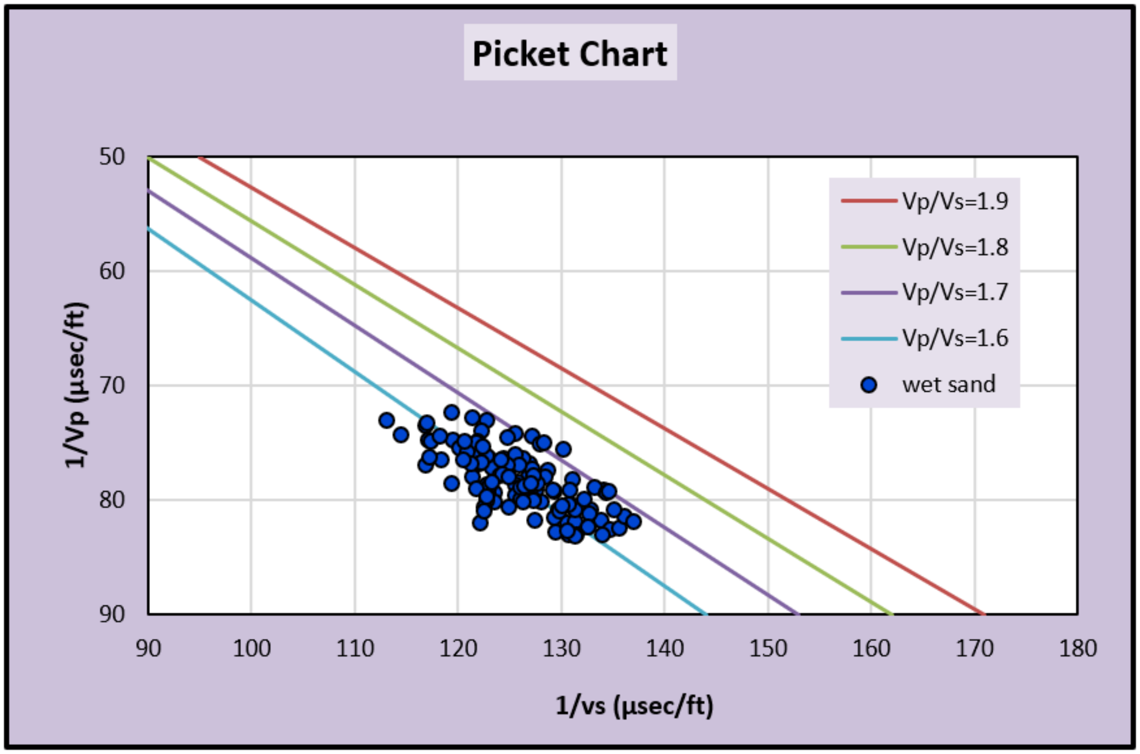

Figure 2.31: Brine-saturated zone of Hutton Formation at Well A on Pickett chart.

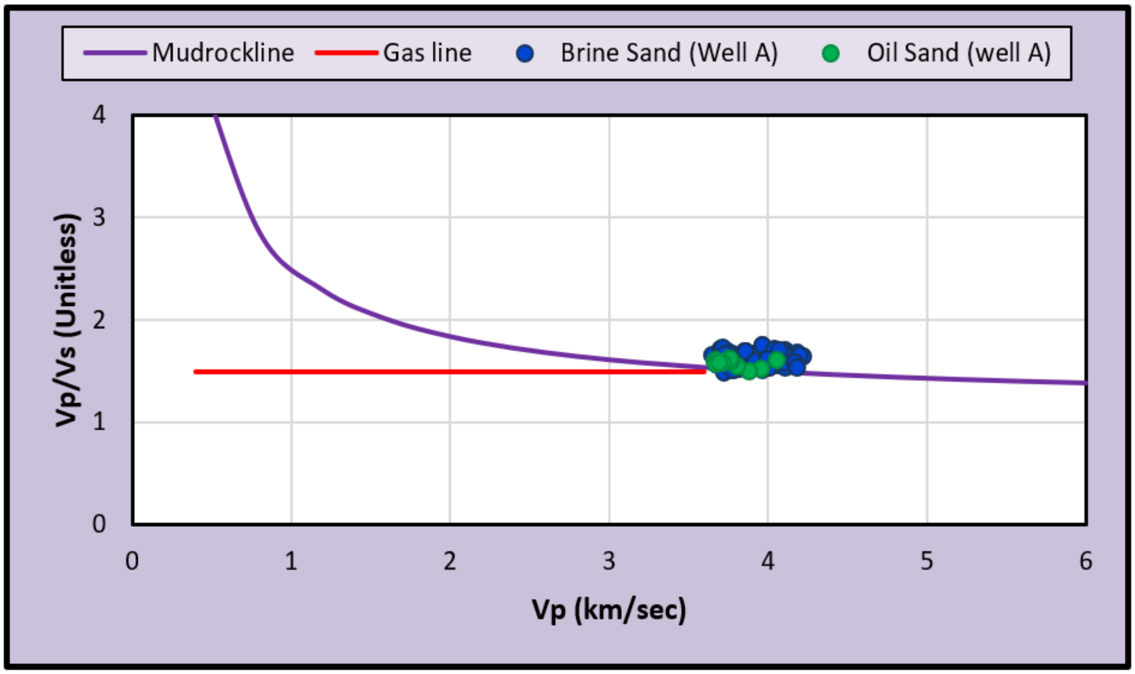

Figure 2.32: Vp/Vs – Vp relationship using the Hutton Formation data at Well A.

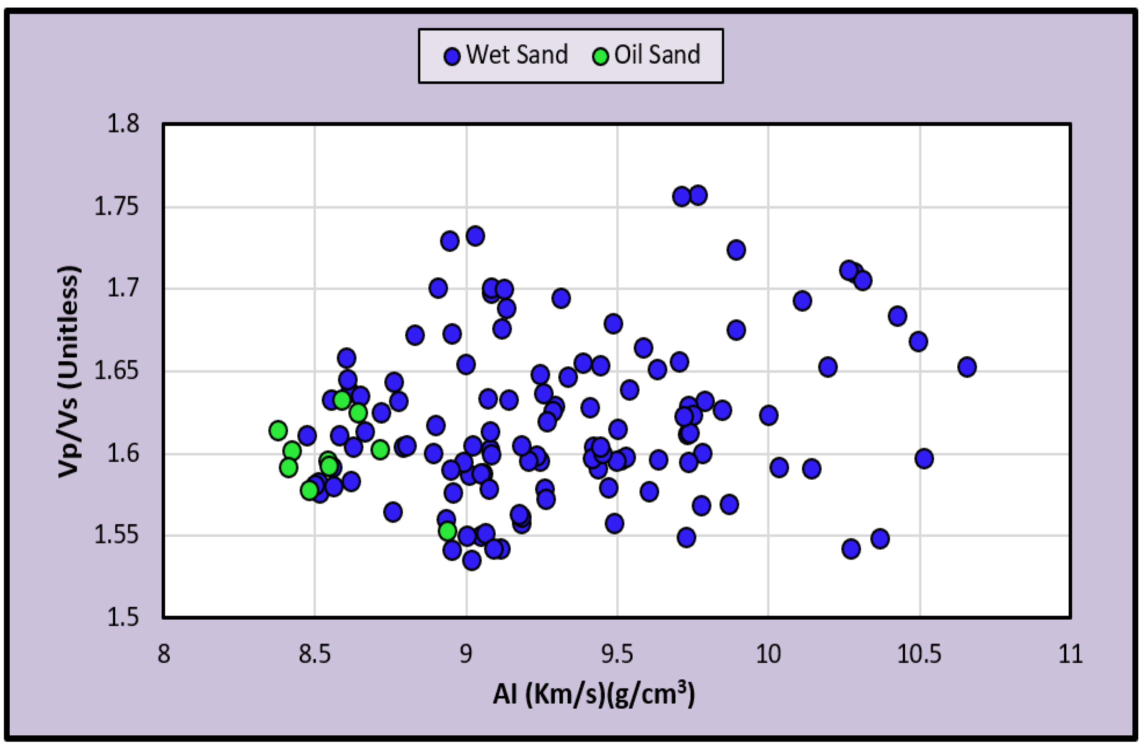

Figure 2.33: Vp/Vs – AI relationship using the Hutton Formation data at Well A.

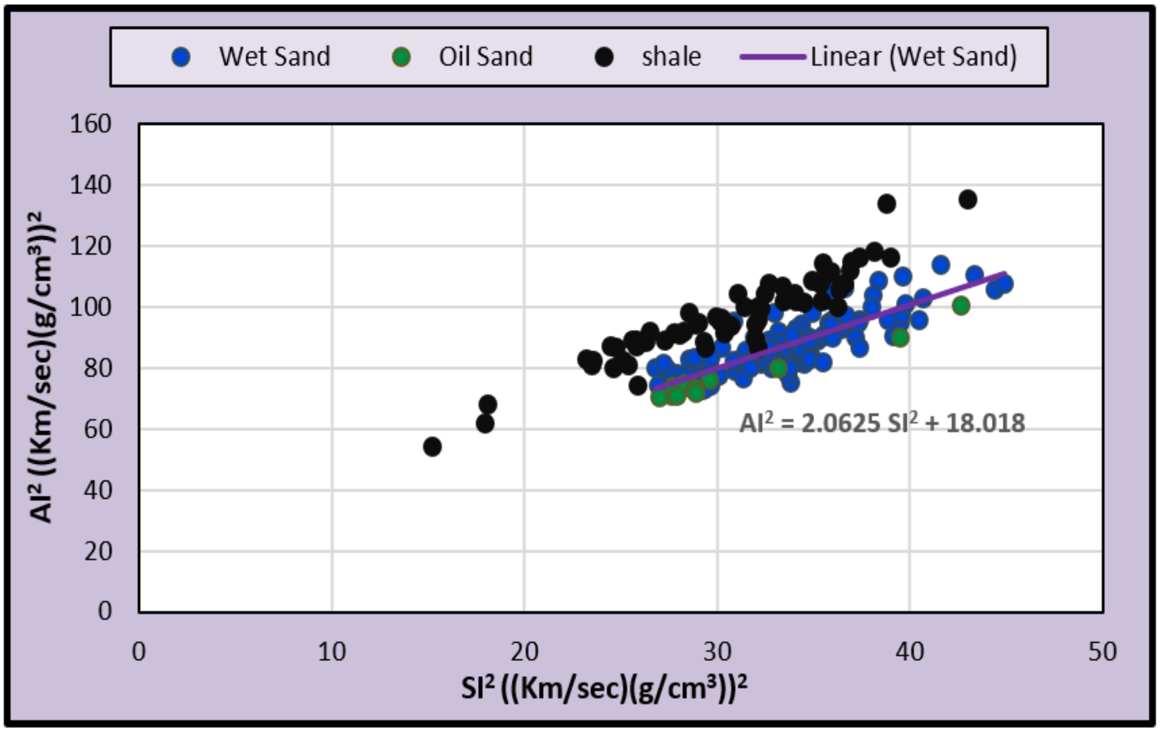

Figure 2.34: AI^2 - SI^2 relationship using the Hutton Formation data at Well A.

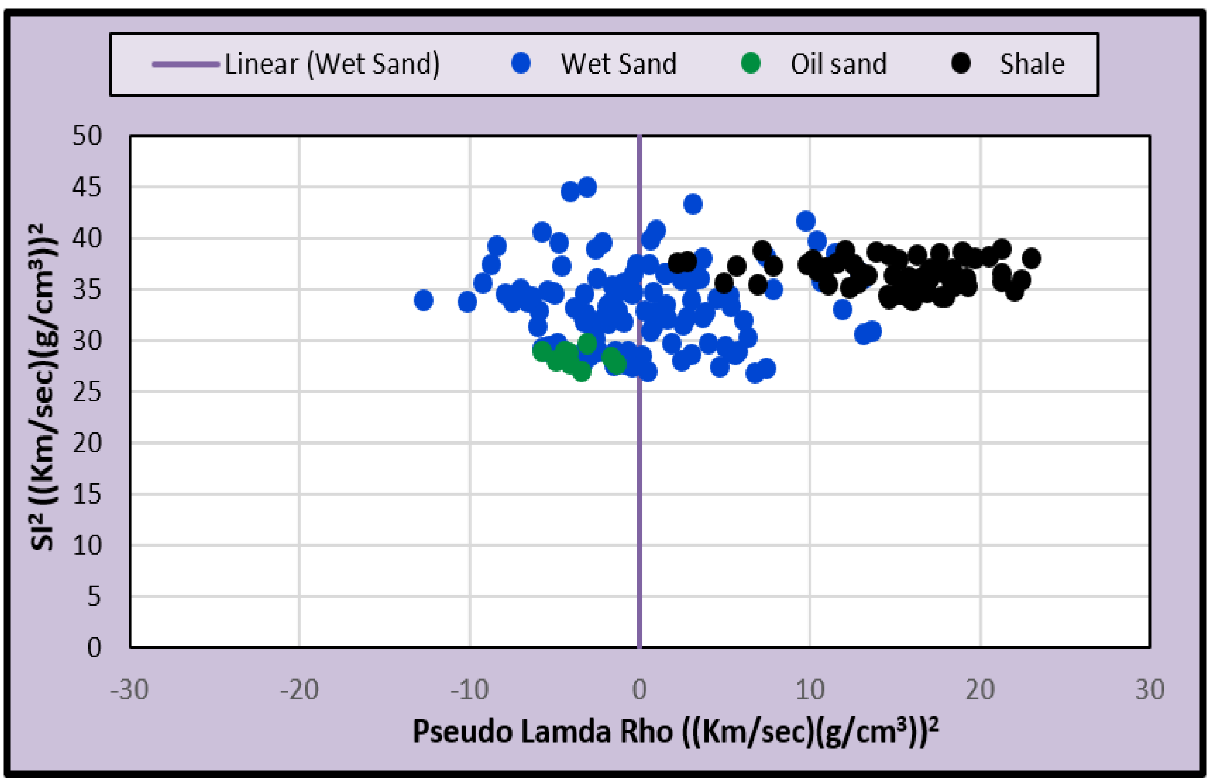

Figure 2.35: Hutton Formation data using pseudo-lambda-rho attribute at Well A.

Chapter 3

Fluid Substitution and AVO Modeling

3.1. Fluid substitution

Fluid substitution was conducted using the Gassmann equations (1951) to monitor moduli change in response to water-saturation change. Consequently, rock moduli with different pore fluids can be addressed, and hence, can be used in identifying pore fluids away from wells. Before conducting fluid substitution, reservoir fluid properties are calculated using Batzle and Wang (1992) as shown in Table 3.1.

Table 3.1: Reservoir pore-fluids properties.

Reservoir pore-fluids properties		
Pore pressure	**Temperature**	**API**
19.7 Mpa	**26.67 ^{o}c**	**32**
Gas gravity	**GOR**	**Salinity**
0.7	**200 ff3/bbl**	**3400 ppm**
Oil pore-fluid physical property		
Rho	**Vp**	**K**
0.831 g/cm^3	**1.41 Km/sec**	**1.645 Gpa**
Brine pore-fluid physical property		
Rho	**Vp**	**K**
1.008 g/cm^3	**1.54 Km/sec**	**2.754 Gpa**

Fluid substitution was started by estimating saturated bulk modulus (K_{sat}) and saturated shear modulus (μ_{sat}) logs from compressional velocity, shear velocity and density logs using equations (2-7). Matrix bulk modulus properties were estimated using the Reuss lower bound and the Voigt upper bound and then averaged using the Hill average by following equations:

$$K_{Reuss} = \left[\frac{F_1}{K_1} + \frac{F_2}{K_2}\right]^{-1}, \tag{3-1}$$

$$K_{Reuss} = [F_1 K_1 + F_2 K_2] \text{ , and} \tag{3-2}$$

$$K_{VRH} = \frac{1}{2}\left[K_{Voigt} + K_{Ruess2}\right], \tag{3-3}$$

where K_1 is bulk modulus for quartz and K_2 is bulk modulus for shale minerals. F_1 and F_2 are sand volume (Vsand) and shale volume (Vsh) fractions respectively. Because of unavailability of core samples, standard quartz physical properties are used while shale physical properties are extracted from a shale interval close to the Hutton Formation zone as shown in Table 3.2.

Table 3.2: Matrix physical properties.

Quartz physical property	
Rho_1	**K_1**
2.65 g/cm^3	**37 Gpa**
Shale physical property	
Rho_2	**K_2**
2.53 g/cm^3	**21.4 Gpa**

Pore-fluids were mixed according to water saturation calculated at wells using:

$$K_{fl} = \left[\frac{S_w}{K_w} + \frac{1-S_w}{K_{hc}}\right]^{-1}, \text{ and} \tag{3-4}$$

$$\rho_{fl} = \rho_{hc}\,(1 - S_w) + \rho_w S_w\,, \tag{3-5}$$

where K_{fl} is the bulk modulus of the fluid mixture, S_w is the water saturation, K_w is the bulk modulus of the water, K_{hc} is the bulk modulus of the hydrocarbon, ρ_{fl} is the density of the fluid mixture, ρ_w is the density of the water, and ρ_{hc} is the density of the hydrocarbon.

Once physical properties were calculated for matrix and pore-fluids, dry rock bulk modulus (K_{dry}) was calculated by the following equation:

$$K_{dry} = \frac{K_{sat}\left(\frac{\emptyset K_{ma}}{K_{fl}} + 1 - \emptyset\right) - K_{ma}}{\frac{\emptyset k_{ma}}{K_{fl}} + \frac{K_{sat}}{K_{ma}} - 1 - \emptyset} \quad , \tag{3-6}$$

where K_{dry} is the bulk modulus of the porous rock frame, K_{sat} is the saturated bulk modulus, K_{ma} is the bulk modulus of the mineral matrix, K_{fl} is the bulk modulus of the pore fluid, and $\emptyset$ is porosity.

Because K_{dry} does not change with changing pore-fluid, in situ water saturation was changed, and bulk fluid modulus of the new pore-fluid mixture was calculated. Then, saturated bulk modulus of rock for the new pore-fluid mixture with different water saturation than the in-situ case was calculated using Gassmann's equation:

$$K_{sat} = K_{dry} + \frac{\left(1 - \frac{K_{dry}}{K_{ma}}\right)^2}{\frac{\emptyset}{K_{fl}} + \frac{(1-\emptyset)}{K_{ma}} - \frac{K_{dry}}{K_{ma}^2}} \ . \tag{3-7}$$

In addition, shear modulus (μ_{sat}) for the rock is held the same, even after water saturation change, but density of the new pore-fluid content was changed and calculated using following equation:

$$\rho_2 = \rho_1 + (\rho_{fl2} - \rho_{fl1}) \ , \tag{3-8}$$

where ρ_1 and ρ_2 densities of rocks with fluid 1 and fluid 2, respectively while ρ_{fl1} and ρ_{fl2} are the original and new pore fluid densities.

Compressional- and shear-wave velocities as changed in response to pore-fluid change were determined from:

$$V_p = \sqrt{\frac{K_{sat} + \frac{4}{3}\mu}{\rho}} \text{ , and} \tag{2-7}$$

$$V_s = \sqrt{\frac{\mu}{\rho}} \text{ ,} \tag{2-7}$$

where K_{sat} is the saturated bulk modulus, μ is the shear modulus and ρ is the density.

Fluid substitution was done several times from brine to oil and vice versa. There is a little discrimination between the original saturation (Sw = 30%) and (Sw = 100%) after fluid substitution using the *Vp/Vs* ratio and Poisson's ratio at Well A and Well B as illustrated in Figures 3.1 and 3.3. However, at Well C and Well D, there is observable pore fluid discrimination between the high water-saturation in situ case and the oil saturation case after fluid substitution as shown in Figures 3.5 and 3.7. This discrimination is larger than that observed in Well A and Well B.

AVO synthetics with and without hydrocarbons were created at the four wells to determine if hydrocarbons can be potentially detected on seismic reflection data as shown in Figures 3.2, 3.4, 3.6 and 3.8. A difference between the AVO synthetics before and after fluid substitution was noted at some wells. There is some possibility of detecting hydrocarbons from seismic data in certain circumstances. However, there are no noticeable AVO changes after fluid substitution for some of the wells such as Well A and Well C. A weak decrease in amplitude was noted at Well B after AVO fluid substitution from oil to brine. A noticeable increase in amplitude of the AVO synthetics occurred at Well D after decreasing water saturation during fluid substitution.

However, these results may be misleading. This noticeable discrimination between pore fluids at Well B and Well C can be attributed to the predicted S-wave velocity used in fluid substitution, especially for the brine-saturated case. In addition, at Well D, there may also be lithologic effects.

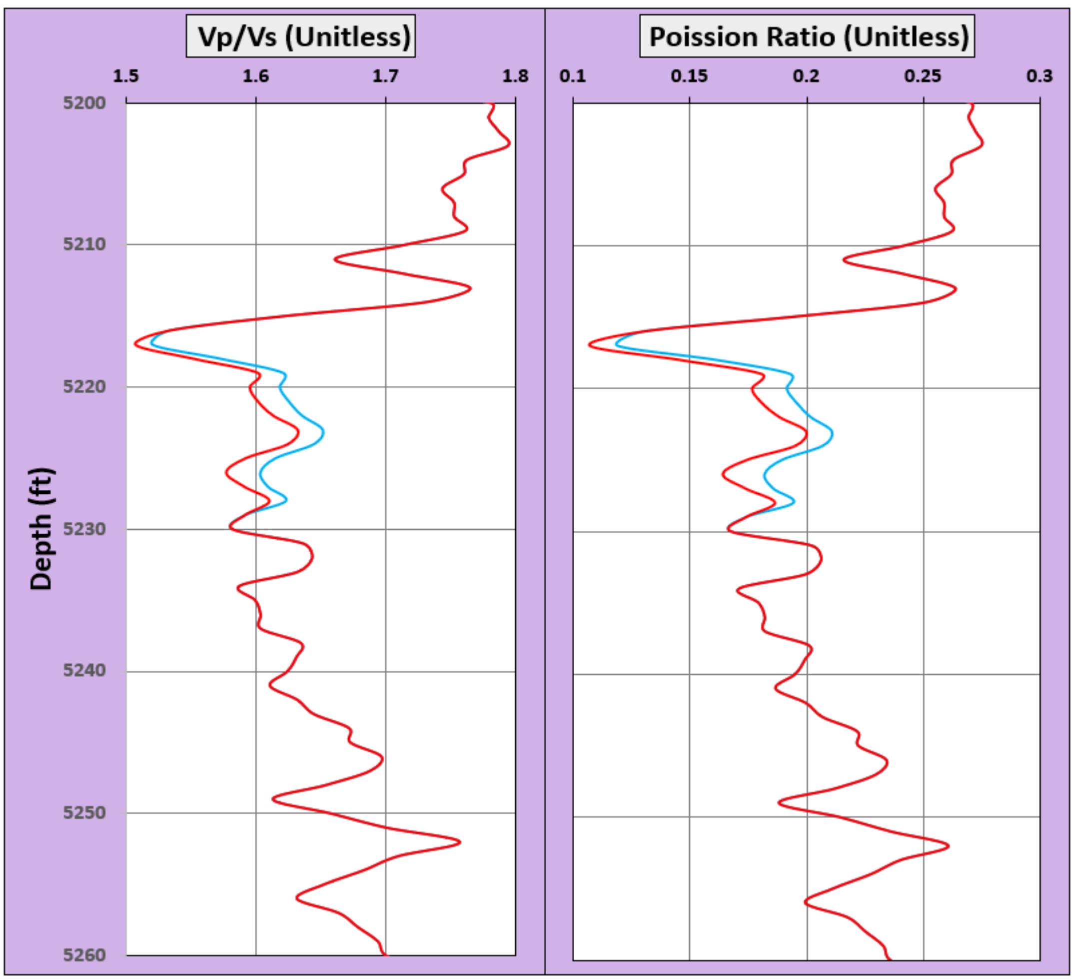

Figure 3.1: Fluid substitution at Well A. Blue curve represents oil zone after fluid substitution to brine (Sw = 100%).

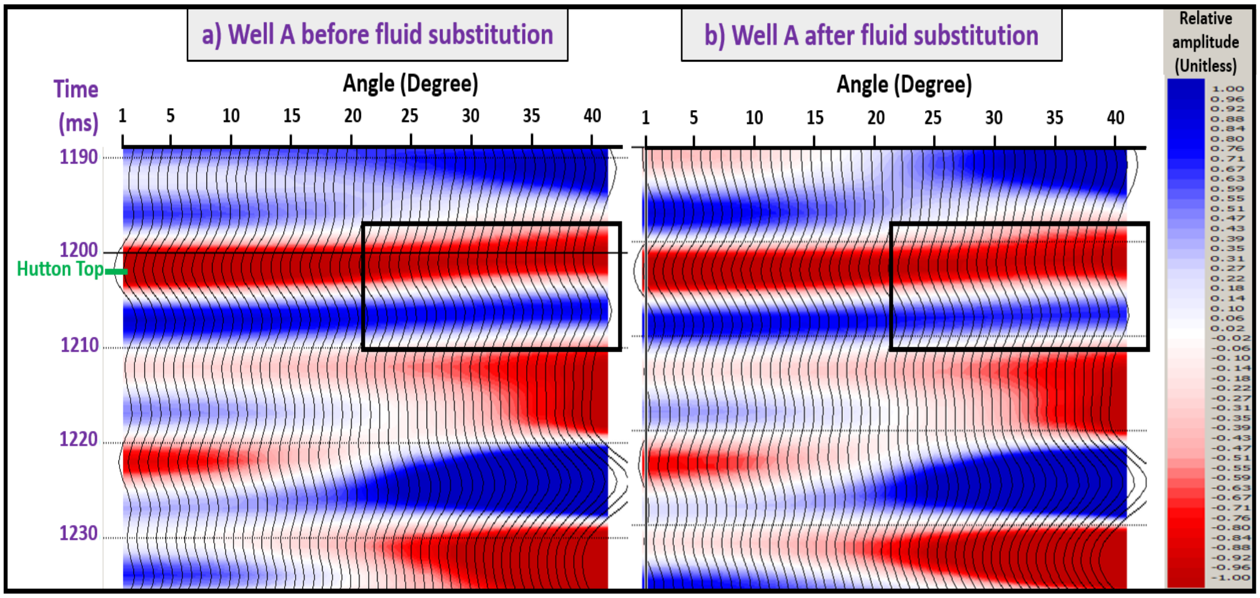

Figure 3.2: AVO fluid substitution modelling at Well A. a) Oil saturated case (Sw = 30%) before fluid substitution. b) After fluid substitution to brine (Sw = 100%).

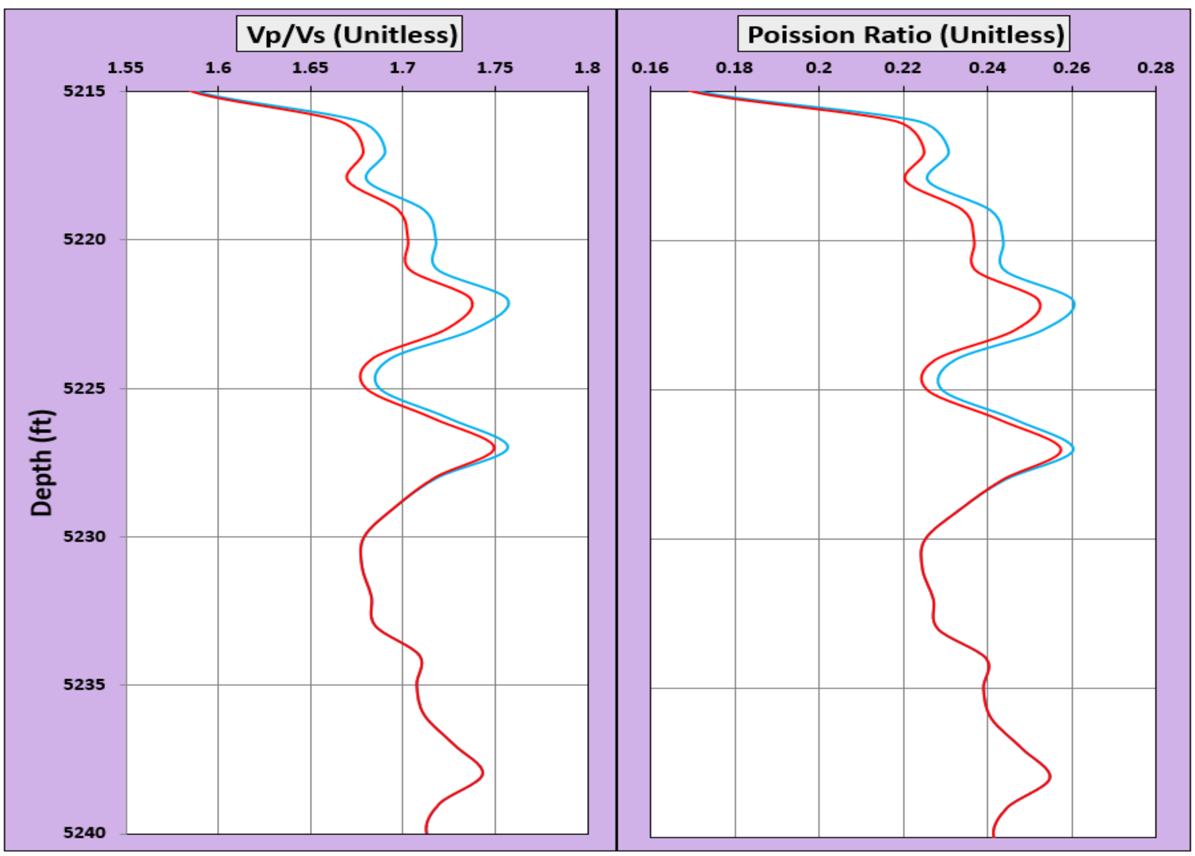

Figure 3.3: Fluid substitution at Well B. Blue curve represents oil zone after fluid substitution to brine (Sw = 100%).

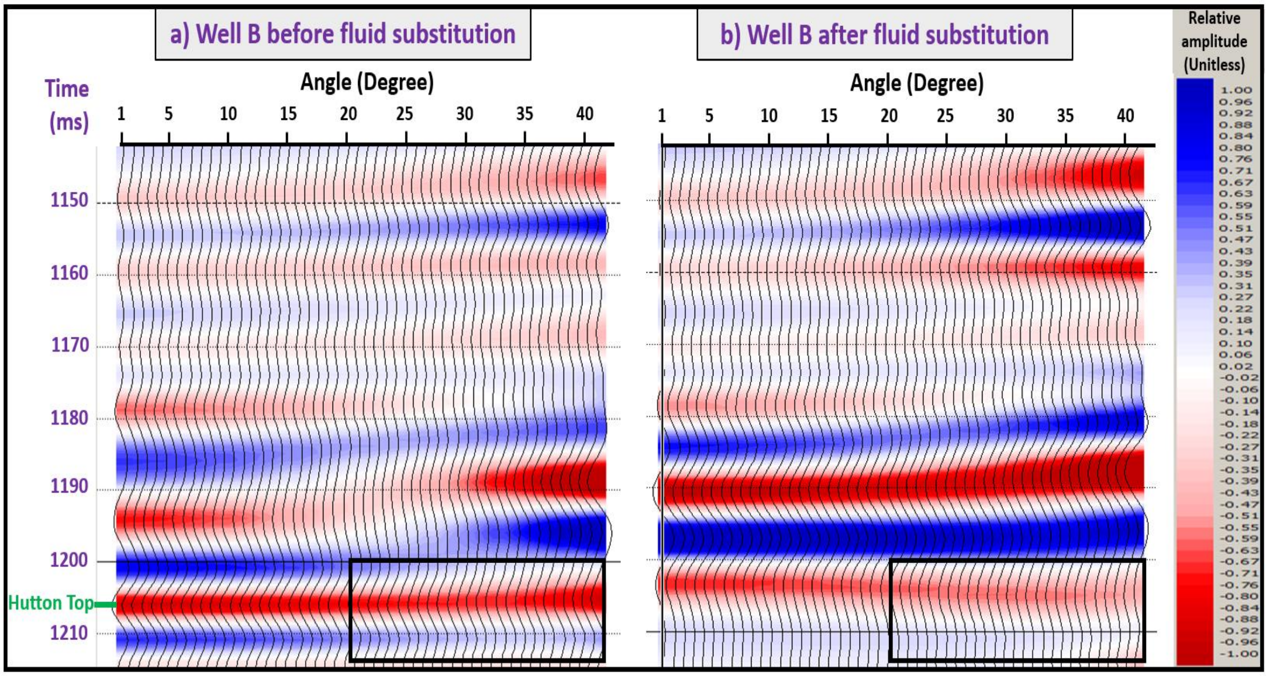

Figure 3.4: AVO fluid substitution modelling at Well B. a) Oil saturated case (Sw = 30%) before fluid substitution. b) After fluid substitution to brine (Sw = 100%).

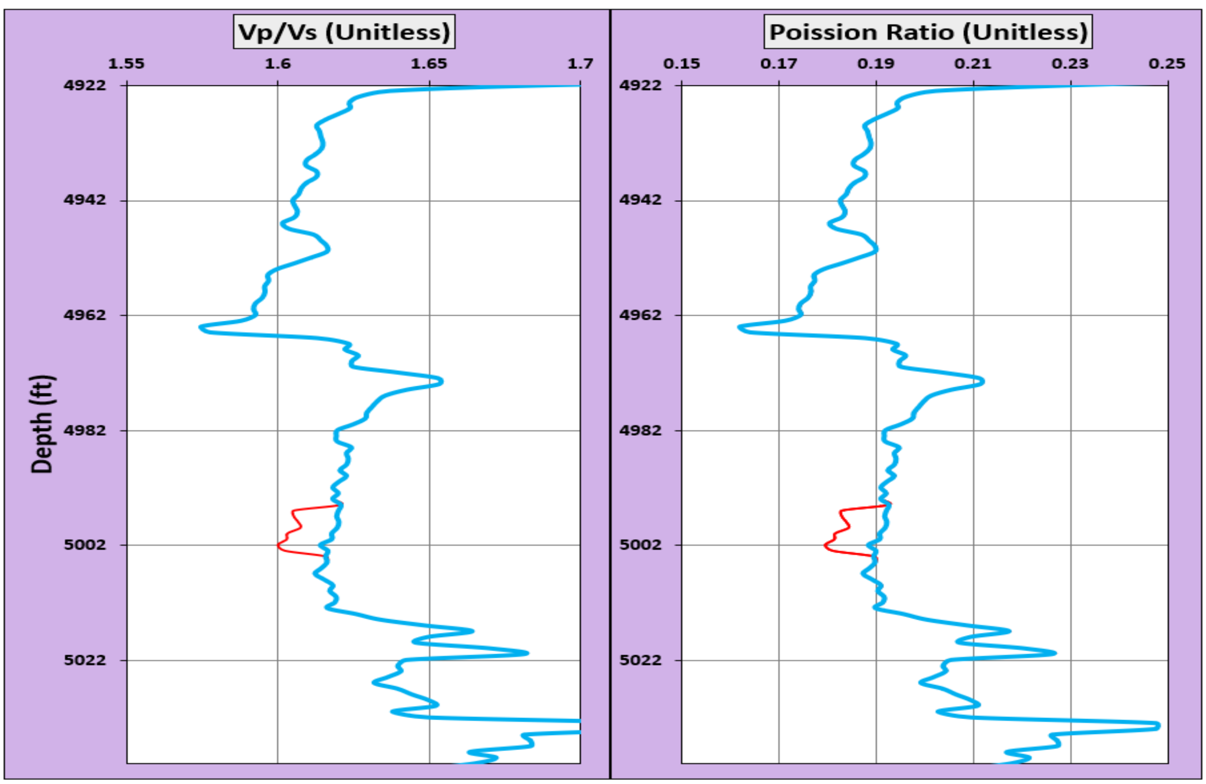

Figure 3.5: Fluid substitution at Well C. Red curve represents oil zone after fluid substitution from oil (Sw = 60%) to oil (Sw = 10%).

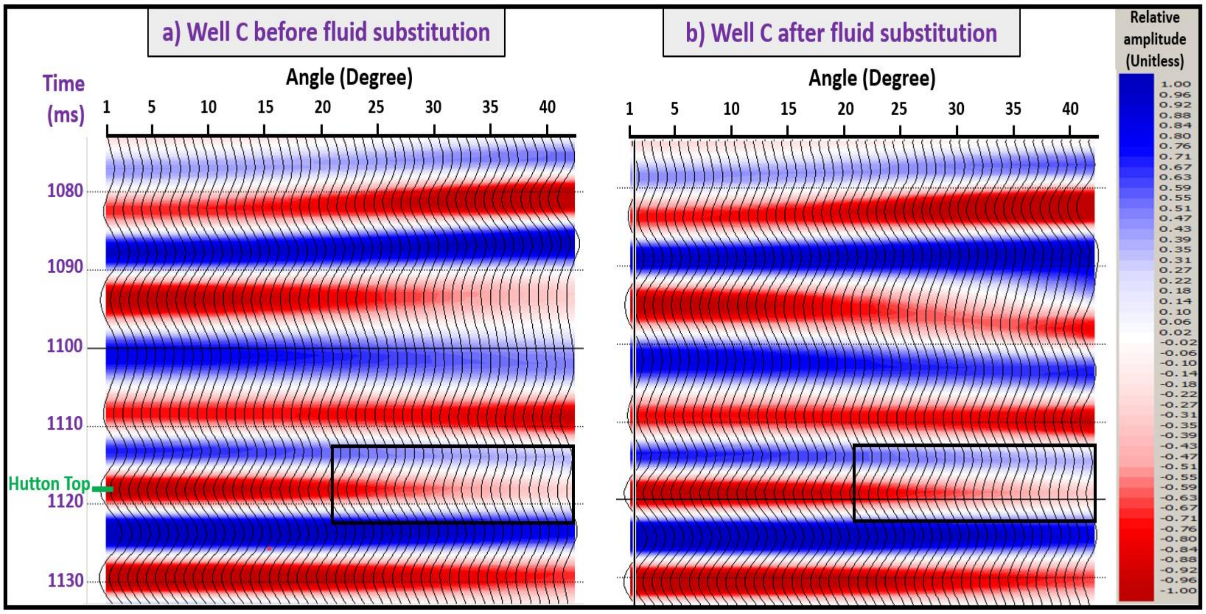

Figure 3.6: AVO fluid substitution modelling at Well C. a) Oil saturated case (Sw = 60%) before fluid substitution. b) After fluid substitution to brine (Sw = 100%).

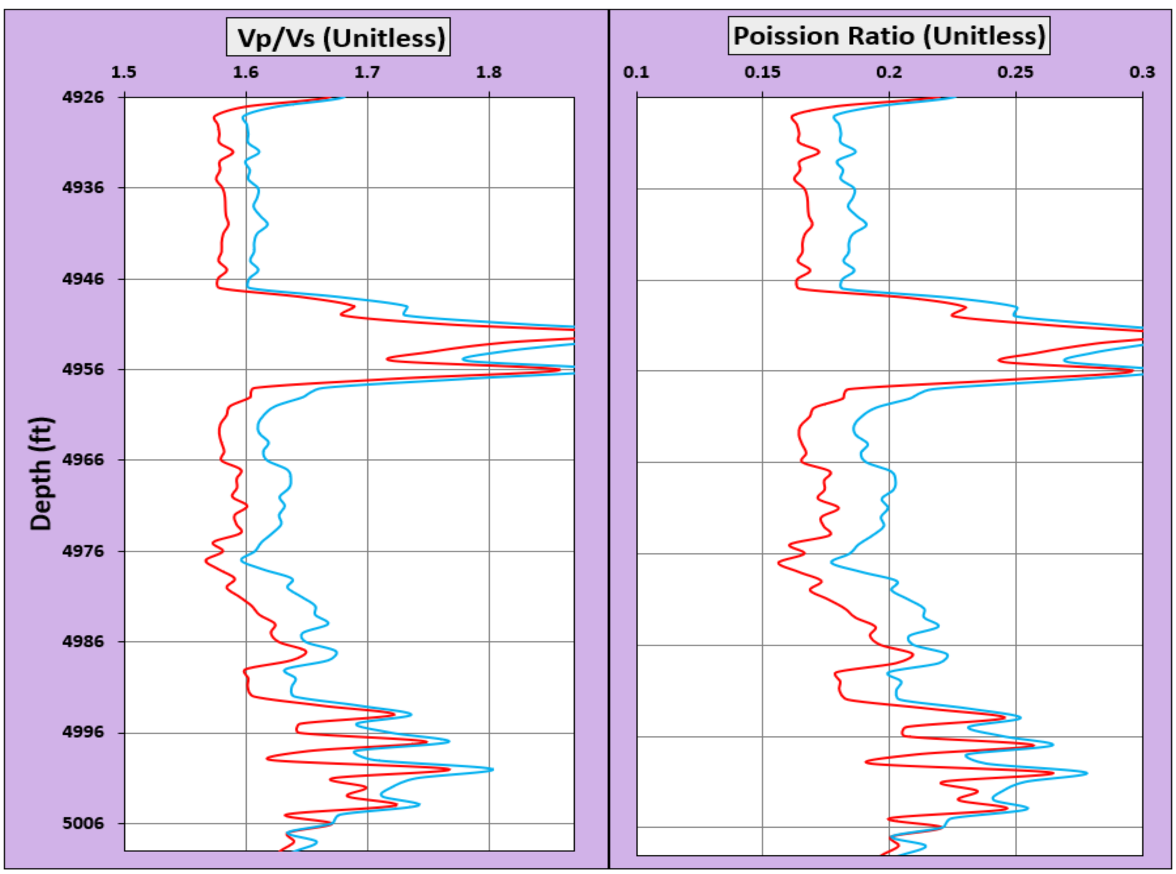

Figure 3.7: Fluid substitution at Well D. Red curve represents the Hutton Sandstone Formation zone after fluid substitution to oil (Sw = 20 %).

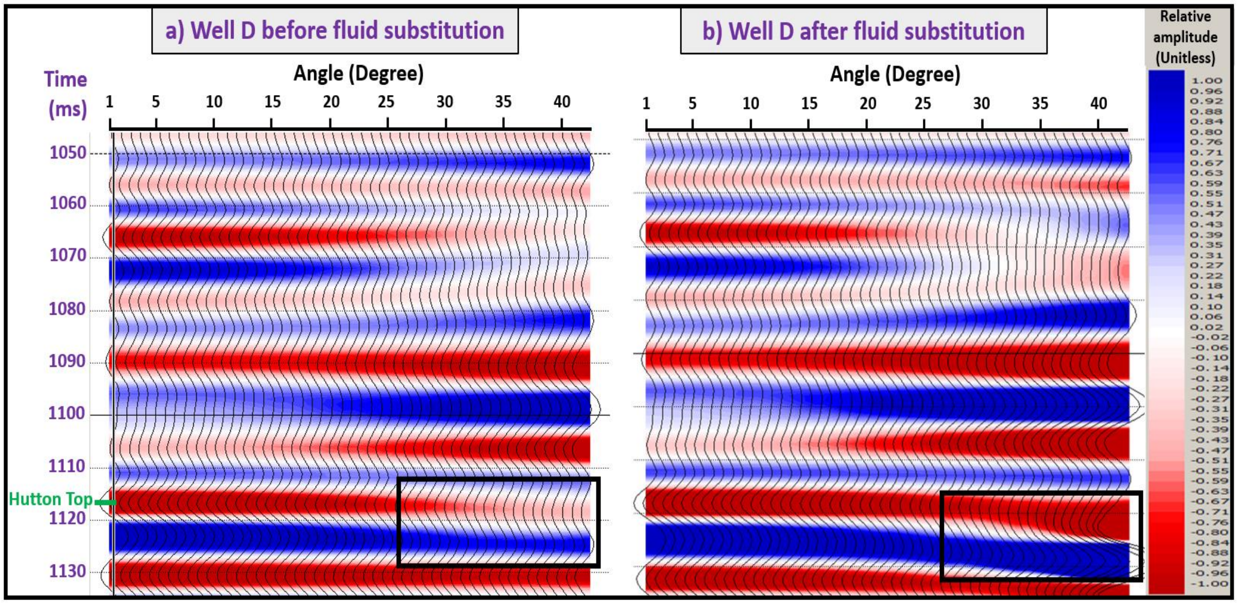

Figure 3.8: AVO fluid substitution modelling at Well D. a) Brine saturated case before fluid substitution. b) After fluid substitution to oil (Sw = 20%).

Brine-saturated values of the Hutton Formation at the four wells are plotted in K_{dry} over K_{min} versus porosity as shown in Figures 3.9, 3.10, 3.11 and 3.12. Within the same porosity range, brine-saturated data have different dry bulk modulus. As dry incompressibility increases, K_{dry} over K_{min} increases, hence, K_{phi} over K_{min} increases. Thus, the rock has a small sensitivity to fluid. On the other hand, as rock become soft, the sensitivity to fluid increases.

Most of brine data for the four wells have moderate values of dry bulk modulus indicating that the Hutton sandstone is not highly consolidated or cemented. There are, however, a few data points that are shifted toward high dry bulk modulus values that indicates increased cementation within some depth ranges. Thus, based on previous results, the Hutton Sandstone can have a moderate degree of sensitivity to fluids.

After conducting a wide variety of rock property crossplots for pore-fluid discrimination, AI versus K_{sat} - K_{dry} achieves the best discrimination between pore-fluids at the four wells as shown in Figure 3.13. AI and K_{sat} can be extracted from inverted seismic data, but it is still a problem to estimate *Kdry* from seismic data.

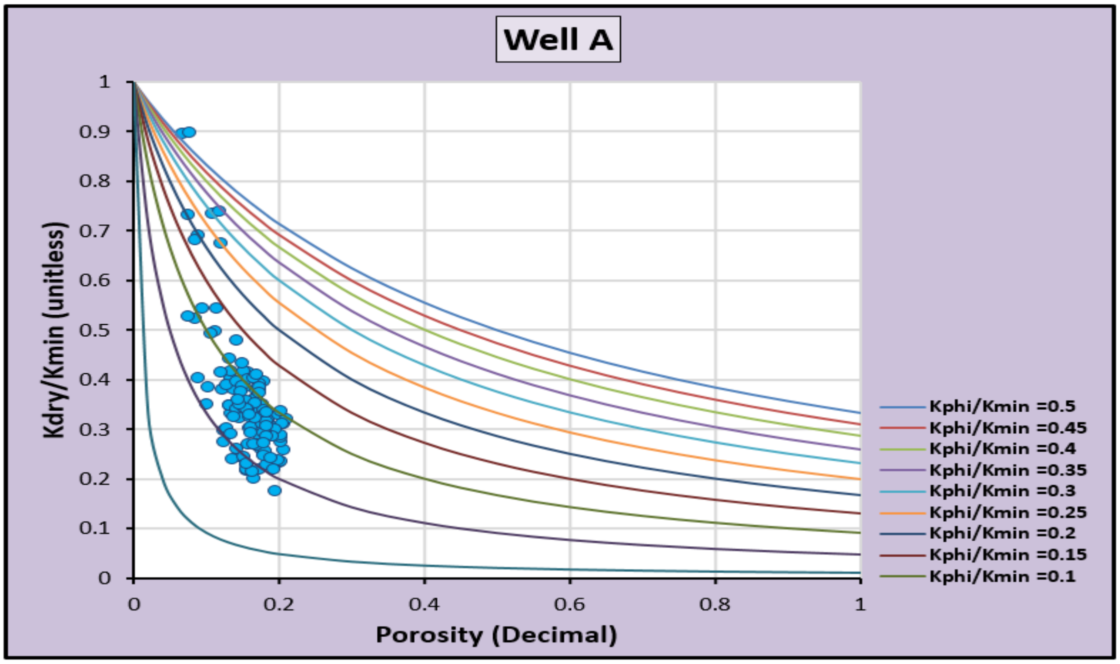

Figure 3.9: Normalized rock bulk modulus. Brine-saturated data of the Hutton Formation at Well A are represented by blue points.

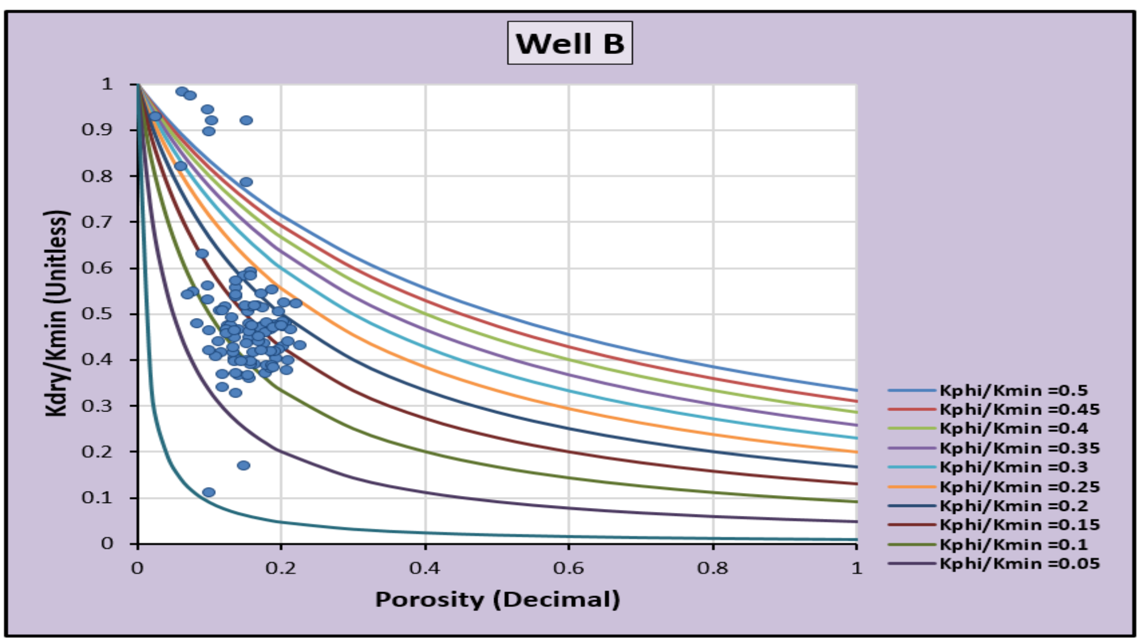

Figure 3.10: Normalized rock bulk modulus. Brine-saturated data of the Hutton Formation at Well B are represented by blue points.

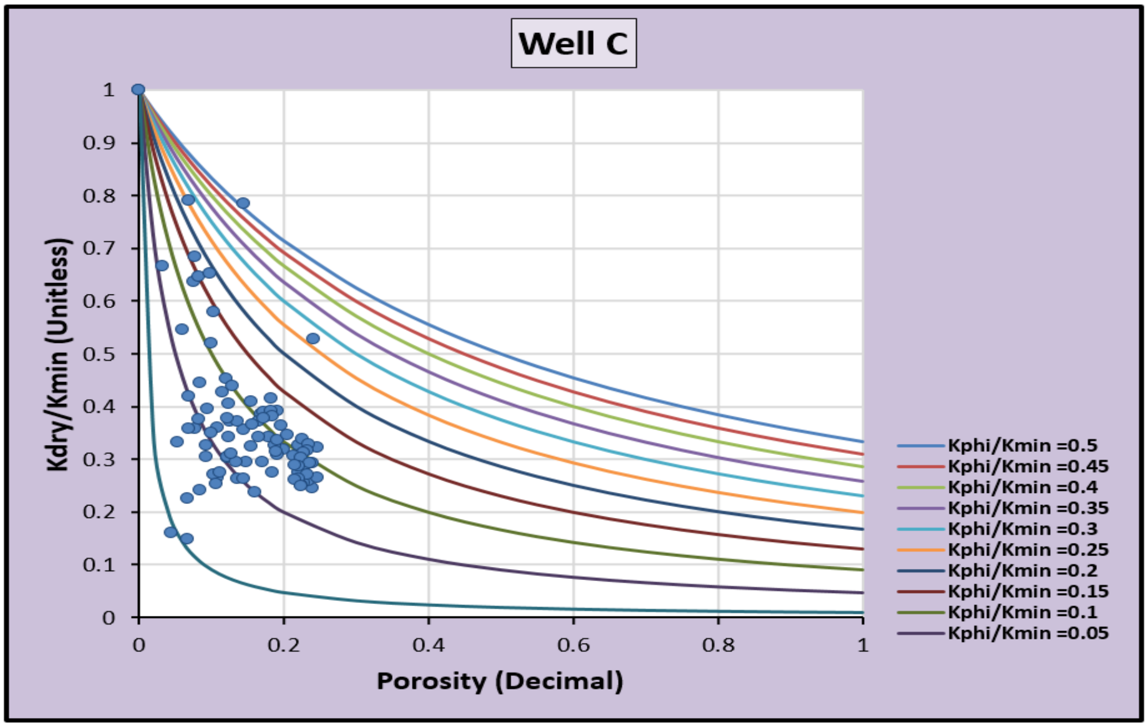

Figure 3.11: Normalized rock bulk modulus. Brine-saturated data of the Hutton Formation at Well C are represented by blue points.

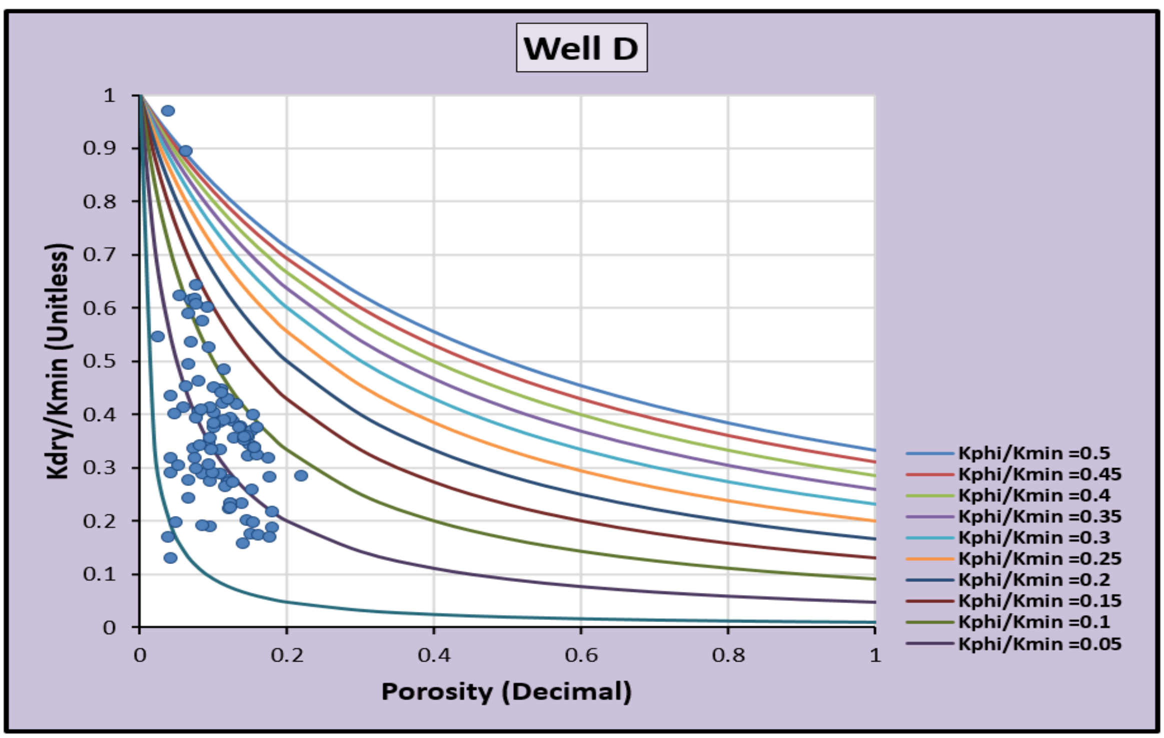

Figure 3.12: Normalized rock bulk modulus. Brine-saturated data of the Hutton Formation at Well D are represented by blue points.

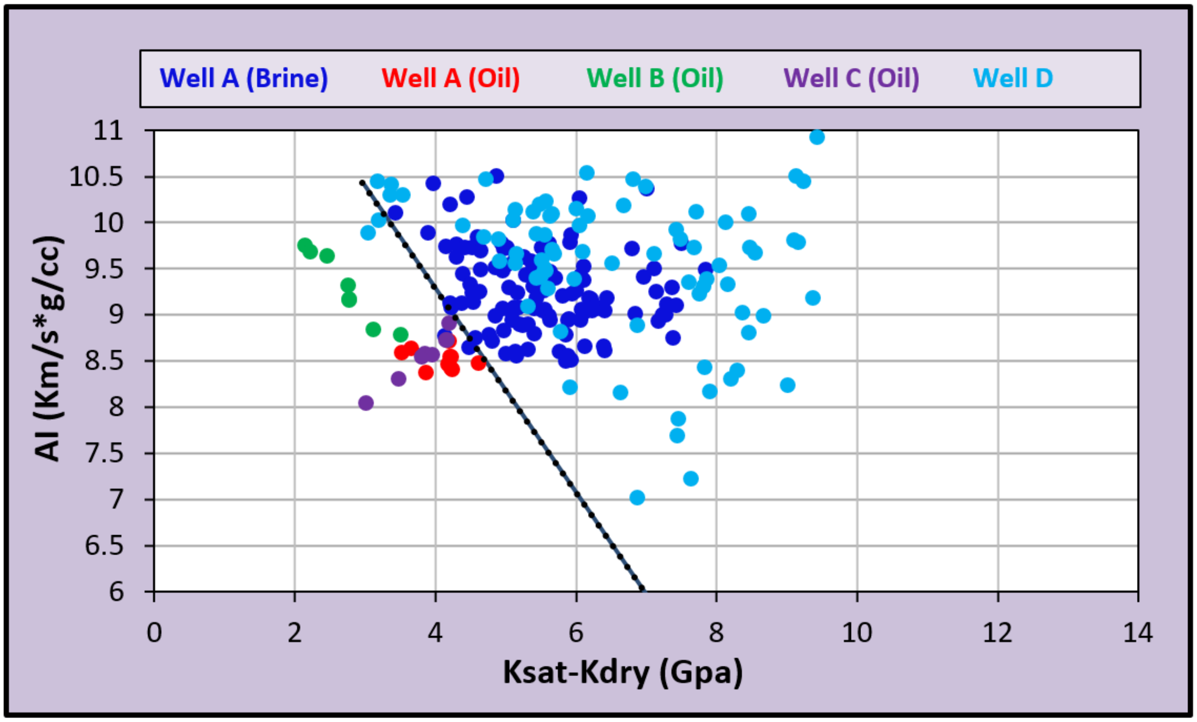

Figure 3.13: AI versus *Ksat-Kdry*. Pore fluid discrimination using the four wells.

3.2. Sensitivity analysis

Because porosity and thickness change within the same reservoir from one location to another, I did sensitivity analyses to see how the amplitude anomaly changes in response to thickness and porosity changes.

I used well B for doing sensitivity analysis because the seismic data at the Well B location does exhibit a Direct Hydrocarbon Indicator (DHI) feature. A bright spot was noticed from the amplitude map established along the Hutton Formation top.

To do sensitivity analysis, forward fluid substitution was first conducted from oil to brine. Figure 3.14 illustrates a difference between the AVO synthetics before and after fluid substitution at Well B. After fluid substitution from oil to brine, an average density = 2.37 gm/cc and average velocity = 13000 ft/sec for full brine-saturation were estimated at Well B. Then, I used the mass balance equation to estimate a porosity of 16.9%.

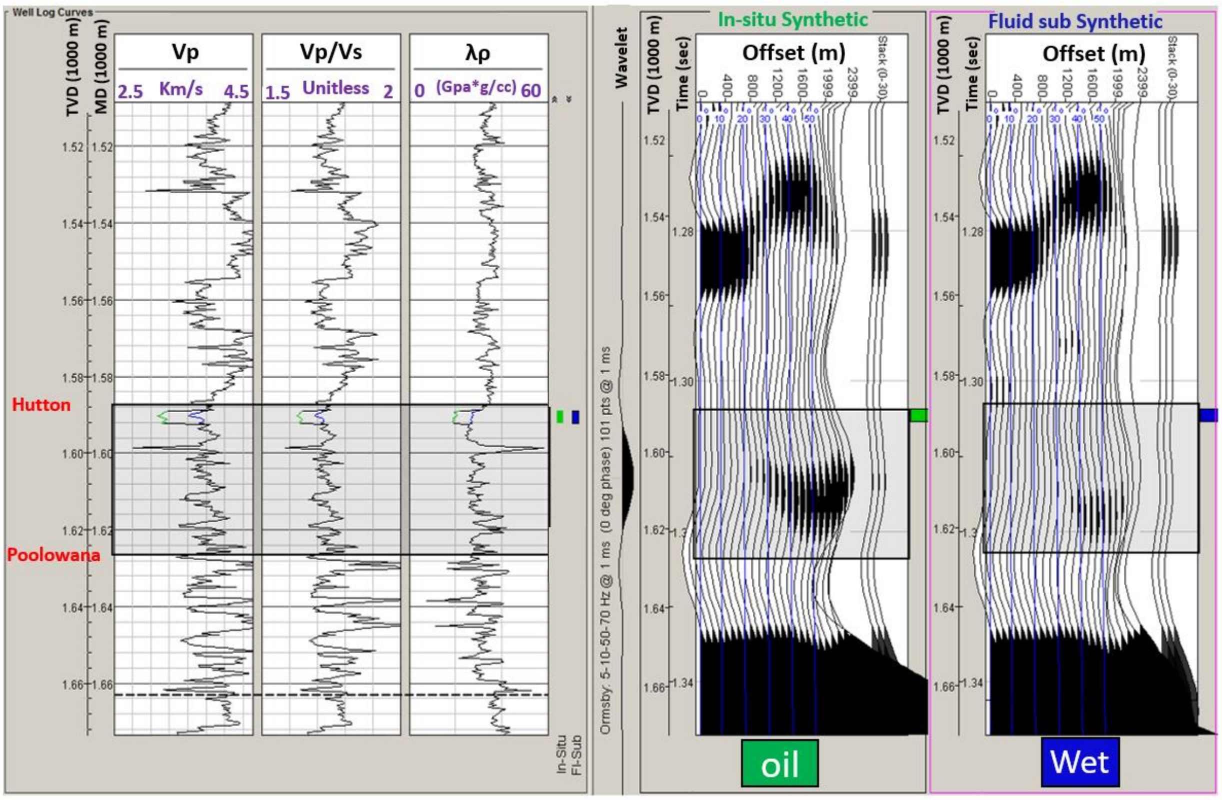

Figure 3.14: Forward fluid substitution at Well B.

The trend line for the oil interval is represented by the black line in Figure 3.15. The red point represents the plot of 100% brine-saturated sandstone average velocity and porosity for this zone after fluid substitution to brine and I assumed that brine (after fluid substitution) has the pink line on the velocity-porosity crossplot. Now, I can change petrophysical properties and measure the sensitivity of amplitude changes in response to porosity and thickness changes. I first did a reverse fluid substitution from brine to oil as illustrated at Figure 3.16. Then, I changed porosity and thickness separately and monitored change of the amplitude anomaly to background amplitude at near and far offset. The results are illustrated in Figures 3.17 and 3.18.

An increase in (A/B) was addressed while increasing porosity to more than 15% as shown in Figure 3.17. Hence, porosity contributes to an increased amplitude anomaly especially for high porosity zones that exceeds 15%. Furthermore, an increase in anomaly to background amplitude (A/B) was noticed at far angles while increasing pay zone thickness. The A/B increase at far angles is much higher compared with near angles as shown in Figure 3.18. Thus, hydrocarbons detection is highly dependent on the hydrocarbon thickness.

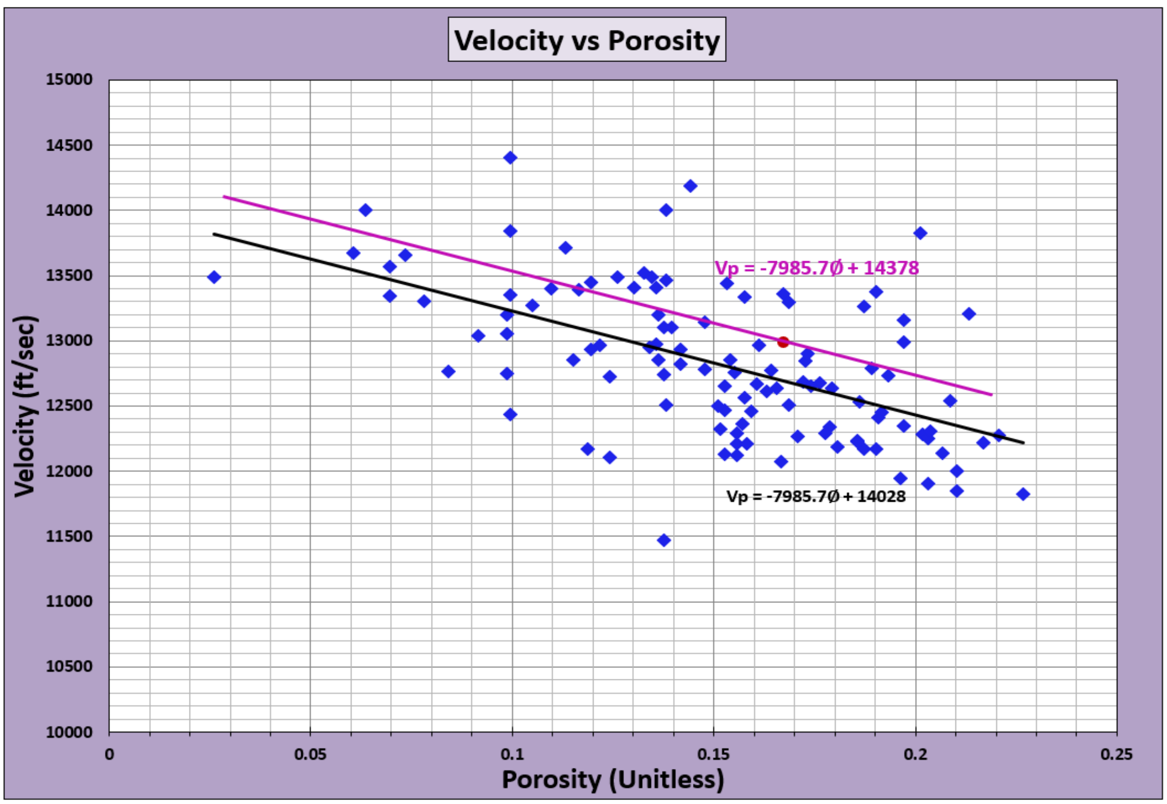

Figure 3.15: Velocity-Porosity crossplot for brine-saturated zone of Well B.

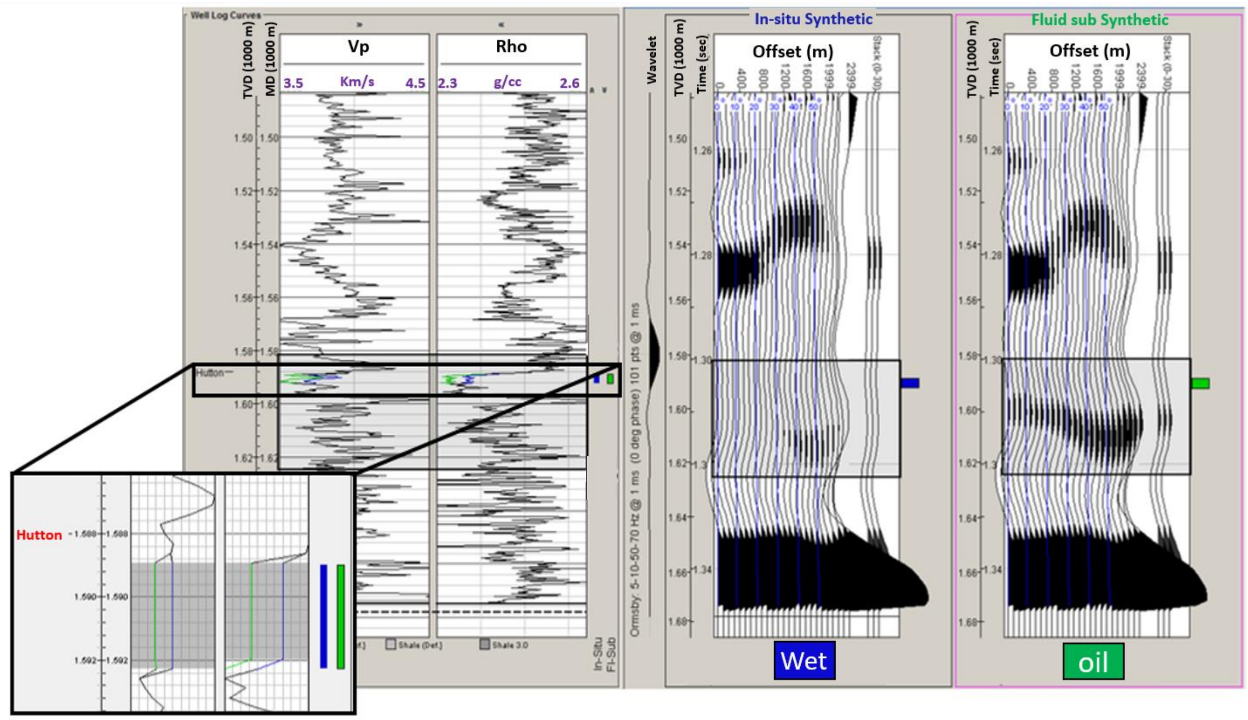

Figure 3.16: Reverse fluid substitution at Well B.

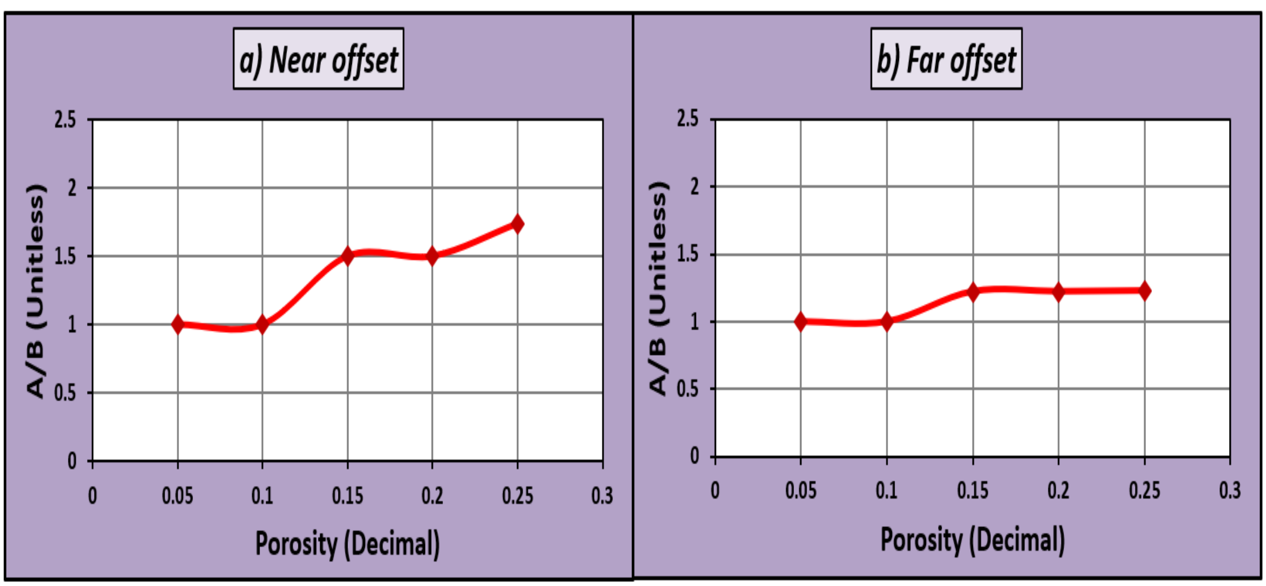

Figure 3.17: Anomaly amplitude to background amplitude at near and far offset in response to porosity change of target zone at Well B.

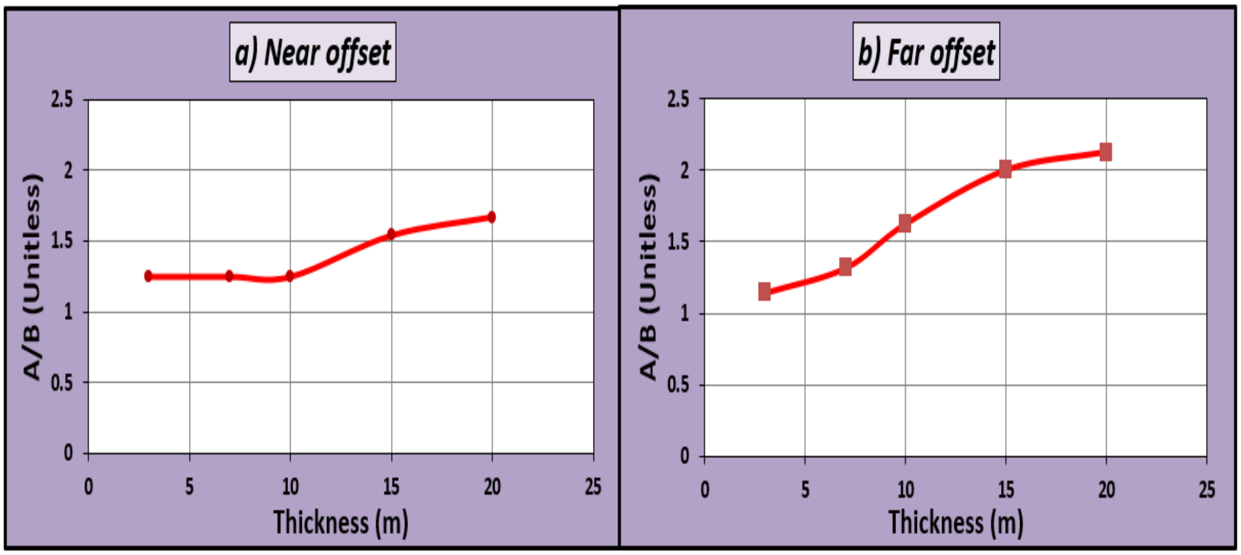

Figure 3.18: Anomaly amplitude to background amplitude at near and far offset in response to thickness change of target zone at Well B. a) Near offset. B) Far offset.

Chapter 4

Qualitative Seismic Interpretation

4.1. Seismic to well tie and wavelet extraction

After extracting rock properties from well logs, these properties are correlated with seismic-reflection data. The correlation is done with a seismic well-tie process. To convert the well depth domain to time domain, check-shot surveys provide an accurate time-depth curve for this process. However, there still remains an ambiguity brought on by near-surface corrections to datum applied to the seismic versus datum corrections that are applied for the check-shot survey. Fortunately, the Cadna-Owie is an easily recognized marker both on the seismic data and the synthetics. This relationship normally allows both the amplitude and phase spectra to be accurately extracted for the seismic wavelet.

4.1.1. Creating synthetics

AVO synthetics were first created from well logs to see if the amplitude changes with offset or not. I noticed that there is an amplitude variation with offset at the target zone as illustrated in Figure 4.1. So, offset-stack seismic volumes can provide better correlation than the full-stack seismic volume because near-offset amplitude will be stacked with far-offset amplitude with the full-stack seismic volume.

The post-stack seismic volume used in the seismic to well-tie process at Well A and Well B has an offset range from (1200-1800 m). So, synthetics were generated for the same offset range. The wavelet applied for the well tie is shown in Figure 4.2. For the seismic to well-tie process, a bulk shift was only applied to the synthetics without applying stretch or squeeze. A good seismic to well tie is observed at Well A and Well B as shown in Figures 4.3 and 4.4. Because of structure complexity on the post-stack seismic volume (1200-1800 m) around Well C and Well D, the post- stack seismic volume of offset rang from (600-1200 m) was used for the seismic to well-tie process at these wells. Although the tie is not good around the Cadna-Owie Formation top, especially at Well C, there is a good seismic to well tie around the pay zone at Well C and Well D as shown in Figures 4.5 and 4.6. To address the Hutton Formation top extension along the survey, an arbitrary line was constructed along the four wells as shown in Figure 4.7. There are continuous reflectors at the wells, and they are pinching out toward Well D. Based on qualitative seismic interpretation, a cartoon model for the arbitrary line passing through wells is shown in Figure 4.8.

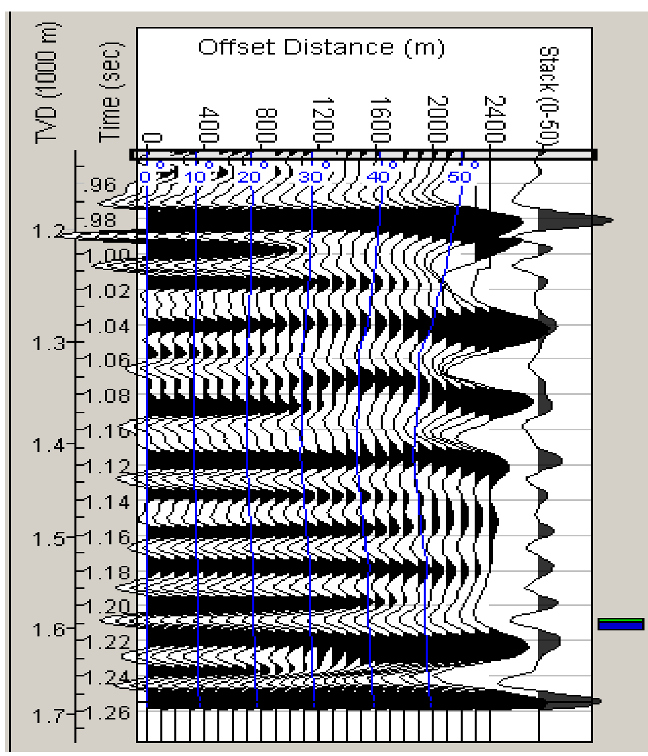

Figure 4.1: AVO synthetic at Well A.

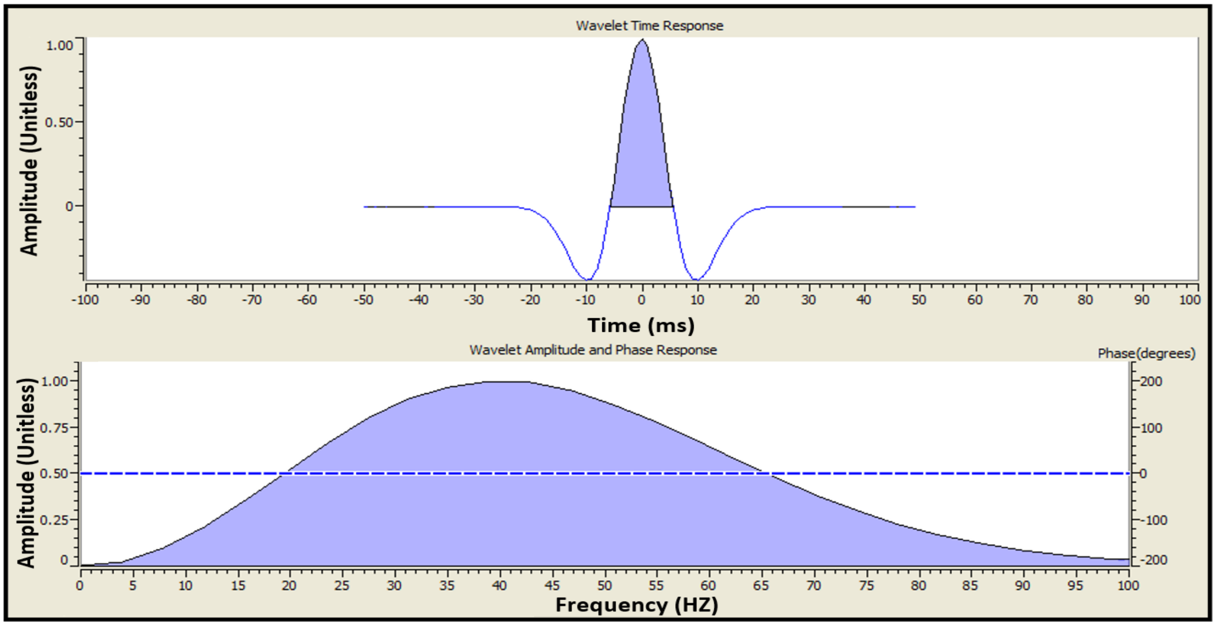

Figure 4.2: Ricker wavelet of 40 Hz used for creating synthetic at Well A, Well B, well C and Well D.

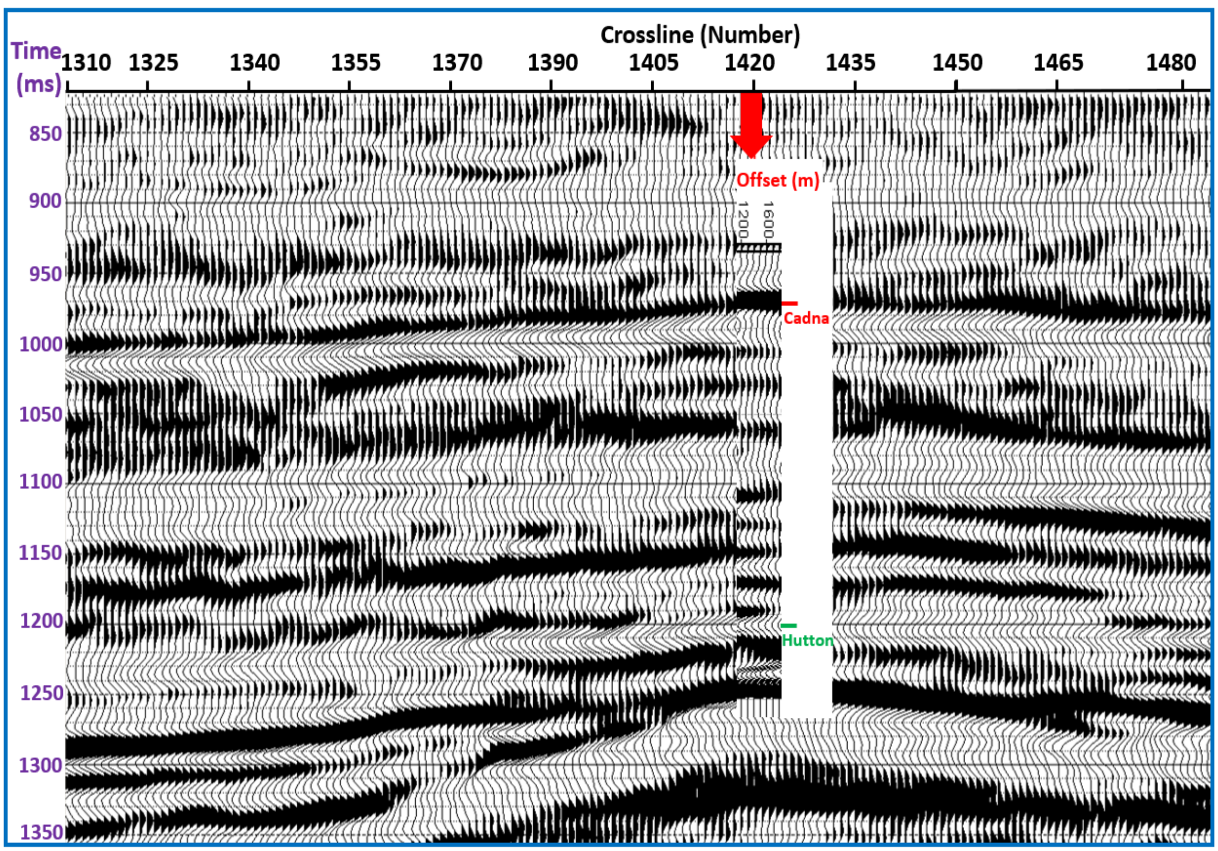

Figure 4.3: Seismic to well tie at Well A.

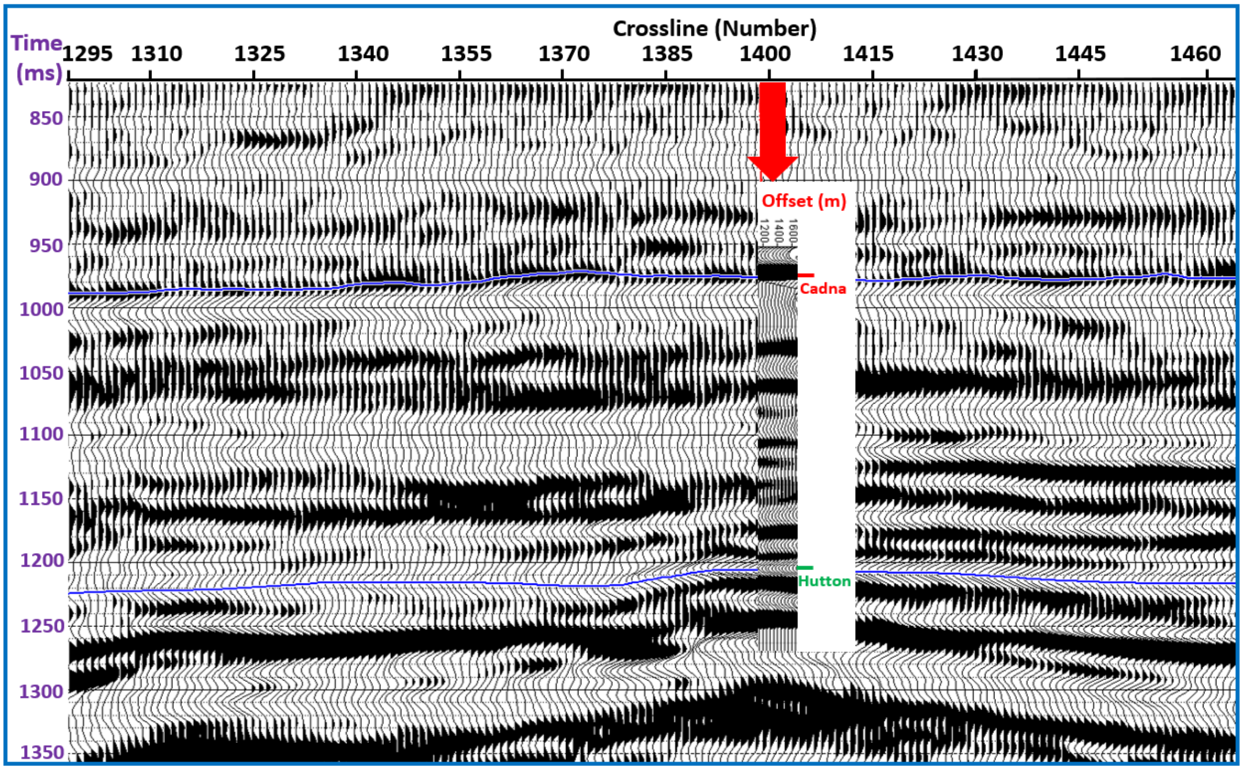

Figure 4.4: Seismic to well tie at Well B.

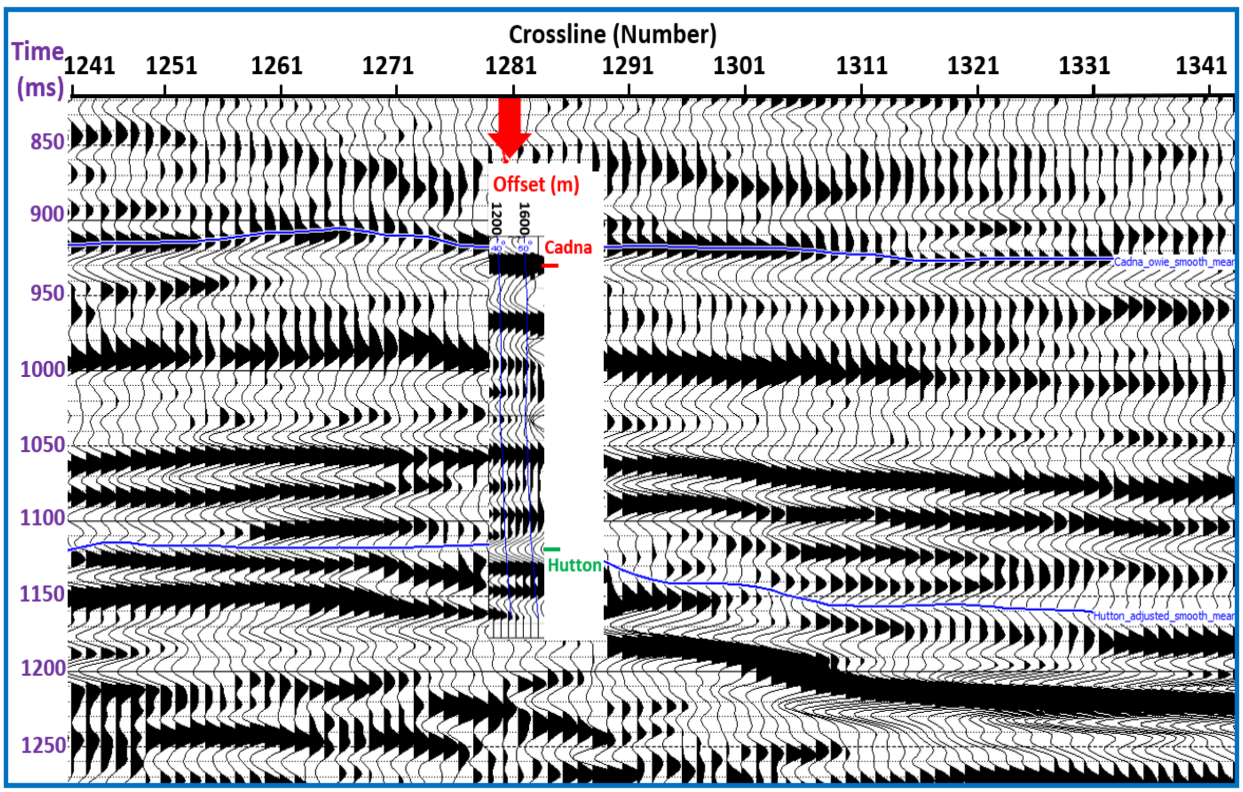

Figure 4.5: Seismic to well tie at Well C.

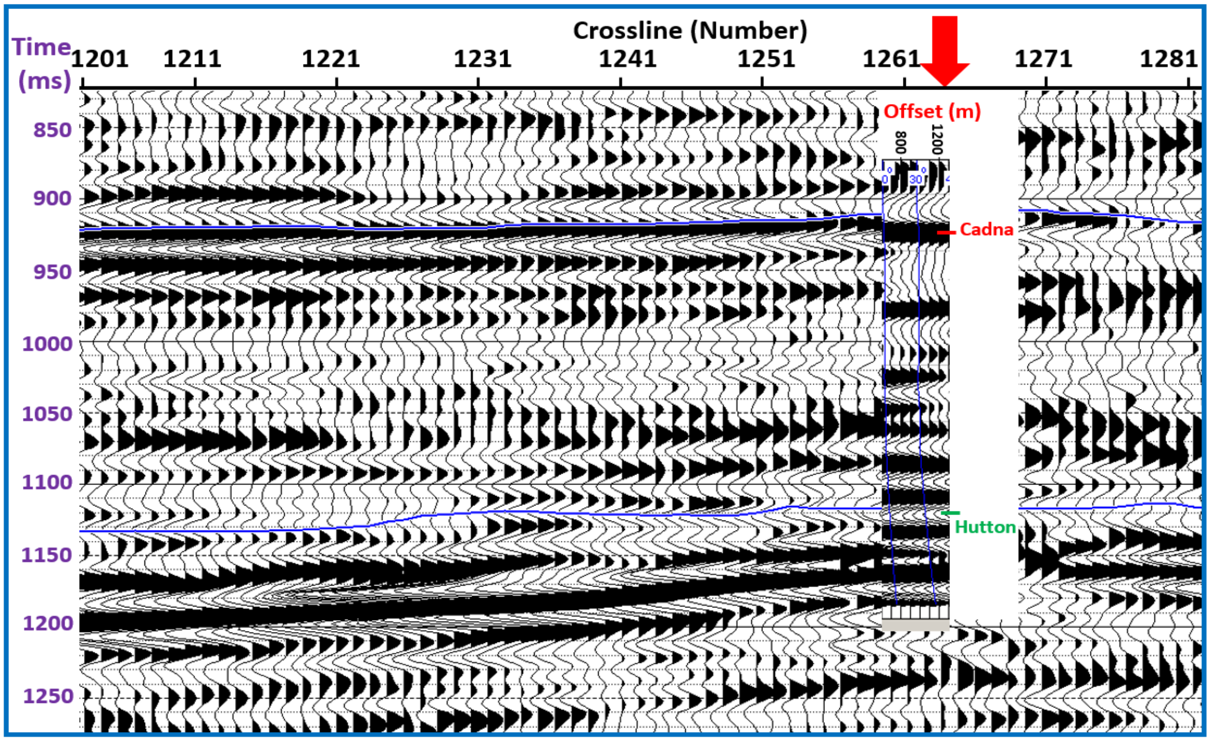

Figure 4.6: Seismic to well tie at Well D.

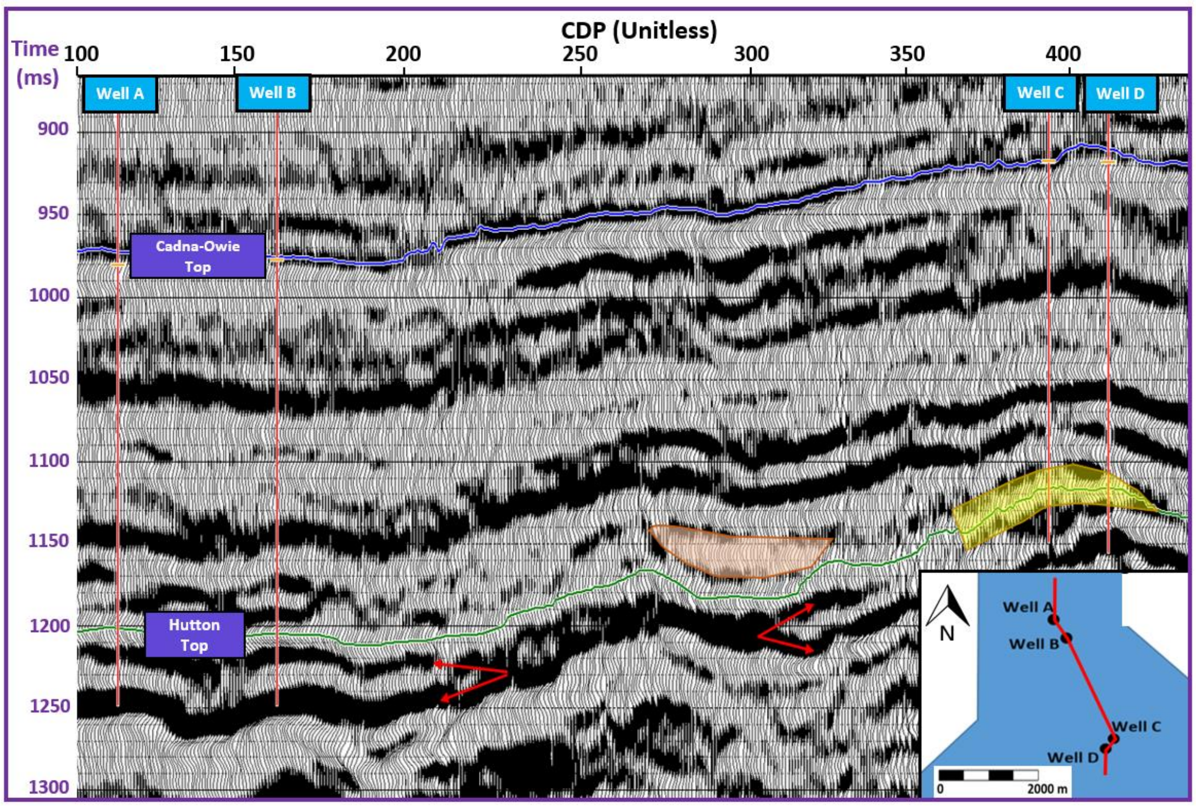

Figure 4.7: Arbitrary line along the four wells.

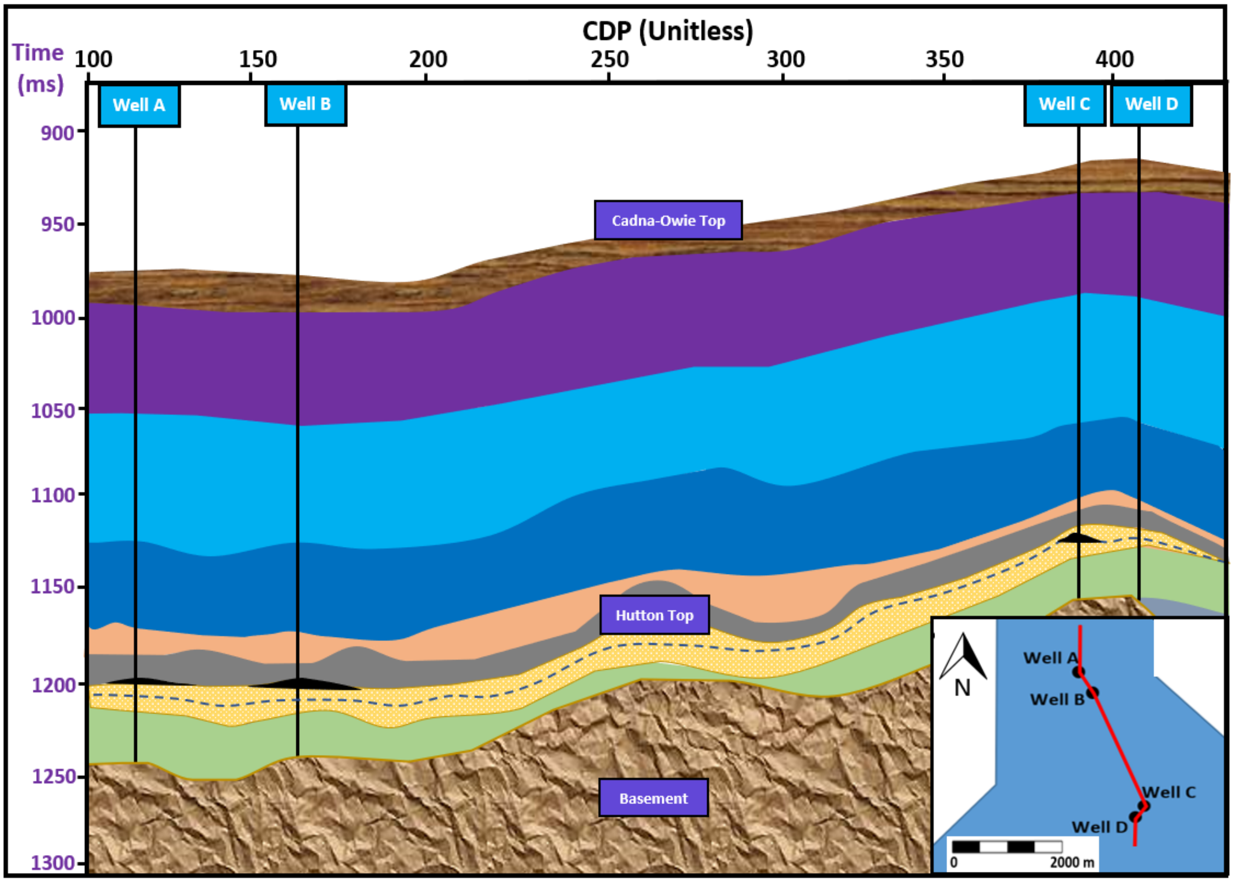

Figure 4.8: Cartoon section along the wells based on seismic interpretation.

A structure contour map for the Hutton Formation top was created as shown in Figure 4.9. It shows four-way and three-way plunging anticline closures which probably are good traps for hydrocarbons. To address possible migration patterns using available data, an isochron map was constructed between the Cadna-Owie Formation top, which represents a good seismic marker, and the Hutton Formation top as shown in Figure 4.10. Closed contours identified from the isochron map are possibly locations for hydrocarbon accumulation after its migration up dip. The isochron and structure contour maps are used to address up-dip structures along the Hutton Formation top. In addition, a basement structure contour map was constructed to show basement relief as shown in Figure 4.11. High structures recognized from the structure contour map of the Hutton Formation are related to the highs on the basement structure contour map. Because of the up-dip migration of hydrocarbons, the Hutton Formation above basement influenced highs is probably hydrocarbon charged. To address this probability, facies and pore fluid should be discriminated first from seismic inversion and multiattribute analysis as will be discussed in the following chapters.

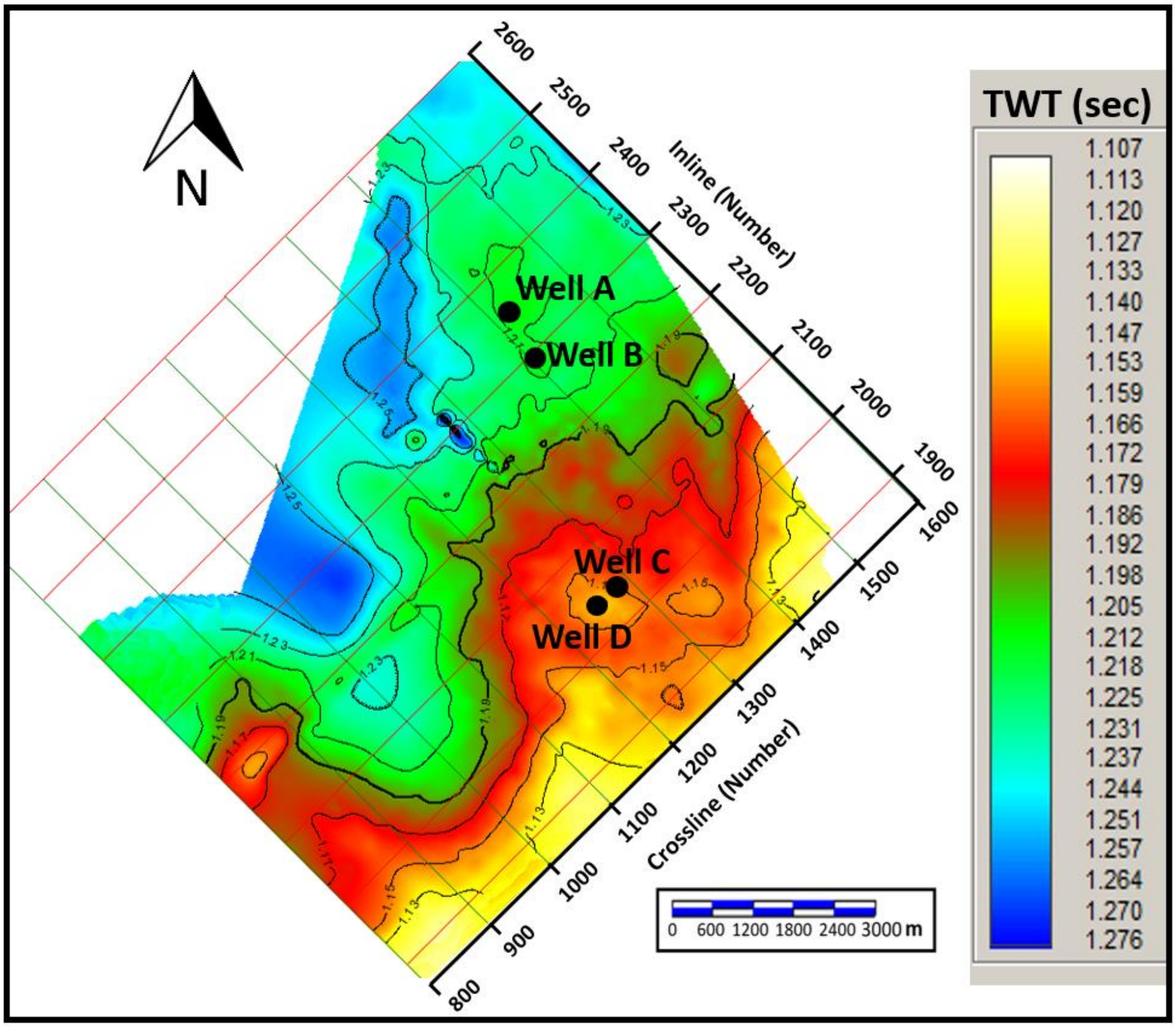

Figure 4.9: Structure contour map of the Hutton Formation top.

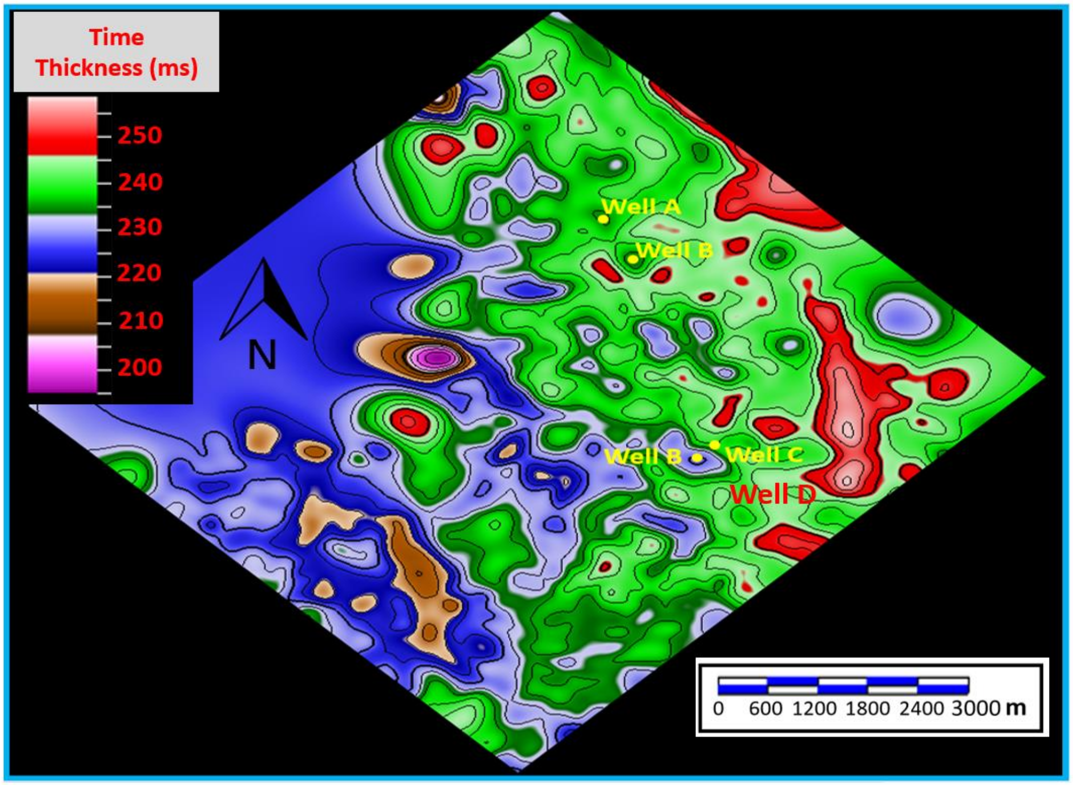

Figure 4.10: Isochron map between Cadna-Owie top and the pay zone top.

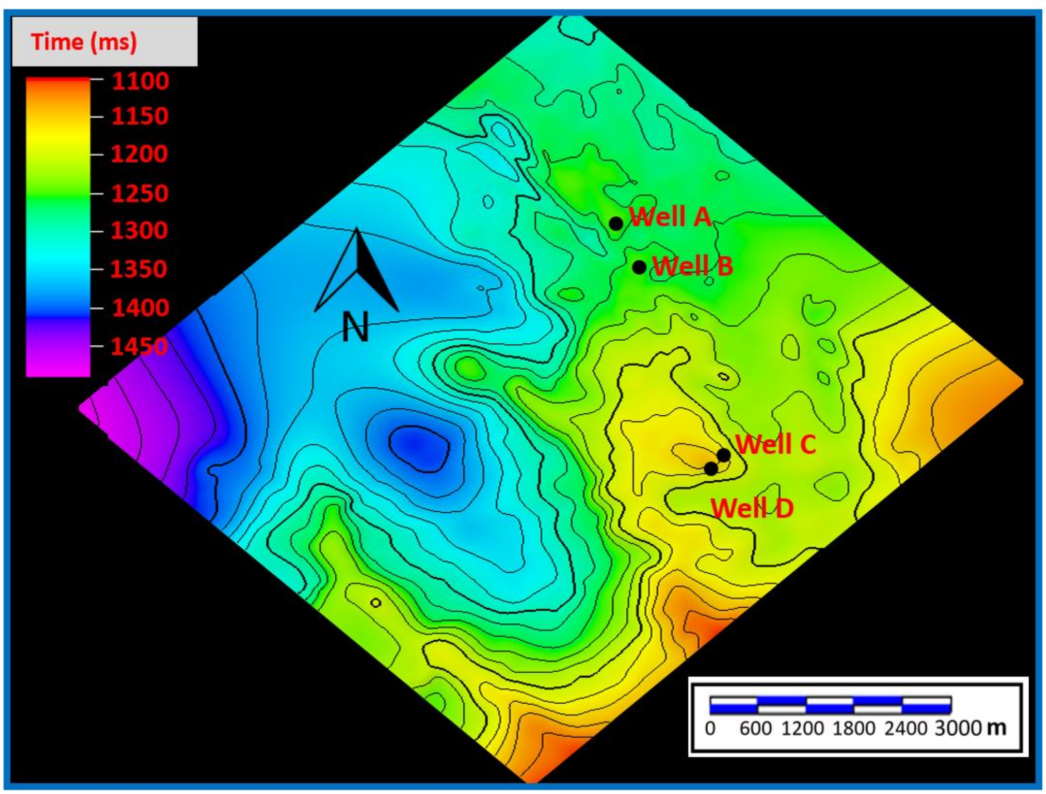

Figure 4.11: Basement top over study area.

4.2. DHI analysis

Bright anomalous amplitude distribution over the study area along the Hutton Formation is shown in Figure 4.12. The amplitudes are conformable with structure in some subareas and unconformable with it at other subareas. The source of these anomalous amplitudes could be hydrocarbon pore fluid, lithology effects, or noises. To address amplitude changes with offset, a 10 ms horizon slice below the Hutton top extracted from the near-angle stack is compared with a horizon of the same time window extracted from the far-angle stack as shown in Figure 4.13. Amplitude values are estimated from near-angle and far-angle stacks along horizons at well locations as illustrated in Table 4.1. There is a noticeable increase in amplitude from near offset to far offset at Well A (S_w = 30%) and Well B (S_w = 30%) while there is a small increase in amplitude at Well D (S_w = 100%). These results strengthen the probability that hydrocarbon pore fluid is the main source for most anomalous amplitudes at the Hutton Formation. However, there is a negligible decrease in amplitude at Well C that has oil with 60% water saturation and that may be attributed to high water saturation estimated from petrophysical analysis at the target zone or due to the thin pay zone at Well C that is below the seismic resolution limit.

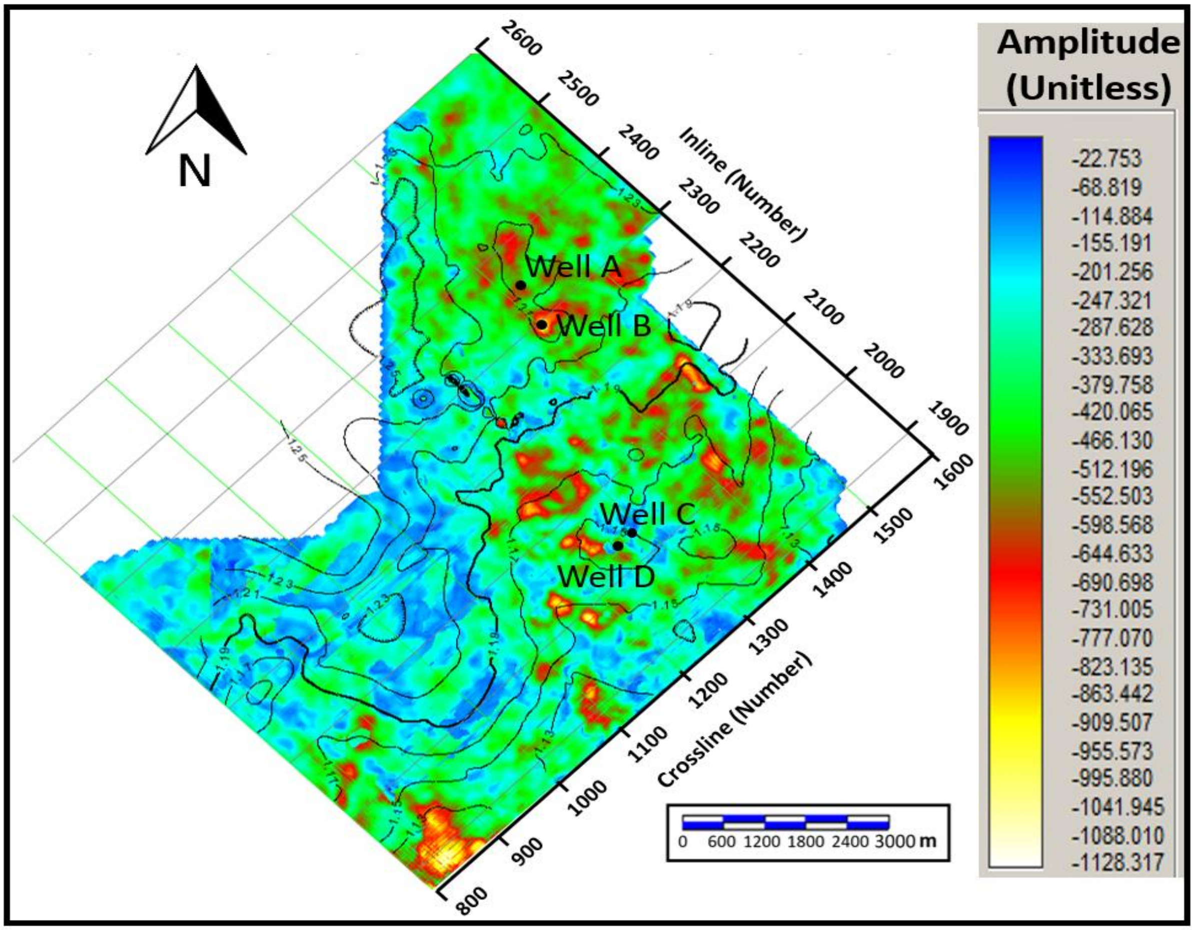

Figure 4.12: RMS amplitude of the Hutton Formation top from far angle stack.

Table 4: Relative amplitudes estimated from near- and far-angle stacks at four well locations using a scale from (0-9).

Wells	Near offset amplitude (Unitless)	Far offset amplitude (Unitless)
Well A	1.179	6.205
Well B	0.527	6.977
Well C	0.967	0.736
Well D	0.768	3.102

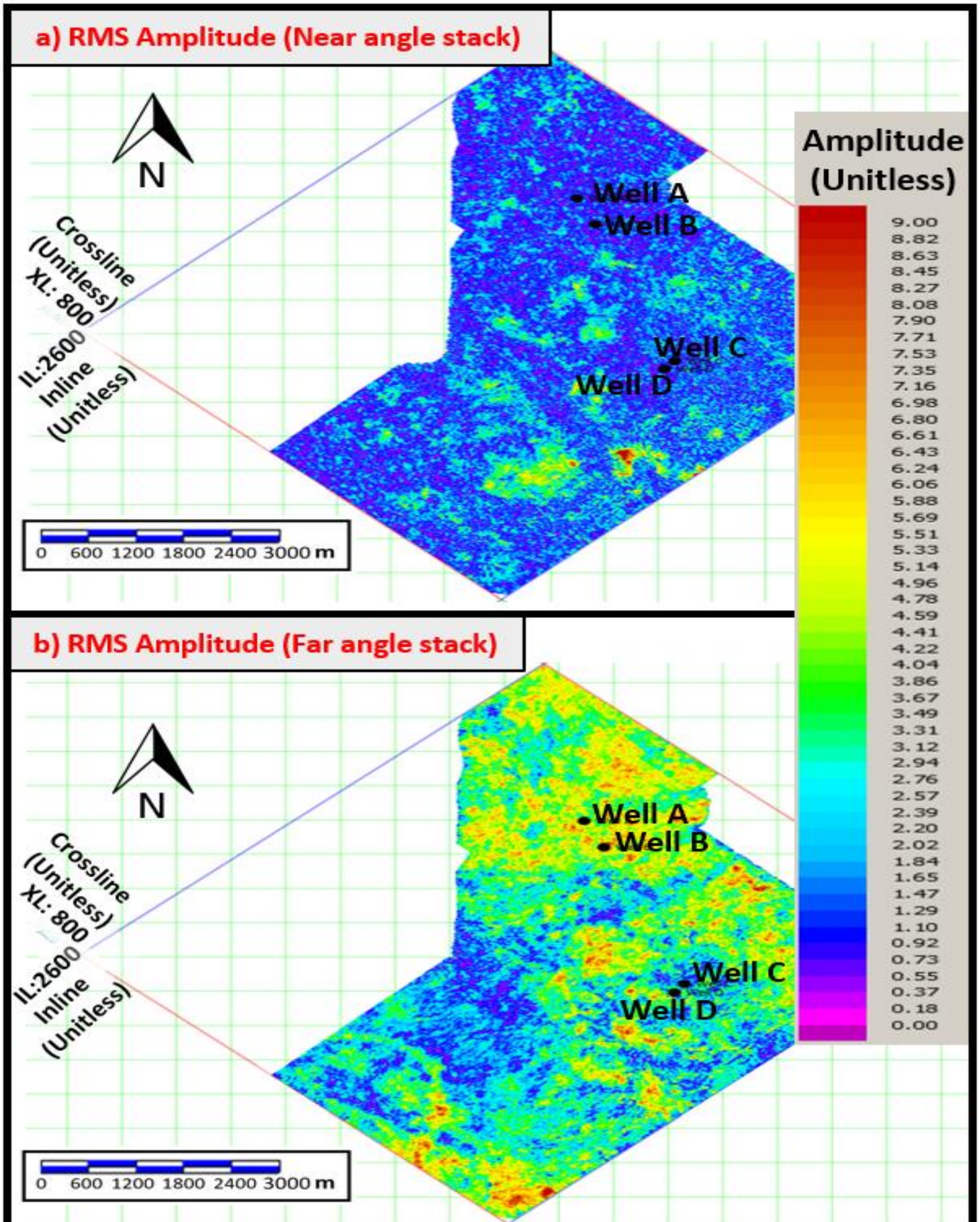

Figure 4.13: Comparison between RMS amplitude extracted from near- and far-angle stacks along horizon slice of 10 ms time window around the Hutton Formation top.

Bright spot methodology is regarded as a starting step for identifying prospects. A bright anomalous amplitude was observed at Well B where a strong negative amplitude occurs between two strong positive amplitudes. Because the stratigraphic column in the study area is basically sand/shale, this strong negative amplitude represents the Hutton Sandstone Formation top. To address the amplitude variation at Well B along the Hutton Formation top, a comparison between observed amplitudes at the pay zone is evaluated in Figure 4.14. There is an increase in amplitude from near-offset to far-offset stacks at the Hutton Formation.

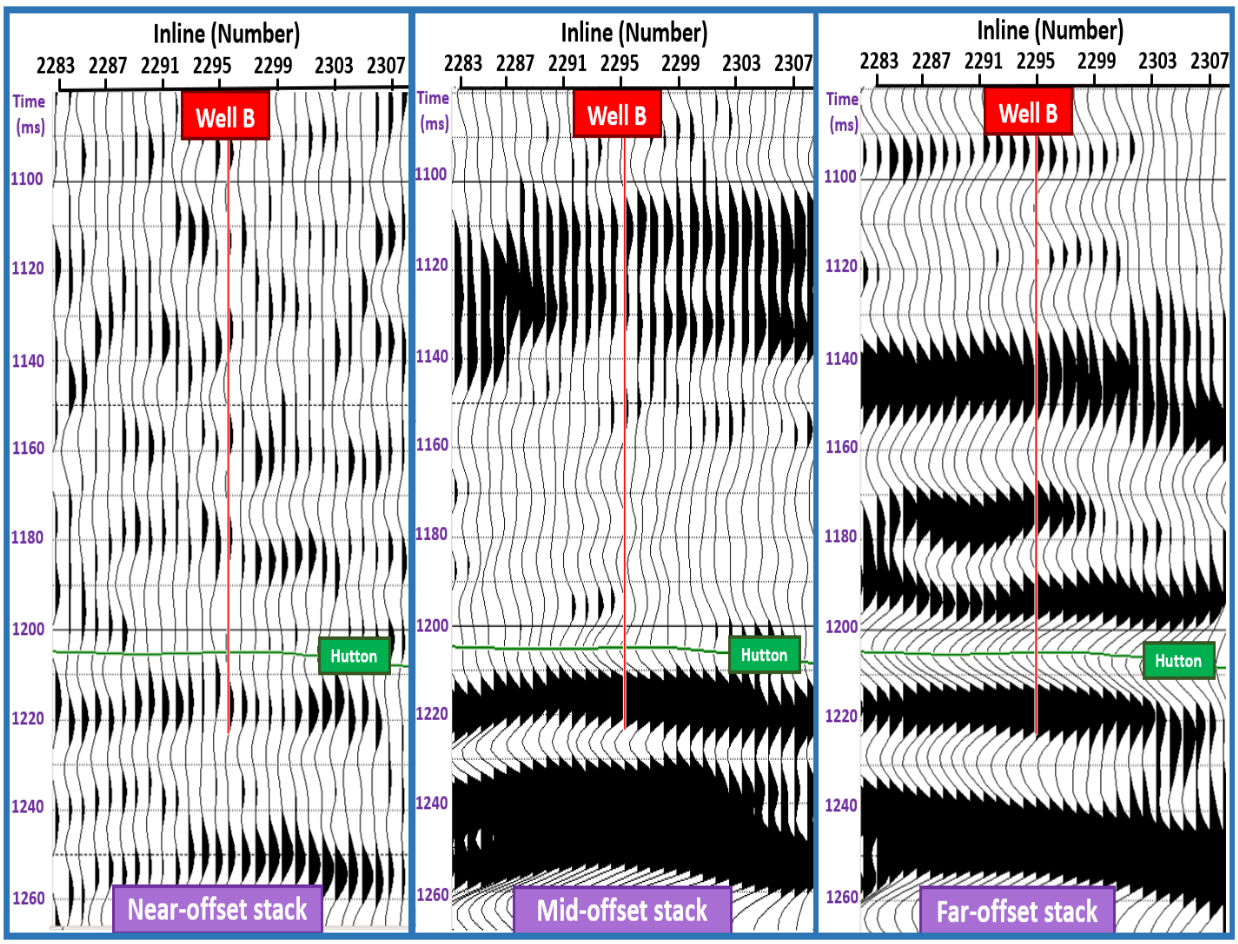

Figure 4.14: Change in amplitude at the Hutton top at Well B from near to mid to far stacks.

4.3. Seismic attributes

Attributes are sensitive to lateral changes in amplitude, reflector orientation, waveforms and reflectivity spectral content. Therefore, they can be used to delineate geological features like channels and faults (Marfurt, 2018). Roberts (2001), Bergbauer et al. (2003), and Al-Dossary and Marfurt (2006) described the principle components of the curvedness attribute (*C*):

$$C = (K_1^2+K_2^2)^{1/2} \tag{4-1}$$

where K_1 is the most positive principle curvature and K_2 is the most negative principle curvature. Figure 4.15 shows curvature attributes where normal to surface vectors are represented by arrows.

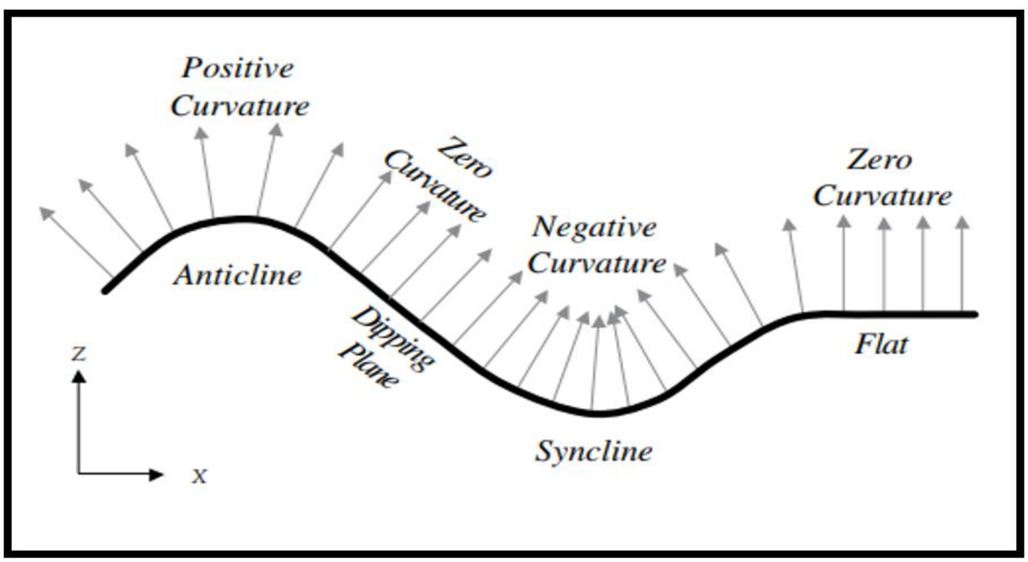

Figure 4.15: Curvature attributes. Vectors, which are normal to surface, are represented by arrows (modified from Roberts, 2001).

Seismic attributes used in this research include dip of maximum similarity, curvature (curvedness), most positive curvature and most negative curvature. Seismic attribute time slices are co-rendered with each other to robustly show structure and stratigraphic features. Time slices were constructed from 3D seismic data to show seismic attributes along 1122 ms, 1150 ms, 1175 ms and 1204 ms within the Hutton Formation as shown in Figures 4.16, 4.17, 4.18 and 4.19. The most positive curvature attribute is co-rendered with the most negative curvature attribute to show more details that are not seen by using dip of maximum similarity attribute as illustrated in Figure 4.20. Most positive curvature shows high structures that are possibly hydrocarbon charged while most negative curvature shows low structures that are possibly brine charged if there are no stratigraphic interferences. After investigating seismic attributes, meandering features are observed that are probably ancient paleo valley system.

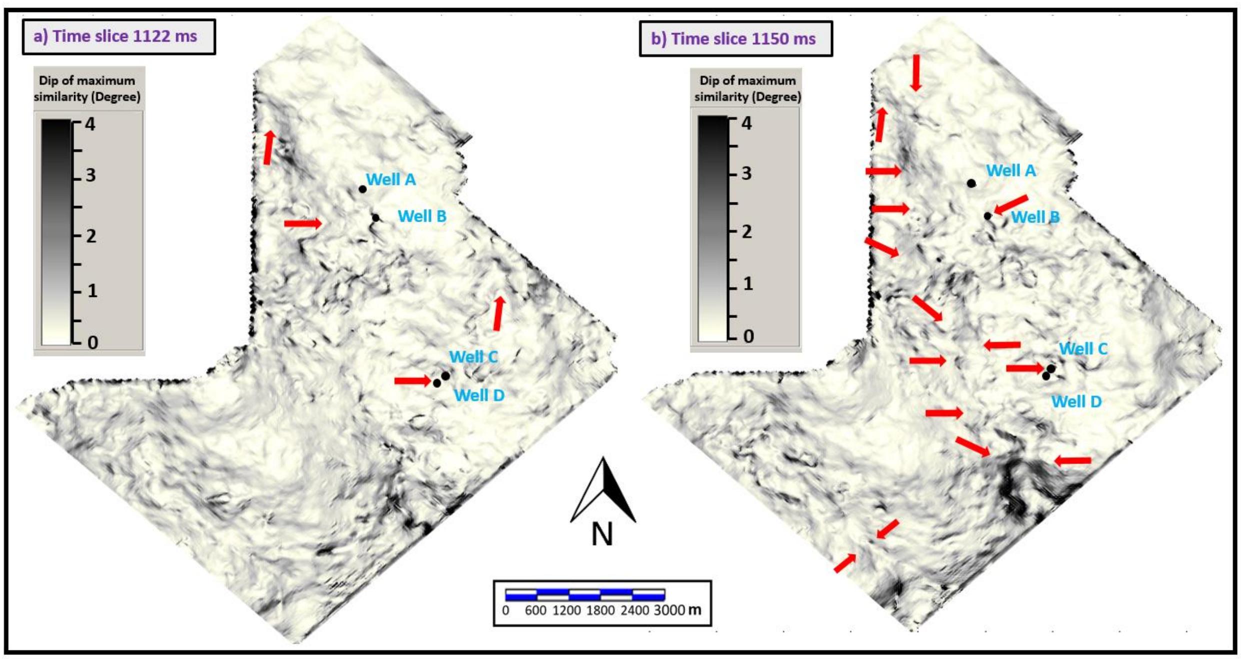

Figure 4.16: Dip of maximum similarity attribute. a) Time slice 1122 ms. B) Time slice 1150 ms.

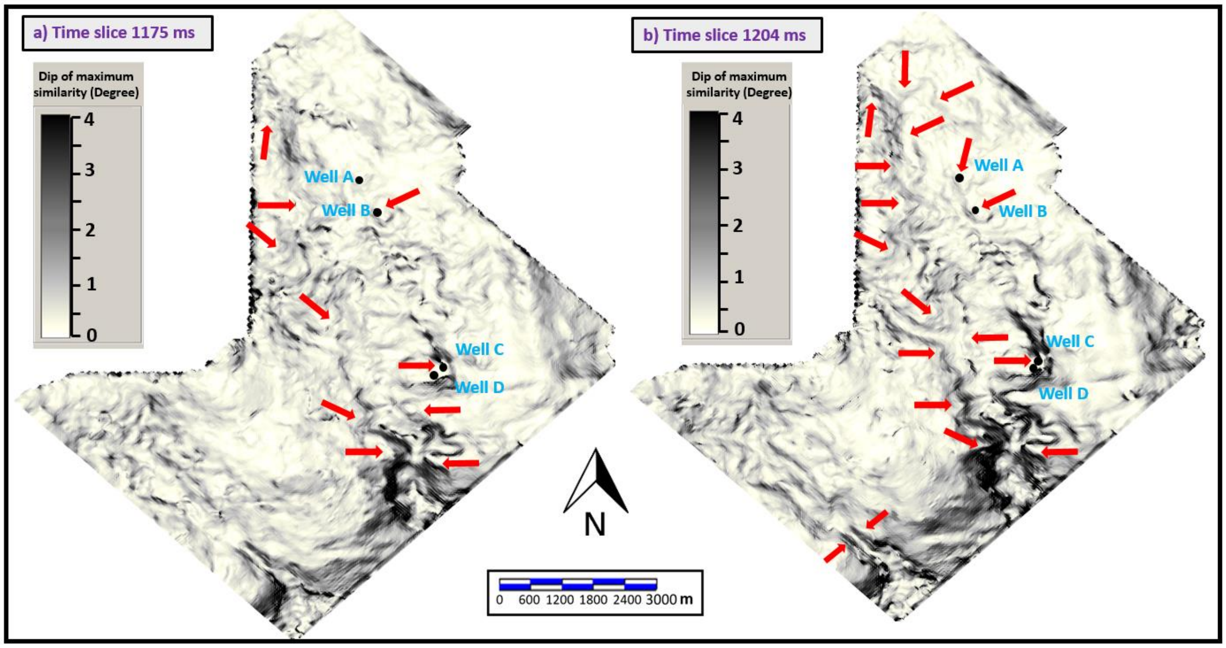

Figure 4.17: Dip of maximum similarity attribute. a) Time slice 1175 ms. B) Time slice 1204 ms.

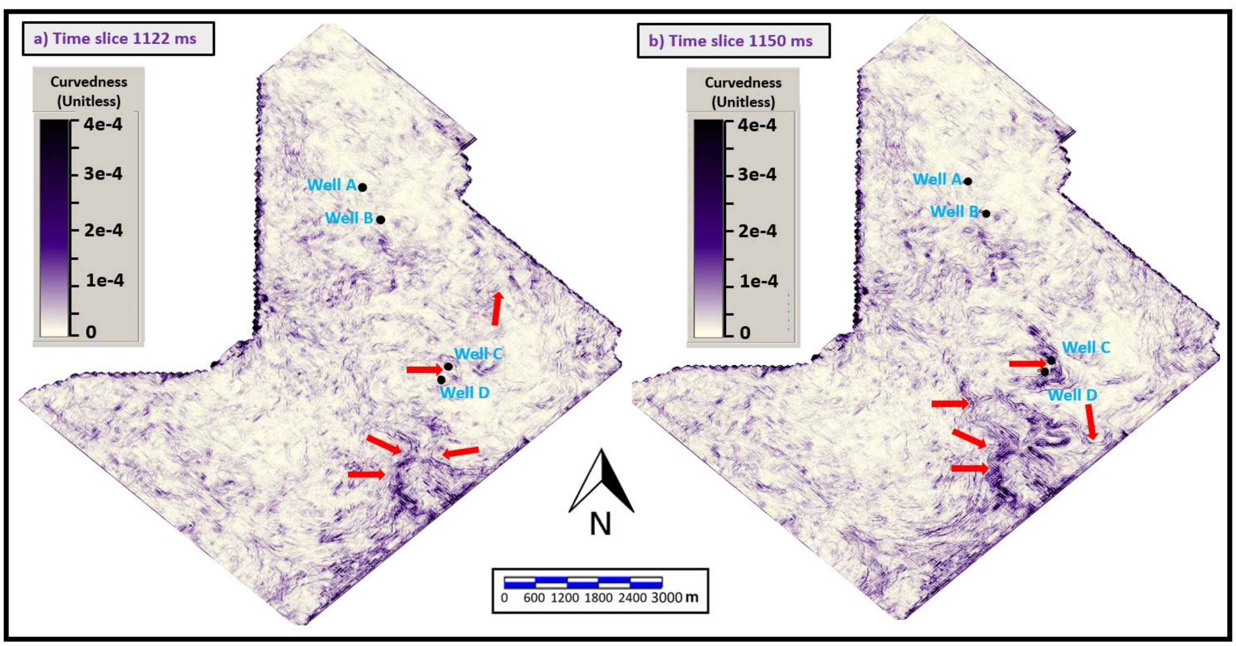

Figure 4.18: Curvature (Curvedness) attribute. a) Time slice 1122 ms. B) Time slice 1150 ms.

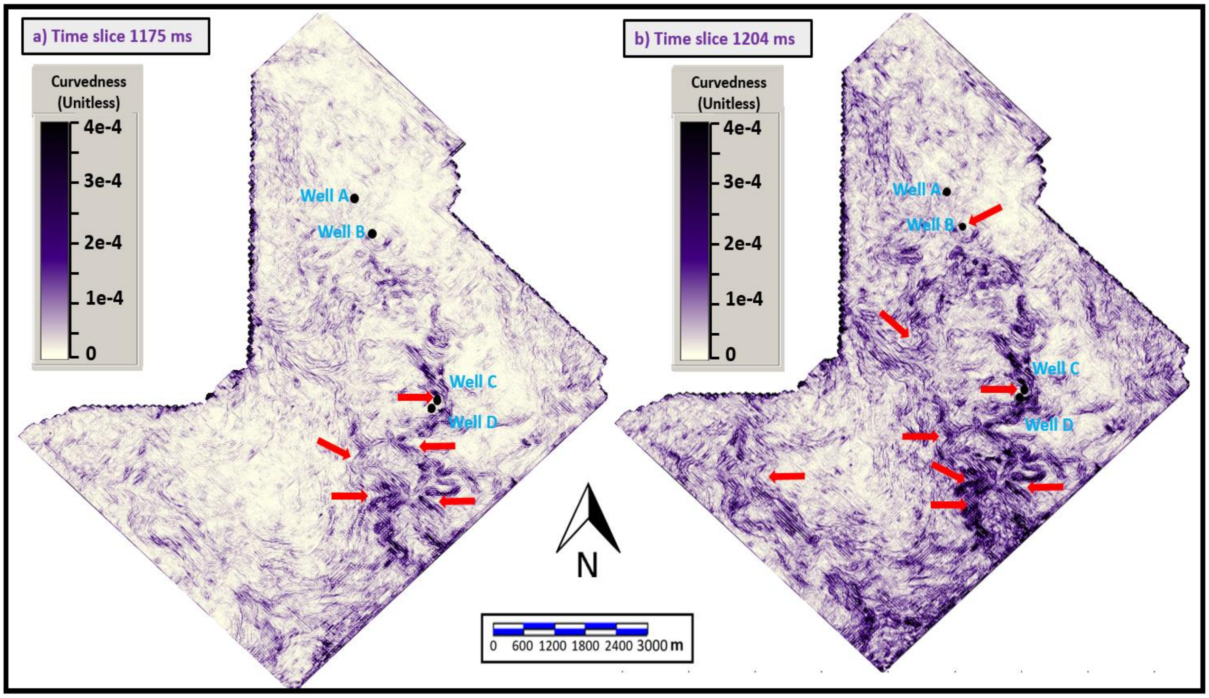

Figure 4.19: Curvature (Curvedness) attribute. a) Time slice 1175 ms. B) Time slice 1204 ms.

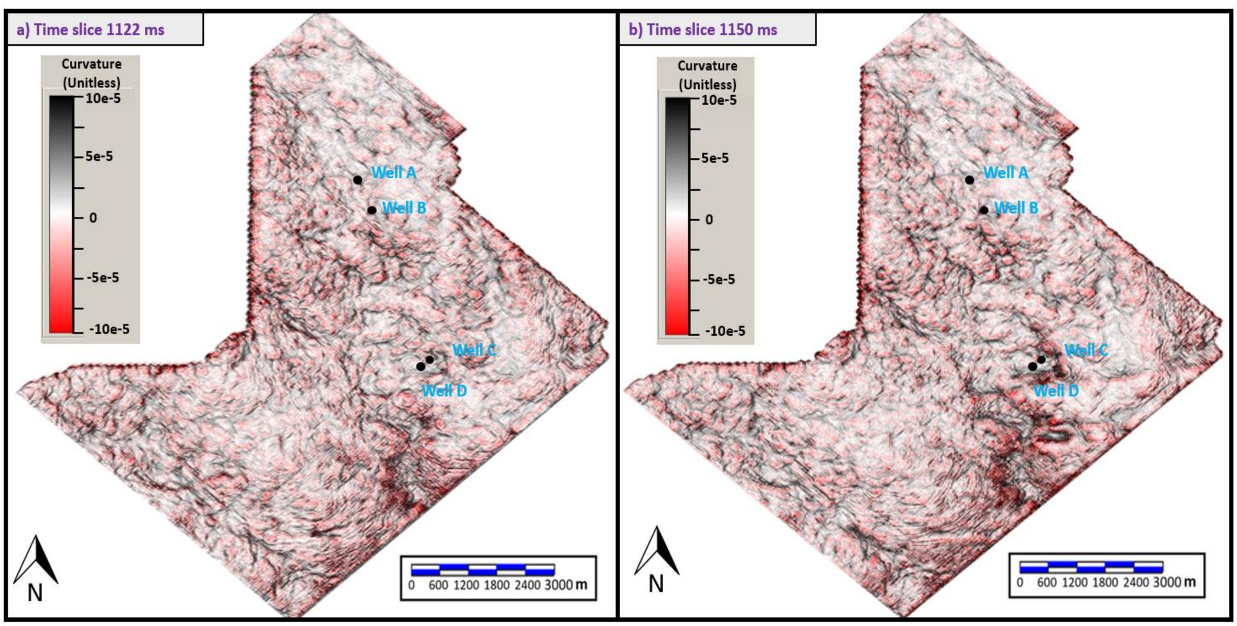

Figure 4.20: Most-positive curvature attribute co-rendered with most-negative curvature attribute. a) Time slice 1122 ms. b) Time slice 1150 ms.

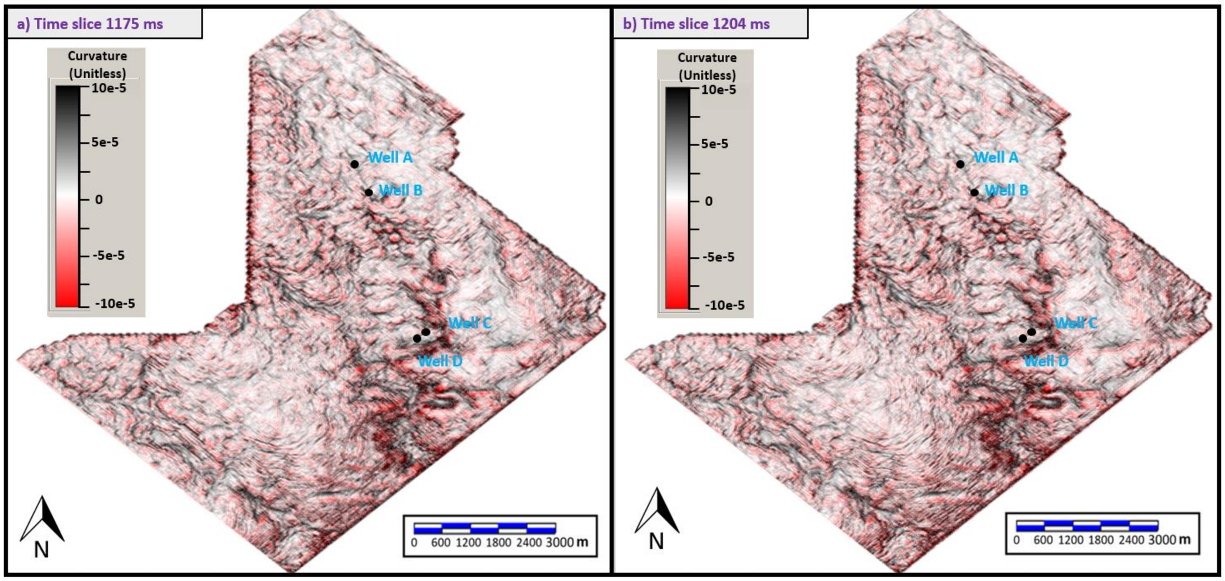

Figure 4.21: Most-positive curvature attribute co-rendered with most-negative curvature attribute. a) Time slice 1175 ms. b) Time slice 1204 ms.

From seismic attributes, basement faults that cut across basement and its overlaying sedimentary section can be seen. Figure 4.22 shows Well A and Well B drilled on high structure surrounded by basement faults as identified from most positive curvature and dip of maximum similarity attributes. Because of structure complexity around Well C and Well D on the far-angle stack, I used seismic attributes extracted from the mid-angle stack to investigate area around Well C and well D as shown in Figures 4.23 and 4.24. Curvature features are noticed around Well C on the curvedness attribute. In arbitrary lines created along these features, they are seen to be fault zones around Well C and between Well C and Well D. They are probably the reason for hydrocarbon accumulation in the Hutton Formation at Well C since these faults could provide a good seal for hydrocarbons and they probably have prevented hydrocarbon migration to Well D. From arbitrary lines, some faults are hardly identified which indicate that they may be syn-depositional faults.

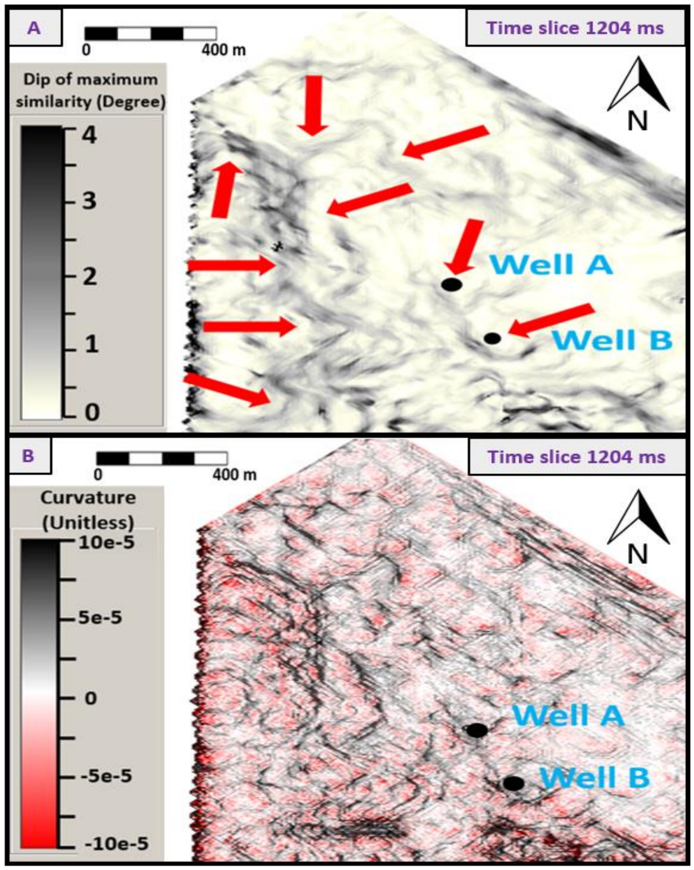

Figure 4.22: a) Time slice shows dip of maximum similarity attribute. b) Time slice co-rendered positive and negative curvature attributes.

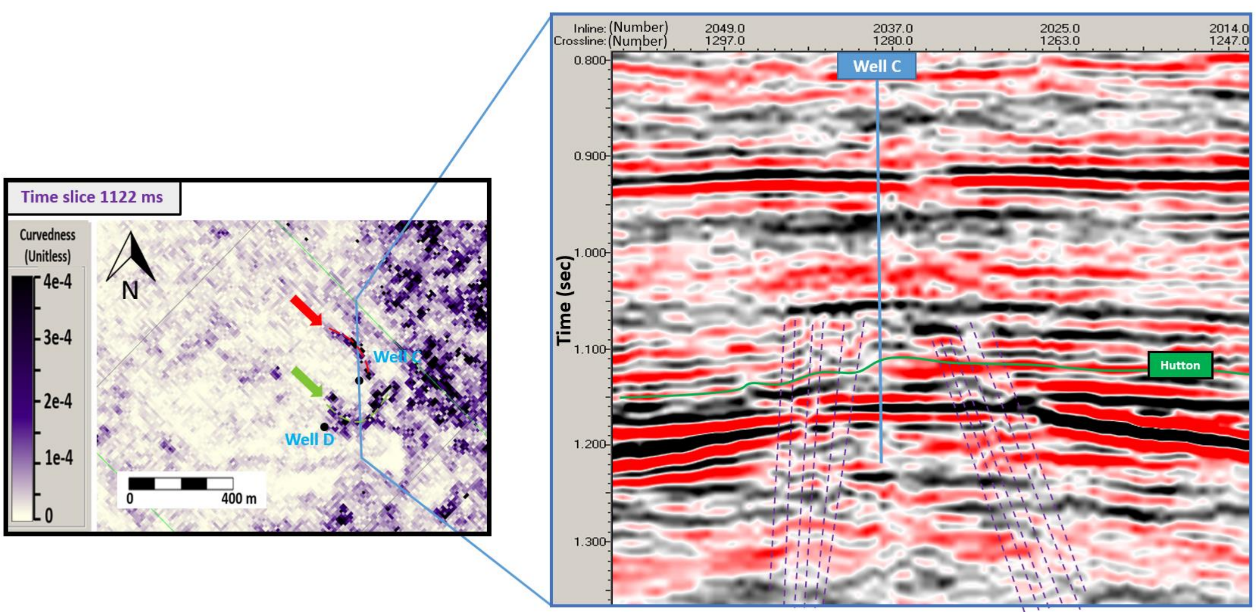

Figure 4.23: a) Time slice shows curvedness attribute at the Hutton Formation top around Well C and Well D. b) Arbitrary line was taken along Well C and Well D.

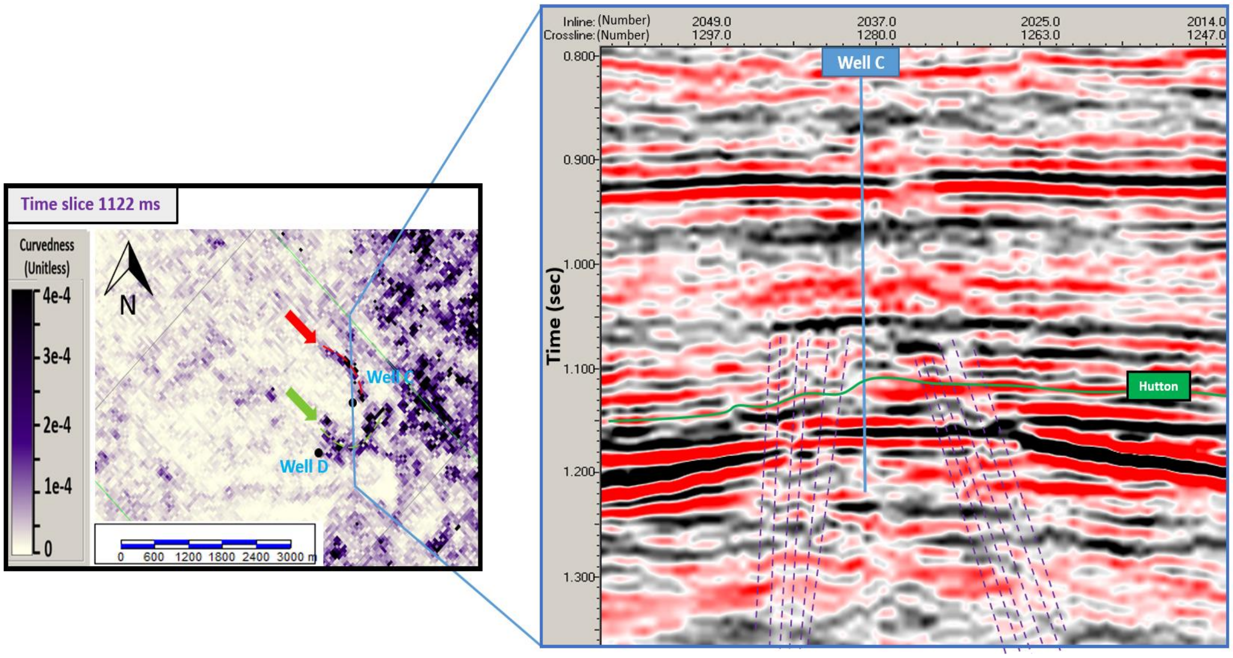

Figure 4.24: a) Time slice shows curvature attribute at the Hutton Formation top around Well C and Well D. b) Arbitrary line was taken along Well C.

For the possibility of stratigraphic features occurrence around Well C and Well D, a big obvious trough and vague peak within it along the Hutton Formation at Well C can be seen as shown in Figure 4.25. When these events are compared with volume of shale (Vsh) estimated from petrophysical analysis at Well C, the trough corresponds with sand rock units while the vague peak corresponds to an increase in volume of shale that represents the seal for the hydrocarbon trap. Furthermore, the lower part of the big trough does not continue until Well D and can be seen to wedge out along the Hutton formation from Well C to Well D. From these observations, I suggest the presence of channel at the Hutton Formation along Well C that provides a reasonable reason for hydrocarbon accumulation at Well C and not Well D.

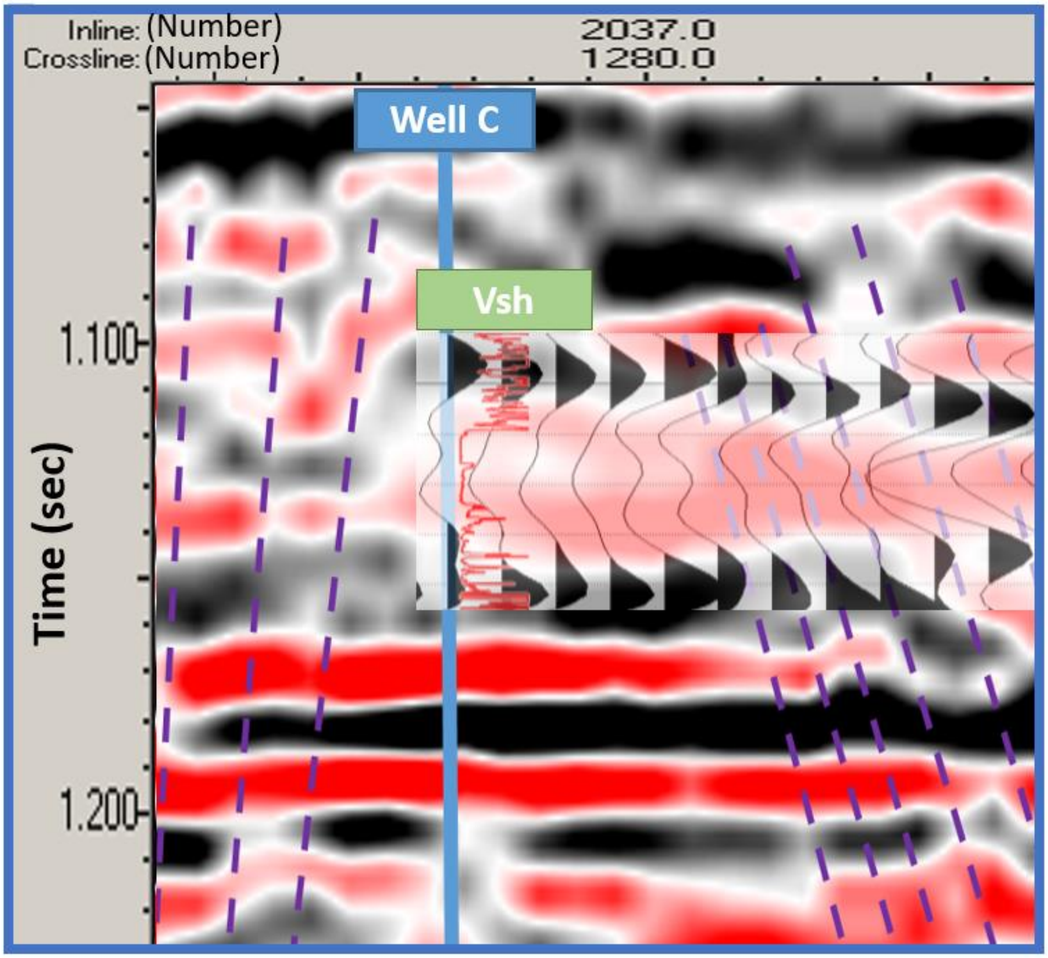

Figure 4.25: Arbitrary line along Well C. Vsh is compared with amplitude of mid-angle stack.

Chapter 5

AVO Analysis

5.1. AVO theory

Reflection and transmission coefficients for plane waves, as a function of the angle of incidence, are given by the Zoeppritz equations (1919):

$$\begin{bmatrix} R_P \\ R_S \\ T_P \\ T_S \end{bmatrix} = \begin{bmatrix} -\sin\theta_1 & -\cos\phi_1 & \sin\theta_2 & \cos\phi_2 \\ \cos\theta_1 & -\sin\phi_1 & \cos\theta_2 & -\sin\phi_2 \\ \sin 2\theta_1 & \frac{V_{P1}}{V_{S1}}\cos 2\phi_1 & \frac{\rho_2 V_{S2}^2 V_{P1}}{\rho_1 V_{S1}^2 V_{P2}}\cos 2\phi_1 & \frac{\rho_2 V_{S2} V_{P1}}{\rho_1 V_{S1}^2}\cos 2\phi_2 \\ -\cos 2\phi_1 & \frac{V_{S1}}{V_{P1}}\sin 2\phi_1 & \frac{\rho_2 V_{P2}}{\rho_1 V_{P1}}\cos 2\phi_2 & \frac{\rho_2 V_{S2}}{\rho_1 V_{P1}}\sin 2\phi_2 \end{bmatrix}^{-1} \begin{bmatrix} \sin\theta_1 \\ \cos\theta_1 \\ \sin 2\theta_1 \\ \cos 2\phi_1 \end{bmatrix} , \qquad (5\text{-}1)$$

where R_P, R_S, T_P, and T_S, are the reflected *P*, reflected *S*, transmitted *P*, and transmitted S-wave amplitude coefficients, θ_1 is the angle of incidence, θ_2 is the angle of the transmitted P-wave, ϕ_1 is angle of reflected S-wave and ϕ_2 is the angle of the transmitted S-wave. Because the Zoeppritz equations are mathematically complex, several approximations to the Zoeppritz equation have been deduced by multiple authors. Table 5.1 summarizes these approximations.

I use the Aki and Richard approximation (1980) in this thesis:

$$R(\theta) \approx \frac{1}{2}\left(\frac{\Delta V_p}{V_p} + \frac{\Delta\rho}{\rho}\right) + \left(\frac{1}{2}\frac{\Delta V_p}{V_p} - 4\frac{V_S^2}{V_p^2}\frac{\Delta V_s}{V_s} - 2\frac{V_S^2}{V_p^2}\frac{\Delta\rho}{\rho}\right) X \ sin^2\theta + \frac{1}{2}\frac{\Delta V_p}{V_p}\left(tan^2\theta - sin^2\theta\right) , \qquad (5\text{-}2)$$

where ρ is density and θ is the angle of incidence. Equation (5-2) has the following form:

$$R(\theta) \approx A + B\, sin^2\theta + C\, sin^2\theta\, tan^2\theta \qquad , \qquad (5\text{-}3)$$

where *A* is AVO intercept or normal incidence reflectivity, *B* is AVO gradient and *C* is curvature. Because of high noise in extracting the third term C (Castagna and Swan, 1997), the first two terms are usually preferable for AVO analysis.

Table 5.1: Approximations for the Zoeppritz equations. Modified from (Castagna and Chopra, 2014) after Li et al., 2007.

Approximation	Solution sought	Assumptions/limitations
Bortfeld	Zero-offset intercept and slope, R_P and R_S	Valid for all pre-critical angles.
Aki and Richards	Zero-offset intercept and slope, R_P, R_S	Good for angles smaller than 35° for typical contrasts in elastic properties, if the average angle is not used.
Hilterman	Change in Poisson reflectivity. $PR = \frac{\Delta\sigma}{(1-\sigma)^2}$	Derived from Shuey's equations; ignores angles >30°, although Shuey's third term can be added; makes no density assumptions.
Smith and Gidlow	P-velocity reflectivity $\frac{\Delta V_p}{V_p}$ S-velocity reflectivity $\frac{\Delta V_s}{V_s}$	Valid for all angles up to the critical angle, makes no assumptions about VP/VS. Assumes density follows Gardner's relation
Fatti et al.	P-impedance reflectivity $\frac{\Delta I_p}{I_p}$ S-impedance reflectivity $\frac{\Delta I_s}{I_S}$	Good out to large pre-critical angles; makes no assumptions about density or VP/VS.

5.2. AVO analysis

Amplitude-variation-with-offset (AVO) has been regarded as a fundamental seismic rock-property tool for lithology and pore-fluid identification. AVO analysis depends mainly on using variation of P-wave reflection coefficients with offset to address contrasts in shear-wave velocities and densities across lithology or pore-fluid interfaces. Ostrander (1984) introduced

AVO to detect gas sands. Rutherford and Williams (1989) identified three distinct classes of gas sand AVO anomalies. Castagna et al., (1998) added a fourth class. Hilterman (2001) illustrated a way to classify any gas sand by comparing near and far offset amplitudes. Foster et al. (2010) addressed effects of reservoir properties change on AVO response. Figure 5.1 shows change of reservoir properties on a gradient-intercept crossplot. Fluid compressibility changes increase as points plot away from a background trend. In addition, porosity increases as data points shifted from class 1 to class 4.

In this study, angle gathers were sorted from near-, mid- and far-angle stacked seismic volumes for conducting AVO analysis and creating AVO attribute volumes. The near-angle stack is very noisy. To avoid noisy results of AVO and inversion, seismic data conditioning was first applied to the angle gathers. This included: Radon filter, time-variant spectral balancing, trim-statics, phase correction (-80° rotation), band-pass filter, and AVO filter. Because of the irregular arrangement of near, mid and far traces, trim statics was applied to flatten arrival times as a convenience for AVO analysis.

Angle gathers before and after noise suppression are shown in Figures 5.2 and 5.3. Noises are well removed along the Hutton Formation top represented by trough wiggles.

After seismic data conditioning, angle gathers were investigated for AVO behavior at well locations. Intercept and gradient were calculated using the Aki-Richards (1980) two-term approximation. The third term was not used to avoid noise. Amplitude change with angle is measured at the four well locations as illustrated in Figures 5.4 and 5.5. There is a great difference between near and far-angle amplitude at Well A and Well B which is attributed to low water saturation. At Well C and Well D, there is a small difference between near- and far-angle amplitude which is attributed to high water saturation. Intercept-verses-gradient crossplots were generated from angle gathers at the four well locations to address pore-fluid discrimination and hydrocarbon sand classes as shown in Figures 5.6. AVO analysis shows good pore fluid discrimination at the Well B location where the plotted point is far from the background trend. The oil sand at Well B has class 3 sand type. At the Well A location, the plotted point is shifted a small distance from the background trend where the oil-bearing layer has class 3 sand type. Well C, however, shows poor pore-fluid discrimination that may be attributed to high water saturation (60%). It has class 4 sand type since amplitude decreases with angle. The points at Well C and Well D plotted close to the background trend.

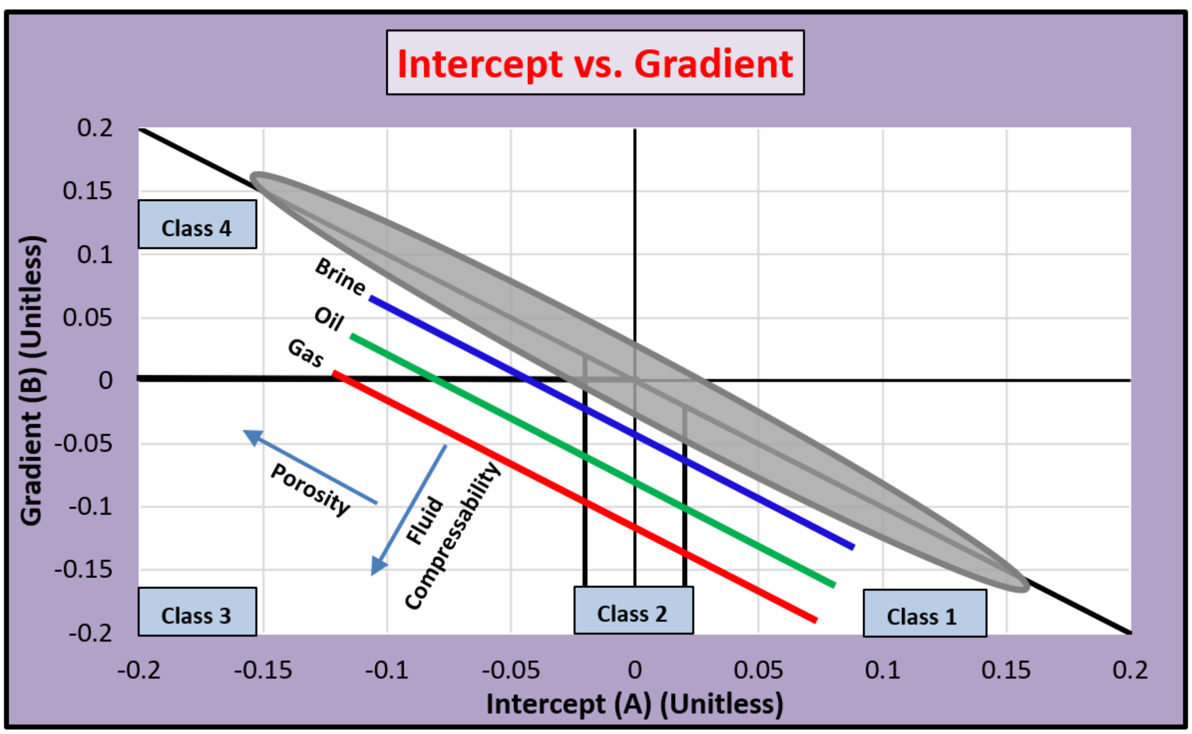

Figure 5.1: Gradient-Intercept crossplot. Modified from Castagna et al., (1998) and Foster et al., (2010).

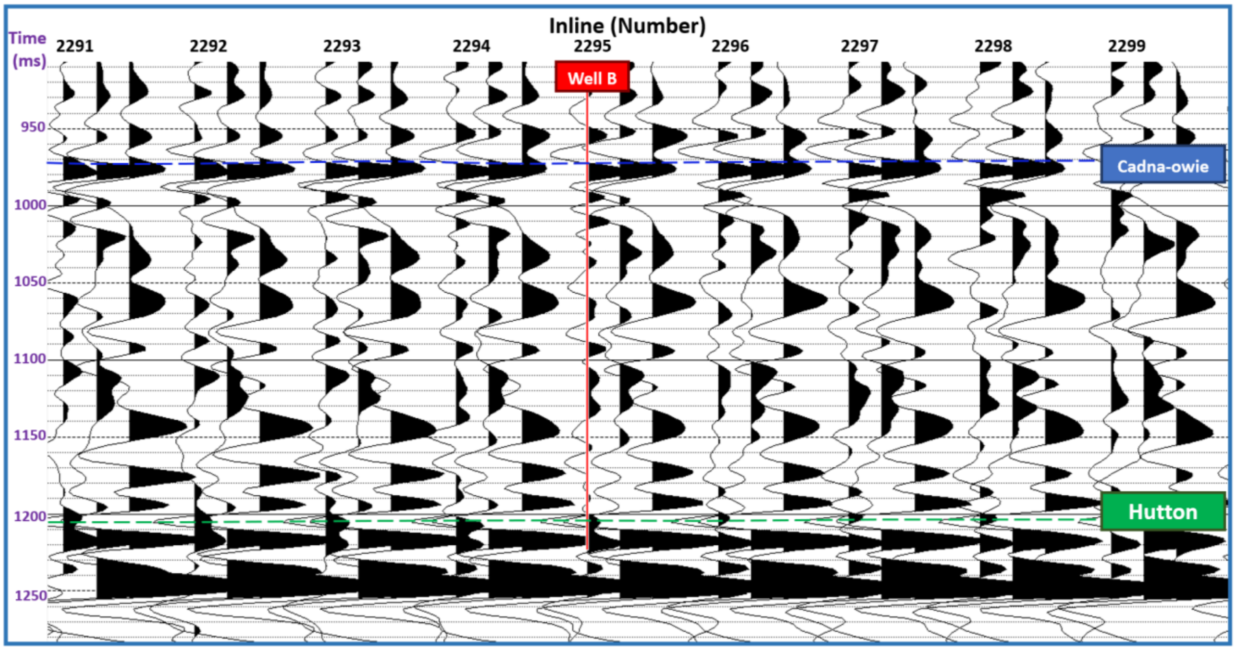

Figure 5.2: Angle gathers before seismic data conditioning.

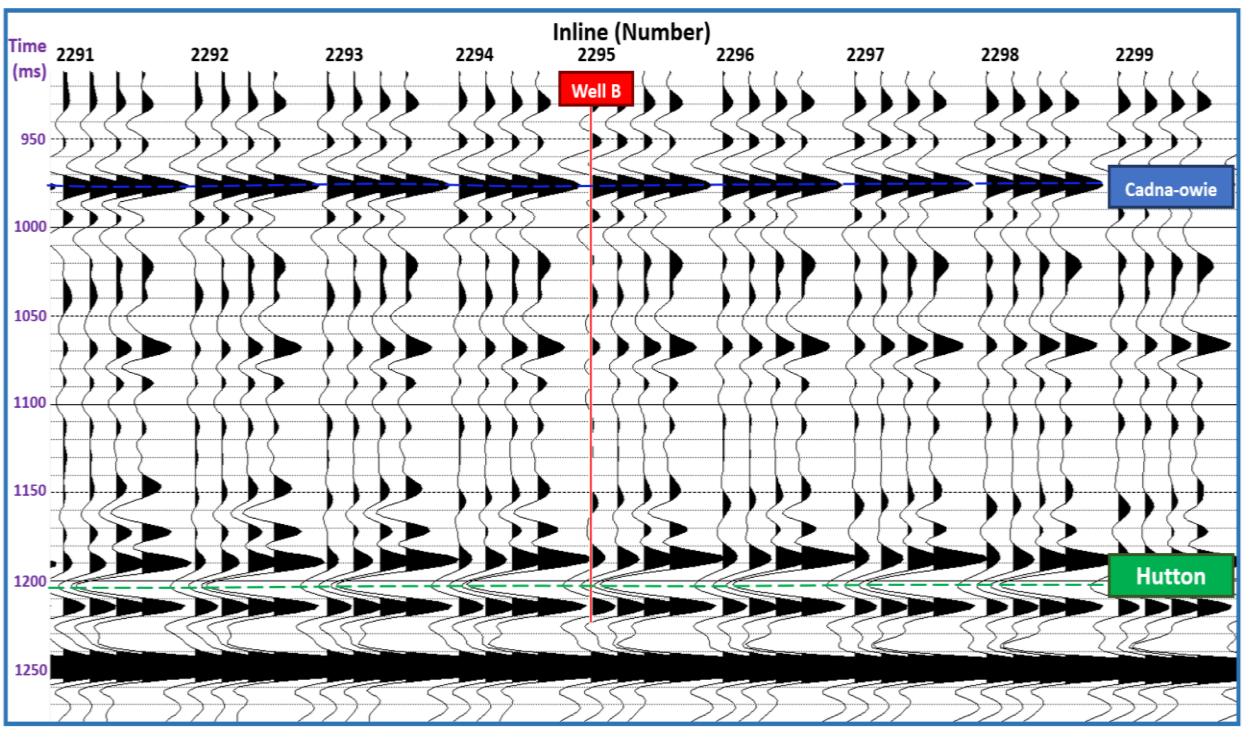

Figure 5.3: Angle gathers after seismic data conditioning.

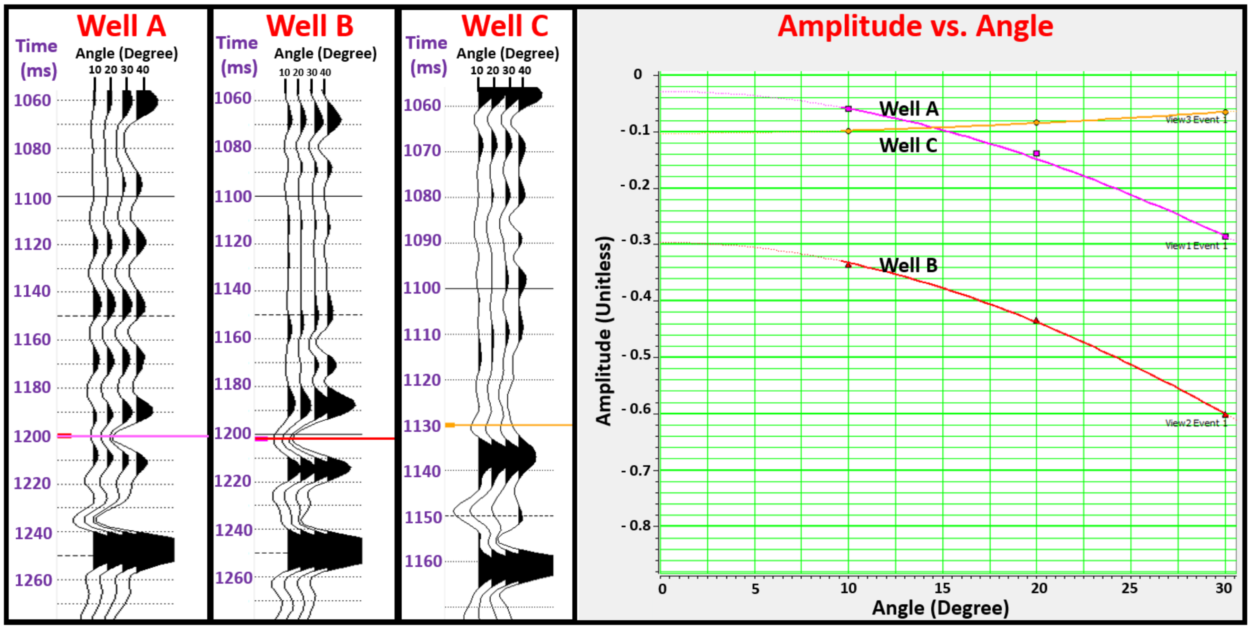

Figure 5.4: AVO analysis from angle gather at Well A, Well B and Well C locations.

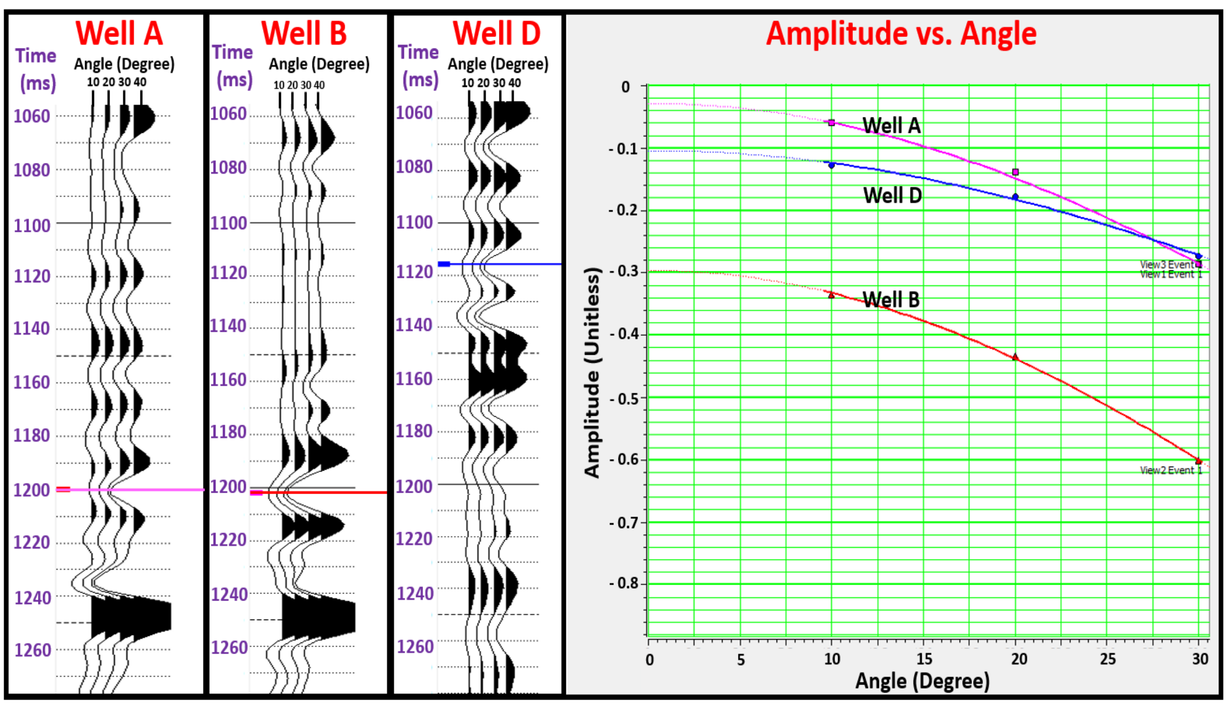

Figure 5.5: AVO analysis from angle gather at Well A, Well B and Well D locations.

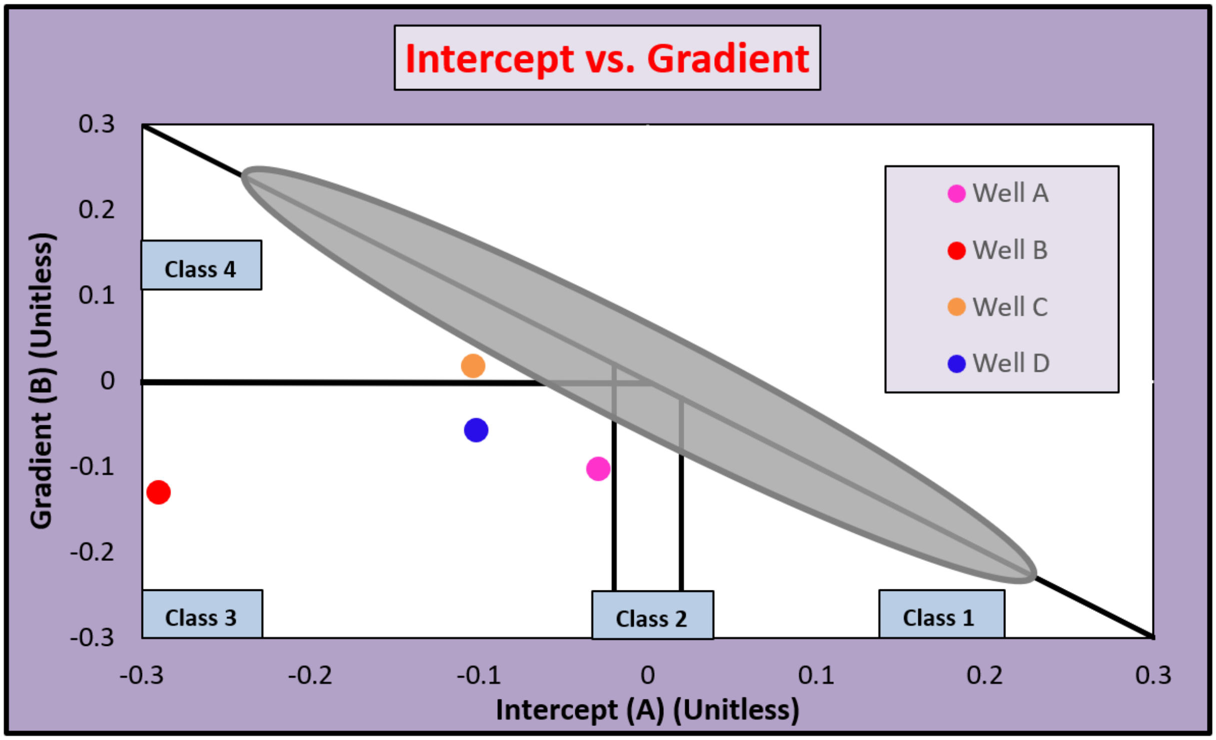

Figure 5.6: Intercept versus gradient crossplot from seismic angle gather at four wells.

As described in Chapter 4 concerning the Hutton Formation, at Well C, a big obvious trough and a vague peak within it occurs on the mid-angle stack at the Hutton Formation at the Well C location. Because of the small peak occurrence within a big trough, I divided the big trough into two troughs and did AVO analysis for both using near-angle and far-angle traces of the angle gather as shown in Figure 5.7. I noticed an increase in amplitude with offset for the upper trough which is a similar behavior to the AVO response at other wells especially Well D that is located very close to Well C. The time window of the lower trough, however, has a decrease in amplitude with offset which is a different behavior compared with what is observed at Well D. From this observation, I suggest that the lower trough at time 1128 ms in the mid-angle stack represents a channel. Because the trough thickness of the proposed channel increases away from Well C, AVO analysis was conducted around Well C along it and its AVO response is compared with Well C as shown in Figure 5.8. An anomalous AVO response occurs at the proposed channel around Well C which has class 4 sand type. This result strengthens the possibility of channel occurrence around Well C.

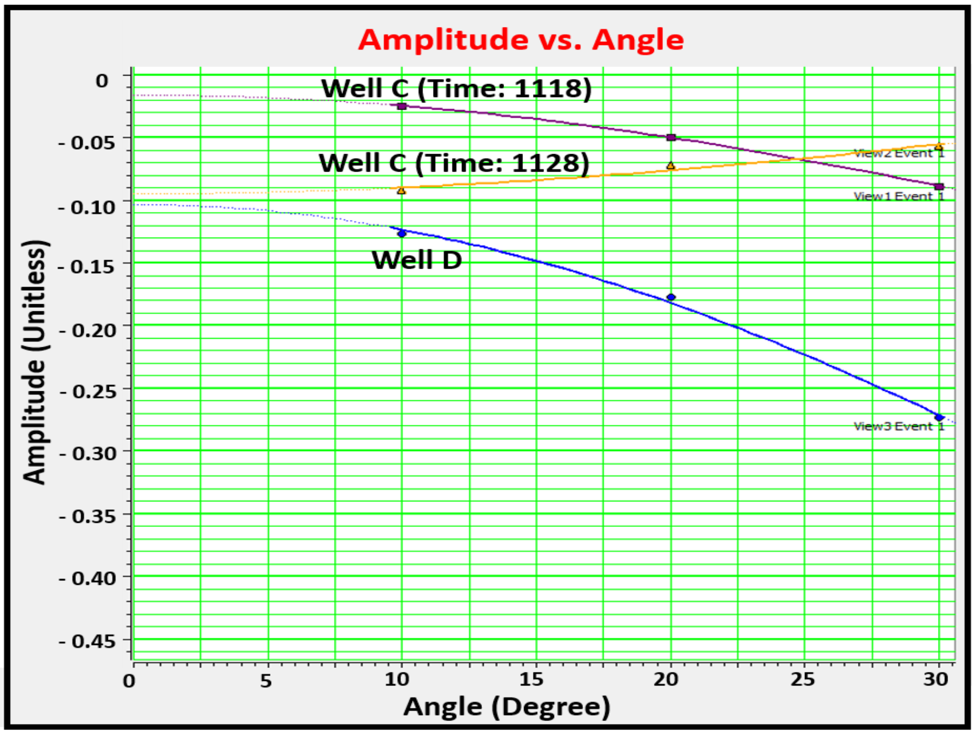

Figure 5.7: Comparison between AVO responses of Hutton Formation top at Well D and Well C.

To address AVO response at wells, a comparison between AVO synthetic and seismic gathers at well locations was conducted. An example of this comparison at Well B is shown in Figure 5.9 and 5.10. Both the AVO synthetic and the seismic gather at Well B exhibit amplitude decreasing with angle. Although both the AVO synthetic and seismic gather at Well B have negative intercepts and gradients, they have, however, different gradients since the estimated gradient from the seismic gather at Well B location is more anomalous than the AVO synthetic.

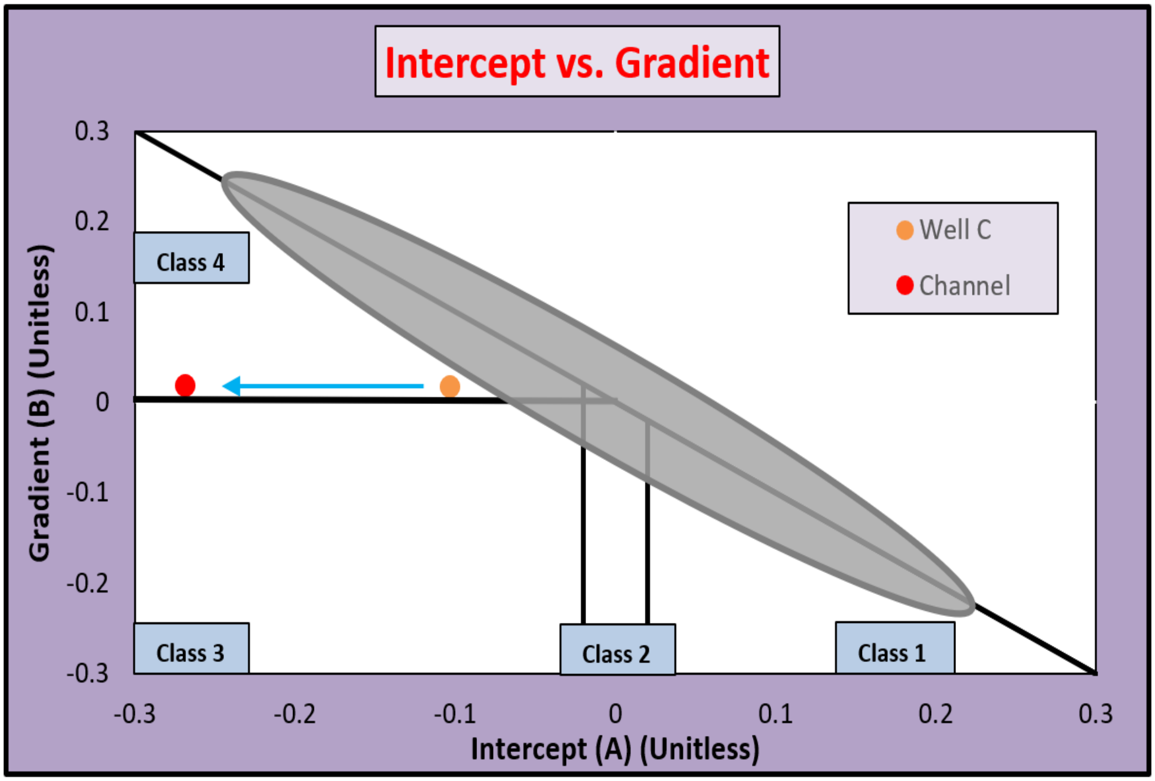

Figure 5.8: AVO analysis of a seismic angle gather at Well C location and the proposed channel.

Furthermore, an intercept verses gradient crossplot was derived from the AVO synthetic of Well B for a 250 ms time window around the Hutton Formation top (Figure 5.11). Background trend and anomalous points are highlighted on the crossplot and then colors are projected on Well B. An anomalous class 2 sand is projected on the pay zone at Well B and coincides with the picked seismic trough at the Well B location.

To address detection of trends within the seismic volume, intercept and gradient were estimated for 30 ms around the Hutton Formation top and then crossplotted as shown in Figure 5.12. Because hydrocarbon pore fluids can exhibit different sand classes at different locations along the reservoir extent, anomalous trends are highlighted by only one red ellipse including all possible sand classes. The red color is projected onto the seismic volume to delineate hydrocarbon lateral distribution on the 3D seismic data. A 10 ms horizon slice around the Hutton Formation top is extracted from the resultant 3D seismic volume as shown in Figure 5.13. Red zones are distributed along Well A and Well B which matches with oil pore fluid detectability. Red zones, however, do not occur at Well C which also has oil pore fluid. This may be attributed to high water saturation estimated from petrophysical analysis at Well C and/or thin pay thickness which is below seismic resolution. In addition, there is no red zone distribution along Well D and this result is consistent with the brine pore fluid identified at Well D.

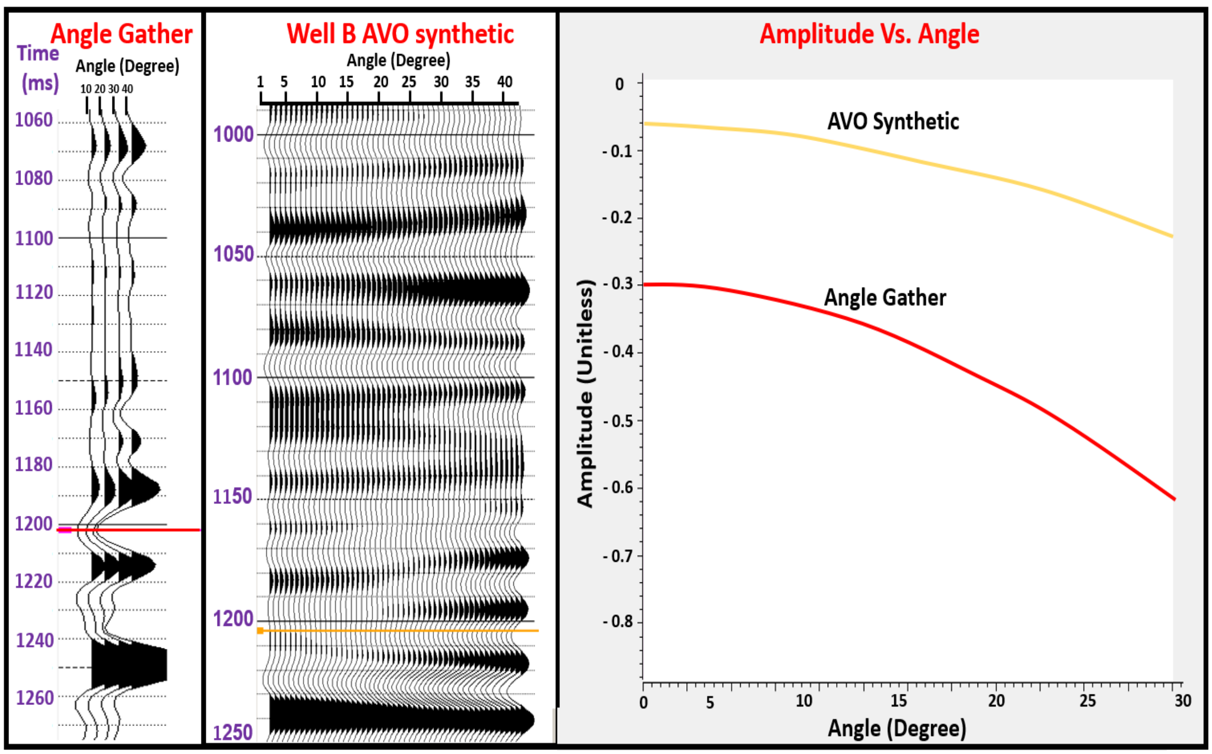

Figure 5.9: Amplitude versus angle crossplot for comparison between the seismic angle gather and AVO synthetic at Well B.

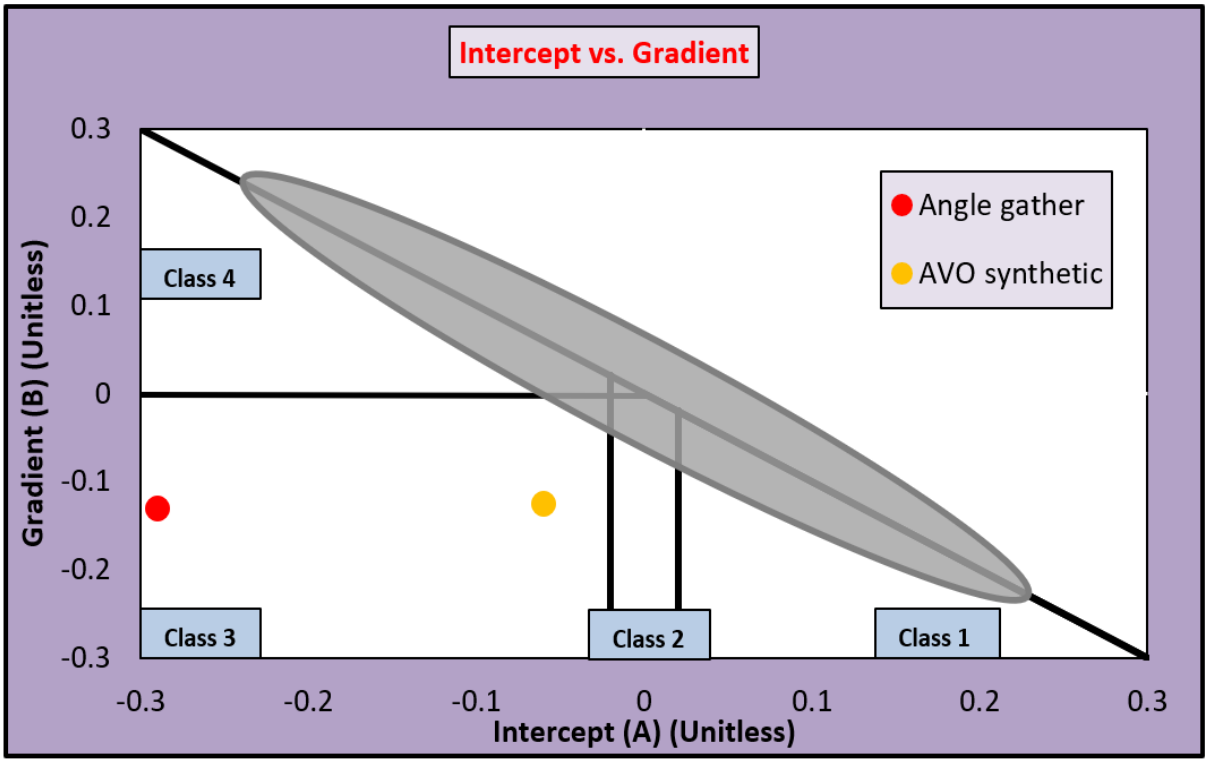

Figure 5.10: Intercept versus gradient crossplot for comparison between the seismic angle gather and AVO synthetic at Well B.

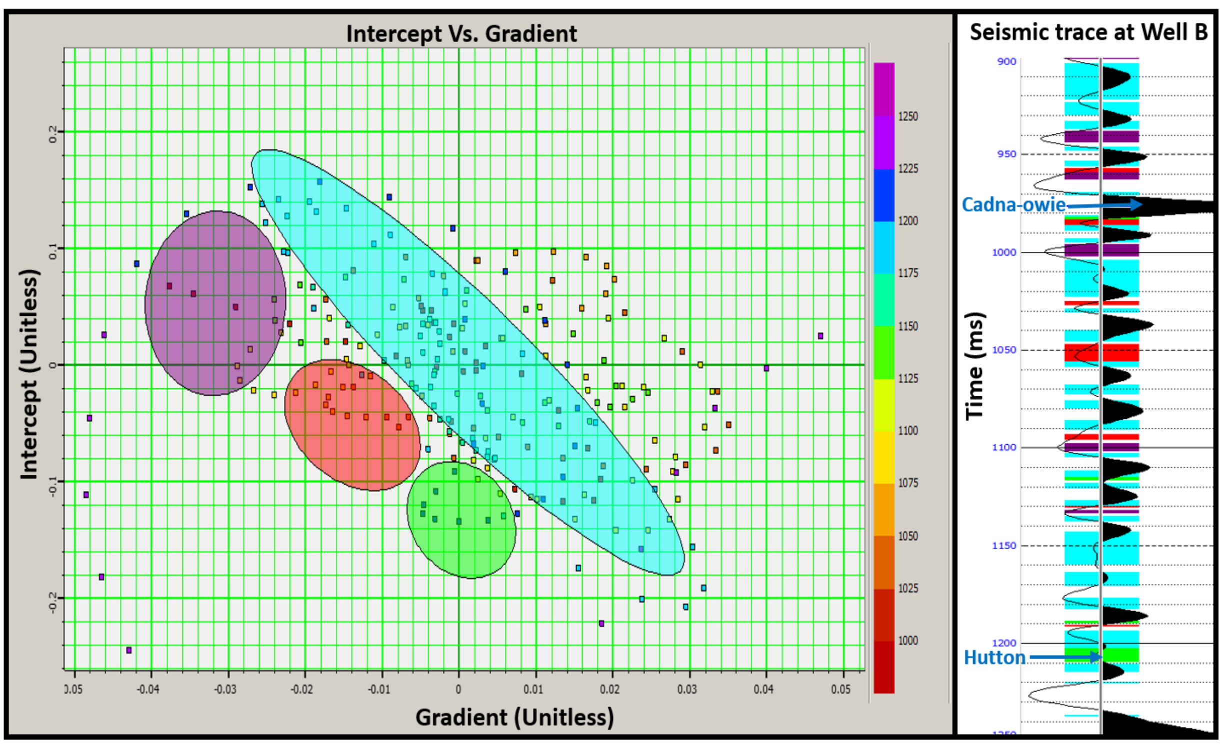

Figure 5.11: Intercept versus gradient crossplot for 250 ms window of the AVO synthetic at Well B. Colors are projected on a seismic trace at the Well B location.

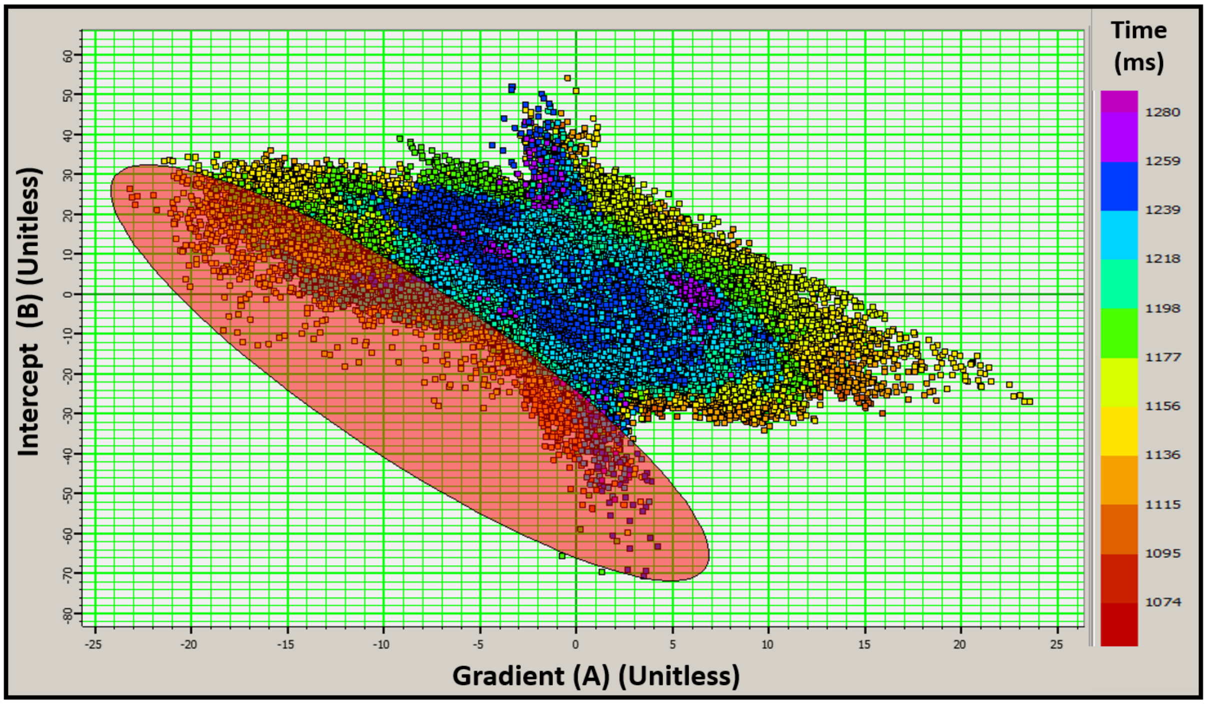

Figure 5.12: Gradient versus intercept for 30 ms around the Hutton Formation top. Red elliptical shape covers possible trends for hydrocarbon pore fluids deviated from the background trend.

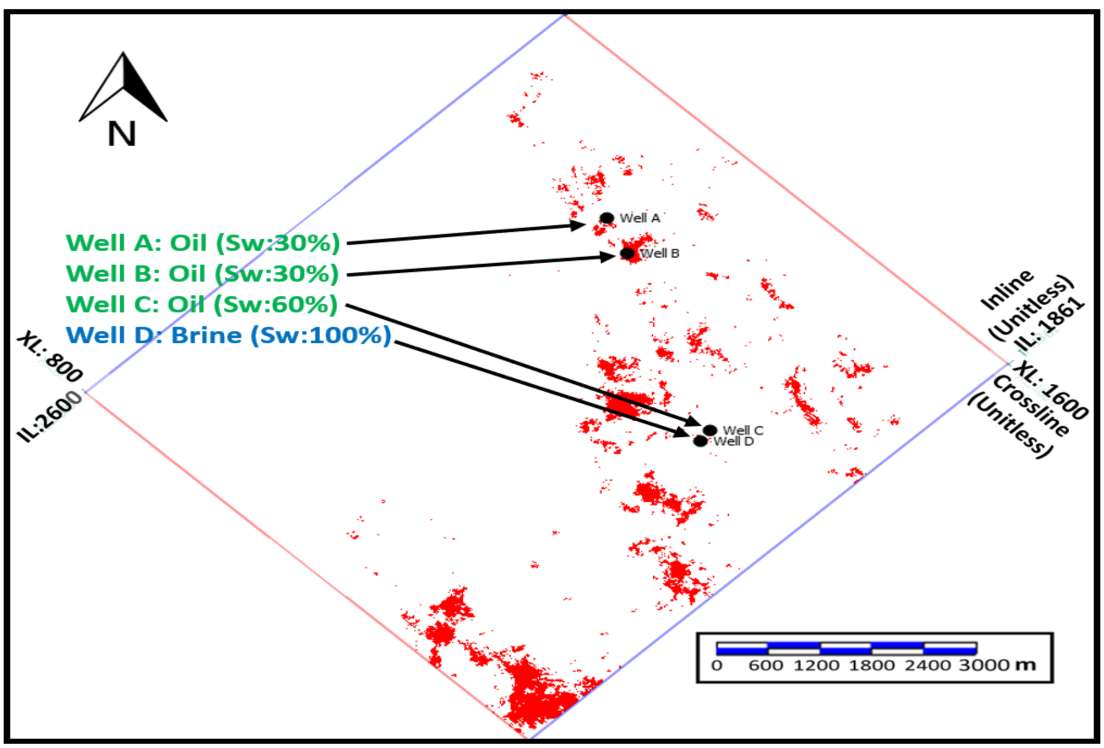

Figure 5.13: 10 ms horizon slice around the Hutton Formation top. Red color indicates possible hydrocarbon pore fluids.

5.3. AVO attributes

AVO attributes were created from seismic angle gathers and are compared with pore fluids identified at wells. Intercept (A) and gradient (B) were calculated using the Aki-Richards (1980) approximation. From gradient and intercept, other AVO attributes were calculated. I selected attributes that have great similarity to anomalous amplitude distribution. The gradient-intercept product (A*B) has been used as a hydrocarbon indicator especially for class 3 sands. The product (A*B) slice was generated below the Hutton Formation Top as shown in Figure 5.14.

In addition, Keho et al., (2001) noticed that AVO attributes are polarized along the background trend for brine data and at angles (called polarization angles) that differ from the background trend for anomalous hydrocarbons. Based on this observation, they suggested crossploting near-angle and far-angle AVO attribute traces. From this idea, Mahob and Castagna., (2003) created polarization attributes as tools for enhancing AVO interpretation. Polarization angle is measured by the following equation

$$\tan^{-1} \emptyset = \frac{P_y}{P_x} \ , \qquad (5\text{-}3)$$

where P_y and P_x are eigenvector components of the correlation matrix. Polar magnitude is one of the attributes used in this research for improving fluid discrimination. This magnitude is represented by the distance between origin and hodogram points. The magnitude (L) is measured by following equation:

$$L = L_{min} + L_{max} \ , \qquad (5\text{-}4)$$

$$L_{min} = \sqrt{A_{min}^2 + B_{min}^2} \quad , \text{ and} \tag{5-5}$$

$$L_{max} = \sqrt{A_{max}^2 + B_{max}^2} \quad , \tag{5-6}$$

where A_{min} and A_{max} are the most positive and most negative numbers on the A axis while B_{min} and B_{max} are the most positive and most negative numbers on the B axis.

The polar magnitude increases as a result of anomalous events. Figure 5.15 shows positive values of polar magnitude at Well A and Well B and negative value at Well D. It, however, has negative value at Well C. This may be attributed to high water saturation or pay zone below resolution limit at Well C. Ross (2002) established extra AVO attributes for distinguishing hydrocarbon pore fluid such as scaled Poisson's-ratio change (the weighted sum of AVO intercept and gradient; aA+bB) and other attributes created from differences between near- and far-angle volumes and multiplying the result by the far angle volume. Negative values of scaled Poisson's-ratio are a high indicator of anomalous hydrocarbon zones as illustrated in Figure 5.16. Distribution of scaled Poisson's ratio matches with pore fluids identified from petrophyiscal analysis at the wells. Negative scaled Poisson's ratio occurs at Well A and Well B having oil pore fluid (Sw = 30%). Low positive scaled Poisson's ratio occurs at Well C that has oil pore fluid with high water saturation (Sw = 60%). Positive scaled Poisson's ratio become high when water saturation reaches 100% at Well D. Thus, scaled Poisson's ratio is a robust attribute for hydrocarbon delineation and shows higher sensitivity to water saturation compared with polar magnitude and product attributes. In addition, the "AMOCO" product, defined as [Far Angle *(Far Angle – Near Angle)], AVO attribute slice is shown in Figure 5.17. A high value of this attribute is an indicator of hydrocarbon pore-fluid as observed at Well A. However, Well C may have low value because the pay zone is classified as class 4 sand which has small amplitude at far angle.

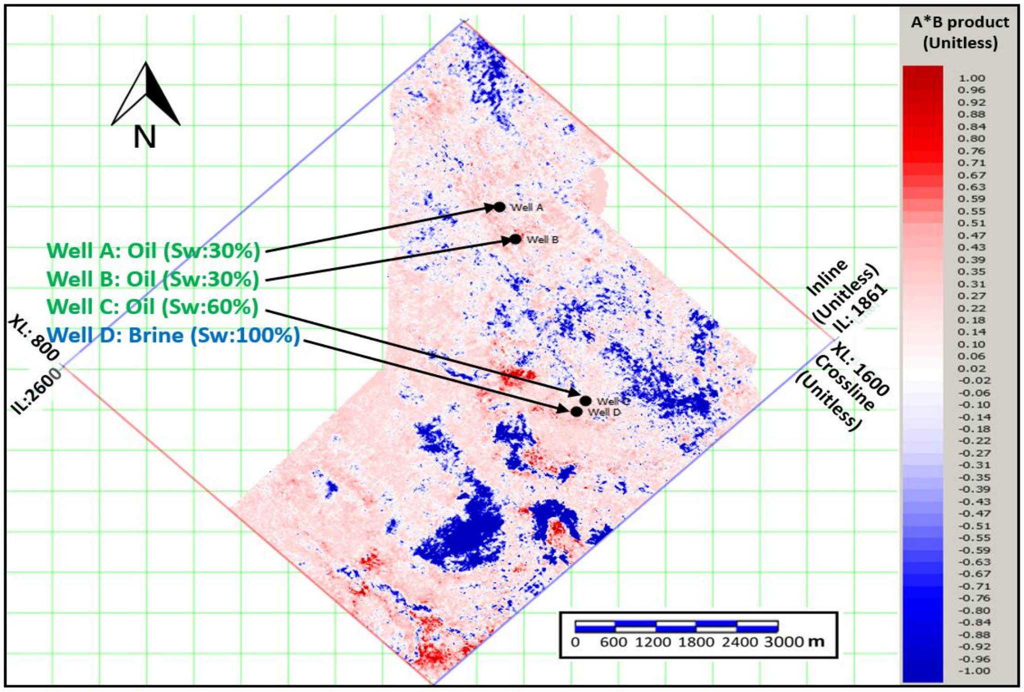

Figure 5.14: Horizon slice shows A*B product AVO attribute.

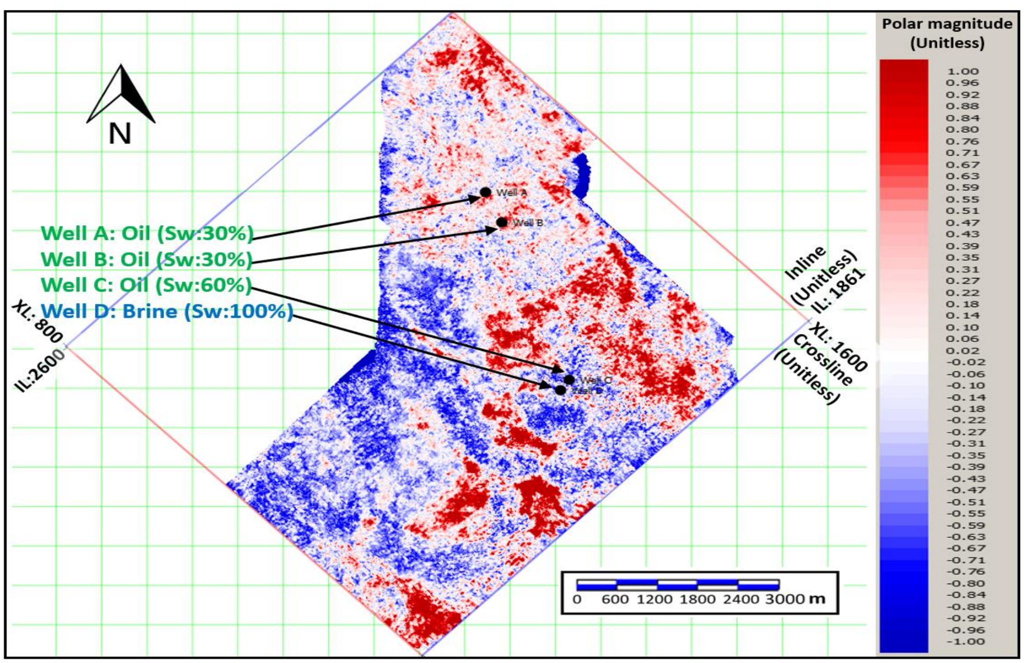

Figure 5.15: Horizon slice shows polar magnitude AVO attribute.

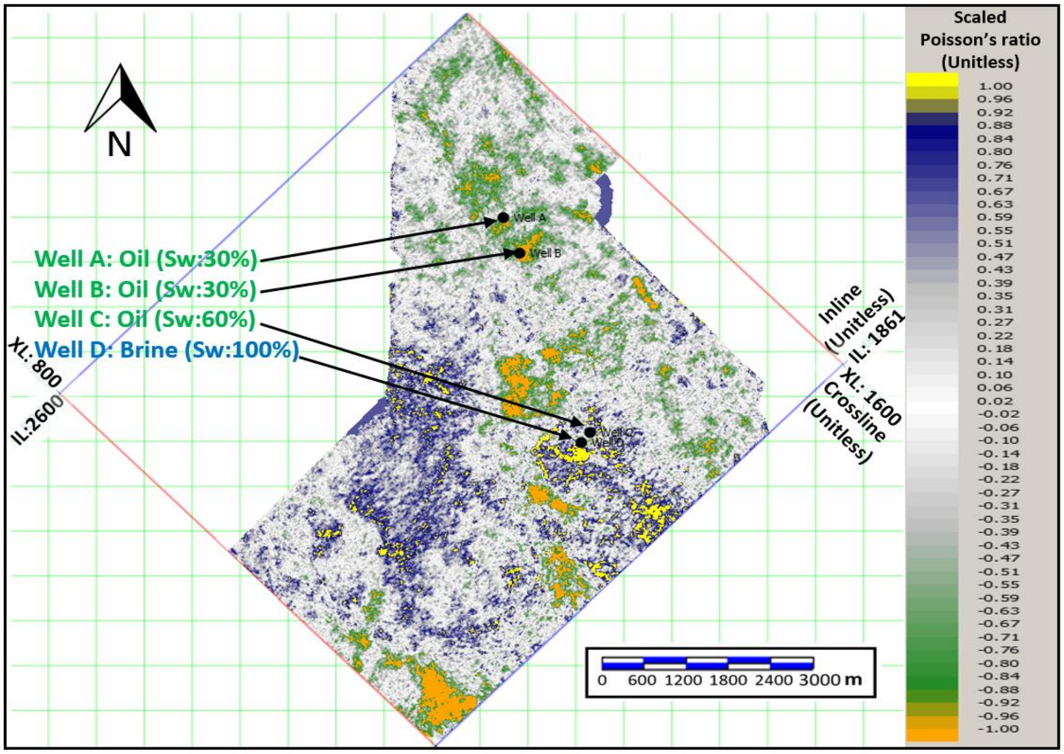

Figure 5.16: Horizon slice shows scaled Poisson's ratio AVO attribute.

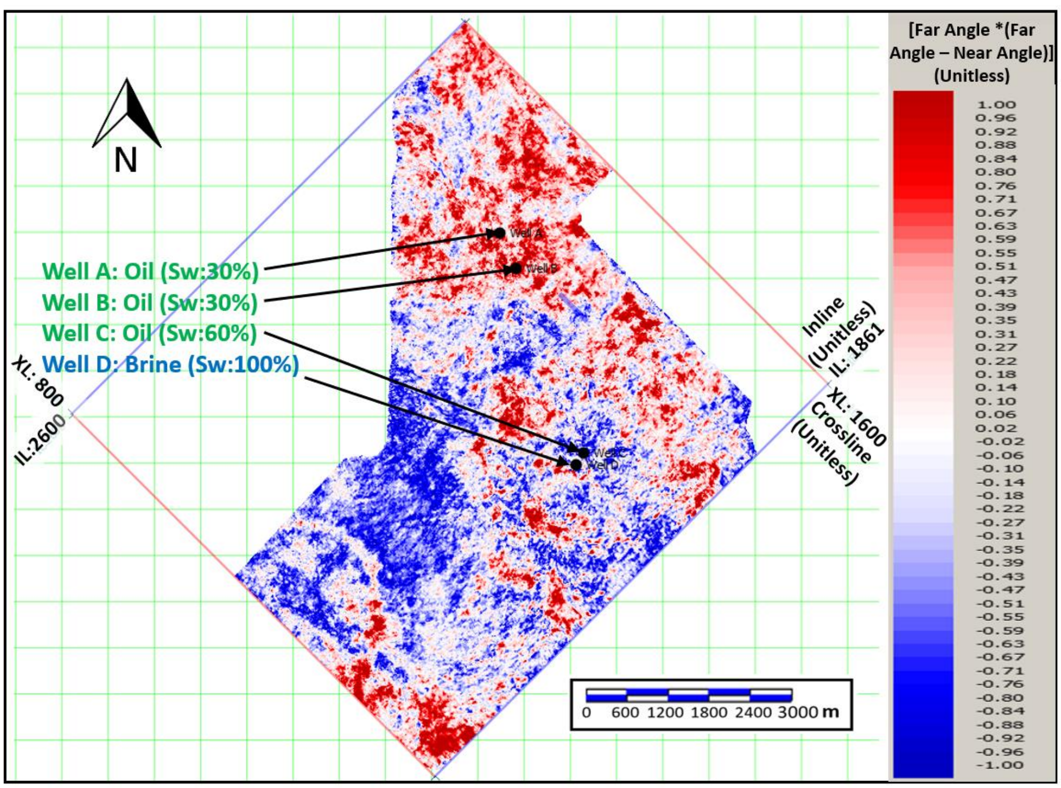

Figure 5.17: Horizon slice shows [Far Angle *(Far Angle – Near Angle)] AVO attribute.

Chapter 6

Seismic Inversion

6.1. Low-frequency model

Before conducting inversion, seismic forward modeling was performed by creating a low-frequency model. Seismic reflection data has a lack of frequency from 0 to 5 Hz as shown in Figure 6.1. That's why a low-frequency model is needed to compensate for frequency content deficiency in seismic data as illustrated in Figure 6.2. Input well logs were first filtered from high frequency. Then, filtered well logs and interpreted horizons were used to construct the low-frequency model. For conducting an accurate inversion, I used Well A, which has measured logs, to create a starting low-frequency model to ascertain that seismic inversion is not influenced by logs from other wells. Once reliability of seismic inversion was investigated, I used other wells to create the low-frequency model. Different inversions were conducted with different starting low-frequency models for comparison. In the case of using more than one well during inversion, inverse distance power was used to interpolate between those wells used.

6.2. Seismic inversion

Seismic inversion converts reflectivity data into either impedances or elastic properties (Russell, 1988). Well-log curves will be integrated into the inversion to account for the absence of low-frequency components in the seismic data. Inversion includes both acoustic-impedance inversion and elastic inversion using simultaneous inversion for either two (no density component) or three elastic components. Figure 6.3 illustrates inversion as a reverse process to forward convolution from geology to seismic.

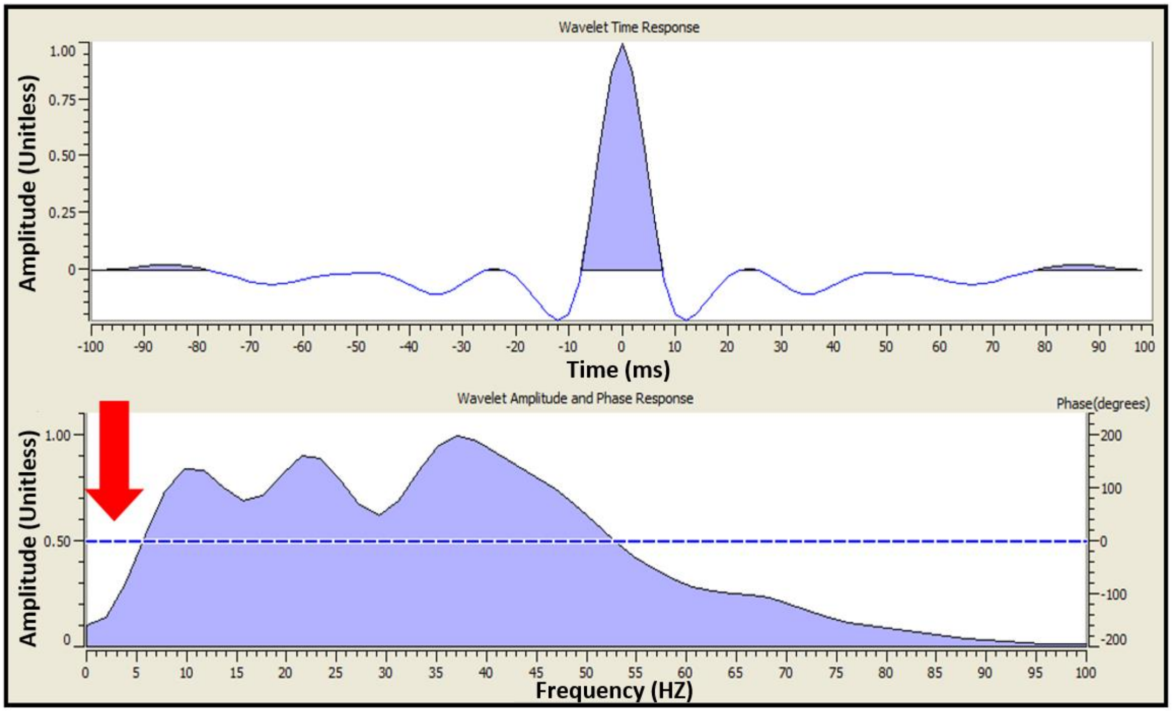

Figure 6.1: A statistical wavelet extracted from seismic data. Red arrow indicates low frequencies deficiency in amplitude spectrum.

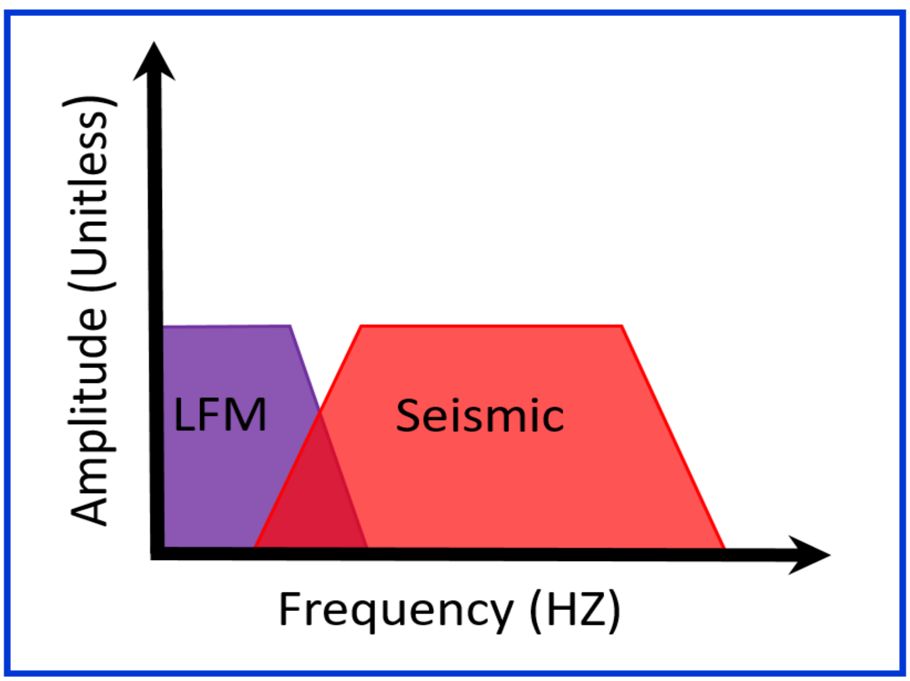

Figure 6.2: The low-frequency model (LFM) compensates for missing low-frequency content of seismic data (modified from Johnson, 2017).

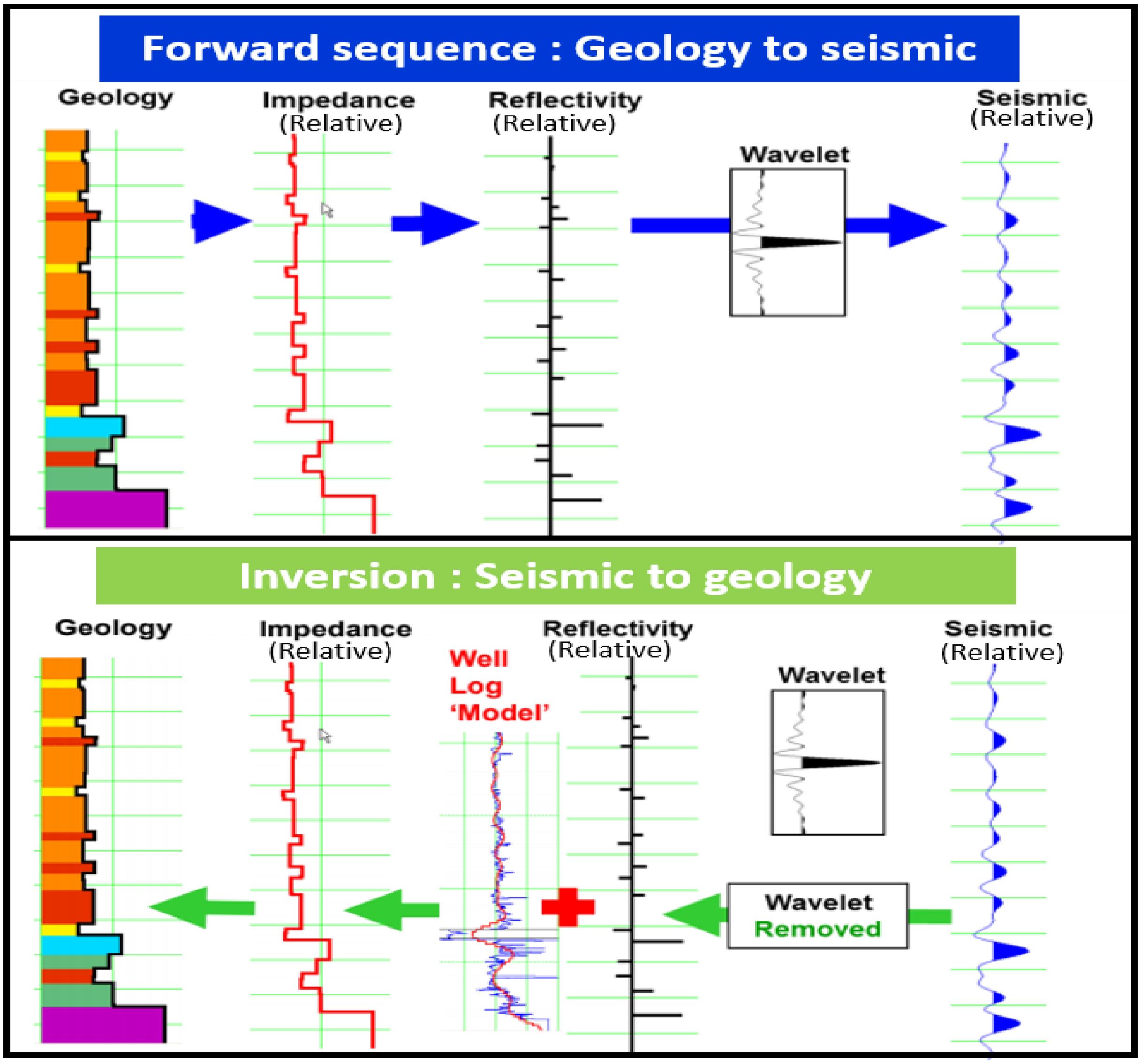

Figure 6.3: Schematic diagram of forward modeling and inversion (modified from CGG, 2017).

6.2.1. Post-stack seismic inversion

Post-stack seismic inversion is the conversion of seismic-reflection data into impedances by removing the wavelet through deconvolution and integrating seismic data and well logs to build a complete model of subsurface elastic properties (Russell, 1988). In this study, model-based seismic inversion was conducted using the far-angle stack. The initial low-frequency model of acoustic impedance was first established to account for the deficiency of low-frequency components in seismic reflection data. Only Well A, that has measured logs, was used to build the low-frequency model. Before inversion is considered, an accurate estimate of the seismic wavelet phase is critical. A statistical wavelet extracted from the far-offset stack within a time window extended around Well A and along the Hutton Formation was used to run post-stack inversion. Before running inversion, a correlation was conducted between initial impedance of the low-frequency model and the inverted impedance. Then, the calculated errors were minimized. Correlation was done in the geological domain (between well impedance and inverted impedance) and in the geophysical domain (between synthetic seismic and real seismic data) as illustrated in Figure 6.4. For inversion parameters, maximum impedance change was governed by hard constraints ranging from 100% to 80%. Prewhitening was set to be 1 and the scalar factor was adjusted to be 0.7. Furthermore, 20 iterations were allowed.

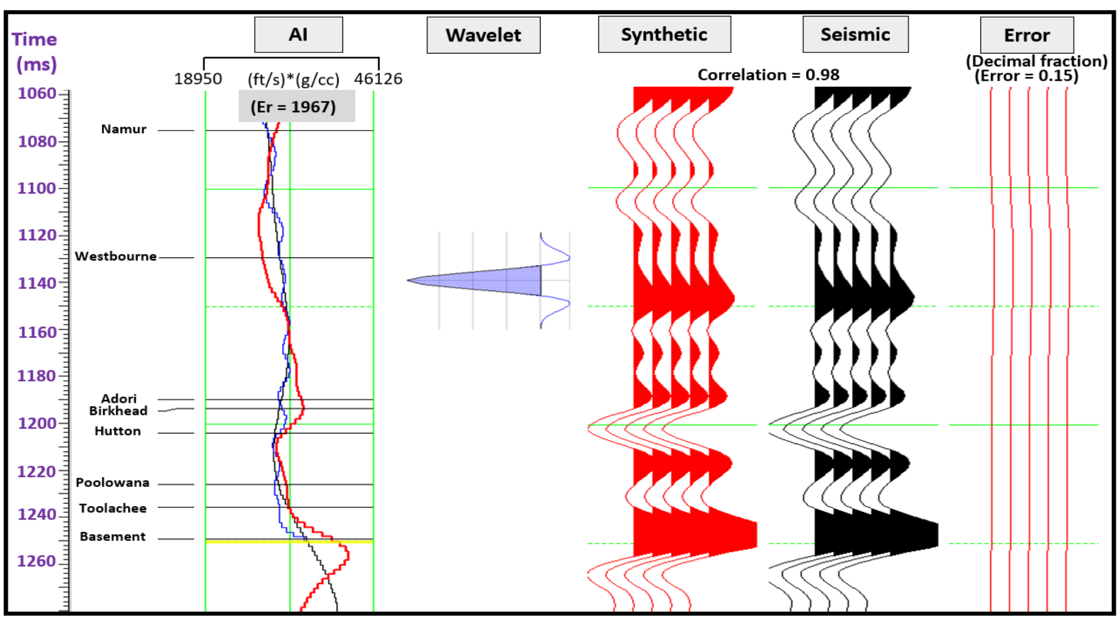

Figure 6.4: Post-stack inversion analysis for far-angle stack at Well A.

An acoustic impedance (AI) horizon slice with a 10 ms time window taken below the Hutton Formation top is shown in Figure 6.5. Low acoustic impedance is distributed along all wells. This result indicates that post-stack inversion of the far-angle stack could predict sand facies distribution but not discriminate pore-fluids since Well D, that has brine pore fluid, shows low acoustic impedance. Figure 6.6 shows AI inversion along an arbitrary line passing through the four wells.

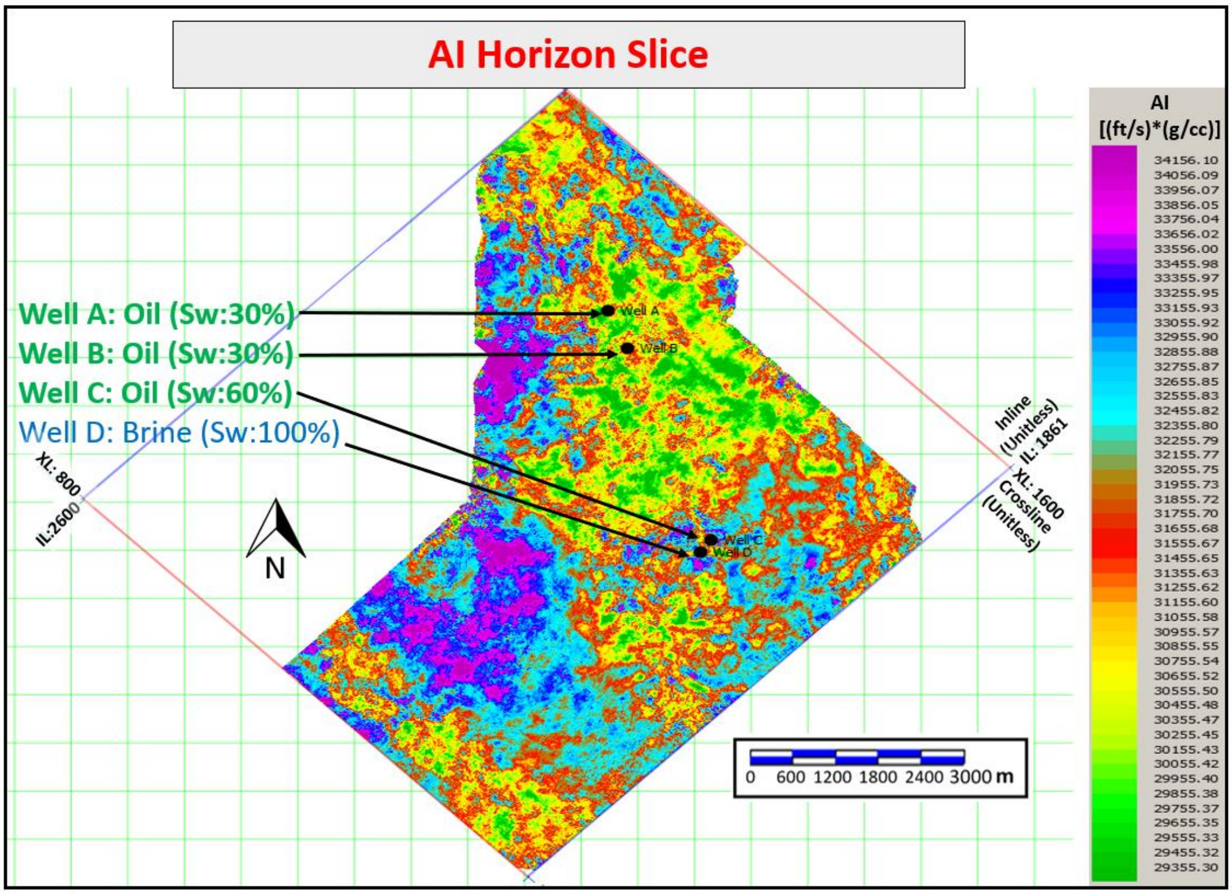

Figure 6.5: Horizon slice shows AI inversion result.

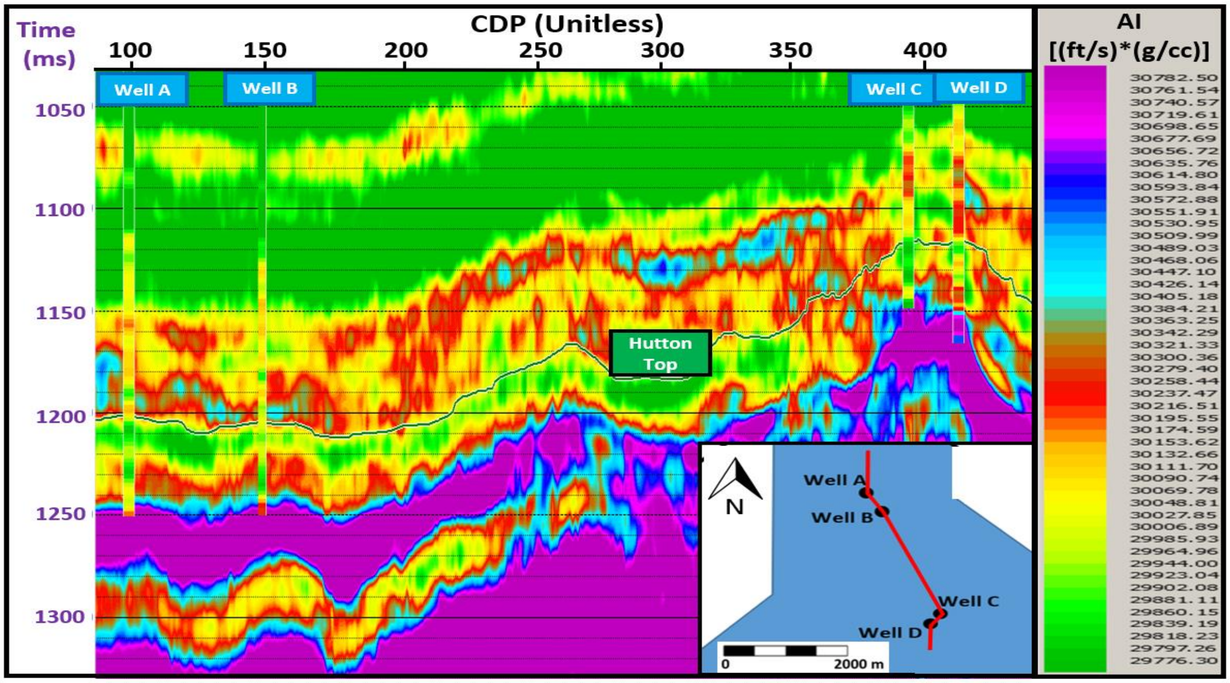

Figure 6.6: Arbitrary line passing through wells shows AI inversion result using post-stack inversion of far-angle stack.

6.2.2. Pre-stack simultaneous inversion

Simmons and Backus (1996) applied inversion using the Aki-Richards approximation that gives reflectivity as a function of angle. Buland and Omre (2003) directly estimated velocity and density instead of determining reflectivity by adding the following reflectivity equation to the Aki-Richards linear approximation:

$$R_i \approx \frac{1}{2} \Delta \ln I_i = \frac{1}{2} (\ln I_{i+1} - \ln I_i), \qquad (6\text{-}1)$$

where I_i is the acoustic impedance of layer i and the reflection coefficient R refers to the interface between layers i and i + 1.

Hampson et al., (2005) reformulated the Fatti et al., (1994) equation and conducted inversion for P-impedance, S-impedance, and density as illustrated in the following equation:

$$R_{pp}(\theta) = c_1 R_{Po} + c_2 R_{So} + c_3 R_D, \qquad (6\text{-}2)$$

where R_{P0} is the P-reflectivity, R_{S0} is the S-reflectivity, R_D is the density reflectivity, and

$$C_1 = 1 + tan^2(\theta), \tag{6-3}$$

$$C_2 = -8 \left(\frac{Vs}{Vp}\right)^2 tan^2(\theta), \text{ and} \tag{6-4}$$

$$C_2 = -\frac{1}{2} tan^2(\theta)+2 \left(\frac{Vs}{Vp}\right)^2 sin^2(\theta). \tag{6-5}$$

Acoustic impedance (Z_p), shear impedance (Z_s) and density (D) volumes are extracted simultaneously in pre-stack simultaneous inversion. From acoustic impedance and shear impedance inverted volumes, Vp/Vs, $\lambda\rho$ and $\mu\rho$ volumes are created using following equations:

$$Vp/Vs = Z_p/Z_s, \tag{6-6}$$

$$\lambda\rho = Z_P^2 - 2Z_S^2, \text{ and} \tag{6-7}$$

$$\mu\rho = Z_S^2. \tag{6-8}$$

As illustrated in Figure 6.7, background trends were established from the relation between Z_p and Z_s and between Z_p and density at wells using the following equations:

$$ln(D)= m\ ln(Z_p) + mc, \text{ and} \tag{6-9}$$

$$ln(Z_s)= k\ ln(Z_p) + kc. \tag{6-10}$$

where D is density, k, kc, m, and mc are coefficients used to balance the inversion (Hampson and Russell, 2005). The calculated coefficients k, kc, m, and mc are 0.875, 0.809, 0.429 and -3.559, respectively.

Deviations from a background linear fit are possible hydrocarbon anomalies. Because there is no discrimination between pore fluids using different rock-physical properties, hydrocarbons do not completely deviate from the background linear fit. Thus, identifying hydrocarbons from inversion results were addressed on a probability basis rather than clear discrimination from brine.

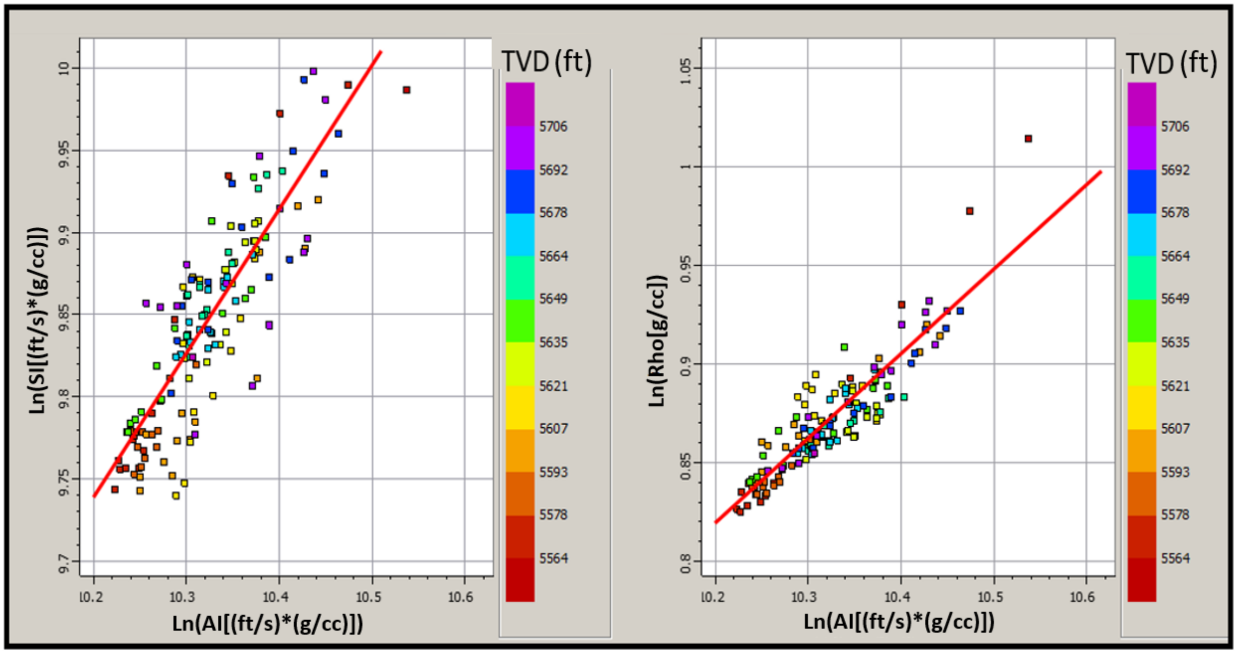

Figure 6.7: Logarithmic P-impedance, S-impedance, and density crossplots at the wells are generated to calculate regression coefficients *k, kc, m*, and *mc*.

The inversion process was run several times using different starting low-frequency models. Initial low-frequency models of acoustic impedance, shear impedance, density and compressional-to-shear-wave velocity ratio were first established using Well A that has measured compressional-velocity, shear-velocity and density logs. Well B, Well C and Well D were used as blind validation wells to assess reliability of the inversion results. Statistical and Ricker wavelets were used for different inversions to determine which wavelet achieves the best inversion result. A 60 Hz Ricker wavelet (shown in Figure 6.8) was used. Prewhitening was set to be 2% and the scalar factor was adjusted to be 0.32. Inversion was conducted for 25 iterations over a 0^{o} to 45^{o}

angle range. Pre-stack simultaneous analysis at Well A using the 60 Hz Ricker wavelet is shown in Figure 6.9.

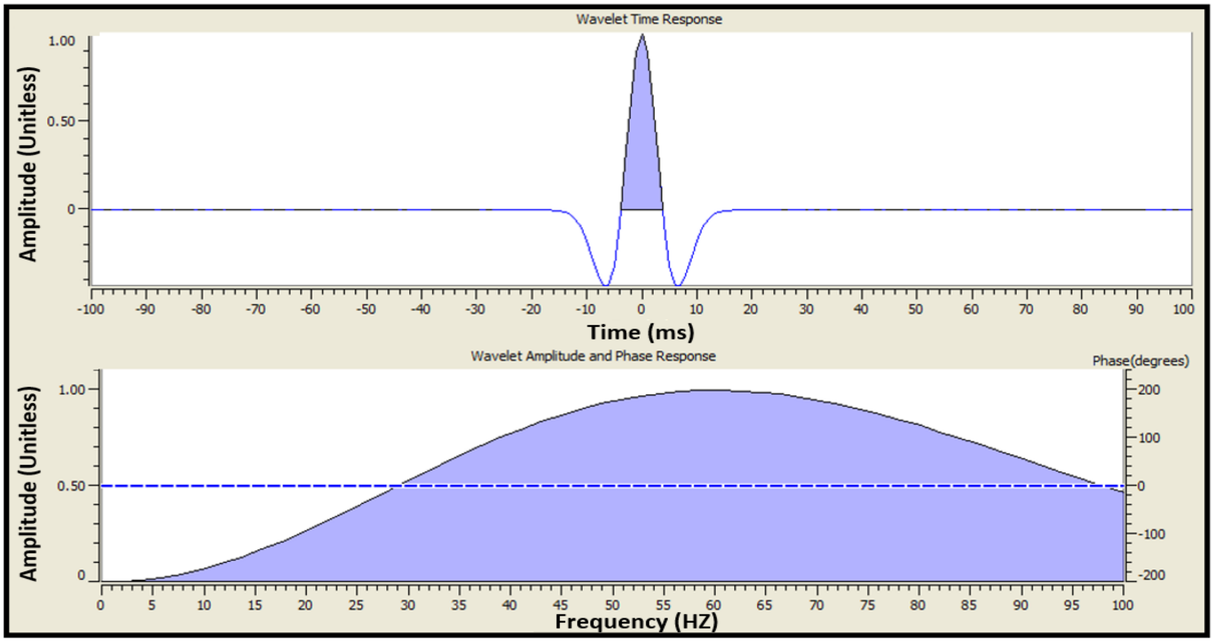

Figure 6.8: Ricker wavelet of 60 Hz.

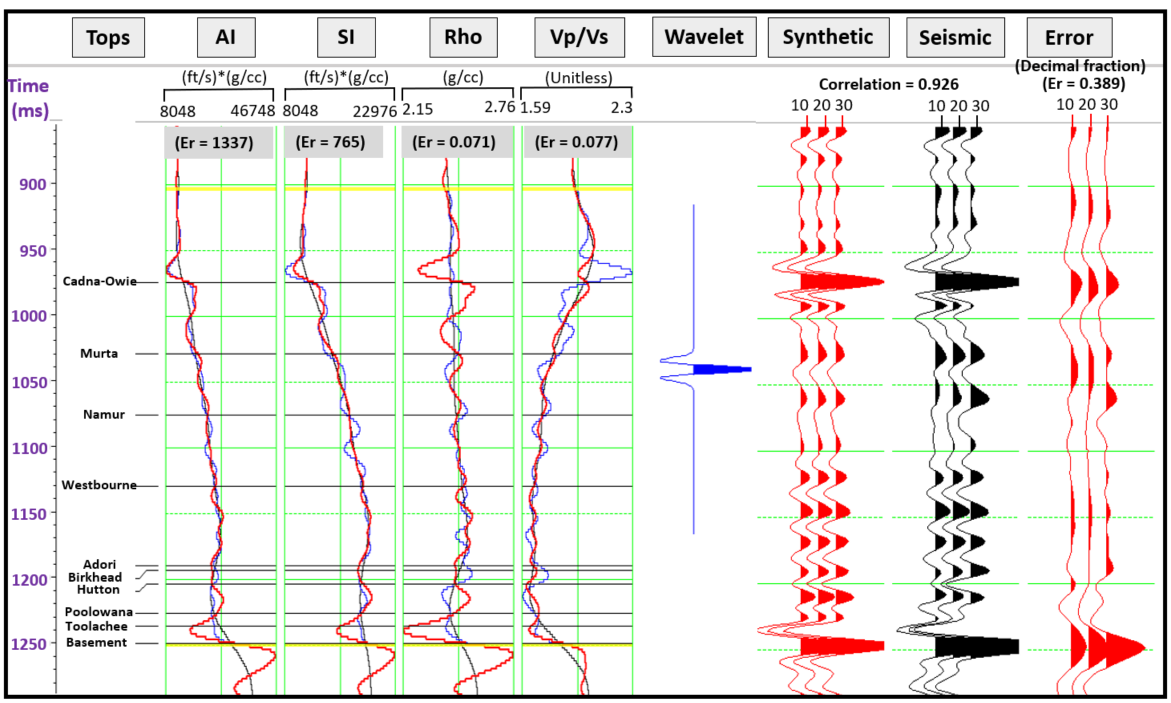

Figure 6.9: Pre-stack simultaneous analysis at Well A. The original logs are in blue, the low-frequency model logs are in black, and the inverted logs are in red.

An arbitrary line of inverted Vp/Vs crossing through the four wells is shown in Figure 6.10. The inversion process was repeated with the same parameters, but with different starting low-frequency models to address if there is an effect from measured or predicted logs to mislead the inversion. Well B, Well C and Well D were used separately to build the starting low frequency model. Vp/Vs horizon slices for inversions with different starting models are shown in Figures 6.11. A consistency between the inversion outputs increases confidence in the results. The Vp/Vs results show reservoir heterogeneity that may be attributed to facies and pore-fluid change. Low Vp/Vs values zones are distributed along Well A and Well B where there is oil reservoir with low water saturation. However, moderate and high Vp/Vs zones occur at Well C and Well D, respectively.

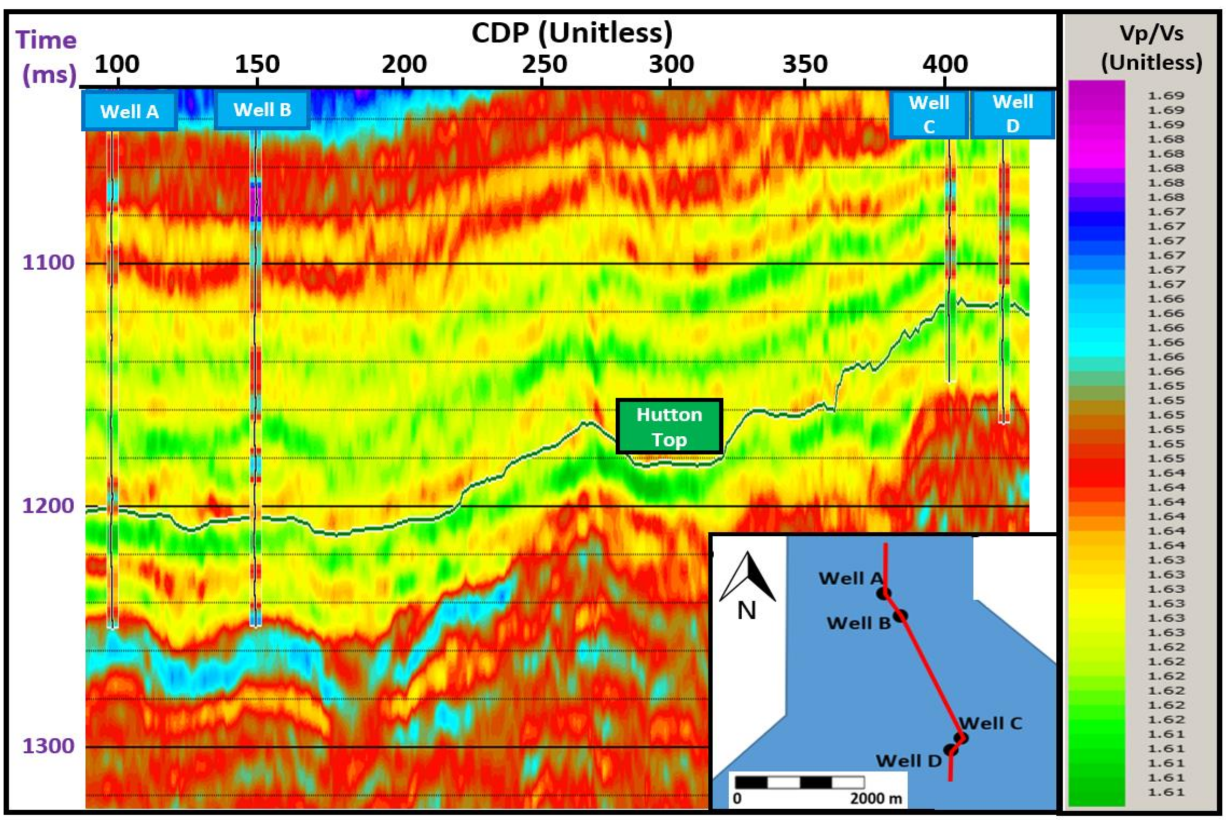

Figure 6.10: Arbitrary line passing through wells shows Vp/Vs inversion result.

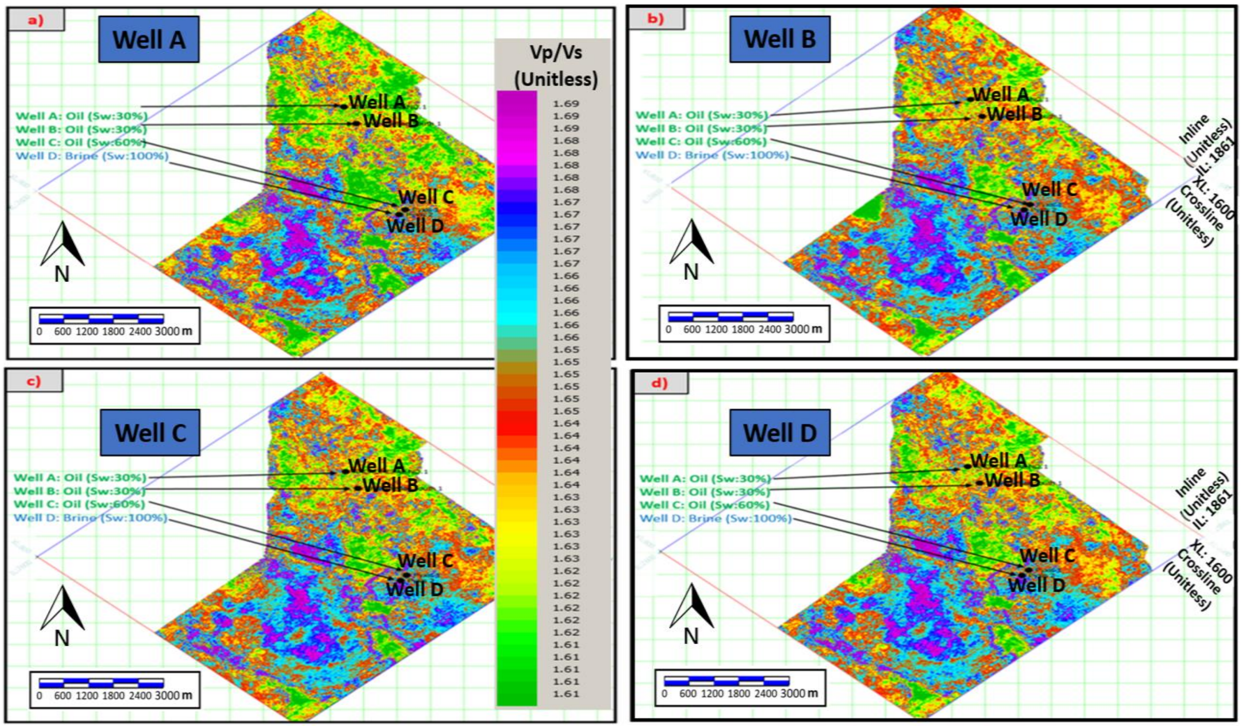

Figure 6.11: Comparing Vp/Vs horizon slices for inversions using different starting low-frequency models built by one well. a) Well A. b) Well B. c) Well C. d) Well D

To address wavelet effects on inversion results, a group wavelet was used for conducting inversion and results are compared with previous inversion results estimated using a Ricker wavelet. The group wavelet is composed of three statistical wavelets extracted from near-angle, mid-angle and far-angle stacks as shown in Figure 6.12. Pre-stack simultaneous inversion analysis using the group wavelet is illustrated in Figure 6.13. There is no significant difference between conducting inversion using Ricker or group wavelets. The Vp/Vs horizon slice below the Hutton Formation top (Figure 6.14) and arbitrary lines (Figures 6.15 and 6.16) show no significant difference in inverted Vp/Vs and AI at the four wells.

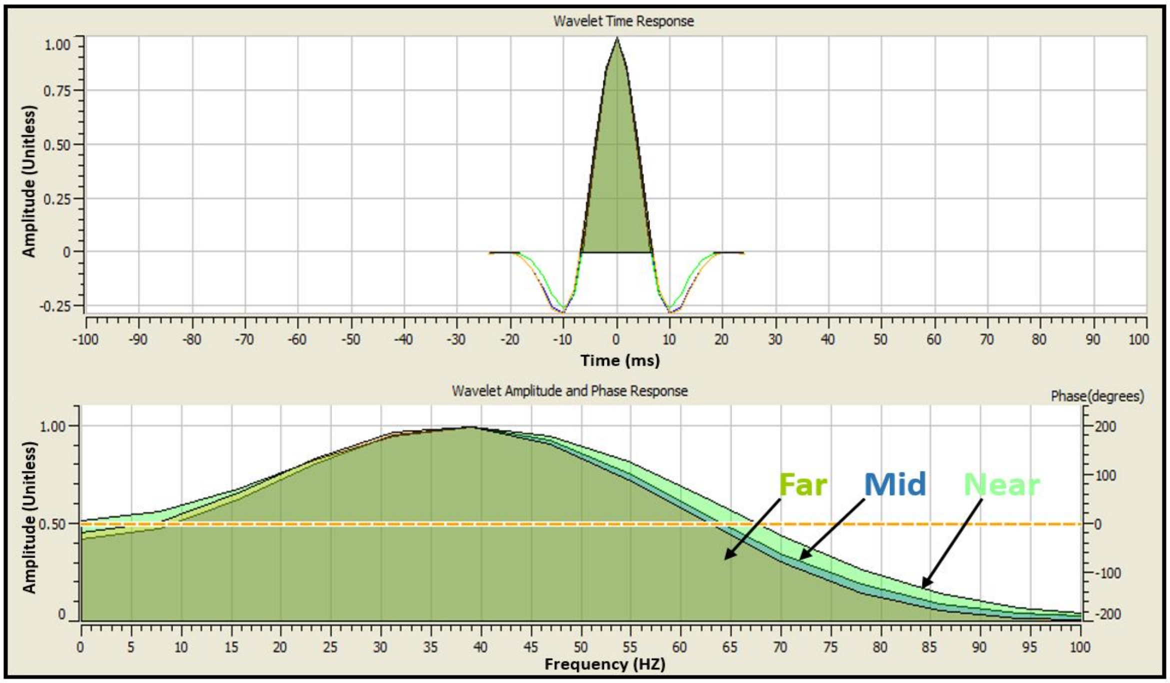

Figure 6.12: Group wavelet created from near-, mid- and far-statistical wavelets estimated around Well A.

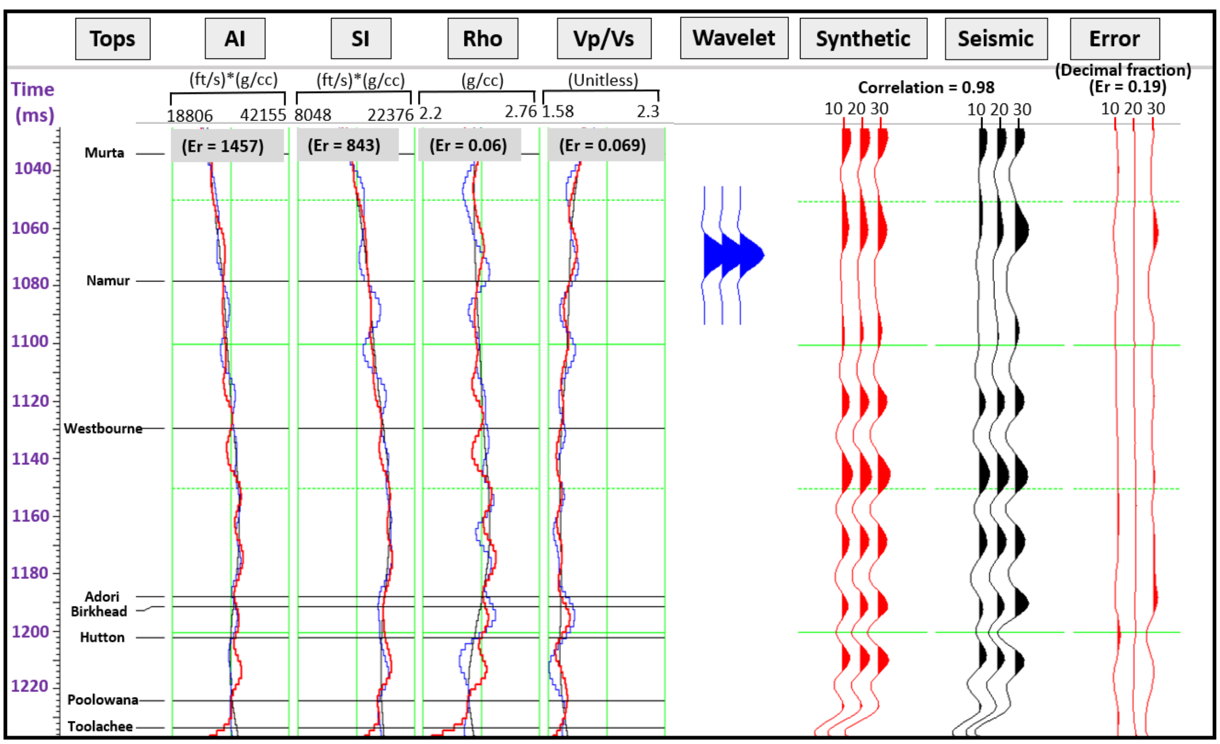

Figure 6.13: Pre-stack simultaneous analysis at Well A using the group wavelet. The original logs are in blue, the low-frequency model logs are in black, and the inverted logs are in red.

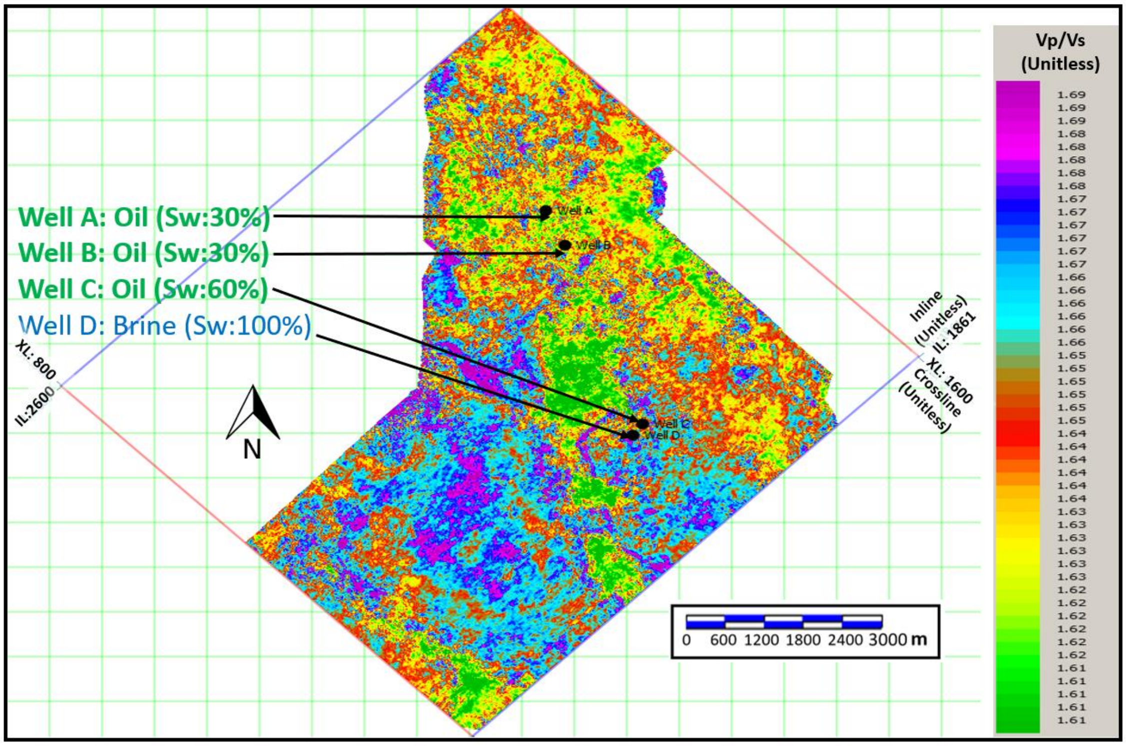

Figure 6.14: Vp/Vs inversion horizon slice using group wavelet.

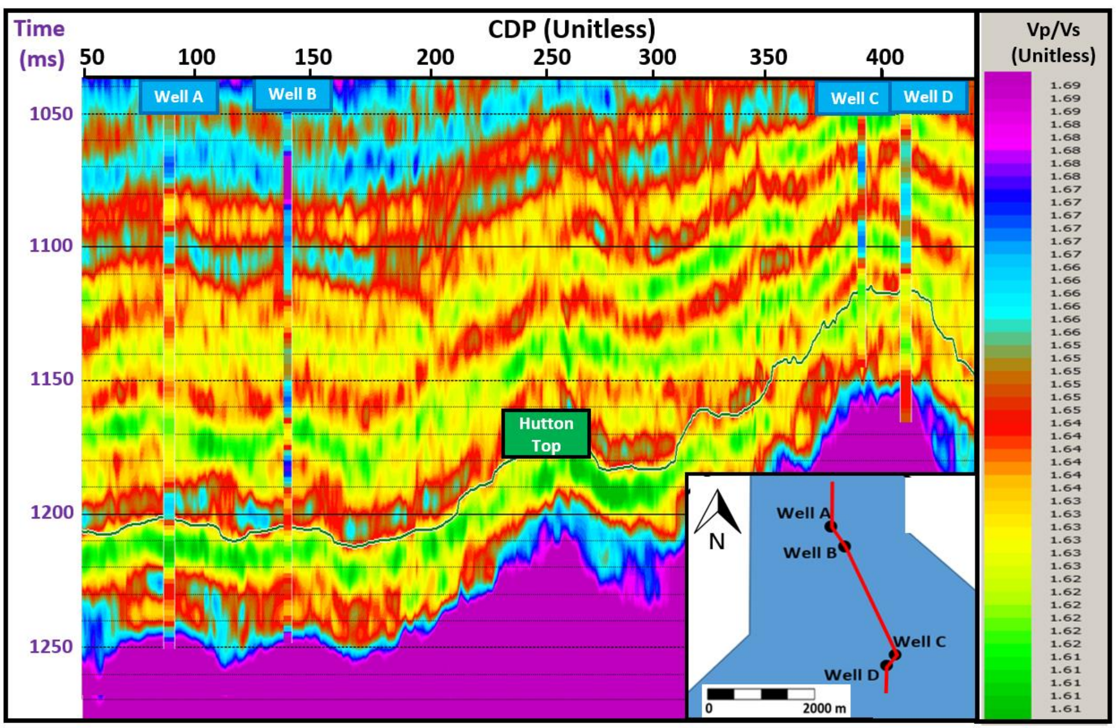

Figure 6.15: Arbitrary line passing through wells shows Vp/Vs inversion result using group wavelet.

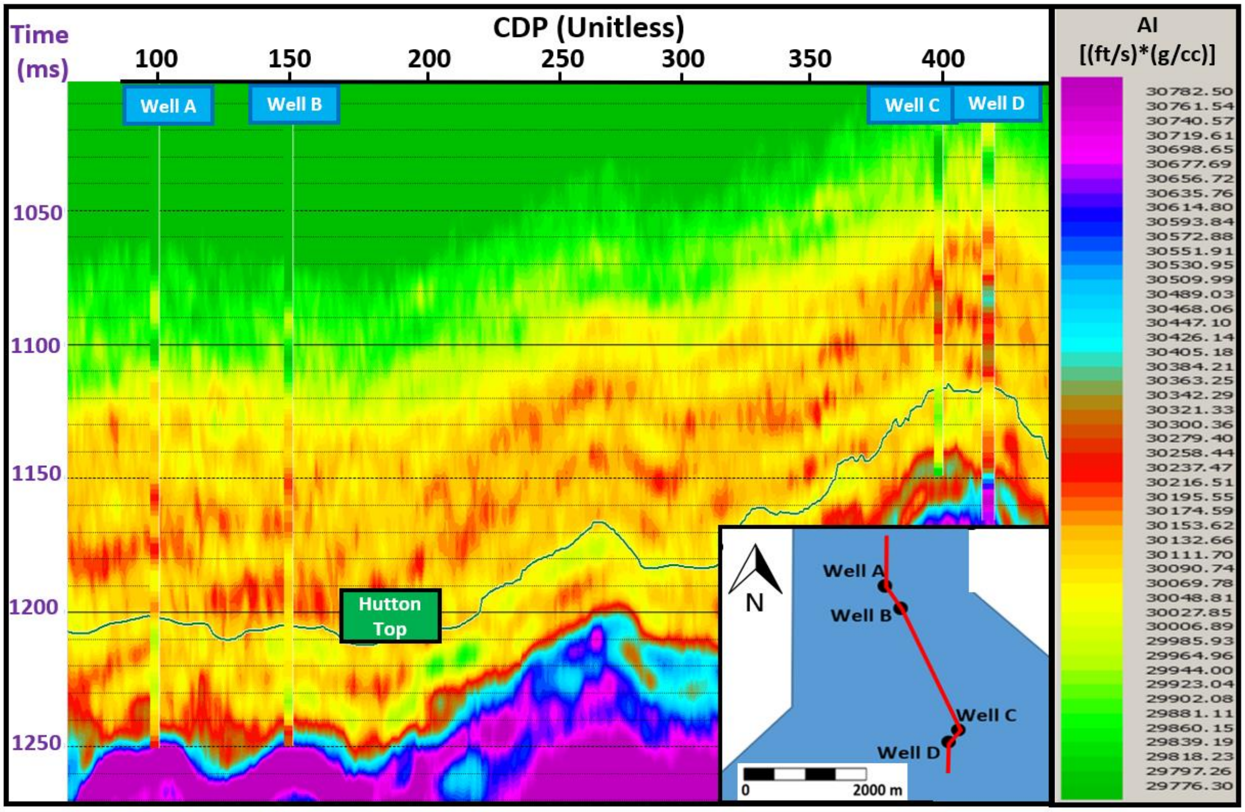

Figure 6.16: Arbitrary line passing through wells shows AI inversion result after conducting pre-stack simultaneous inversion.

6.3. Sparse-layer inversion

Based on the assumption that reflection coefficient pairs are odd, the Widess (1973) limit of resolution is one-quarter wavelength ($\lambda/4$) at which amplitude reaches its peak due to constructive interference. Partyka et al., (1999) observed a notch periodicity in the frequency spectrum of layer reflectivity.

Peak frequency and peak amplitude for even, odd, and composite reflection coefficients were estimated by (Puryear and Castagna, 2008) as shown in Figure 6.17 and their result shows that resolution depends on the contribution of both odd and even pairs since amplitude decreases for odd pairs and increases for even pairs below $\lambda/4$ which means that information can be extracted below the Widess tuning limit. Chopra et al., (2006) suggested improving seismic resolution by broadening the bandwidth of the original seismic data.

Based on Puryear and Castagna (2008), spectral inversion has been used to convert original seismic data to high-resolution broader-bandwidth seismic data since local attributes are extracted from original seismic data after being spectrally decomposed into volumes of amplitude and phase at different frequencies.

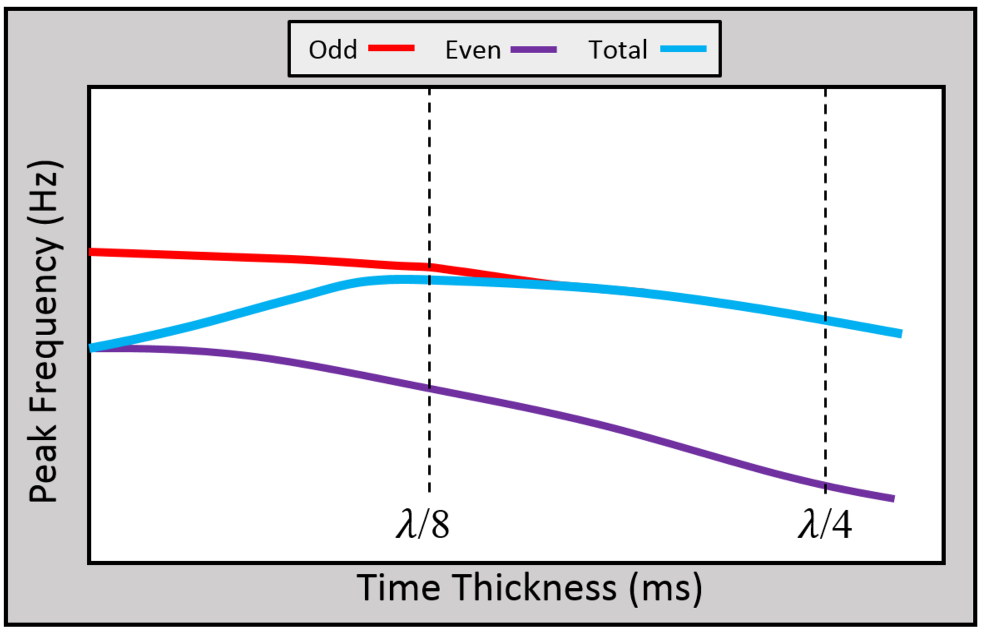

Figure 6.17: Peak frequency versus time thickness. Modified from (Puryear and Castagna, 2008; Izarra Dial, L.A 2011; and Okonkwo, 2014).

Although conventional seismic data inversion has shown good results verified by using Well B and Well D as blind validation wells, the area around the Well C validation well is still problematic since this well has oil and oil occurrence is only verified by drill stem test and still not detected by seismic data. Furthermore, conventional seismic data does not show geologic details around Well C and Well D.

After investigating the AVO synthetic at Well C created with a 40 Hz Ricker wavelet, a big trough along the Hutton Formation Top divides into two troughs at near offset as shown in Figure 6.18. These troughs correspond to the upper two member tops of the Hutton Formation. After increasing frequency to 60 Hz, two troughs are clearly separated as shown in Figure 6.19. Thus, each trough corresponds to one rock unit, and hence, seismically characterizes it. From this observation, high-frequency seismic data is badly needed to separate productive from non-productive layers. Therefore, spectral decomposition was applied to the far-offset stack to construct a high-frequency far-stack volume since spectral balancing using local attributes was conducted by Lumina Geophysical and SAExploration companies to improve seismic resolution. Then, post-stack inversion was conducted again with the high-frequency seismic volume.

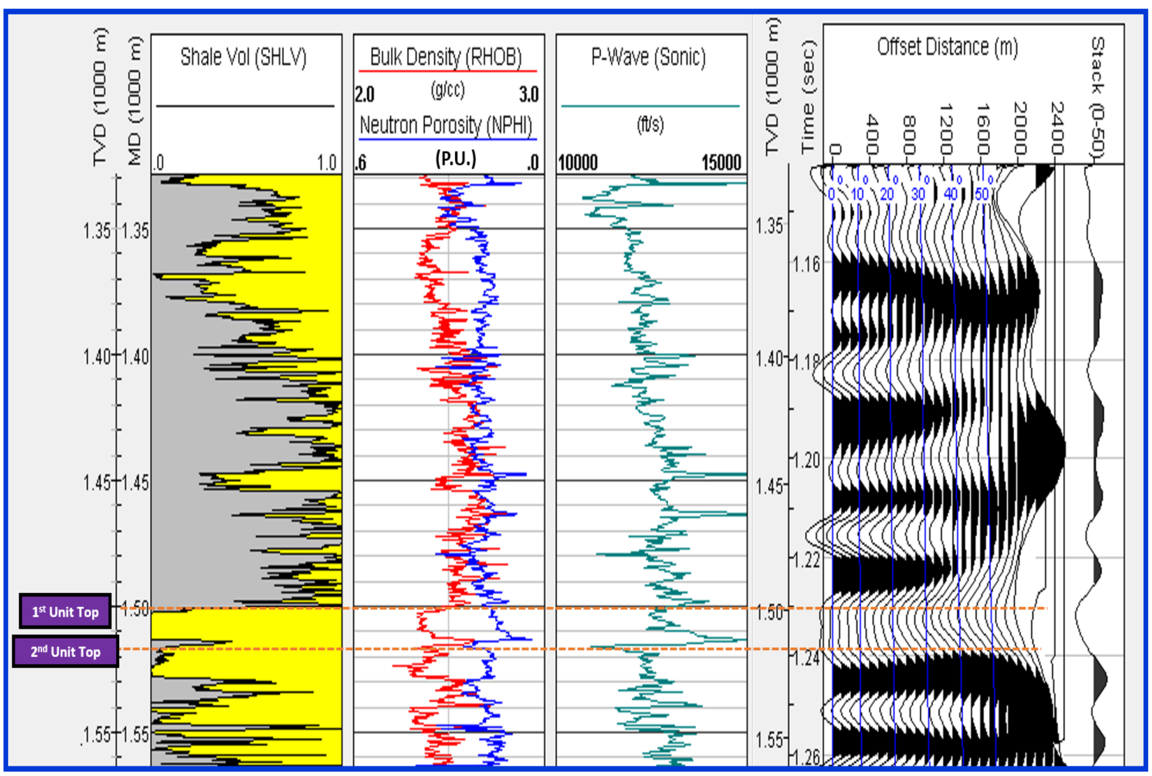

Figure 6.18: AVO synthetic at Well C constructed with 40 Hz Ricker wavelet.

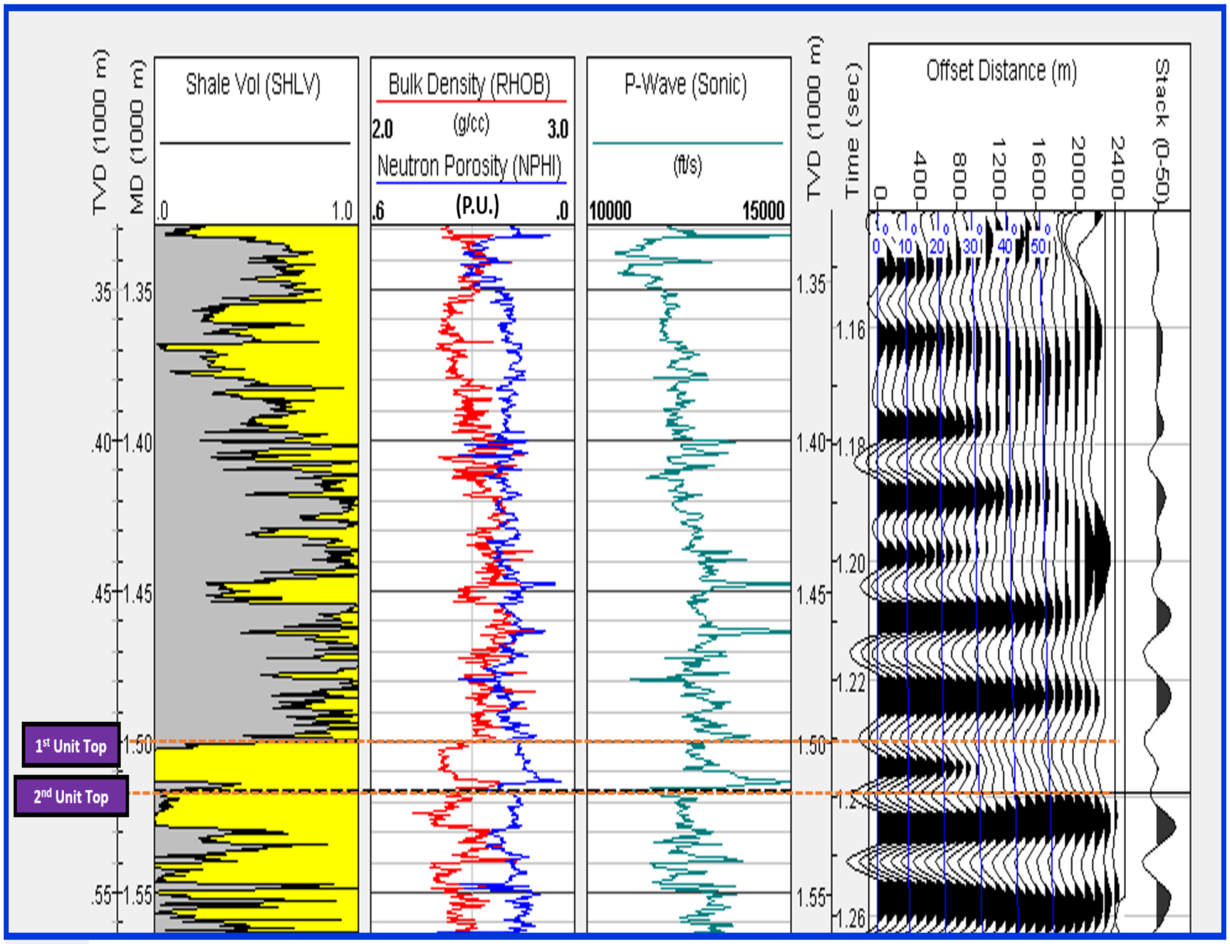

Figure 6.19: AVO synthetic at Well C constructed with 60 Hz Ricker wavelet.

Figure 6.20 shows the difference between the conventional-seismic far-angle stack and the high-frequency far-angle stack. High-frequency seismic data can monitor fine details that cannot be seen by conventional seismic data. The channel feature that is hardly observable with conventional seismic data, is clearly obvious on the high-frequency seismic data.

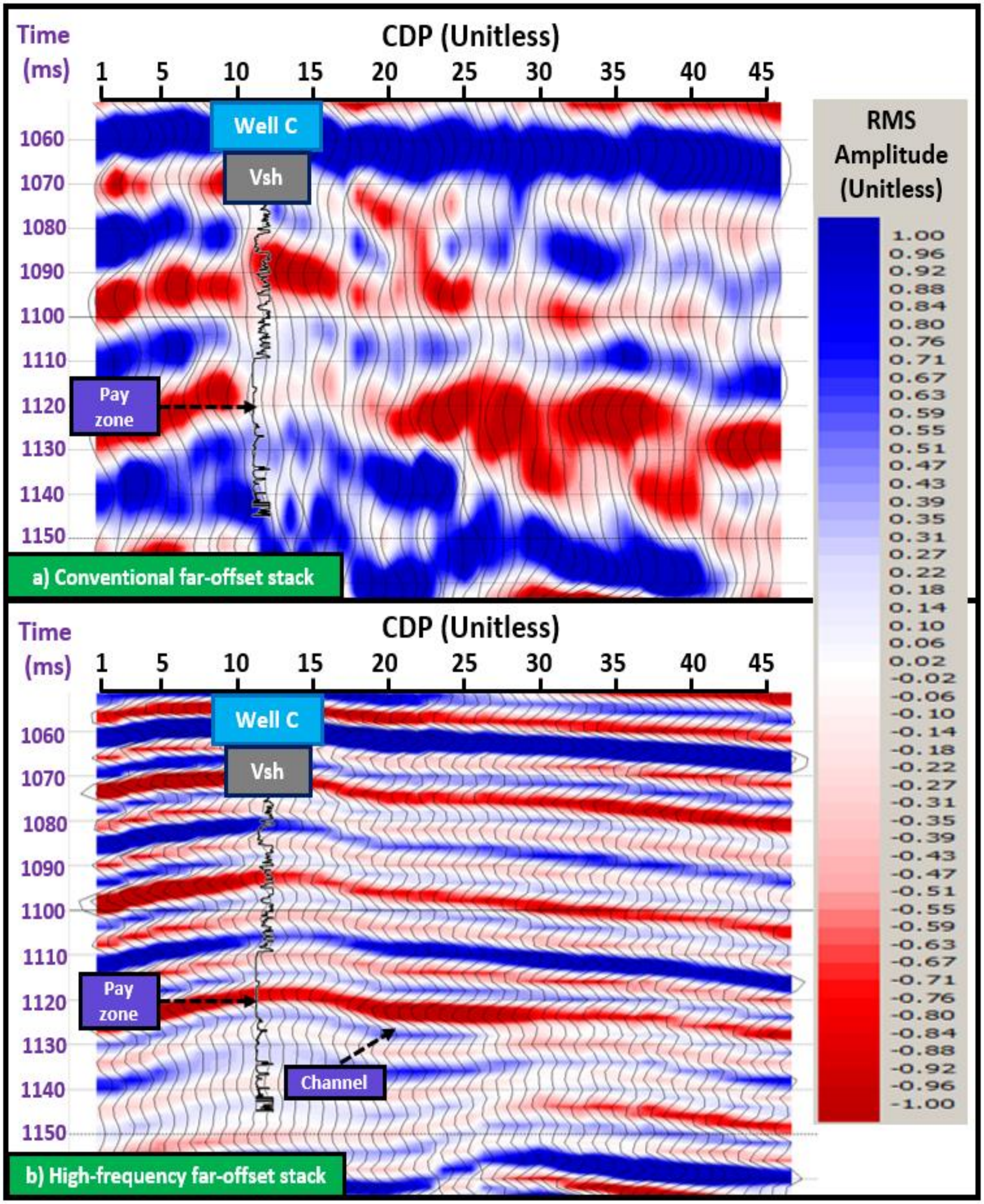

Figure 6.20: Comparison between a) Conventional and b) High-frequency far-offset stacks.

The high-frequency far-angle stack was inverted in the same way with the same parameters as the conventional seismic data. The main difference is the wavelet used for running inversion. The high-frequency seismic data inversion was conducted using a 60 Hz Ricker wavelet. Post-stack inversion analysis for the high-frequency seismic data is shown in Figure 6.21.

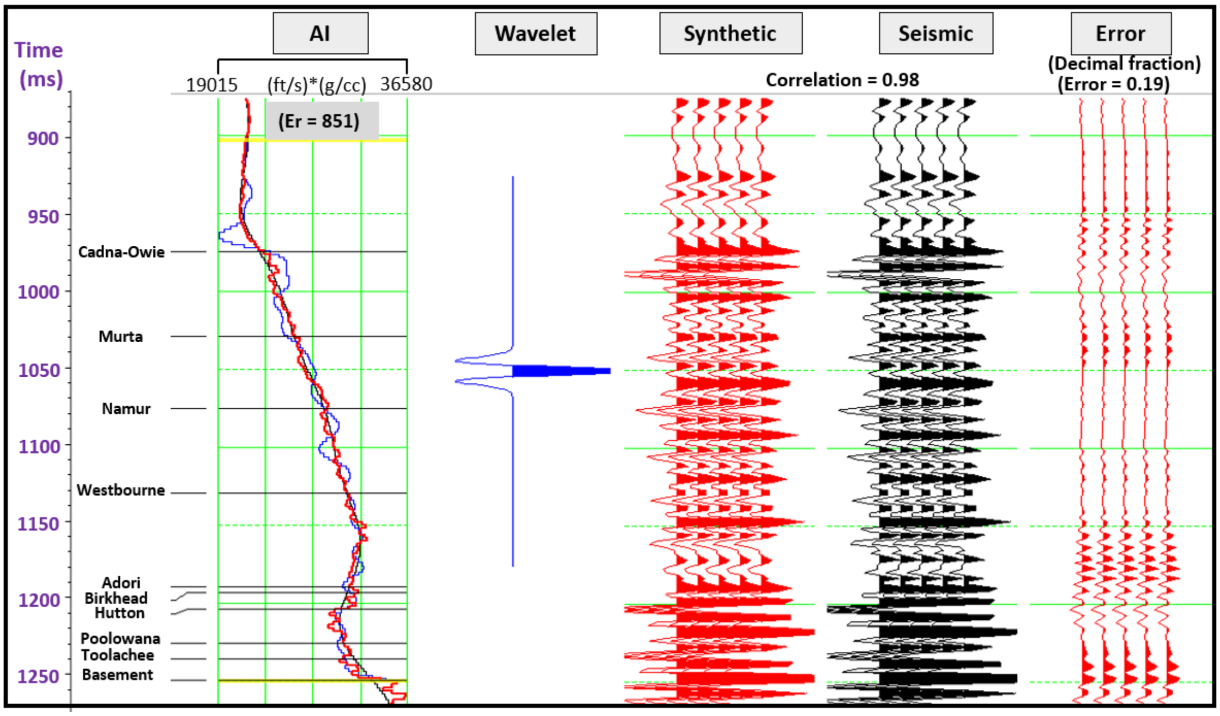

Figure 6.21: Post-stack inversion analysis for high-frequency far-angle stack at Well A.

An arbitrary line was created connecting the four wells as shown in Figure 6.22. The acoustic impedance inverted from the high-frequency seismic data shows more geological details than the conventional acoustic impedance inversion. The acoustic impedance horizon slice for a 10 ms time window constructed below the Hutton Formation top is shown in Figure 6.23. Well A and Well B have low acoustic impedance at the reservoir. Acoustic impedance changes to intermediate at Well C and high at Well D. The acoustic impedance change is attributed to water saturation change.

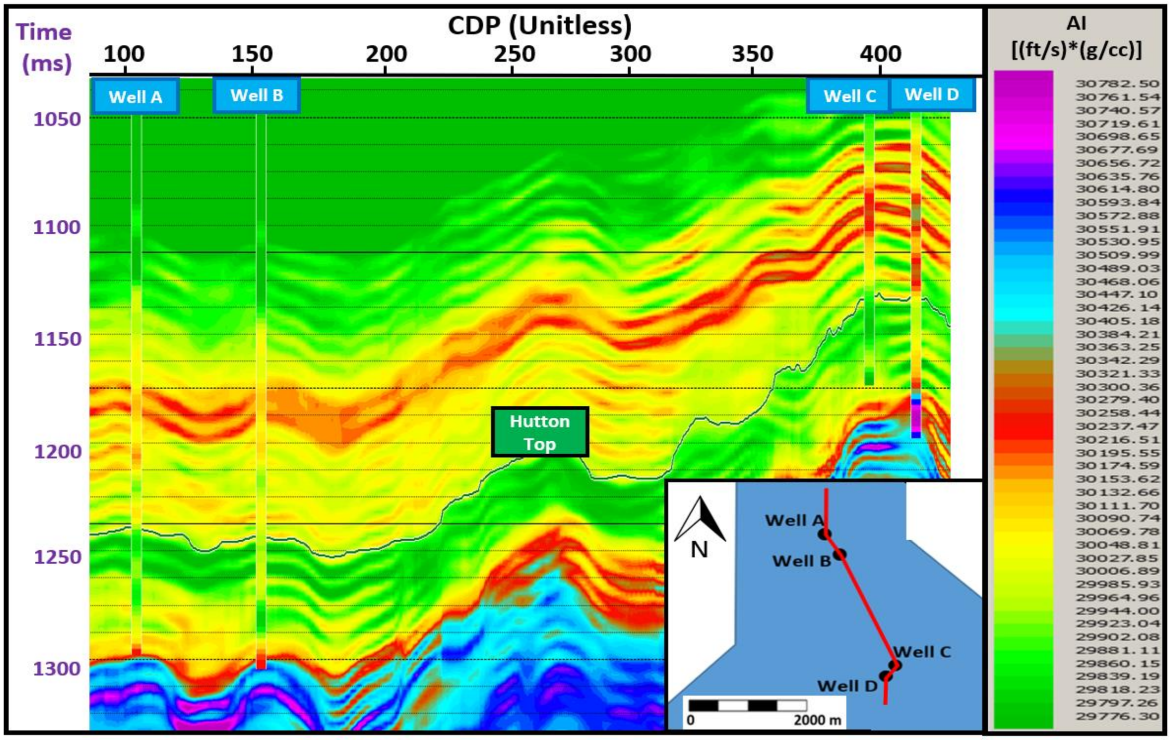

Figure 6.22: Arbitrary line passing through wells shows AI inversion result for the high-frequency seismic data.

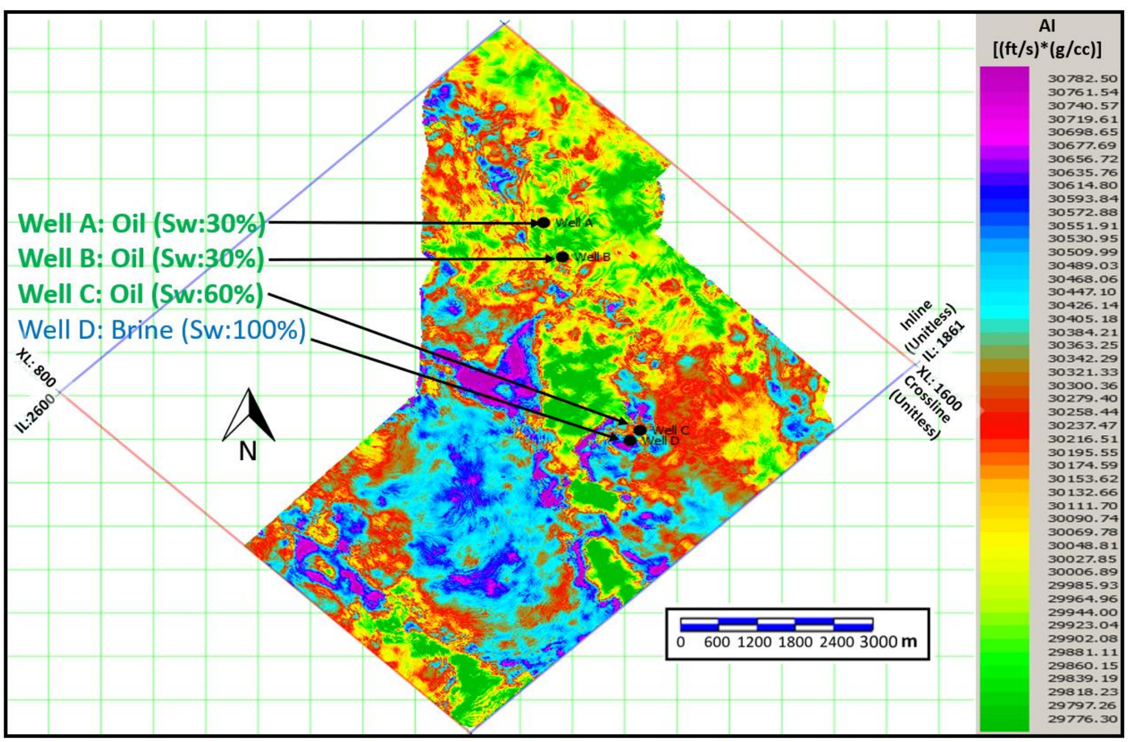

Figure 6.23: AI horizon slice below the Hutton Formation top for the high-frequency seismic data.

After looking around 10 ms acoustic impedance horizon slice constructed from post-stack inversion of the high-frequency far-angle stack, a low acoustic impedance zone was observed near to Well C as shown in Figure 6.24. There is a gradient decrease in acoustic impedance from Well C to this zone. To accurately investigate this zone, an arbitrary line was created from Well C to the low acoustic impedance zone around it as shown in Figure 6.25. An astonishing result is observed on the arbitrary line: a channel feature in the low acoustic impedance zone and located just below the Hutton Formation top. The astonishing point is that the low acoustic impedance of the proposed channel is connected to Well C at the pay zone evident in this blind validation well. Since the pay zone at Well C is only 2 m thick, the high-frequency seismic data is needed to see it. In addition, some faults can now be seen around Well C from shifts of the acoustic impedances. To address oil occurrence at Well C and oil absence at Well D, an arbitrary line was constructed from Well C to the proposed channel to Well D as shown in Figure 6.26. It is noticed that acoustic impedance of the proposed channel is connected to Well C and not connected to Well D at target zone.

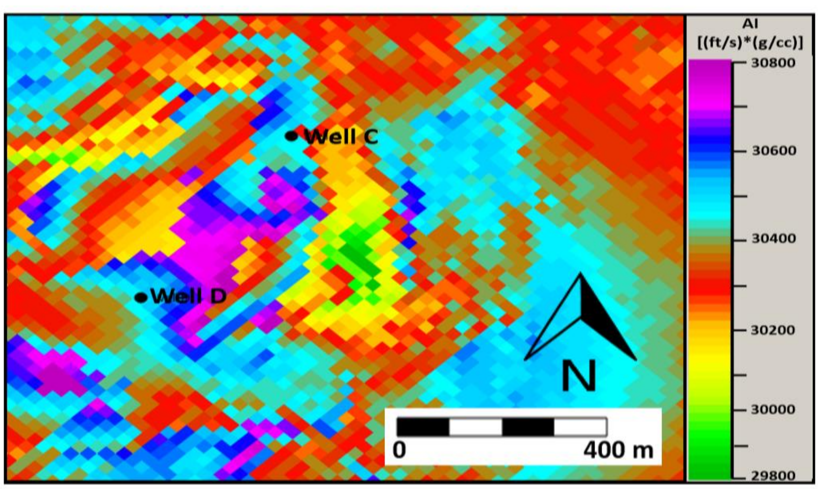

Figure 6.24: AI horizon slice from high-frequency seismic data below the Hutton Formation top around the Well C and Well D area.

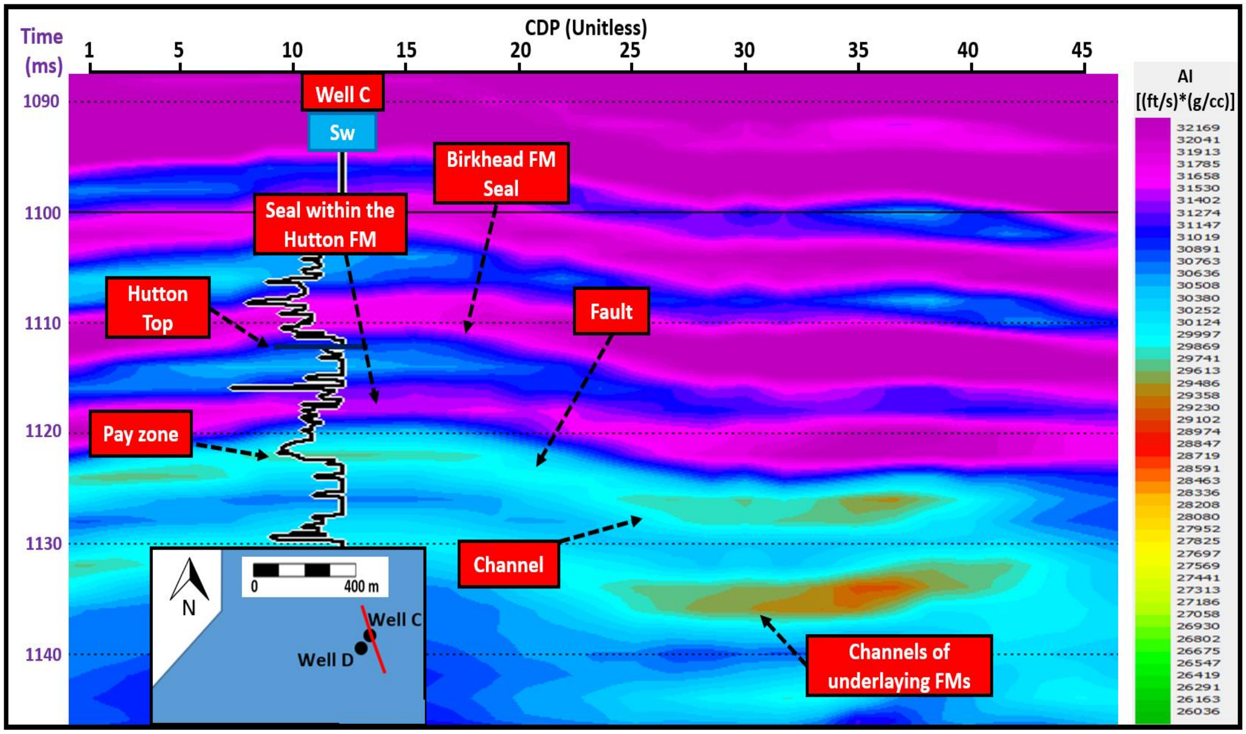

Figure 6.25: Arbitrary line through Well C and the proposed channel.

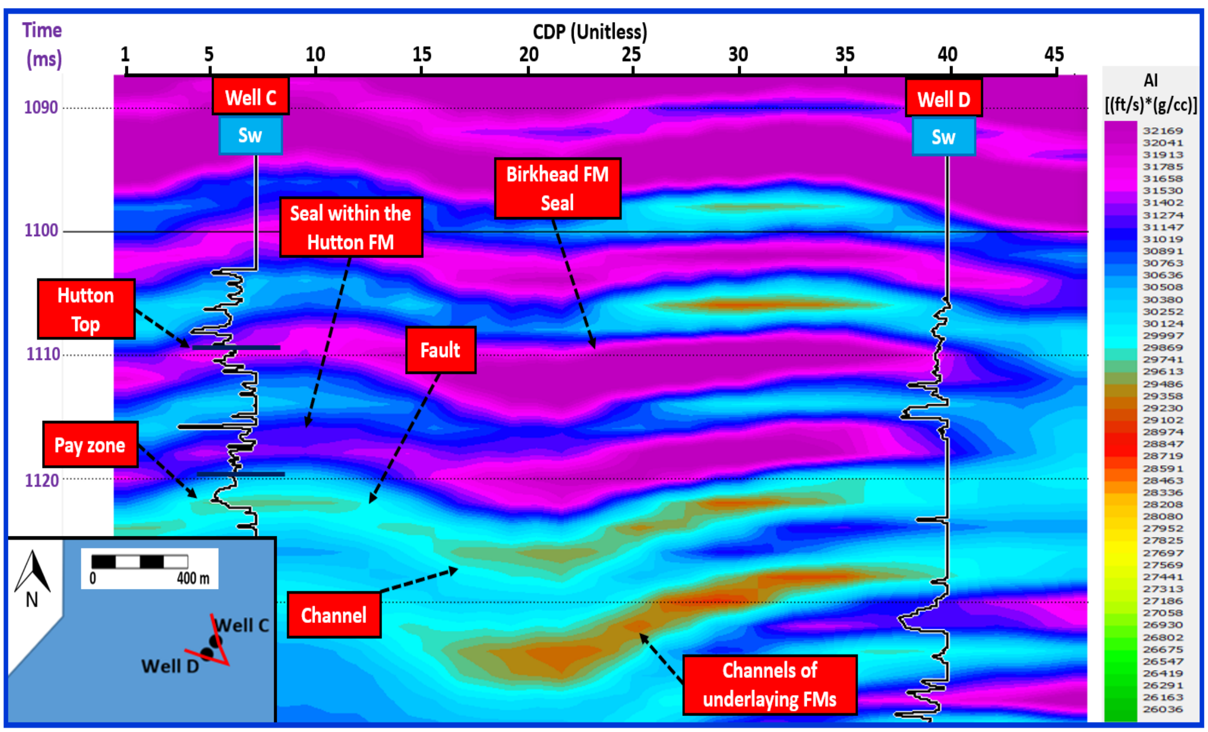

Figure 6.26: Arbitrary line constructed from acoustic-impedance inversion from high-frequency seismic data passing through Well C, proposed channel, and Well D.

A high acoustic impedance above the channel feature indicates seal occurrence within the Hutton Formation that probably prevents oil migration upward. This seal extends along the channel, Well C and Well D periphery. High acoustic impedance does not extend to Well D. To have a greater focus on addressing seal occurrence above and around the wells, a 10 ms horizon slice was constructed above the Hutton Formation as shown in Figure 6.27. High acoustic impedance is observed at all wells. However, an intermediate acoustic impedance occurs near to Well D suggesting a channel of mixed facies in the Brikhead Formation. This is consistent with what well log correlation indicates since the Brikhead shale facies are continuous along Well A, Well B and Well C. Then, shale facies change to mixed facies of sand and shale at Well D. The presence of these facies around Well D may not have good seal properties providing pathways for upward migration. This provides a reasonable reason for oil absence at Well D although it is located high on structure.

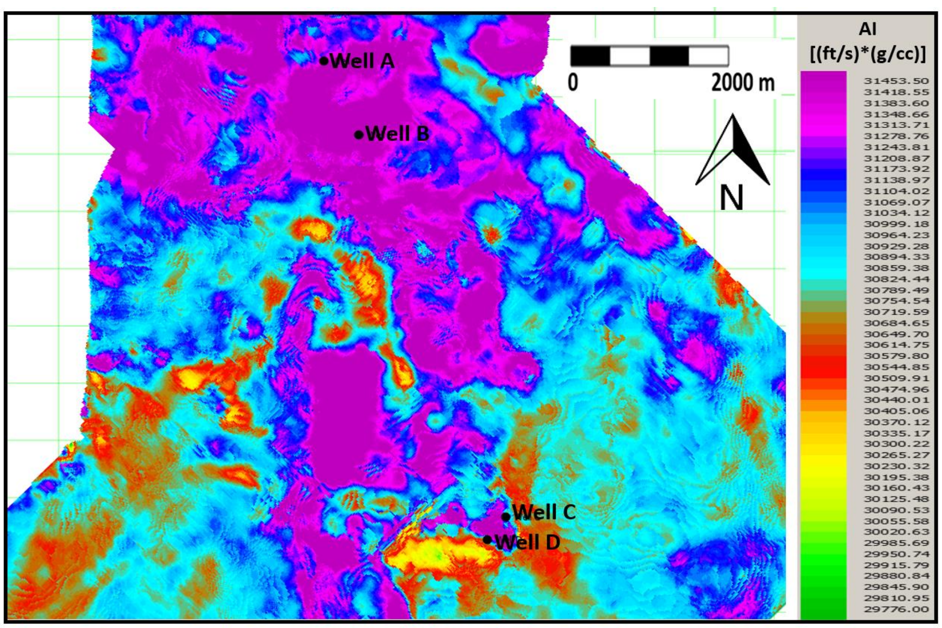

Figure 6.27: A 10 ms acoustic impedance horizon slice above the Hutton Formation to address seal occurrence of the overlying Birkhead Formation.

Chapter 7

Probabilistic Facies Prediction

7.1. Rock-physics templates

Based on Dvorkin and Nur (1996), Ødegaard and Avseth (2004) developed the idea of the rock-physics template (RPT) which uses petrophysical properties estimated at wells for classifying seismic inverted data. An example of a standard rock-physics template used in lithology and pore-fluid discrimination of sand/shale sequences is shown in Figure 7.1. In my study area, calculated petrophysical properties at wells were used to discriminate lithology and pore-fluids with a local RPT. These properties include shale volume (Vsh), porosity, and water saturation (Sw). Establishing rock-property crossplots colored by petrophysical properties can help in dividing data into clusters or zones of different lithofacies and pore fluids.

Since brine-saturated sandstones have different trends depending on degree of cementation as shown in Figure 7.2, a theoretical model trend should be incorporated in rock-physics template adjustment. Brine-sandstone data of low gamma-ray values are plotted along a constant cement model trend as illustrated in Figure 7.3. As gamma-ray values increase, data is shifted to a friable-sand model trend. Using a constant-cement model, a rock-physics template is constructed on a Vp/Vs versus AI crossplot where volume of shale, porosity and water saturation trends are highlighted as shown in Figure 7.4.

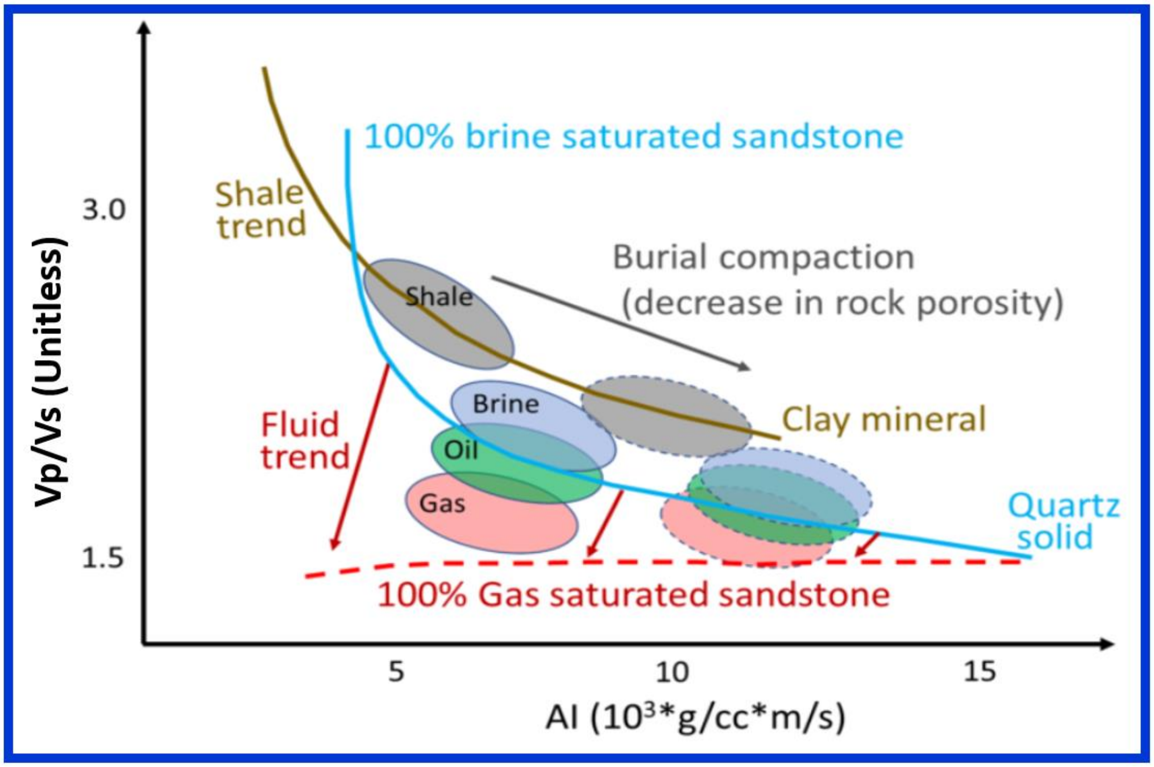

Figure 7.1: Rock-physics template (RPT) for gas, oil and brine-saturated sandstones and shale illustrated on a Vp/Vs versus AI crossplot. Modified from (Avseth and Veggeland 2015).

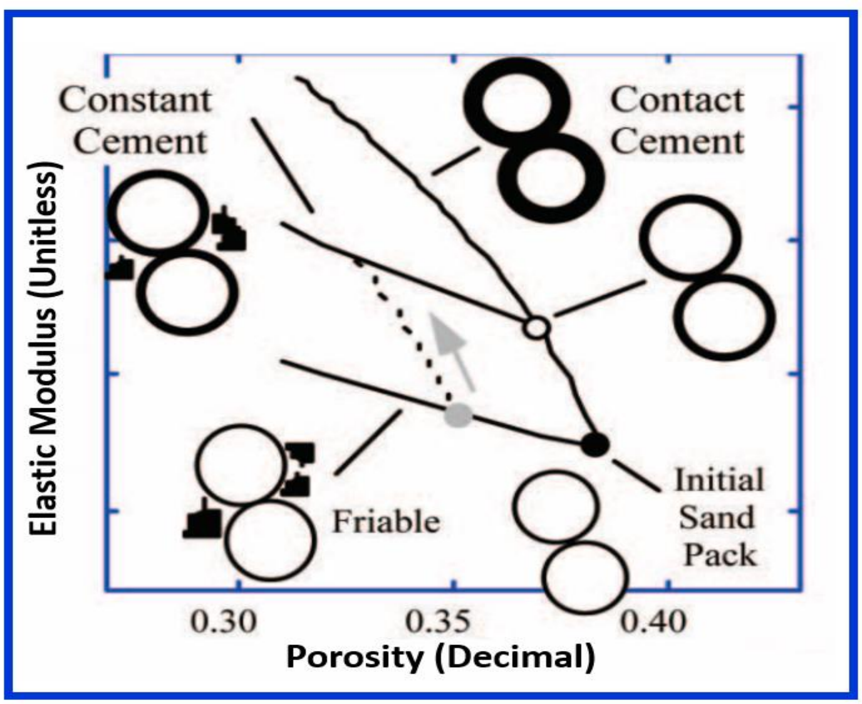

Figure 7.2: Effective-medium model trends for sandstone. Modified from (Avseth et al., 2005).

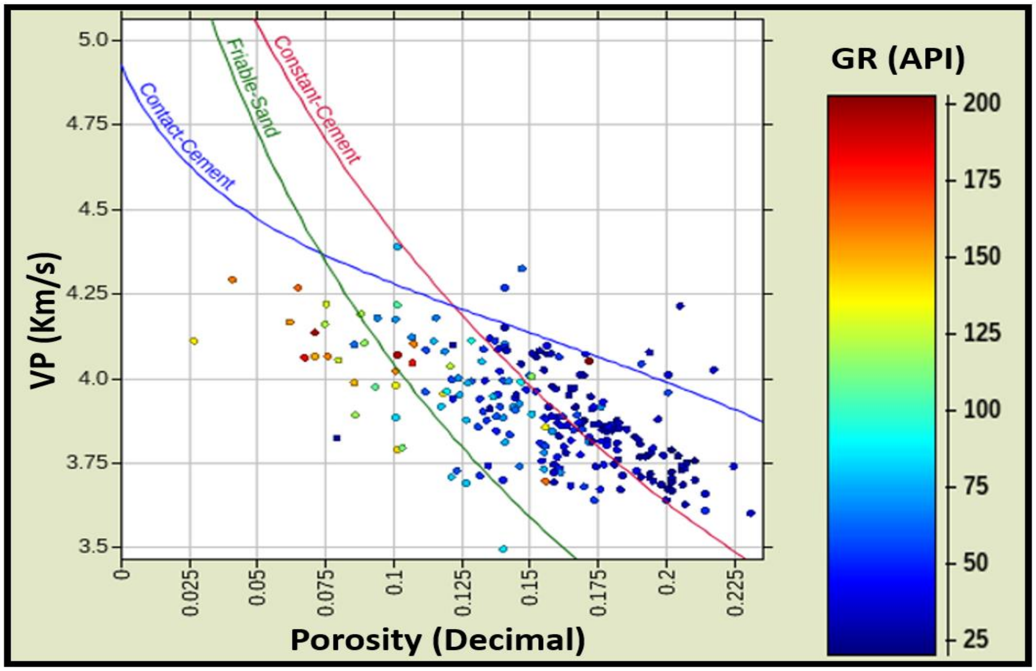

Figure 7.3: Rock-physics template of friable, constant-cement and contact-cement sandstone using a Vp versus porosity crossplot. Brine data of Well A and Well B are colored by gamma ray.

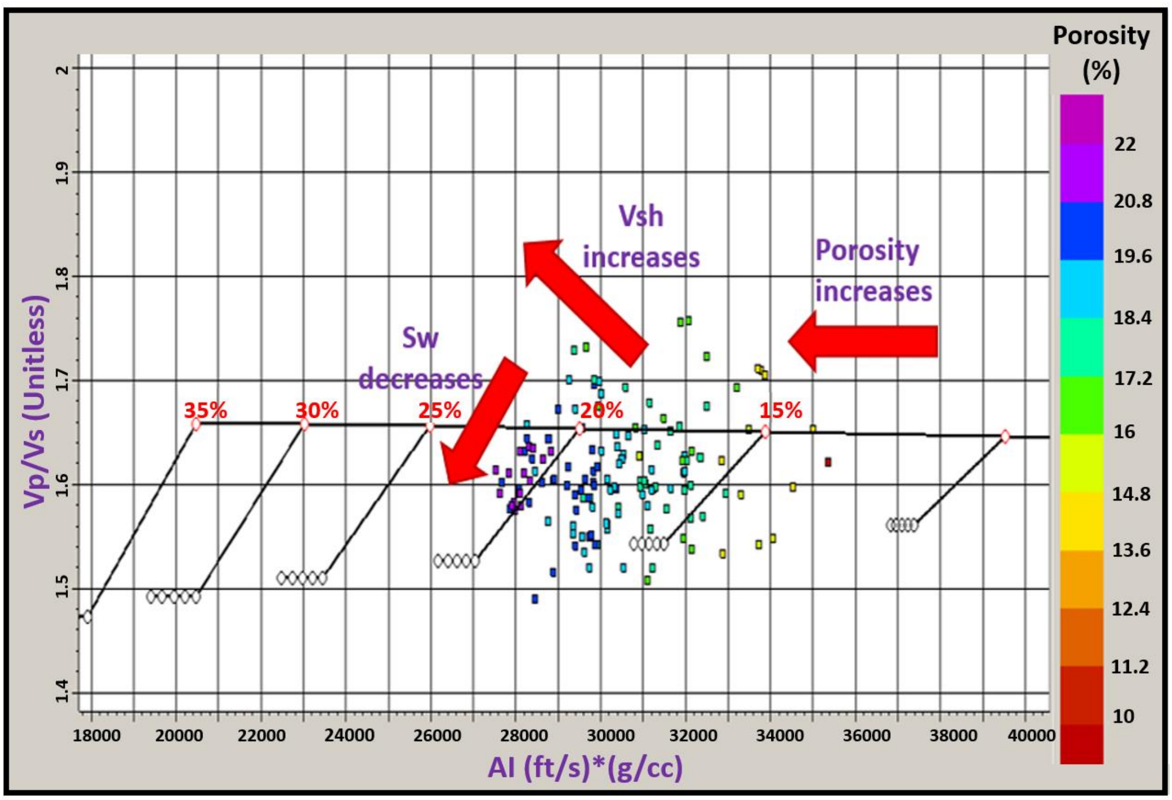

Figure 7.4: Vp/Vs versus AI crossplot of the Hutton Formation at Well A colored by porosity.

Compressional-to-shear-wave velocity ratio and acoustic impedance calculated at the four wells are used to separate data into different lithofacies and pore fluids. For a more accurate separation, data of the Hutton Formation at Well A was only used since it is the only well having measured shear-wave velocity. Calculated shear-wave velocities at the other wells may produce anomalous and inaccurate estimation that will lead, in turn, to improper separation. Data extracted from Well A was selected along the Hutton Sandstone Formation pay zone as well as 100 ft above and below the target zone.

7.1.1. Lithofacies discrimination

Based on shale volume (Vsh) calculated at Well A, sandstone and shale facies are separated with a small area of intersection that represents shaly sand using a Vp/Vs versus AI crossplot as shown in Figure 7.5. The highlighted zones on the Vp/Vs versus AI crossplot represent physical-property ranges of facies that can be projected on either well logs or seismic data to show sand/shale facies distribution over the 3D volume. Projection of sand and shale facies at Well A is shown in Figure 7.6. Facies distribution in Well A shows a great match with volume of shale (Vsh).

Acoustic impedance estimated from post-stack inversion of the high-frequency far-angle seismic volume and the compressional-to-shear-wave velocity ratio estimated from pre-stack simultaneous inversion of conventional seismic data are the physical properties used for zones projection on the 3D seismic volume. Sand and shale facies also are delineated along different arbitrary lines across the 3D seismic volume as shown in Figures 7.7, 7.8 and 7.9.

On these figures, sand, represented by red color, is distributed below the Hutton Formation top along the four wells. Above the Hutton Formation top, there is a distribution of shale facies that represents a seal for hydrocarbon updip migration. From arbitrary lines passing through Well C, Well D, and the interpreted channel, facies change from sand to shale in the Hutton Formation at Well D. In addition, the upper unit of the Hutton Formation at Well C is separated from a lower sand by shale intercalation that probably seals hydrocarbon migration to the upper unit in Well D from Well C. When it comes to the proposed hydrocarbon-charged channel, it has a good distribution of sandstone facies overlain by shale seal. A 10 ms horizon slice is constructed below the Hutton Formation top to show lithofacies distribution over the study area as illustrated in Figure 7.10. Shale is distributed along meandering and forked features.

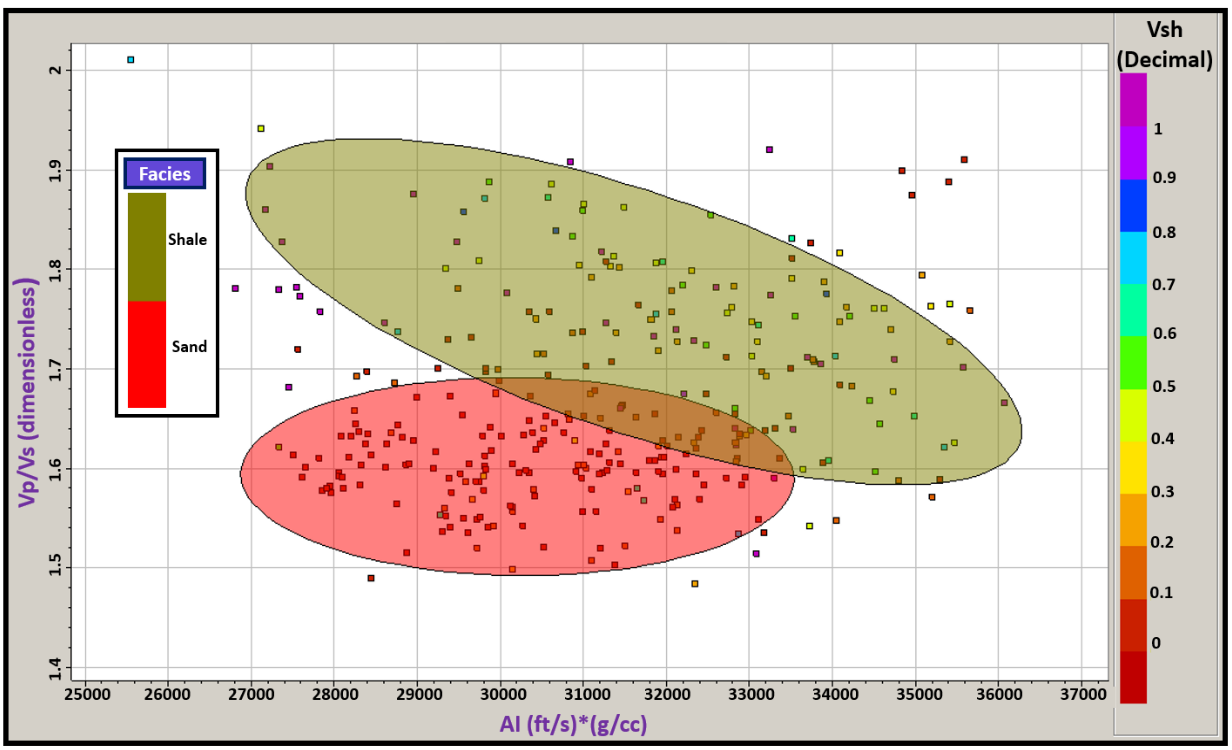

Figure 7.5: Separation between sand and shale facies on a Vp/Vs versus AI crossplot. Well A data is colored by volume of shale.

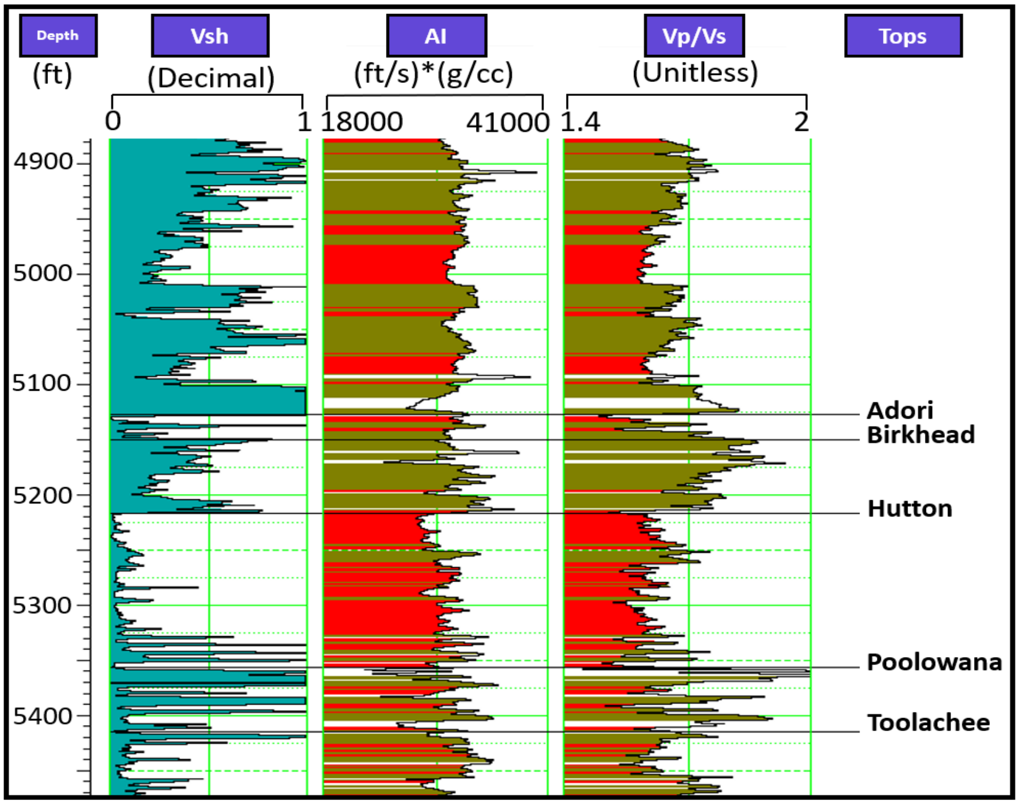

Figure 7.6: Projection of sand and shale facies zones at Well A. Sand facies is represented by red.

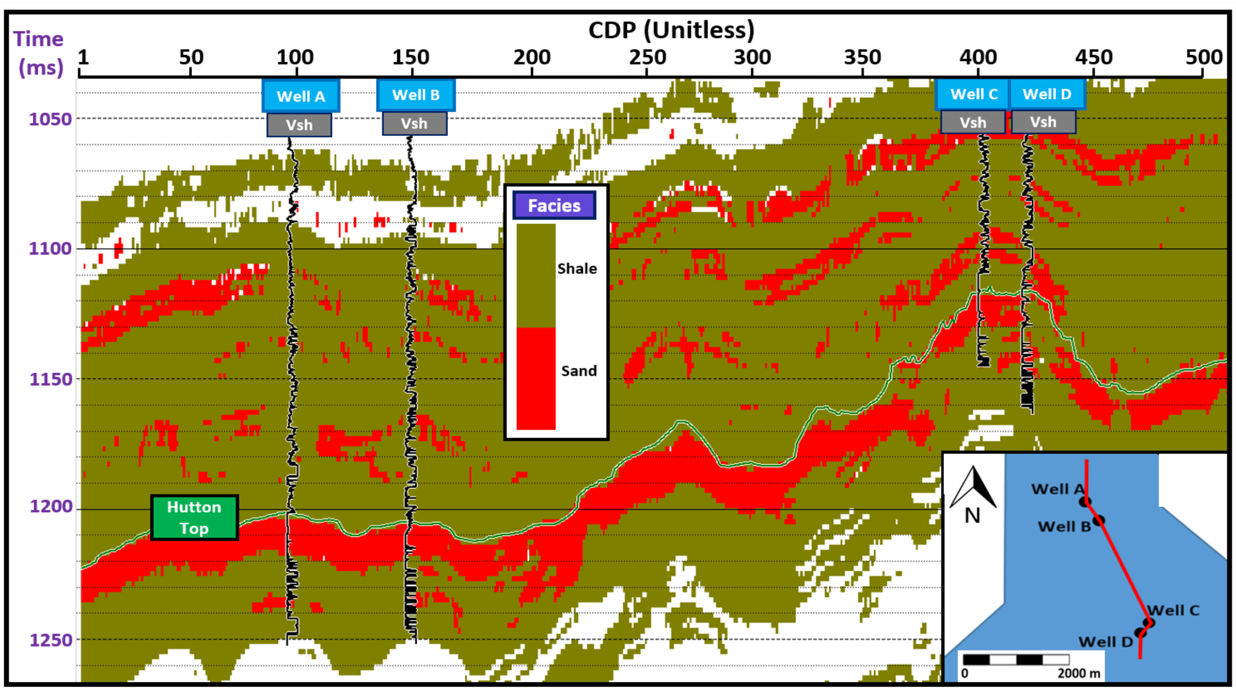

Figure 7.7: Lithofacies distribution along arbitrary line passing through the four wells.

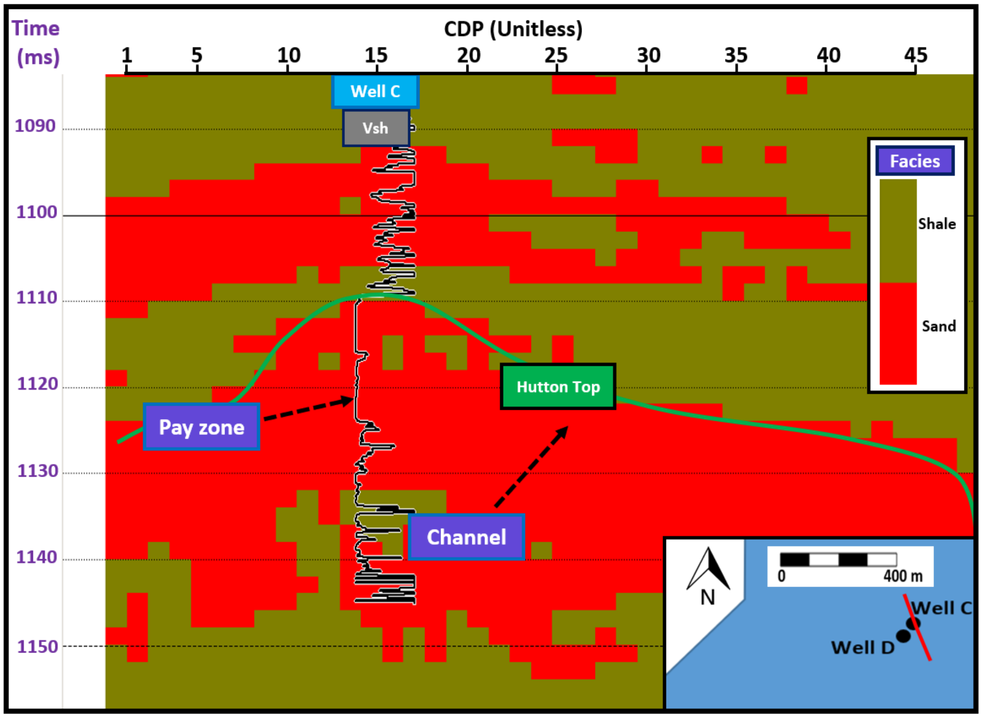

Figure 7.8: Lithofacies distribution along arbitrary line passing through Well C and proposed channel.

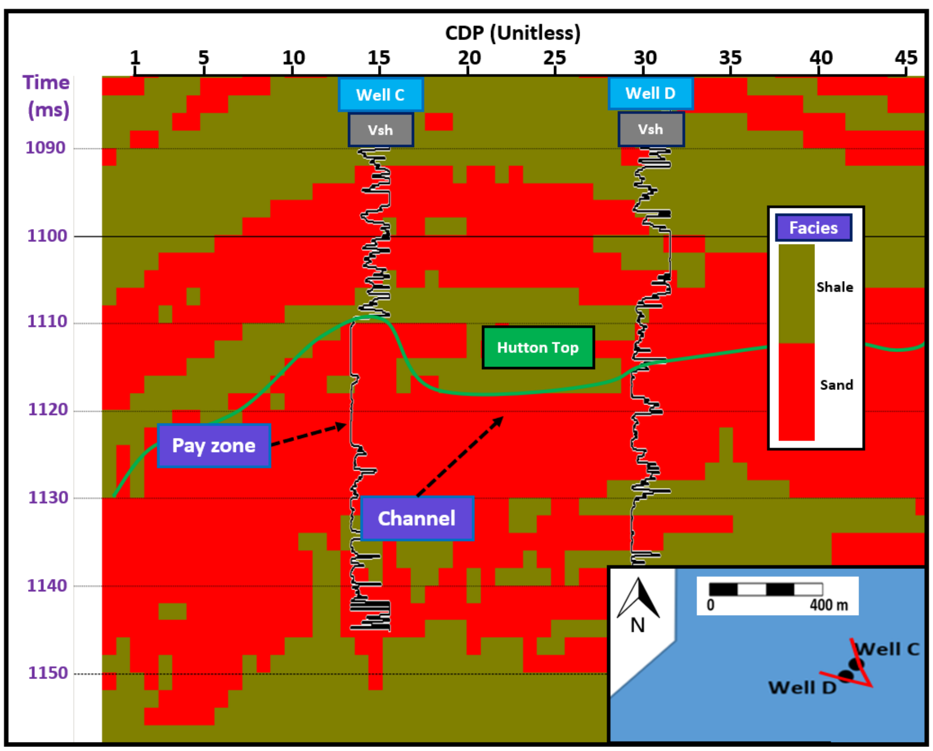

Figure 7.9: Sand and shale facies distribution along arbitrary line passing through Well C, proposed channel and Well D.

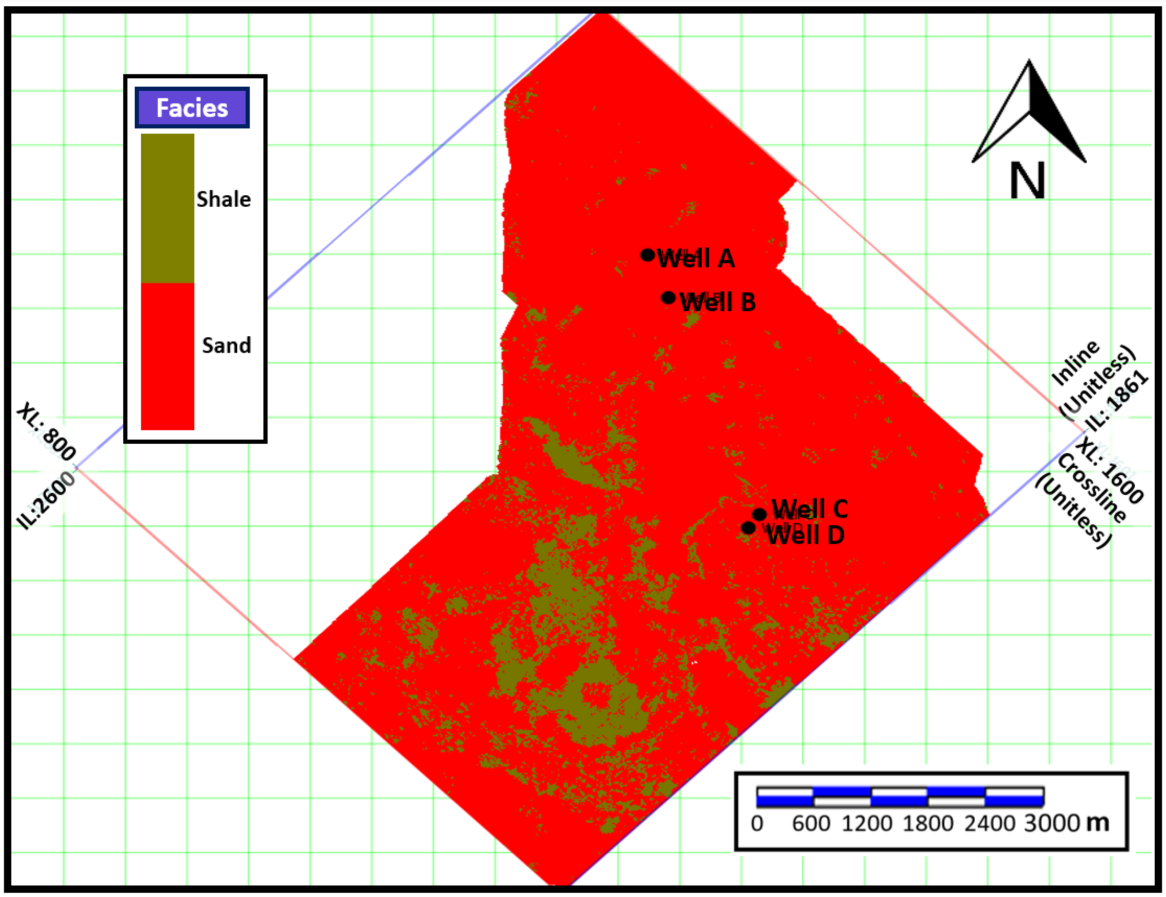

Figure 7.10: Horizon slice shows sand and shale facies distribution over the study area.

Based on porosity estimated at Well A, sandstone facies are separated into high-porosity and low-porosity sand clusters using the Vp/Vs versus AI crossplot as shown in Figure 7.11. The low-porosity sand facies are probably cemented sand or siltstone. The highlighted zones on the Vp/Vs versus AI crossplot are projected on Well A as shown in Figure 7.12. Shale and low-porosity sand intercalations occur within the lowest part of the Hutton Formation that means decreasing porosity in some intervals. However, clean-sand facies are distributed along the upper part of the Hutton Formation where the pay zone is located. Then, high-porosity sand, low-porosity sand and shale facies are projected on the 3D seismic volume. These facies are delineated along different arbitrary lines across the 3D seismic volume as shown in Figures 7.13, 7.14 and 7.15.

Clean sand is distributed below the Hutton top while low-porosity sand is intercalated with clean sand at some locations especially at Well C and Well D. At Well C, there is an intercalation of low-porosity sand or siltstone facies at the boundary between the two upper units of the Hutton Formation. This intercalation of a low-porosity zone probably provides a seal for hydrocarbon upward migration. In addition, many low-porosity sand or siltstone facies intercalations are observed along the Hutton Formation at Well D. A 10 ms horizon slice is established below the Hutton Formation top to illustrate porosity distribution over the study area as shown in Figure 7.16. Shale and low-porosity sand are distributed along meandering and Y features.

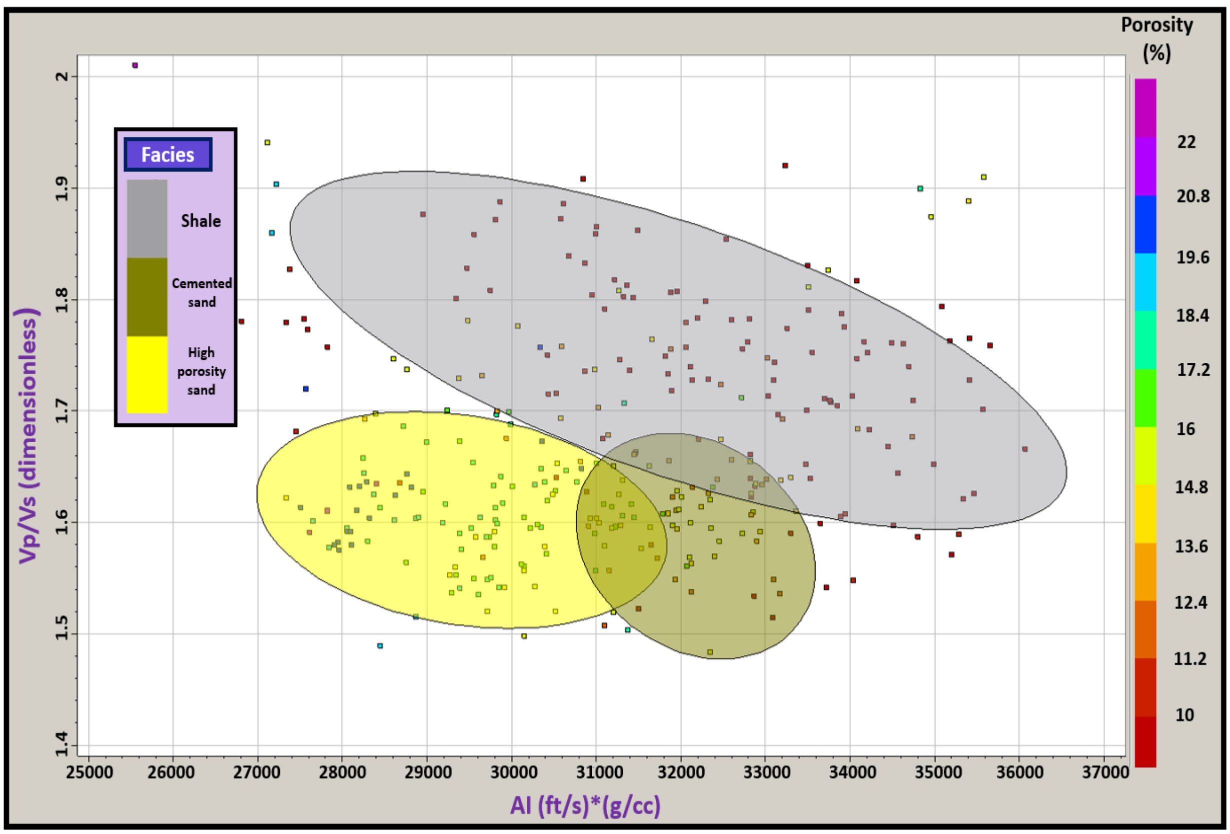

Figure 7.11: Separation between high-porosity sand, low-porosity sand and shale facies on a Vp/Vs versus AI crossplot. Well A data is colored by porosity.

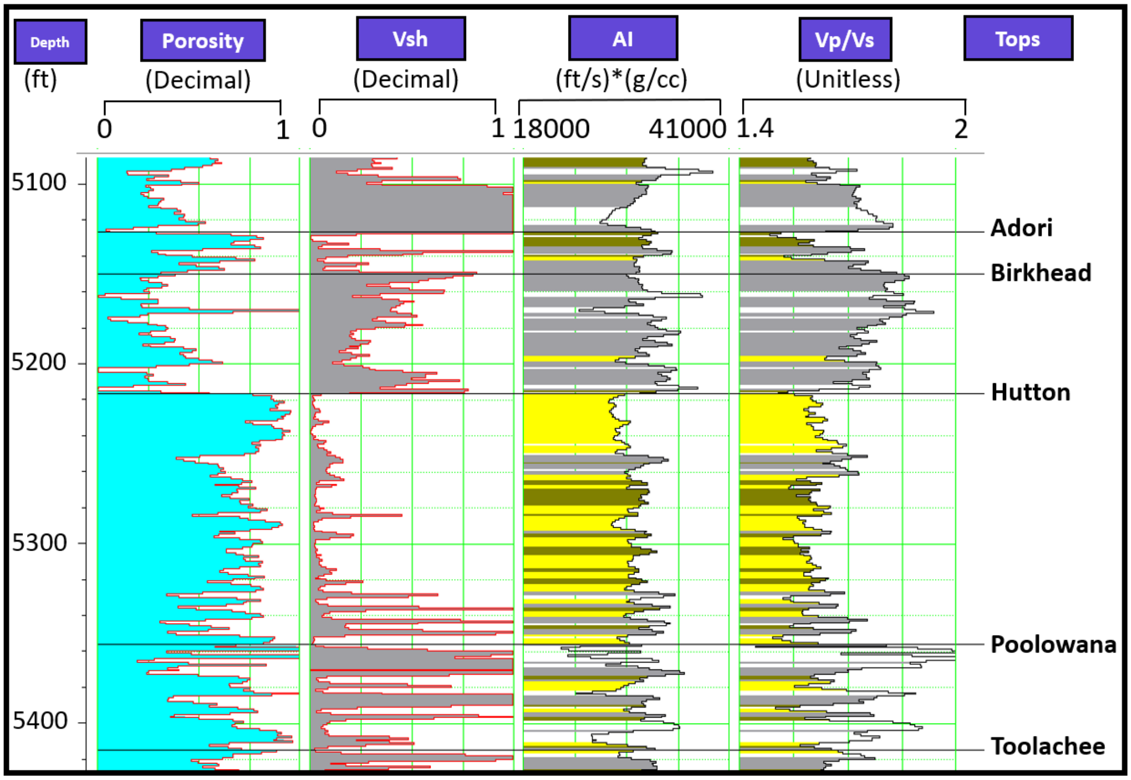

Figure 7.12: Projection of high-porosity sand, low-porosity sand and shale facies zones at Well A. High-porosity sand facies is represented by yellow color.

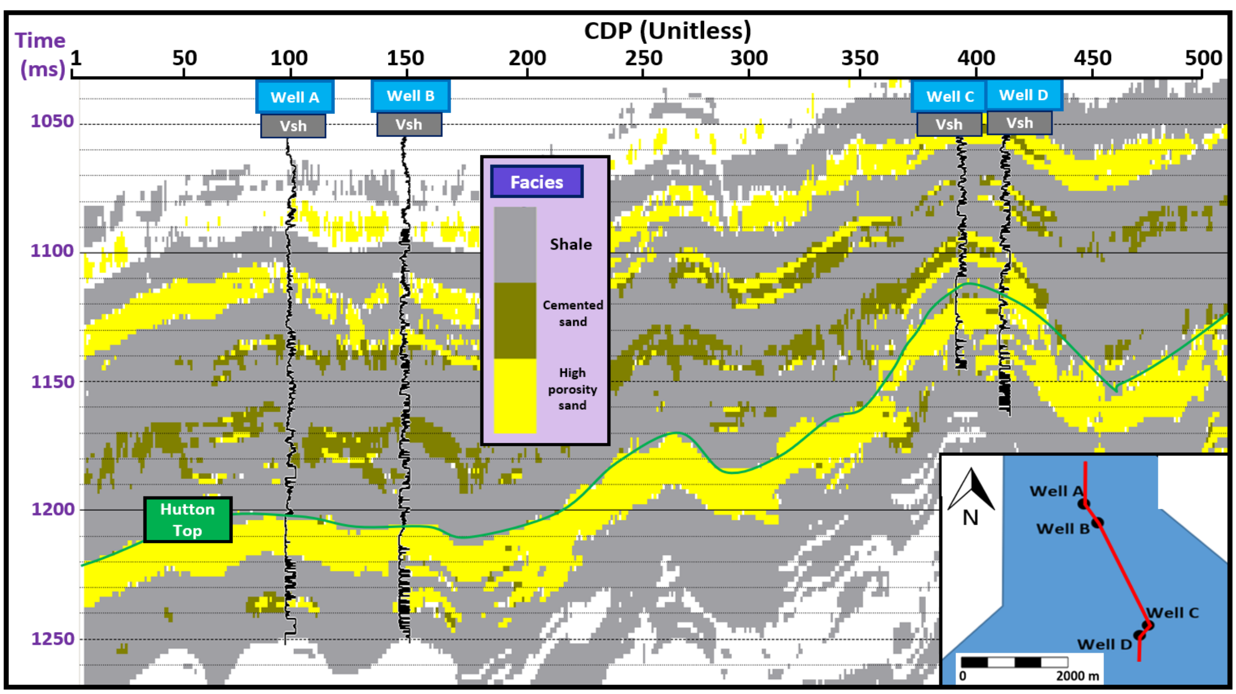

Figure 7.13: High-porosity and low-porosity sand facies distribution along arbitrary line passing the four wells.

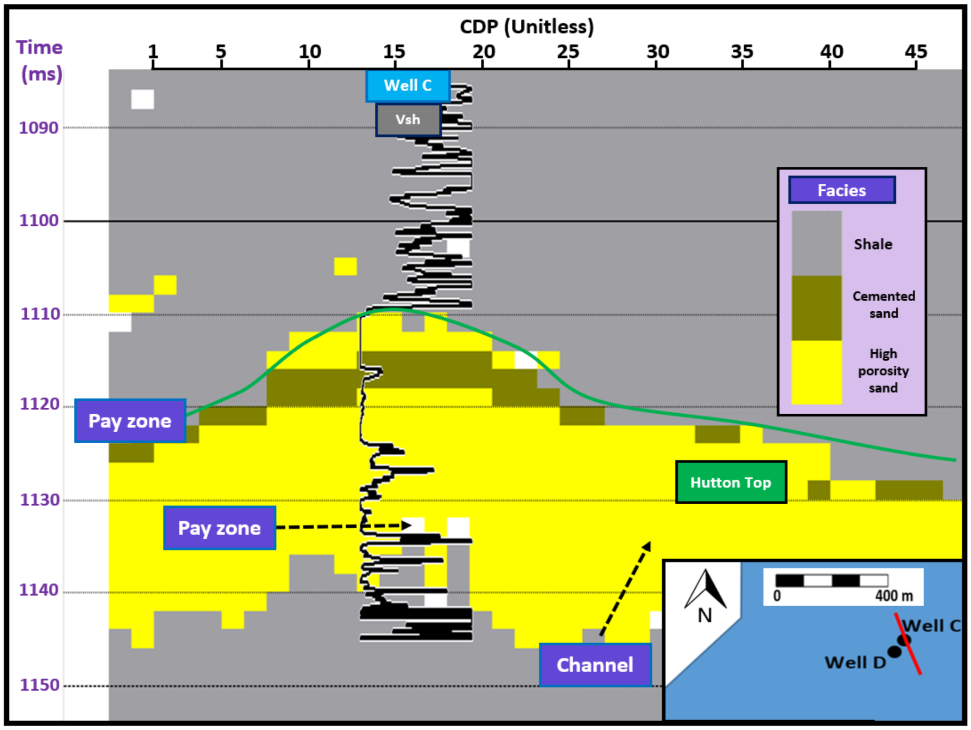

Figure 7.14: High-porosity and low-porosity sand facies distribution along arbitrary line passing through Well C and proposed channel.

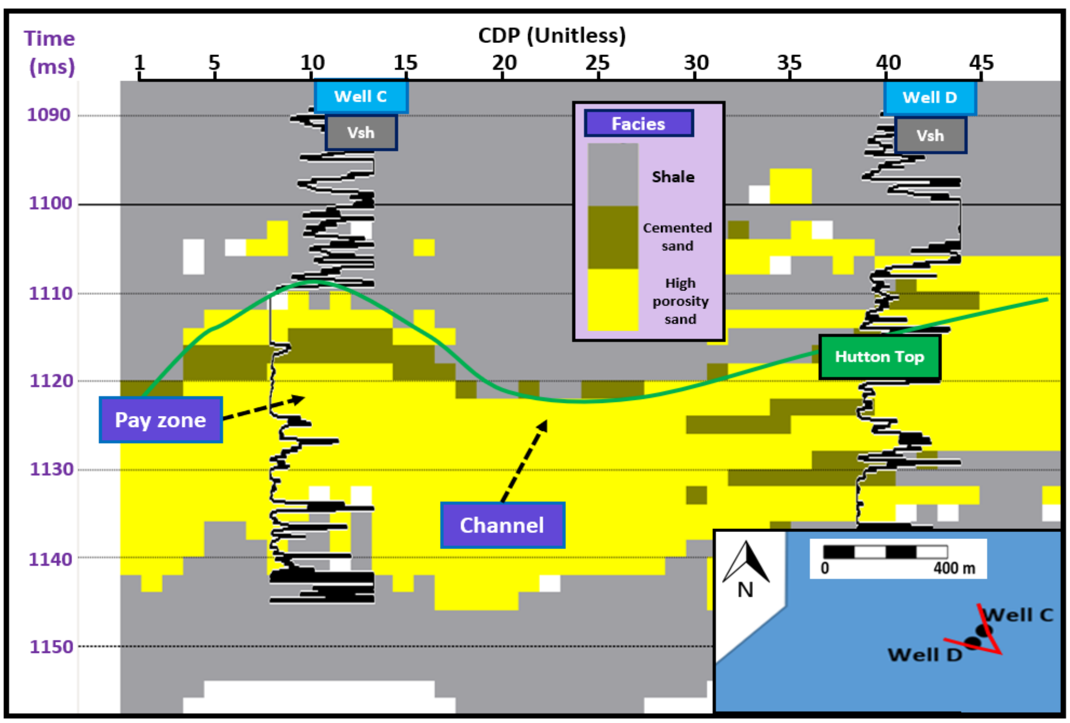

Figure 7.15: High-porosity and low-porosity sand facies distribution along arbitrary line passing through Well C, the channel and Well D.

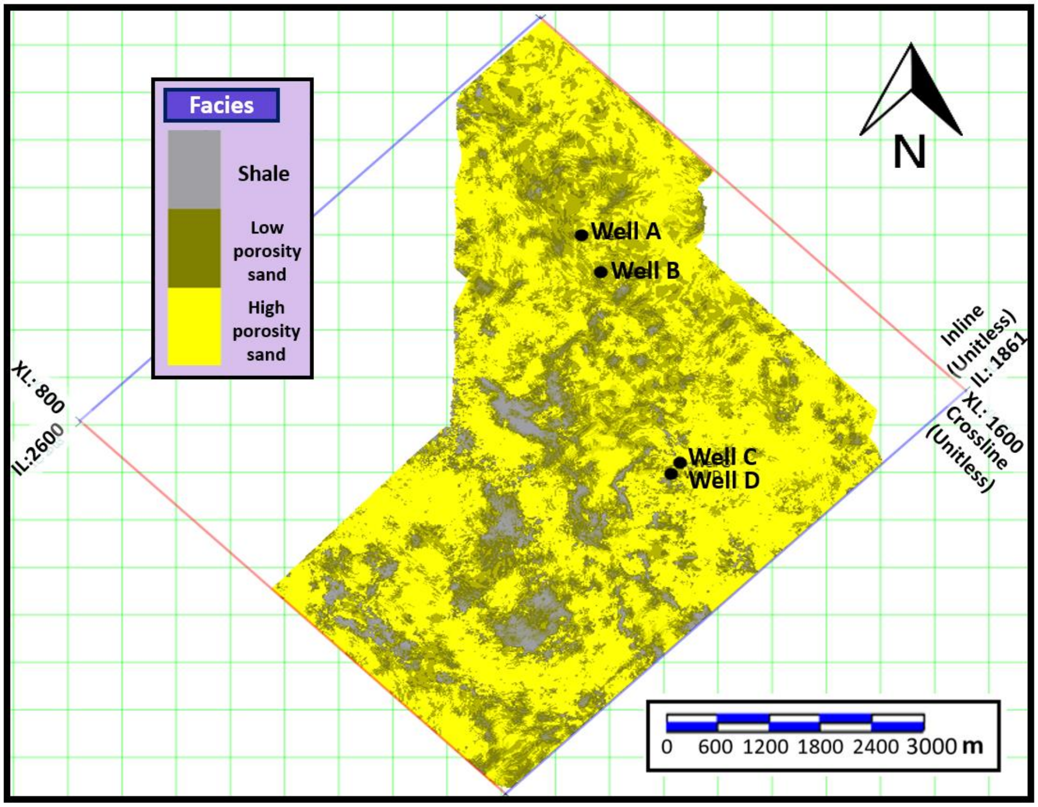

Figure 7.16: Horizon slice shows high- and low-porosity sands and shale facies distribution over the study area.

7.1.2. Pore-fluid discrimination

Oil sand is not discriminated from brine sand at wells using the different rock-property crossplots. However, the oil data cluster range represents high-probability oil sand which can be recognized on the crossplot (Figure 7.17). After highlighting oil and brine-sand facies clusters, they are projected on both Well A and the 3D seismic volume. Projection of facies clusters on Well A is shown in Figure 7.18. High-probability oil distribution along Well A shows a great match with low water saturation and high resistivity below the top of the Hutton Formation. Different arbitrary lines across the 3D seismic volume are shown in Figures 7.19, 7.20 and 7.21. High probability oil distributes along the proposed channel until it completely matches with the thin pay zone at Well C. However, there is no oil distribution along the Hutton Formation at Well D.

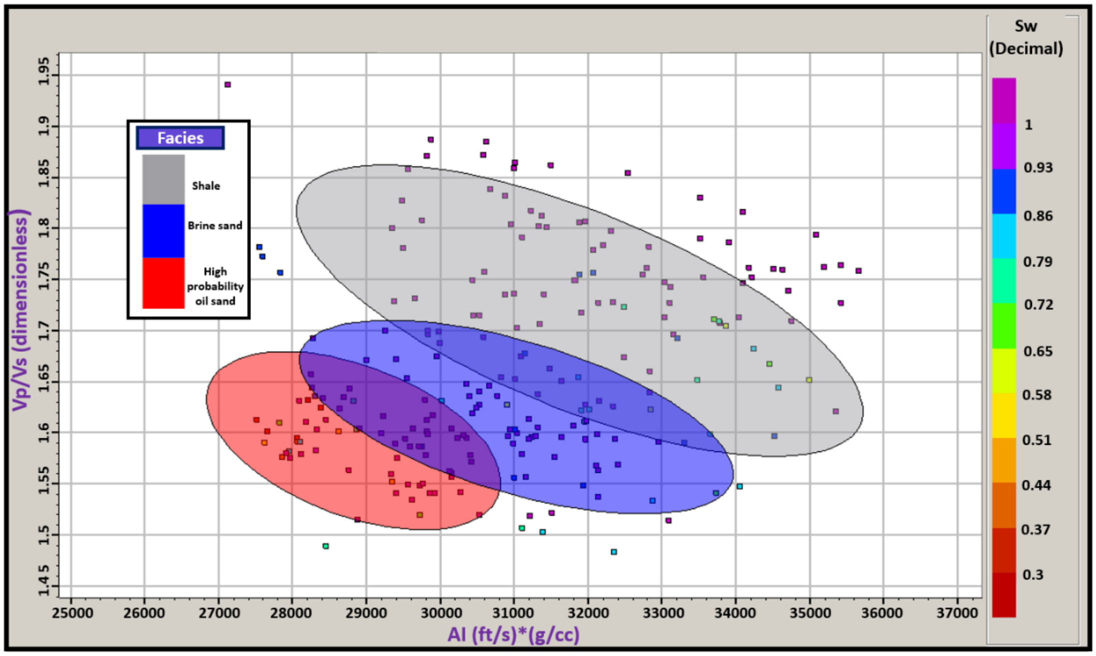

Figure 7.17: Separation between high-probability oil sand, brine sand and shale facies on the Vp/Vs versus AI crossplot. Well A data is colored by water saturation.

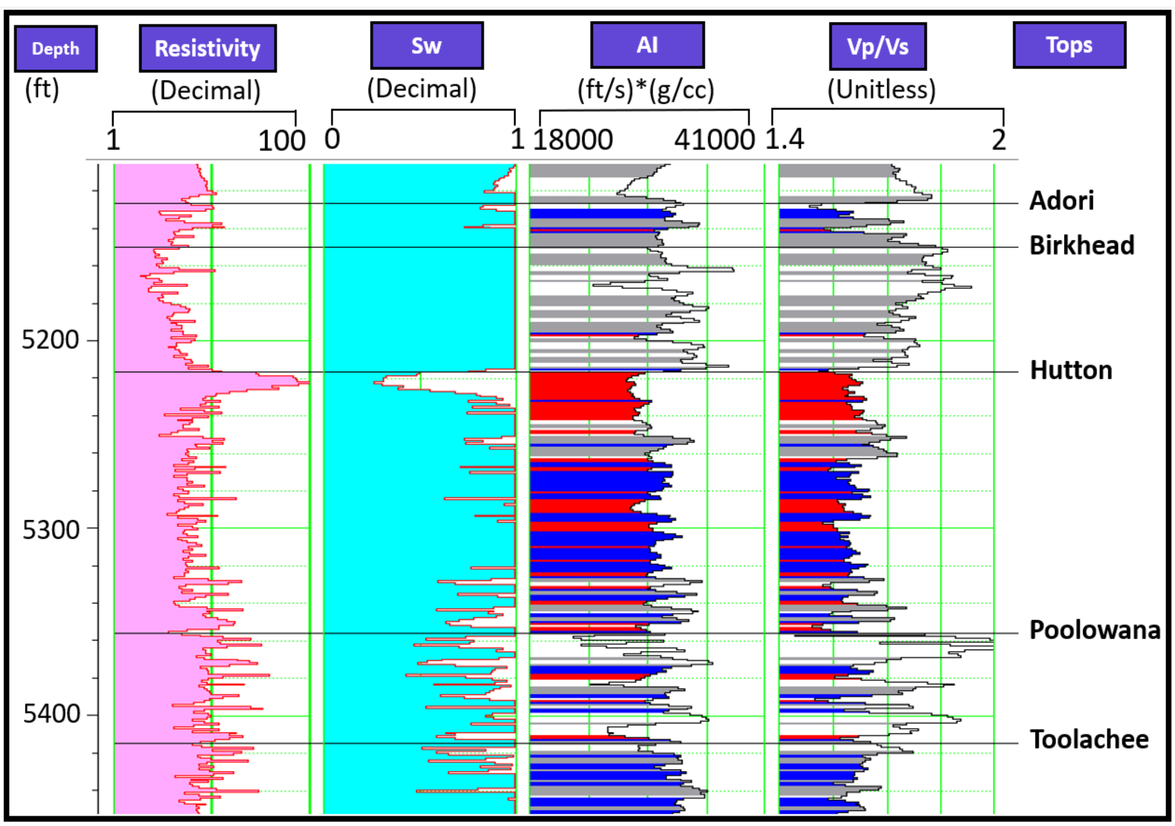

Figure 7.18: Projection of high-probability oil, brine-filled sandstone, and shale facies at Well A. High-probability oil facies are colored red.

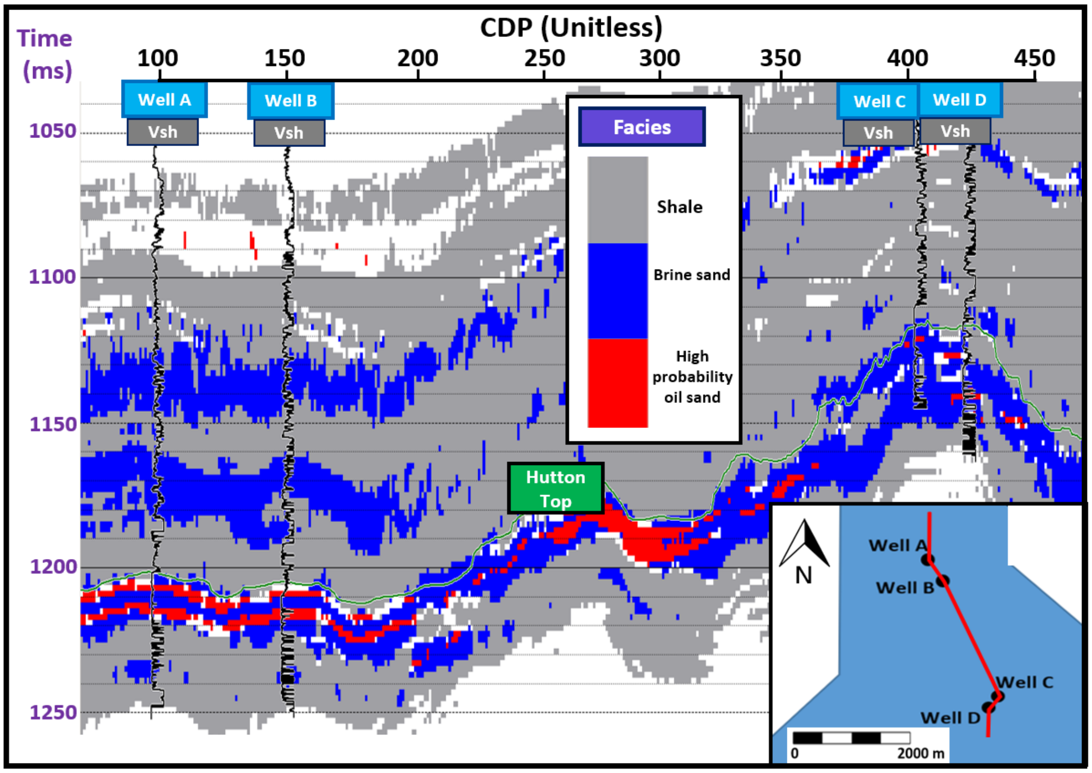

Figure 7.19: High-probability oil and brine-sand facies distribution along arbitrary line passing through all wells.

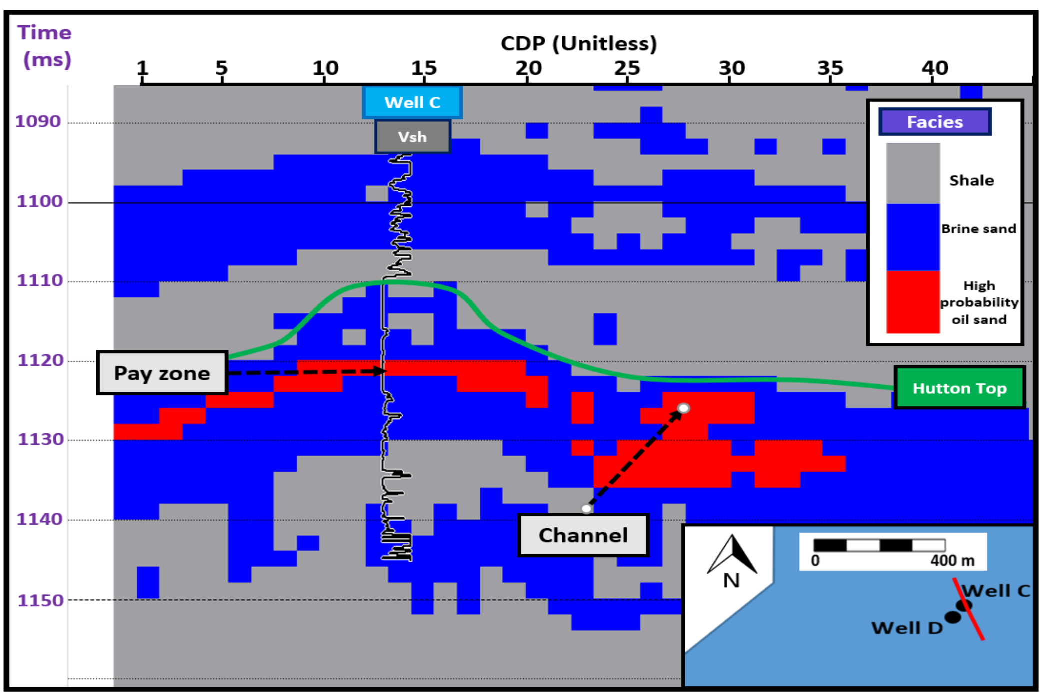

Figure 7.20: High-probability oil and brine-sand facies distribution along arbitrary line passing through Well C and the channel.

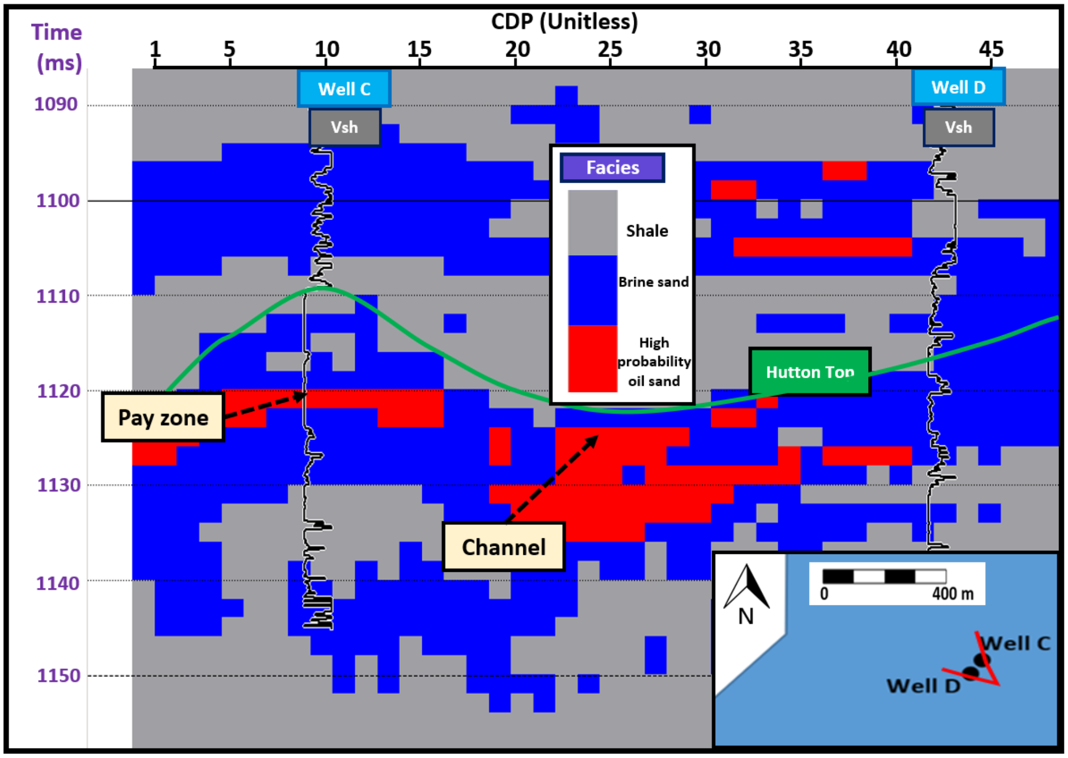

Figure 7.21: High-probability oil and brine-sand facies distribution along arbitrary line passing through Well C, the channel and Well D.

A 10 ms horizon slice extracted below the Hutton formation top shows high-probability oil and brine-sand facies distribution over the study area as shown in Figure 7.22. Oil is distributed along Well A and Well B. However, as magnified in Figure 7.23, Well C occurs in the brine zone area and this probably is attributed to the small thickness of the pay zone compared with a 10 ms time window chosen for the horizon slice or it may be attributed to uncommercial oil quantitates at Well C since the pay zone has 60% water saturation. However, high-probability oil distribution along the channel location indicates that the channel has possible commercial oil quantities.

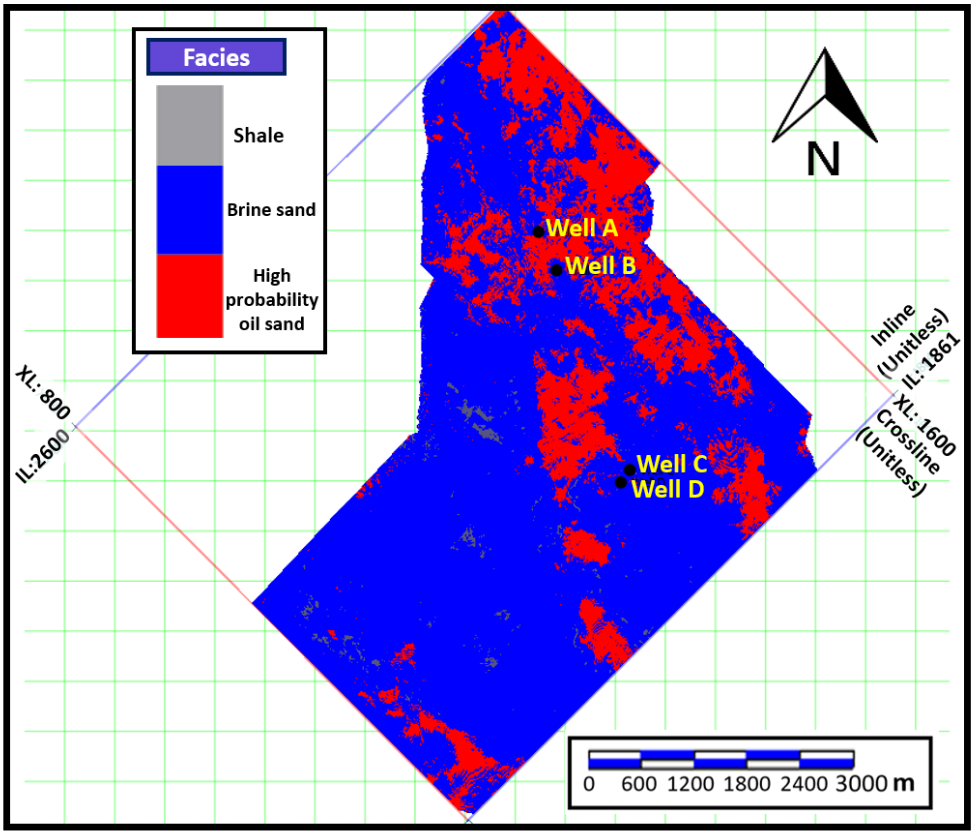

Figure 7.22: Horizon slice shows high-probability oil and brine sand facies distribution over study area.

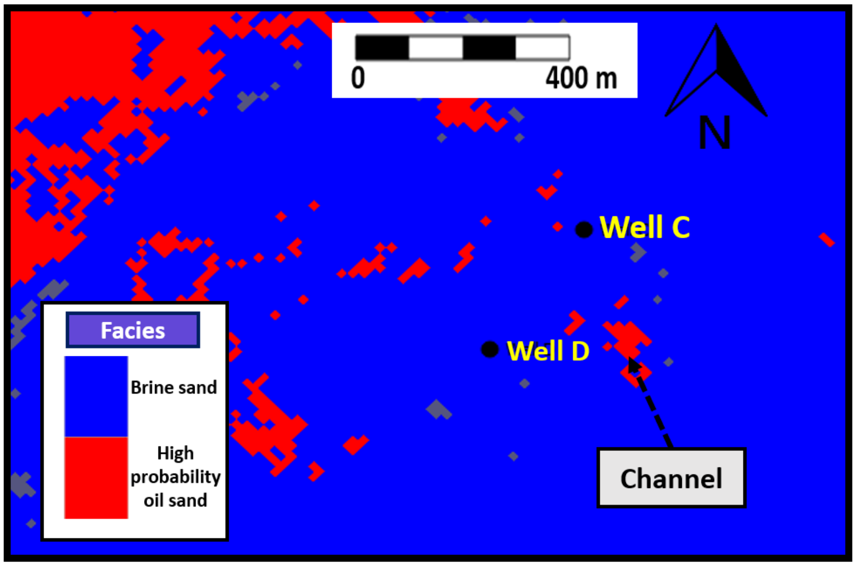

Figure 7.23: The proposed channel has high probability of oil occurrence with commercial quantities compared with Well C that has high water saturation.

7.2. Bayesian classification

Bayesian classification is a statistical approach used to reduce uncertainty and exploration risk. One of the main problems in zone separation using the rock physics template is intersectional areas between two zones. To partially solve this problem, a Bayesian classification was applied to zones to maximize separation and minimize misclassification errors. Thus, statistics should be taken into consideration in this stage to maximize lithology and pore fluids prediction from the rock physics template.

Bayes classification uses prior information and incorporates it with probability density functions (PDF) to estimate posterior probability, *P(c|x)*, using the Bayes formula:

$$\text{Posterior probability} = \frac{\text{Prior} * \text{Likelihood}}{\text{evidence}},$$

and

$$P(c|x) = \frac{P(c) * P(x|c)}{P(x)} \quad , \tag{7-1}$$

where, *P(c)* is prior probability, *P(x|c)* is estimated from the well information and *P(x)* is the PDF for the attribute or property used.

An example of applying Bayesian classification is discussed at Well A. A gamma-ray cutoff at 65 API units is assumed to separate sand and shale facies at Well A. Then, prior probability was estimated for the Well A in Table 1. Then, mean and standard deviation of the Hutton Formation were estimated for creating PDFs as shown in Table 1 and Figure 7.24. Using these PDFs and prior probability, posterior probability was calculated for sand and shale facies within the Hutton

Formation using the Bayes equation as shown in Figure 7.25. The vertical dashed line at which prediction changes from one class to another is called the decision boundary. The decision boundary for gamma ray is shifted from 84 to 68 API units after applying Bayesian classification.

Table 7.1: Statistical analysis at Well A.

Facies	Sandstone	Shale
Gamma cut off	<65	>65
Prior probability	0.18	0.82
Mean	45.27	122.55
Standard deviation	26.00	29.37

The Gaussian PDF is represented by a single curve in the previous example because the variable (gamma ray) is a single variable. In the case of using two variables of Vp/Vs and AI, the PDF will be represented by an ellipse shape or two-dimensional vector. This 2D probability density function is the bivariate Gaussian PDF that represents the two-variable distribution. Gaussian parameters including AI mean, Vp/Vs mean, AI variance, Vp/Vs variance and covariance, were first estimated for each facies cluster. Then, prior probability of a given cluster is calculated by dividing its data points by the total number of data-cluster points and finally Bayes classification is applied.

Using Gaussian parameters, each facies cluster is represented by bivariate Gaussian PDF which is divided into concentric rings. Each ring or contour represents a standard deviation from the mean since zone color changes gradually from dark color at the cluster center which represents the bivariate distribution peak to white color at the cluster periphery that represents the decision boundary (Russell, 2016). Thus, the zone of maximum probability is represented by dark color and as we go away from the bivariate distribution peak at the cluster center, as we approach the decision boundary with another cluster, the minimum probability is represented by faint color.

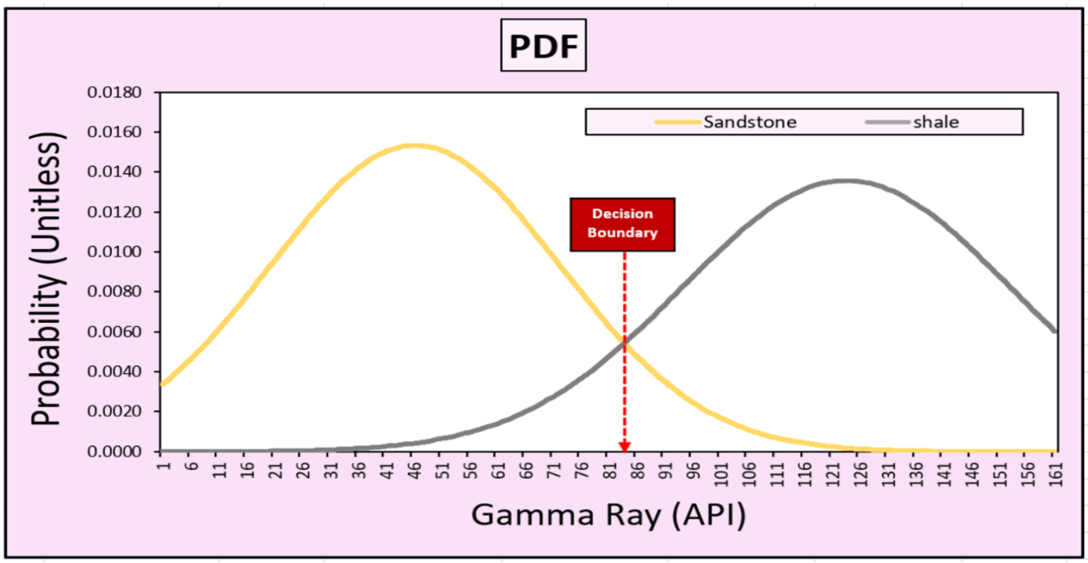

Figure 7.24: Probability density function for the Hutton Formation lithofacies at Well A.

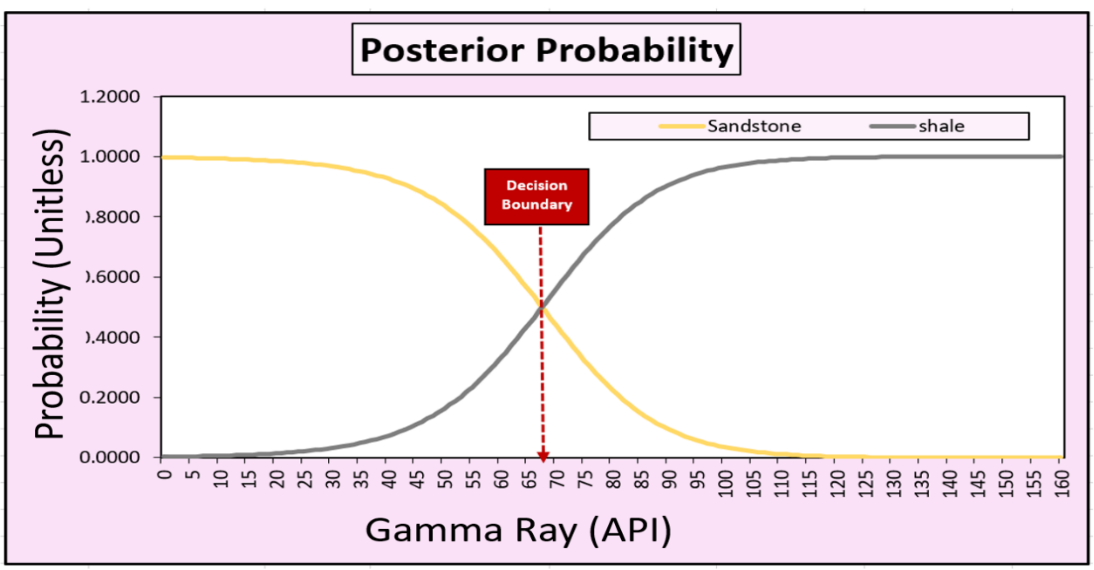

Figure 7.25: Posterior probability for the Hutton Formation facies at Well A.

7.2.1. Probabilistic lithofacies discrimination

After applying Bayesian classification to facies zones, intersectional area between facies clusters decreases and hence, facies separation is improved. Separation between sand and shale facies on the Vp/Vs versus AI crossplot after applying Bayesian classification is shown in Figure 7.26. Table 7.2 shows Gaussian parameters for each facies cluster. Sand and shale facies are delineated along different arbitrary lines across the 3D seismic volume as shown in Figures 7.27, 7.28 and 7.29.

On arbitrary lines showing sand/shale facies, facies distribution is better matched with shale volume (Vsh) at the four wells. In addition, the upper unit of the Hutton Formation at Well C is identified as a sand facies from conventional zones, but after applying Bayesian classification, this unit is identified as a sand facies with low probability. This indicates that this unit is in a grey area between sand and shale facies such as shaly sand. Furthermore, there is high probability of sand facies downdip in the interpreted channel.

Table 7.2: Gaussian parameters for sand and shale facies.

Gaussian Parameters	Sand facies	Shale facies
AI mean [(ft/s)*(g/cc)]	30473.9	32180.2
Vp/Vs mean (Unitless)	1.60	1.74
AI variance [(ft/s)*(g/cc)]	2.31e+06	3.74e+06
Vp/Vs variance (Unitless)	0.0015	0.0051
Covariance [(ft/s)*(g/cc)]	2.25	-83.91

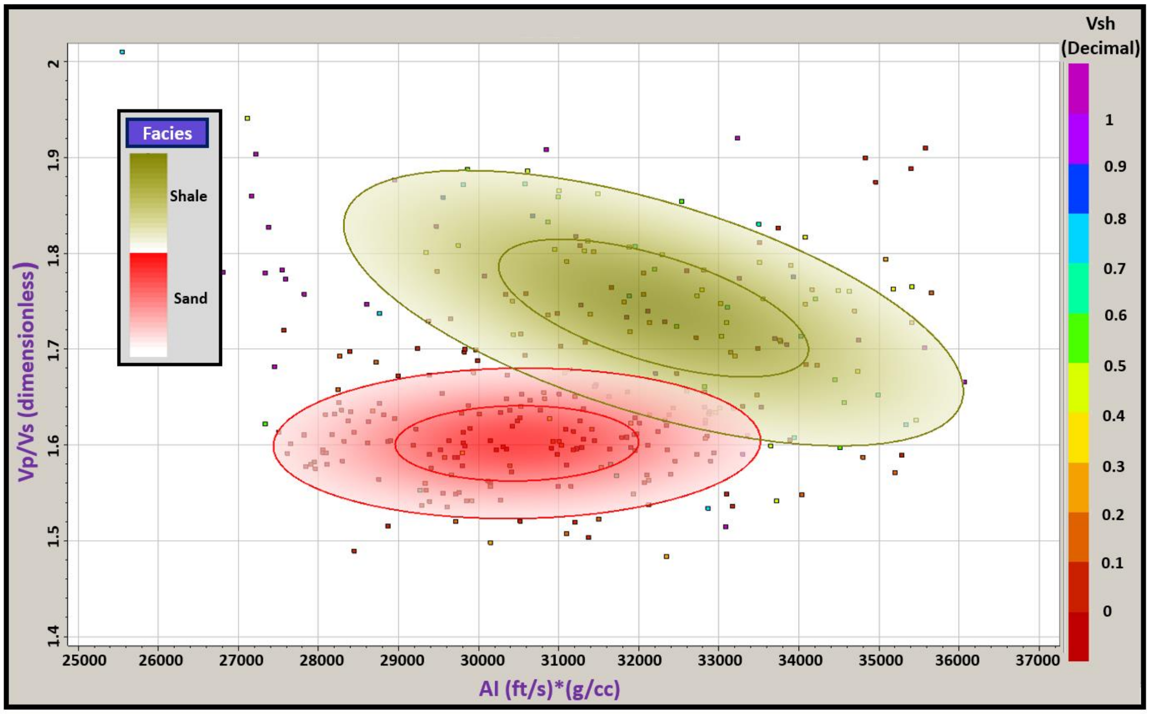

Figure 7.26: Separation between sand and shale facies on a Vp/Vs versus AI crossplot after applying Bayesian classification.

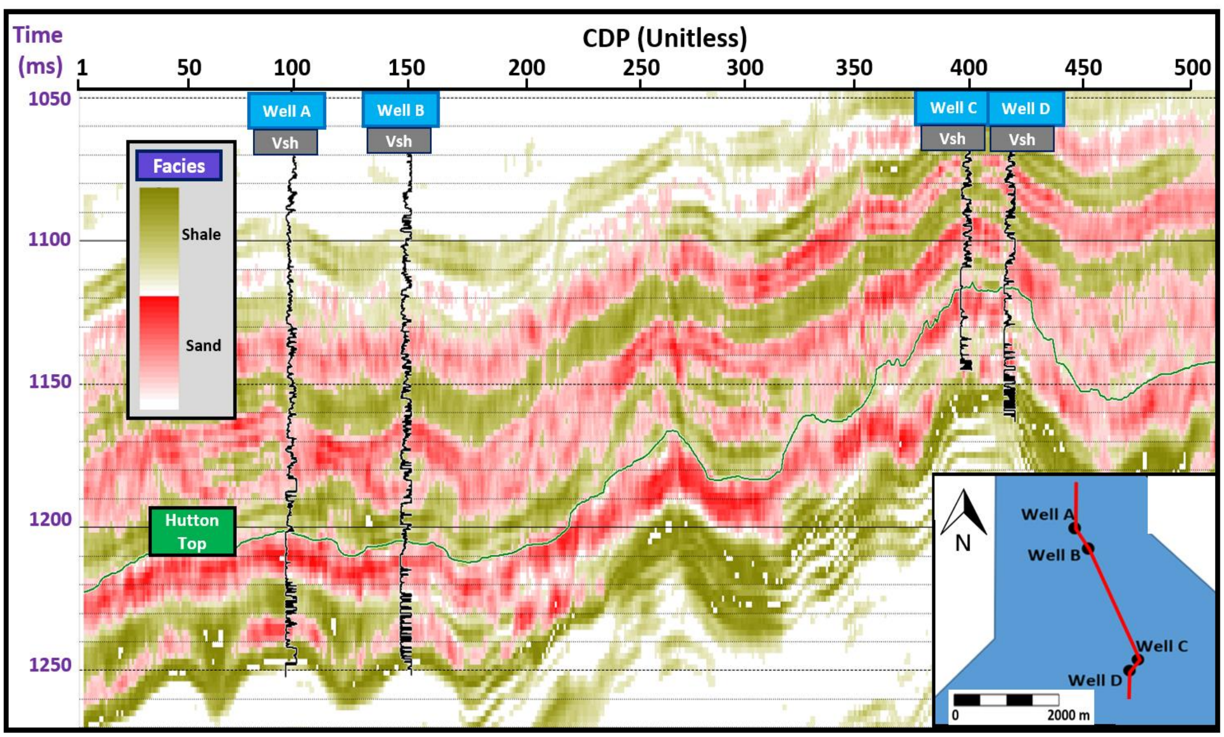

Figure 7.27: Lithofacies distribution along an arbitrary line passing through the four wells after applying Bayesian classification.

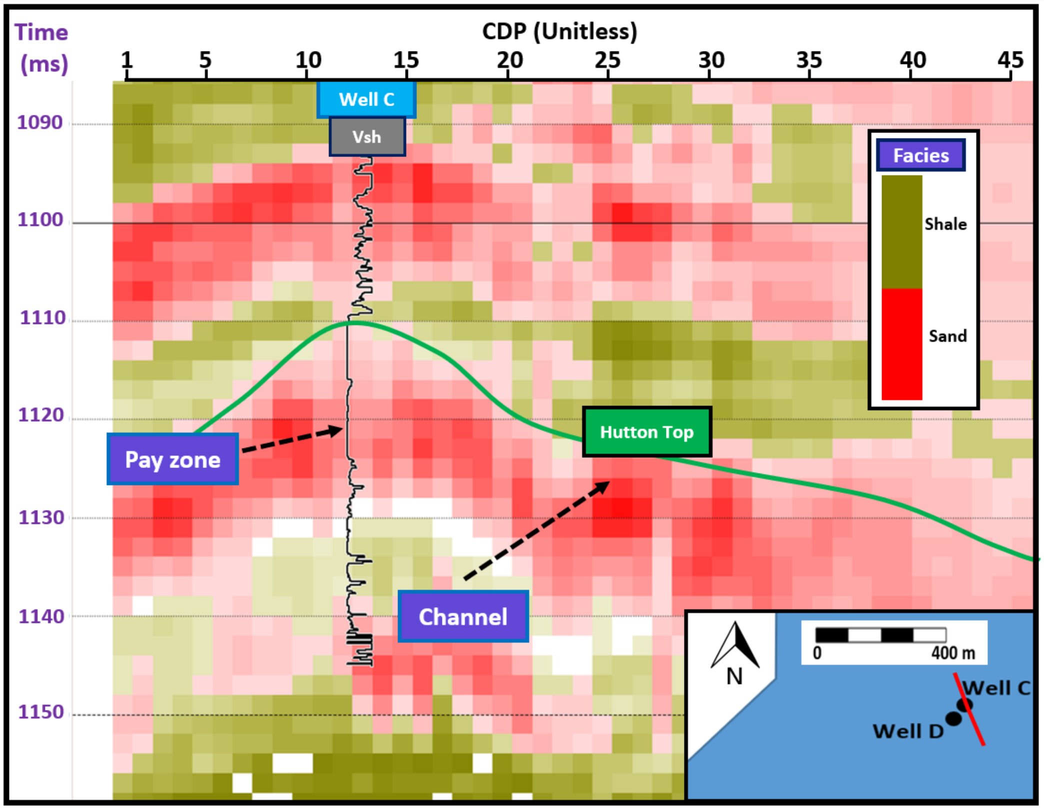

Figure 7.28: Lithofacies distribution along arbitrary line passing through Well C and proposed channel after applying Bayesian classification.

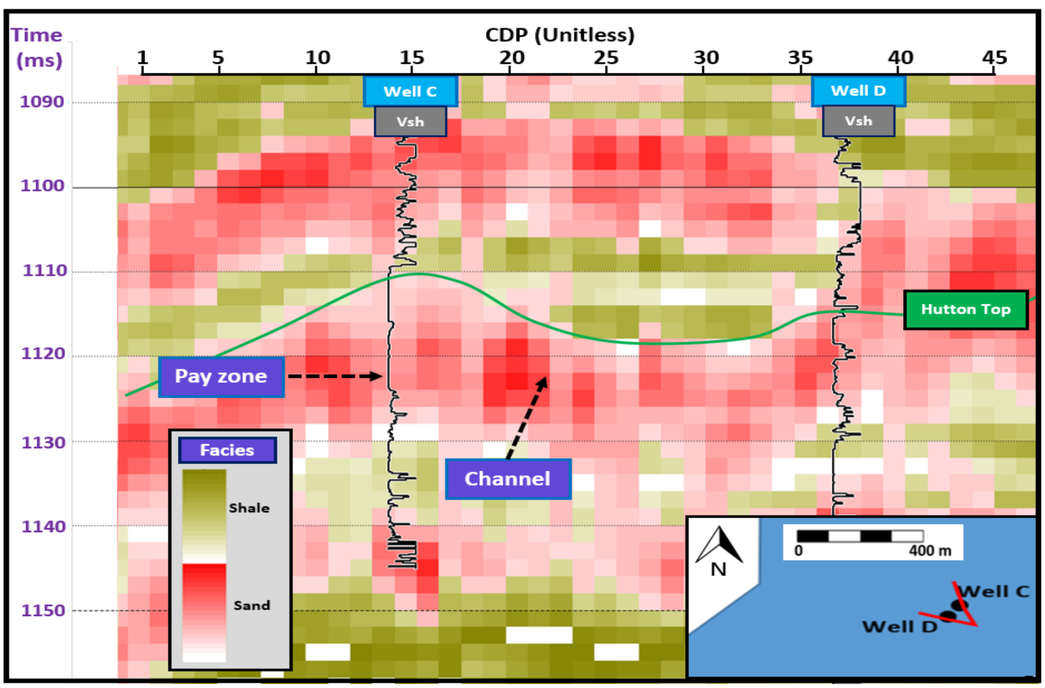

Figure 7.29: Lithofacies distribution along arbitrary line passing through Well C, proposed channel and Well C after applying Bayesian classification.

High-porosity sand, low-porosity sand and shale facies clusters are distributed on the Vp/Vs versus AI crossplot after applying Bayesian classification as shown in Figure 7.30. Table 7.3 shows Gaussian parameters for each cluster. High-porosity sand, low-porosity sand and shale facies are delineated along different arbitrary lines across the 3D seismic volume as shown in Figures 7.31, 7.32 and 7.33. The proposed channel feature exhibits high-porosity sand.

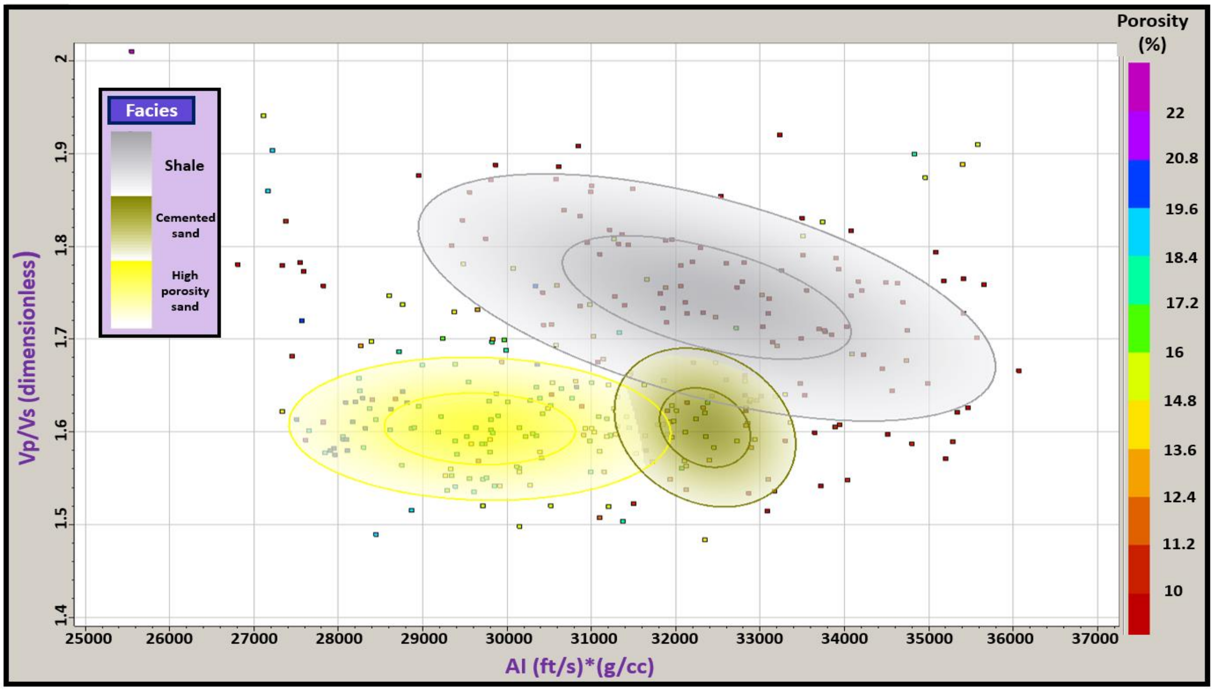

Figure 7.30: Separation between high porosity sand, low porosity sand and shale facies on the Vp/Vs versus AI crossplot after applying Bayesian classification.

Table 7.3: Gaussian parameters for high-porosity sand, low-porosity sand and shale facies.

Gaussian Parameters	High-porosity sand facies	Low-porosity sand facies	Shale facies
AI mean [(ft/s)*(g/cc)]	29671.9	32342.3	32363.1
Vp/Vs mean (Unitless)	1.60	1.60	1.74
AI variance [(ft/s)*(g/cc)]	1.28e+06	289279	2.93e+06
Vp/Vs variance (Unitless)	0.0014	0.0018	0.0044
Covariance [(ft/s)*(g/cc)]	-2.89	-4.90	-63.86

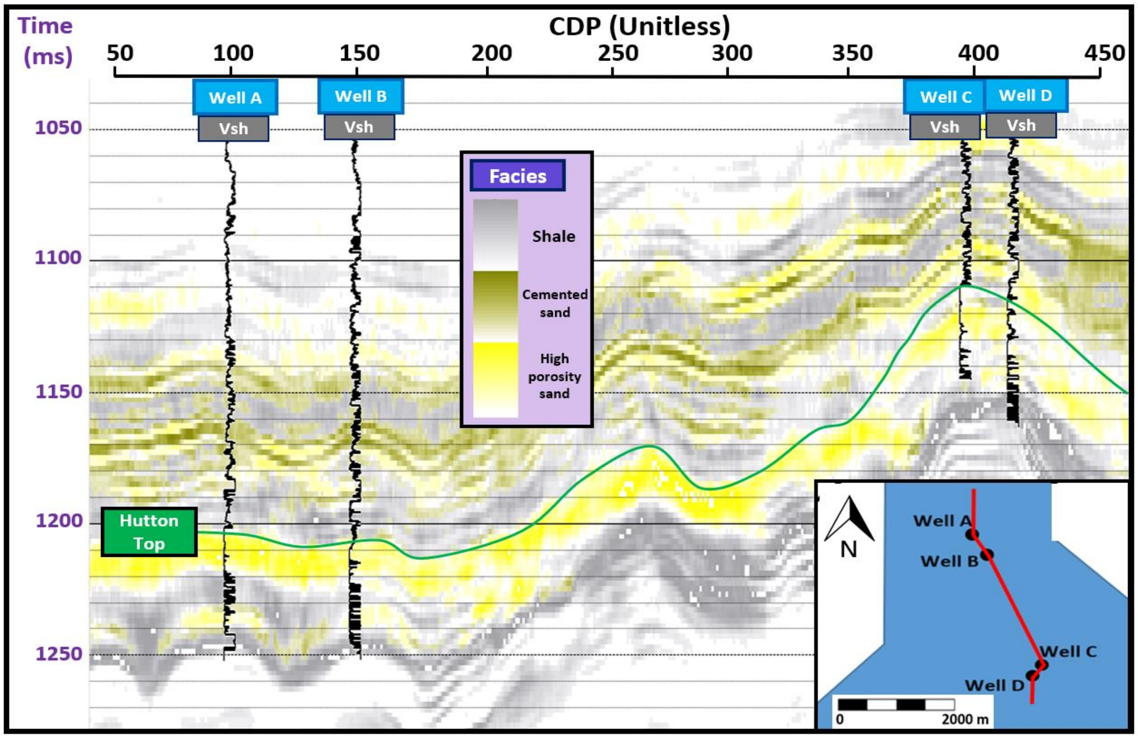

Figure 7.31: High-porosity and low-porosity sand facies distribution along arbitrary line passing through the four wells after applying Bayesian classification.

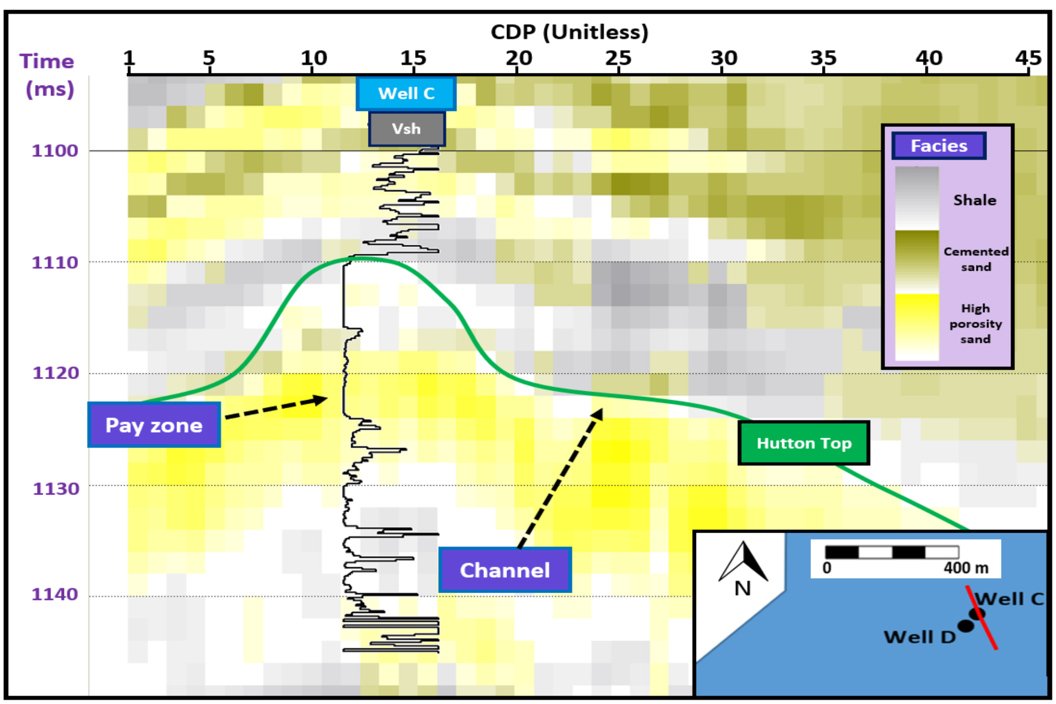

Figure 7.32: High-porosity and low-porosity sand facies distribution along Well C and proposed channel after applying Bayesian classification.

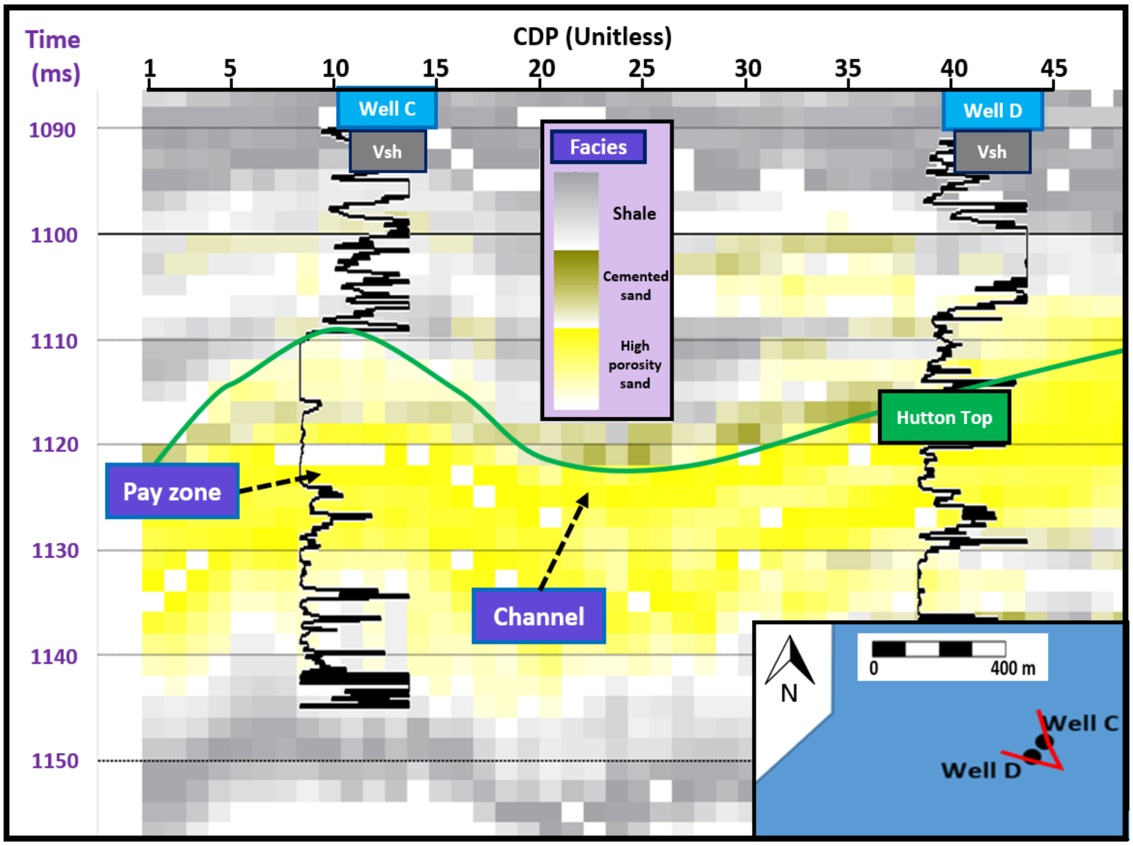

Figure 7.33: High-porosity and low-porosity sand facies distribution along Well C, proposed channel and Well D after applying Bayesian classification.

7.2.2. Probabilistic pore-fluid discrimination

After applying Bayesian classification, high-probability oil sand, brine-sand and shale facies clusters on the Vp/Vs versus AI crossplot are shown in Figure 7.34. Table 7.4 shows Gaussian parameters for each cluster. To address the pore fluid distribution over the 3D seismic volume, high-probability oil and brine-sand facies are delineated along different arbitrary lines as shown in Figures 7.35, 7.36 and 7.37. The high probability oil-sand facies are distributed along Well A, Well B and the channel. However, there is no oil sand facies evident at Well C. This result indicates the robustness of Bayesian classification in delineating the high probability cluster since Well C has high water saturation (Sw=60%) which may be non-commercial. Thus, drilling at the channel location, which has a high-probability oil classification, may be a better drilling location. This matches with the acoustic impedance gradual increase from the channel to Well C as observed from previous results.

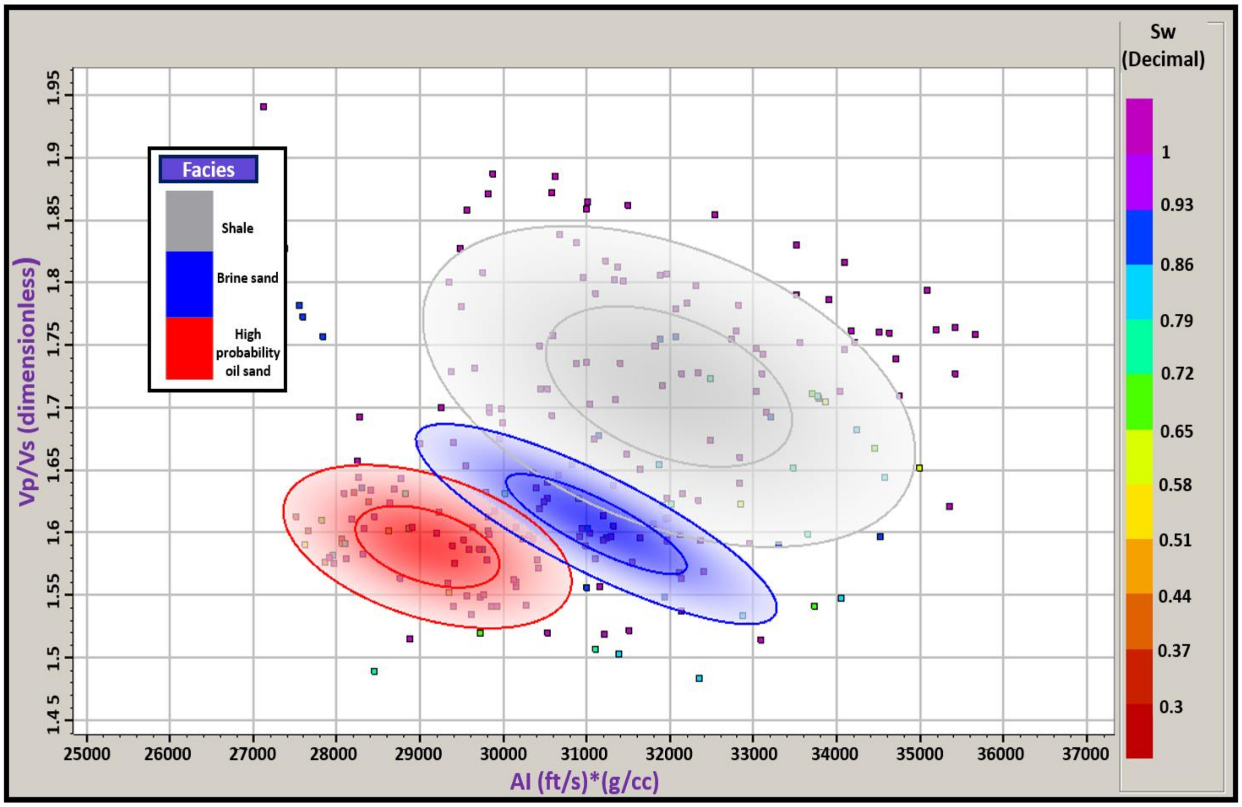

Figure 7.34: Separation between high-probability oil sand, brine sand and shale facies on Vp/Vs versus AI crossplot after applying Bayesian classification.

Table 7.4: Gaussian parameters for high-probability oil, brine-filled sandstone, and shale facies.

Gaussian Parameters	High-probability oil sand facies	Brine sand facies	Shale facies
AI mean [(ft/s)*(g/cc)]	29026.6	31566.4	31794.4
Vp/Vs mean (Unitless)	1.59	1.62	1.74
AI variance [(ft/s)*(g/cc)]	771538	1.05e+06	4.93e+06
Vp/Vs variance (Unitless)	0.00069	0.00057	0.0019
Covariance [(ft/s)*(g/cc)]	-6.66	-13.78	-27.29

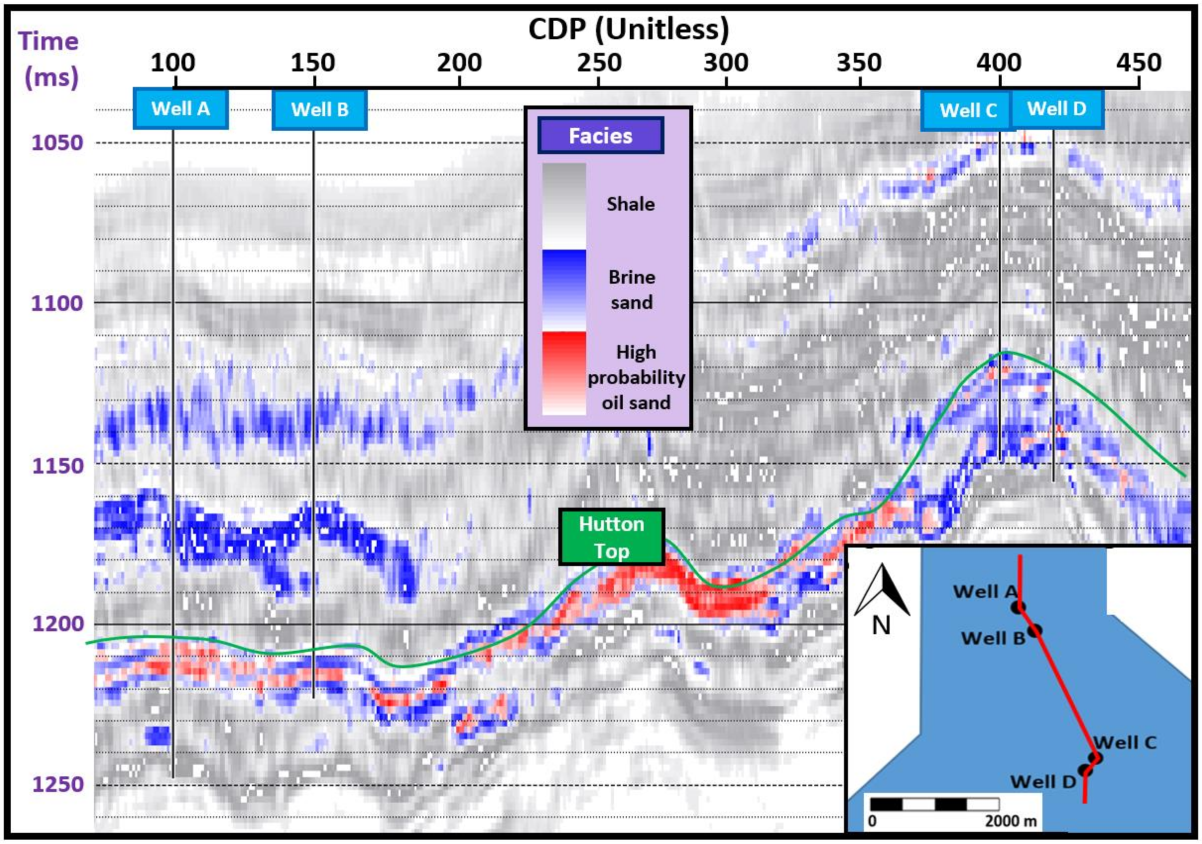

Figure 7.35: High-probability oil and brine-sand facies distribution along an arbitrary line passing through the four wells after applying Bayesian classification.

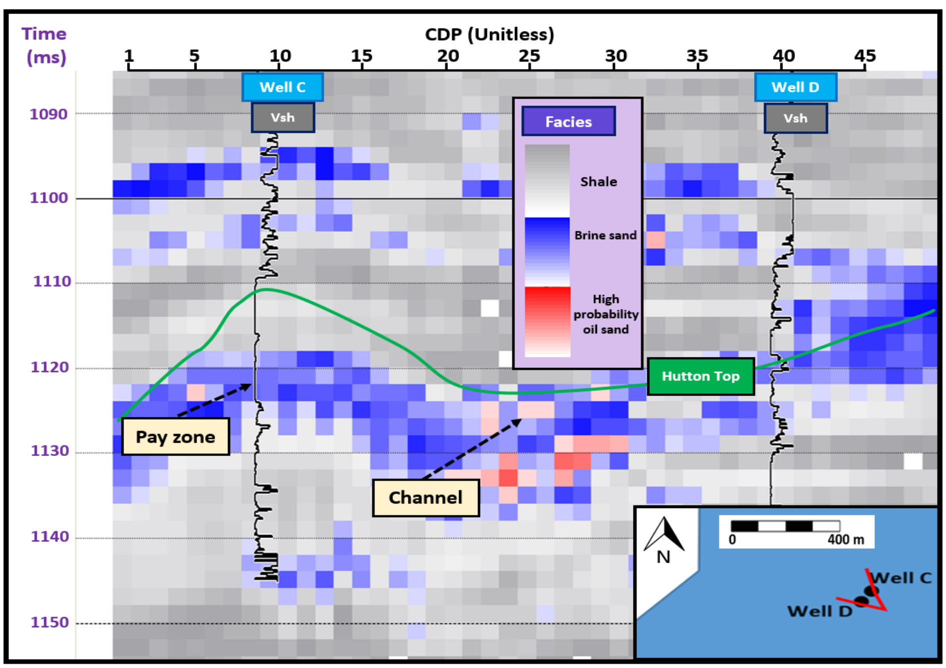

Figure 7.36: High-probability oil and brine-sand facies distribution along an arbitrary line passing through Well C, the channel and Well D after applying Bayesian classification.

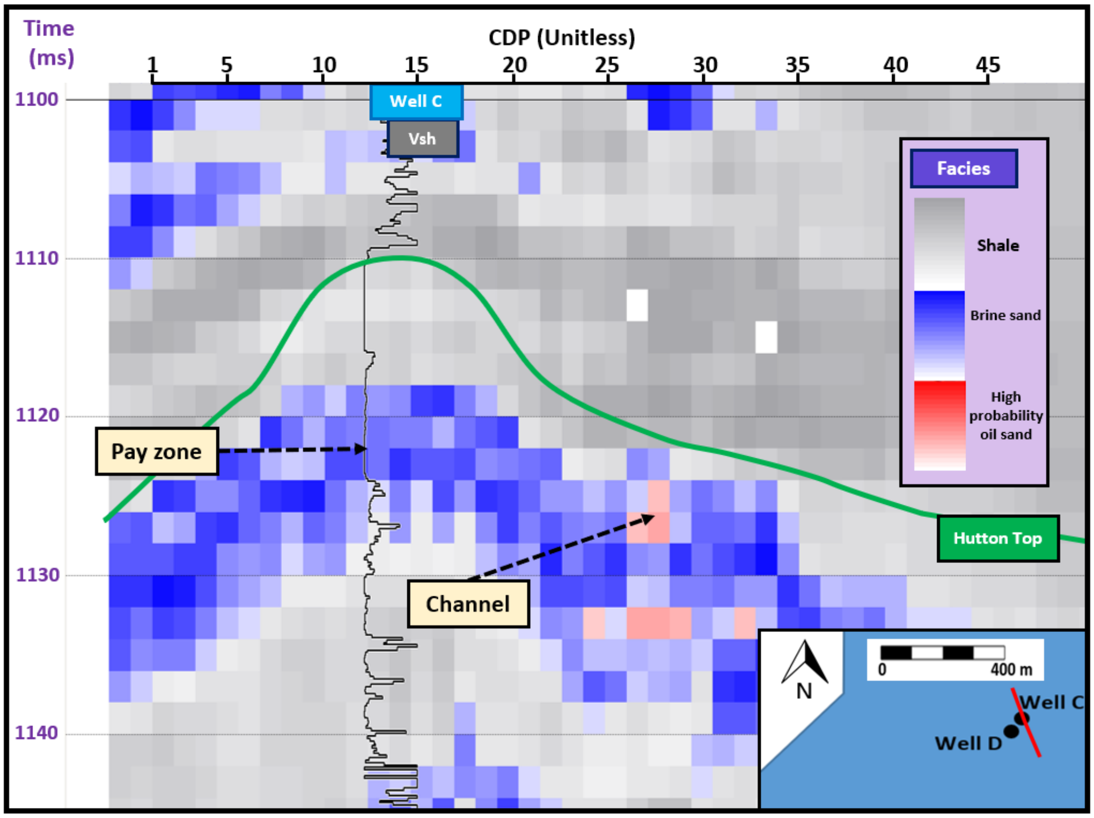

Figure 7.37: High-probability oil and brine-sand facies distribution along an arbitrary line passing through Well C and the channel after applying Bayesian classification.

Chapter 8

Facies and Rock Properties Prediction Using Machine Learning

There are two types of machine learning, supervised and unsupervised as shown in Figure 8.1. In supervised machine learning, facies are predicted using labeled data. Input data (x) consisting of seismic attributes extracted at well locations, is crossploted against output data (y) represented by well logs of labeled information. Then, regression and classification techniques are applied to find a relation between the input and output data. This is called training. After training, the algorithm is validated with well logs that are not used in the training. Once validation is achieved with small validation error, facies are predicted between wells depending on the established relationship between input and output data. In unsupervised machine learning, only input unlabeled data represented by seismic data, are used to predict patterns of similar attribute characteristics. In this research study, supervised and unsupervised machine learning were used to address facies distribution over study area and to compare their results with physics guided methods discussed in previous chapters.

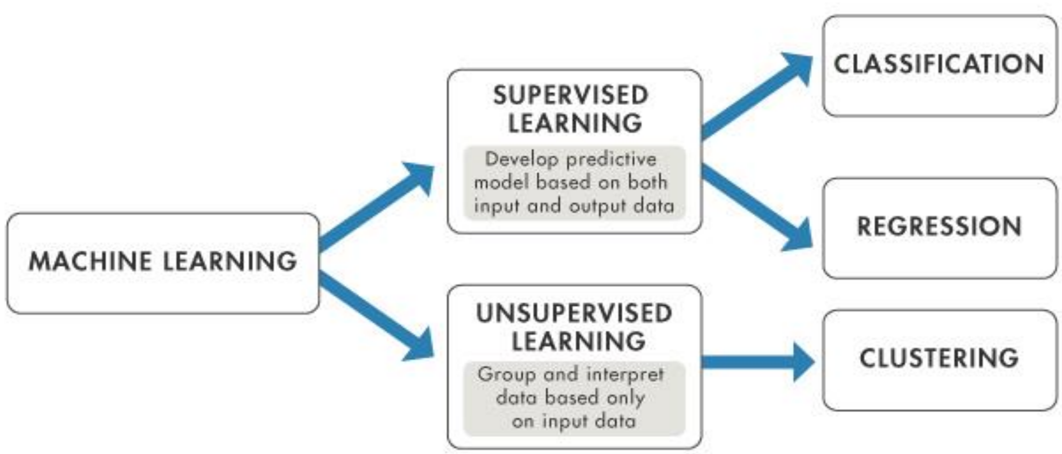

Figure 8.1: Types of machine learning (modified from Mathworks, 2019).

8.1. Supervised machine learning

Multiattribute analysis using neural networks has been used to statistically estimate petrophysical properties from seismic data. In this research study, the objective is to predict a porosity cube from 3D seismic data. In the supervised machine learning, I used input data (x) represented by extracted seismic attributes, and output data (y) represented by porosity well logs. Selecting appropriate seismic attributes is regarded as a starting step for conducting supervised machine learning. Stepwise regression analysis, introduced by (Draper and Smith, 1966), was conducted to select a seismic attribute set that best predicts the target log. It arranges attributes in a descending order according to their contribution. Then, cross-validation was used to divide the data into two datasets (a training dataset and a validation dataset). For the training dataset, supervised machine learning using neural networks was conducted to find a nonlinear operator between the input data (x) and the output data (y). Least square optimization was used in training to estimate weight coefficients (Kabaka, 2018). Once the nonlinear operator was established, the training model was applied to predict the 3D porosity cube from the 3D seismic volume. When it comes to the validation dataset, it was used to evaluate the degree of fitting after crossplotting actual and predicted porosity. To accurately estimate porosity, the process was run iteratively changing the seismic attributes used until validation error was minimized.

One of the drawbacks of using multiattribute statistical analysis is that input logs and seismic attributes have different resolutions. This limitation cannot be just solved by smoothing well logs that have higher resolution than seismic attributes when using more than one seismic attribute with different resolutions, and because the smoothed logs may not resolve the layer of interest. To solve this problem, a deconvolution operator for each attribute that assumes that each sample in the log is related to a group of samples can be used (Hampson et al., 2001) as illustrated in Figure 8.2.

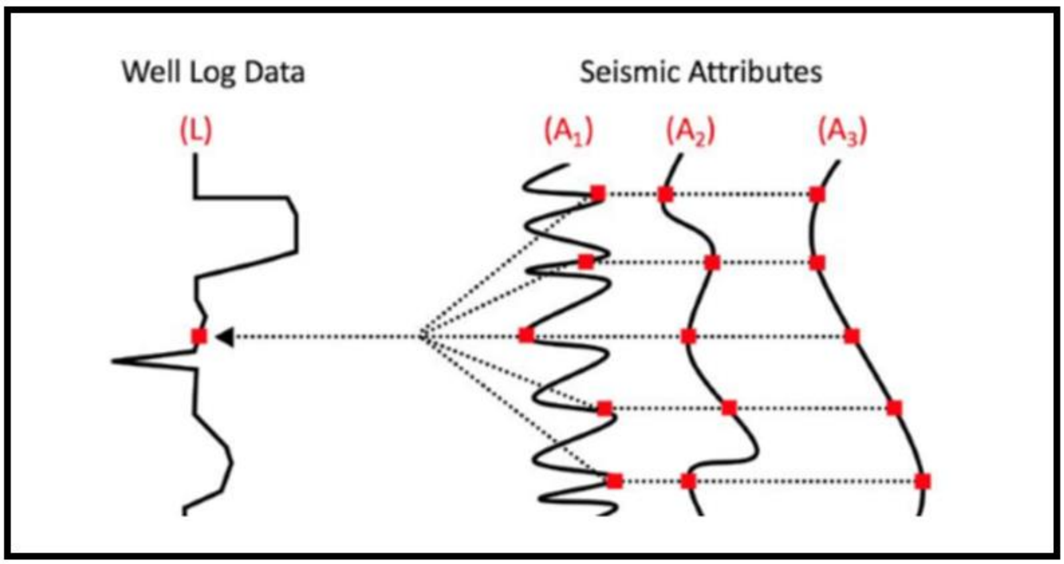

Figure 8.2: Each sample in well log is related to a weighted group of samples in seismic attributes using a multi-channel deconvolution operator. Modified from (Hampson et al., 2001; and Kabaka, 2018).

The Multilayer Feedforward Neural Network (MLFN) was used by Yao and Liu (1998) to predict log properties. As described in Figure 8.3, MLFN consists of different layers; input layer, hidden layer and output layer (Hampson et al., 2001). The layers consist of nodes that have assigned weights. The input layer nodes represent seismic attributes that are used to predict one property represented by one node in the outer layer.

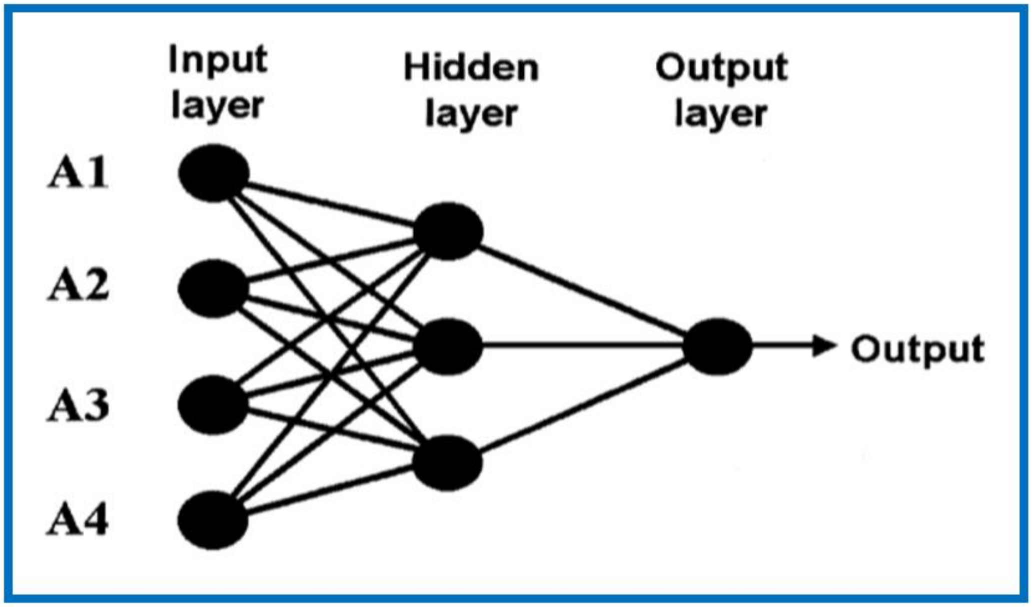

Figure 8.3: Multilayer Feedforward Neural Network. Modified from (Hampson et al., 2001).

A better neural network approach called the Probabilistic Neural Network (PNN) was introduced by Masters (1995) and Specht (1990 and 1991). In PNN, the target log value (L) is estimated by the following equations:

$$\hat{L}(x) = \frac{\sum_{i=1}^{n} L_i \exp(-D(x, x_i))}{\sum_{i=1}^{n} \exp(-D(x, x_i))} \quad \text{, and} \qquad (8\text{-}1)$$

$$D(x, x_i) = \sum_{j=1}^{3} \left(\frac{x_j - x_{ij}}{\sigma_j} \right)^2. \qquad (8\text{-}2)$$

where, $D(x, x_i)$ is the distance between the input point (x) and the training points (x_i), and σ_j is a smoothing parameter for each attribute.

After conducting multiattribute analysis using regression and neural networks, an F-test was conducted to address the fit between the statistical model and the data. The F-test is define by:

$$F = \frac{explained\ variance}{unexplained\ variance},$$

and computed using:

$$F = \frac{[R^2 / K]}{[(1-R^2)/(n-K-1)]} , \quad (8\text{-}3)$$

where, *K* is the number of parameters, *n* is the number of data points, and *R* is the correlation coefficient. An F-value less than 1 indicates that the correlation cannot be assumed to be statistically significant.

High-frequency and conventional seismic data were incorporated in the multiattribute analysis. Because one of the main objectives of this research study is to address the prediction accuracy of different methods, external attributes such as inversion results were not incorporated into the multiattribute analysis.

8.1.1. Porosity estimation

8.1.1.1. Broadband seismic data

For porosity estimation, porosity logs at the four wells and 28 seismic attributes extracted from the high-frequency far-offset stack were used in a multiattribute analysis process. Validation error decreases as seismic attributes are added to the prediction process, but increases at the eighteenth seismic attribute, as illustrated in Figure 8.4. To achieve more reliable predictions, only seventeen seismic attributes were selected. The selected attributes are shown in Table 8.1. Using these attributes in multiple regression, actual and predicted porosity are crossploted at the four wells as illustrated in Figure 8.5 where correlation coefficient is 0.686 and estimated error is 3.05% porosity.

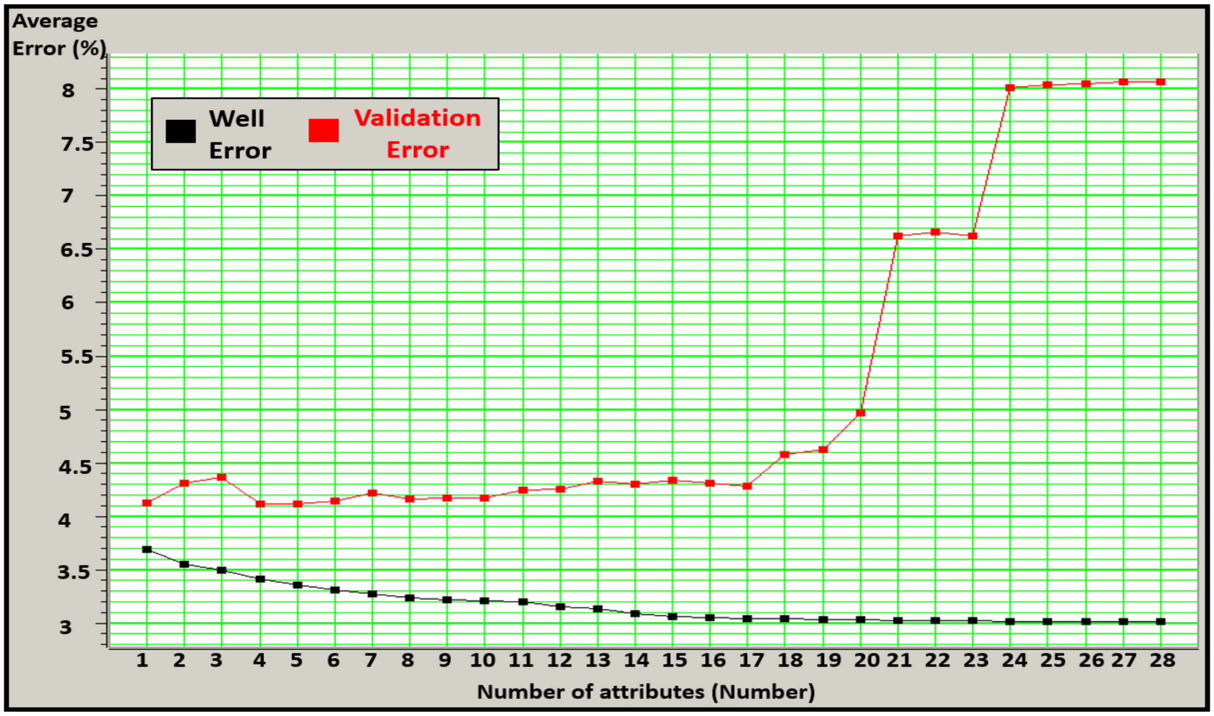

Figure 8.4: Average errors versus number of attributes used for predicting porosity. Training errors are represented by black dots and validation errors are represented by red dots.

Because of high error using multiple regression, the seismic attributes identified in table 8.1 were incorporated in a probabilistic neural-network (PNN) prediction. Porosity predicted by the PNN has a better linear relation than porosity predictions from multiple regression when crossploted versus measured porosity as shown in Figure 8.6. The correlation coefficient increases to 0.967. An arbitrary line passing through the four wells shows lateral porosity variations (Figure 8.7). There is a significant correlation at the four wells. To address porosity at the proposed channel, the neural network process was repeated by taking out Well C from training and using the other three wells to evaluate how well the neural network method predicts the channel feature. An arbitrary line passing through Well C, the channel and Well D is shown in

Figure 8.8. The channel porosity ranges from 13% to 15%. Porosity varies continuously from the channel to Well C. On the other hand, porosity decreases toward Well D which indicates facies change toward it.

Table 8.1: Seismic attributes used in multiple-regression prediction of porosity using high-frequency seismic data.

No	**Seismic attributes**	**Training error (%)**	**Validation error (%)**
1	Filter 5/10-15/20	3.70	4.13
2	Average Frequency	3.56	4.31
3	X-Coordinate	3.50	4.37
4	Y-Coordinate	3.41	4.12
5	Filter 25/30-35/40	3.36	4.12
6	Filter 45/50-55/60	3.32	4.15
7	Integrated Absolute Amplitude	3.27	4.22
8	Amplitude Weighted Frequency	3.24	4.17
9	Filter 15/20-25/30	3.22	4.17
10	Second Derivative Instantaneous Amplitude	3.21	4.17
11	Integrate	3.20	4.25
12	Instantaneous Phase	3.16	4.26
13	Filter 35/40-45/50	3.14	4.33
14	Filter	3.10	4.31
15	Quadrature Trace	3.06	4.35
16	Amplitude Weighted Phase	3.06	4.31
17	Cosine Instantaneous Phase	3.05	4.29

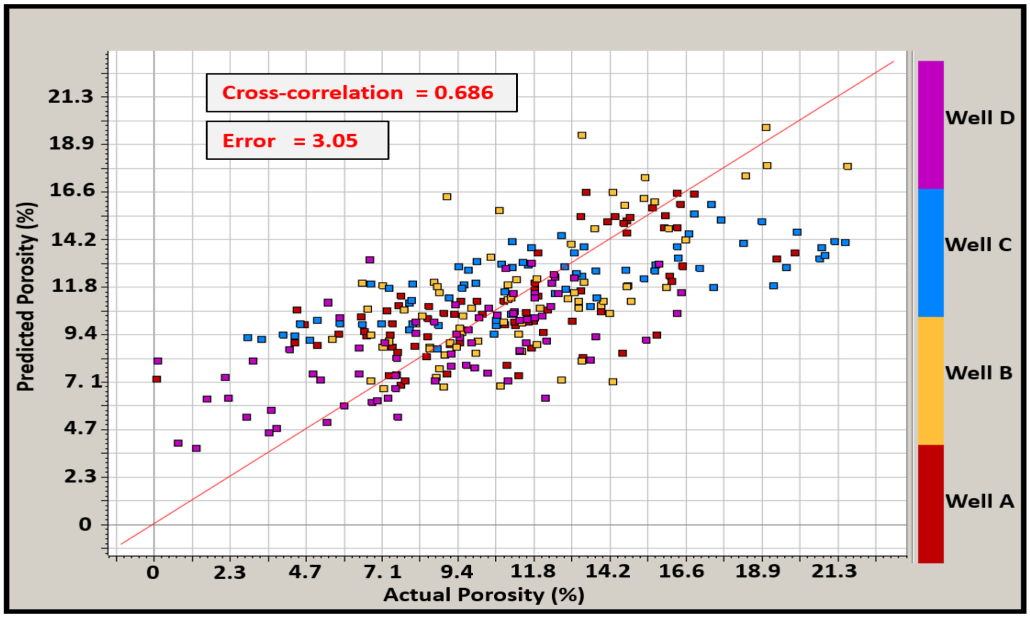

Figure 8.5: Predicted porosity versus measured porosity crossplot at the four wells using multiple regression.

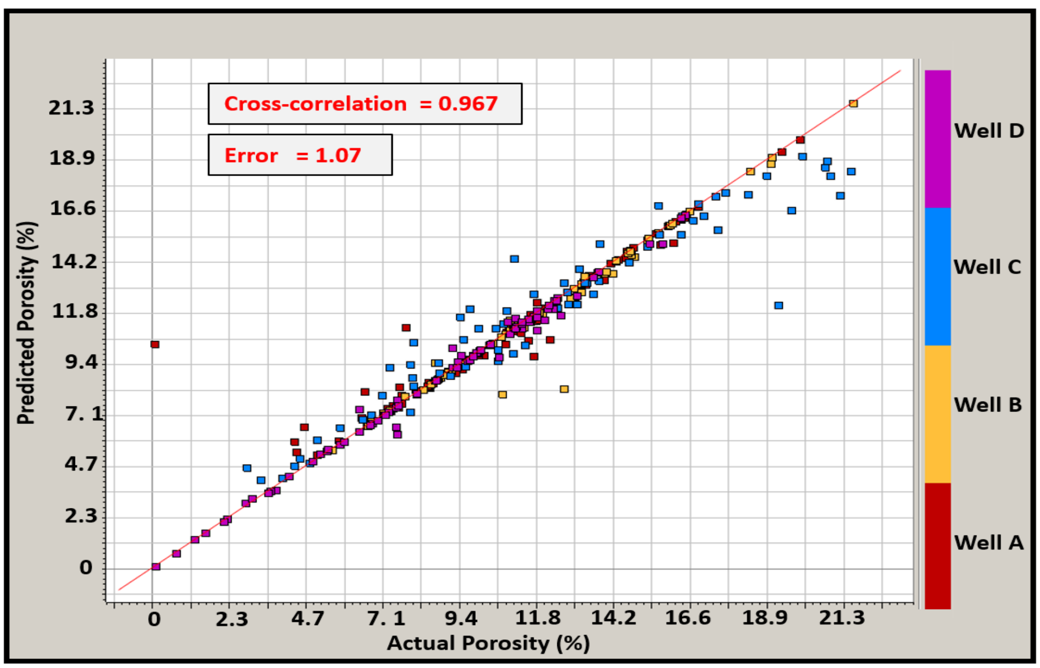

Figure 8.6: Predicted porosity versus measured porosity at the four wells using a probabilistic neural network.

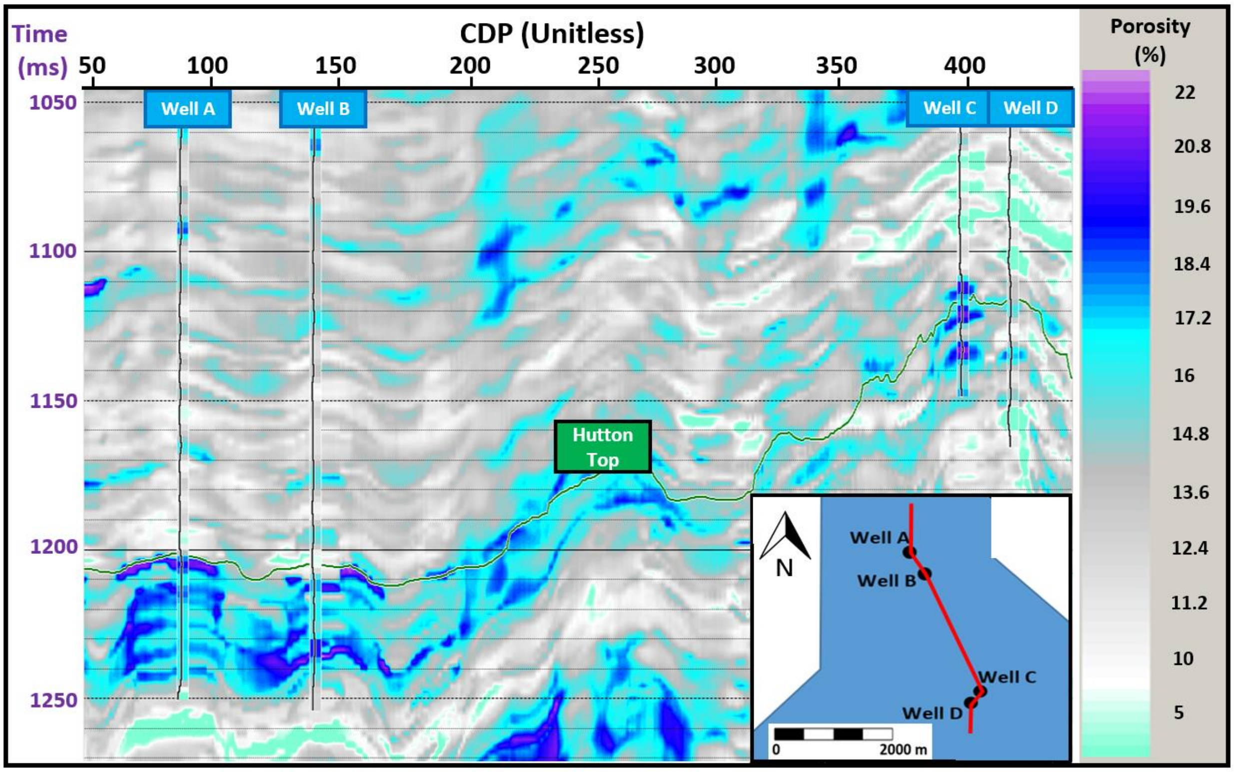

Figure 8.7: Arbitrary line passing through the four wells shows porosity estimated from neural network analysis with high-frequency seismic data.

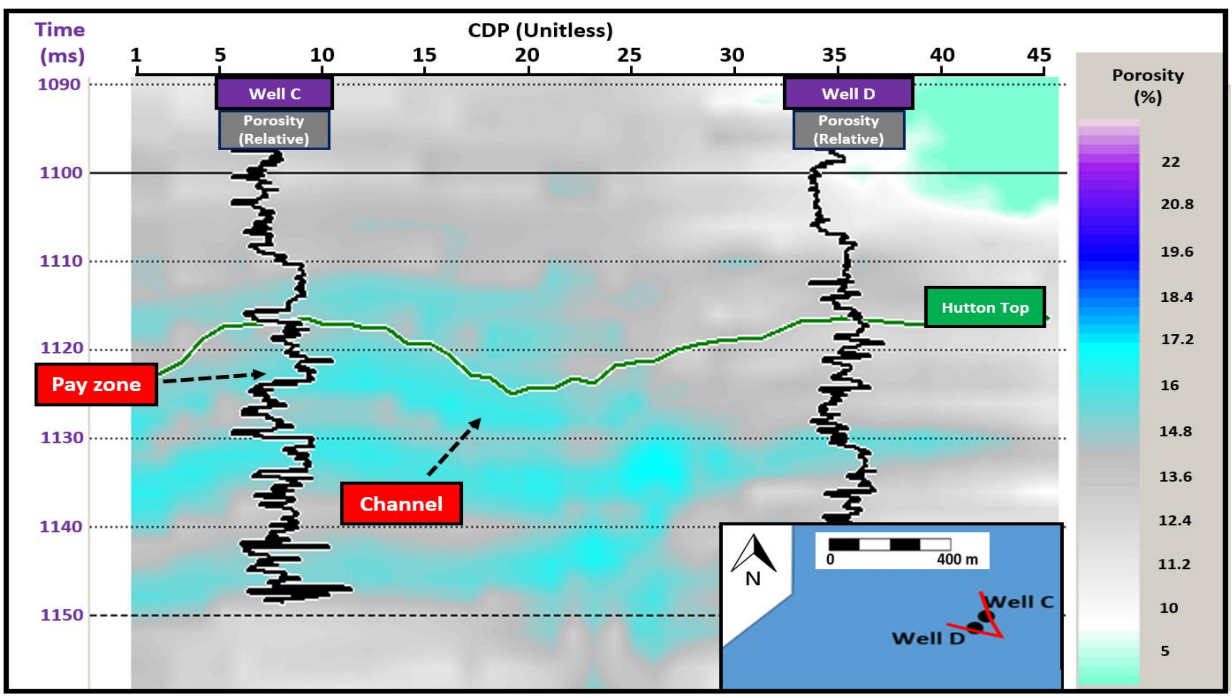

Figure 8.8: Arbitrary line passing through Well C, channel and Well D. Well C is used as a blind validation well to test porosity estimates.

Since the number of attributes used in multiattribute analysis are 17, number of data points are 200 and correlation coefficient is 0.686, the F-value was estimated to be 9.5. However, F-value increases to 154 after incorporating selected seismic attributes in the neural network process.

8.1.1.2. Conventional seismic data

To compare between conventional and high-frequency seismic data, porosity was also estimated at the four wells and 5 seismic attributes extracted from the original far-offset stack. Validation error decreases with increasing number of seismic attributes, but it begins to increase at the sixth seismic attribute as illustrated in Figure 8.9. That is why only five seismic attributes were selected. The selected seismic attributes are shown in Table 8.2. Actual and predicted porosity are crossplotted at the four wells as illustrated in Figure 8.10 where the correlation coefficient is 0.53 and estimated error is 3.56% porosity. Using a probabilistic neural network, the correlation coefficient increases to 0.96 and estimated error is 1.15% porosity as shown in Figure 8.11. An arbitrary line passing through all wells is shown in Figure 8.12 to illustrate porosity prediction from conventional seismic data.

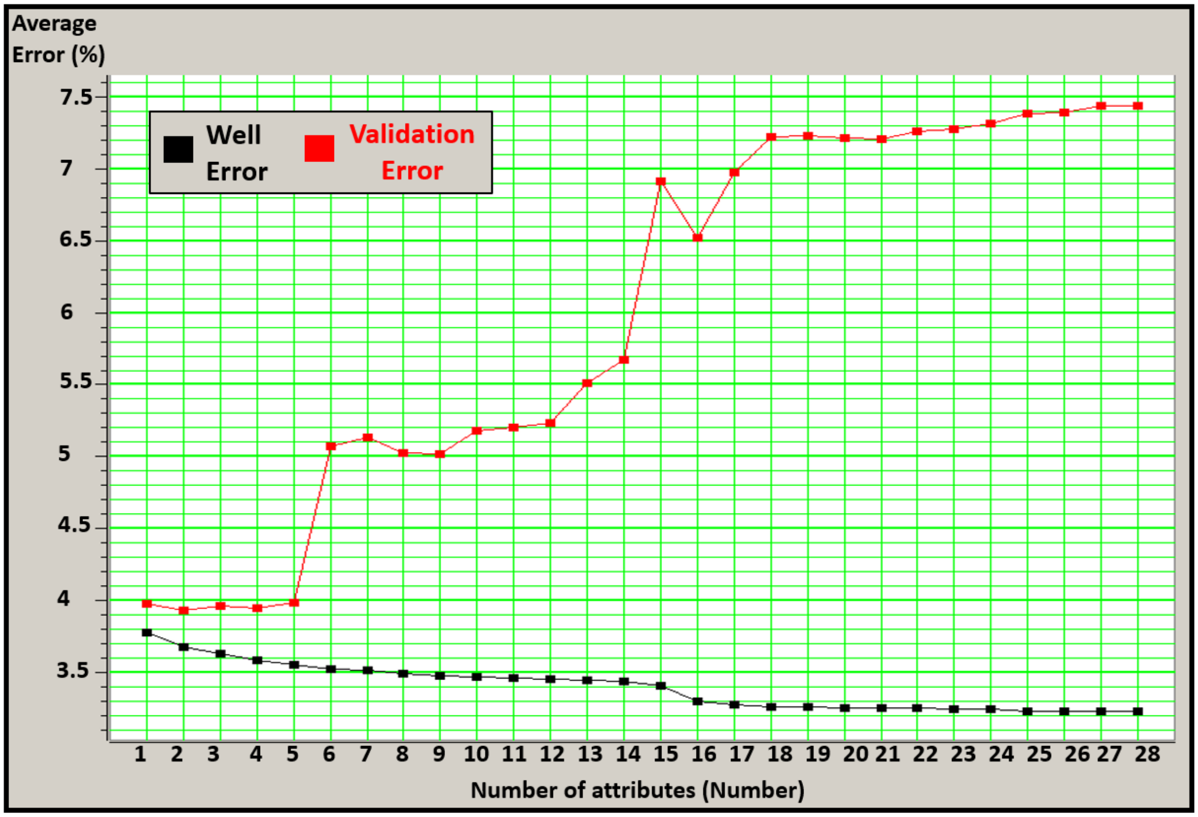

Figure 8.9: Average errors versus number of attributes used for predicting porosity.

Table 8.2: Seismic attributes used in multi attribute analysis to original seismic data.

No	Seismic attributes	Training error (%)	Validation error (%)
1	Filter 5/10-15/20	3.78	3.98
2	Derivative Instantaneous Amplitude	3.68	3.94
3	Filter 45/50-55/60	3.63	3.96
4	Integrate	3.59	3.95
5	Filter 55/60-65/70	3.56	3.99

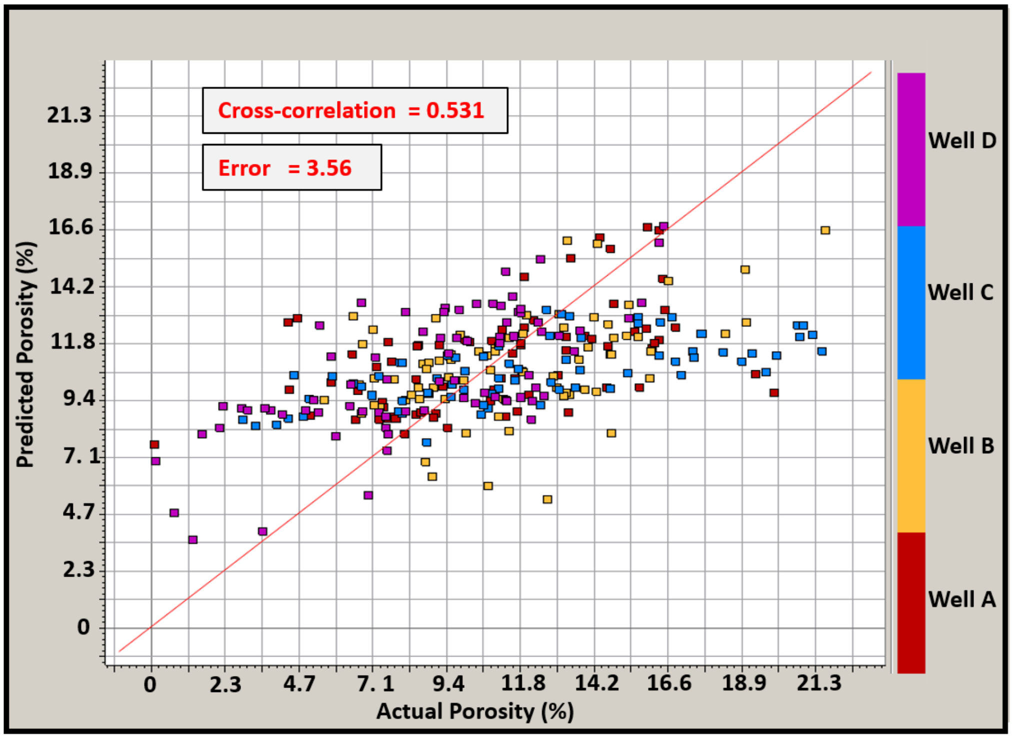

Figure 8.10: Predicted porosity versus measured porosity crossplot at the four wells using multiple regression.

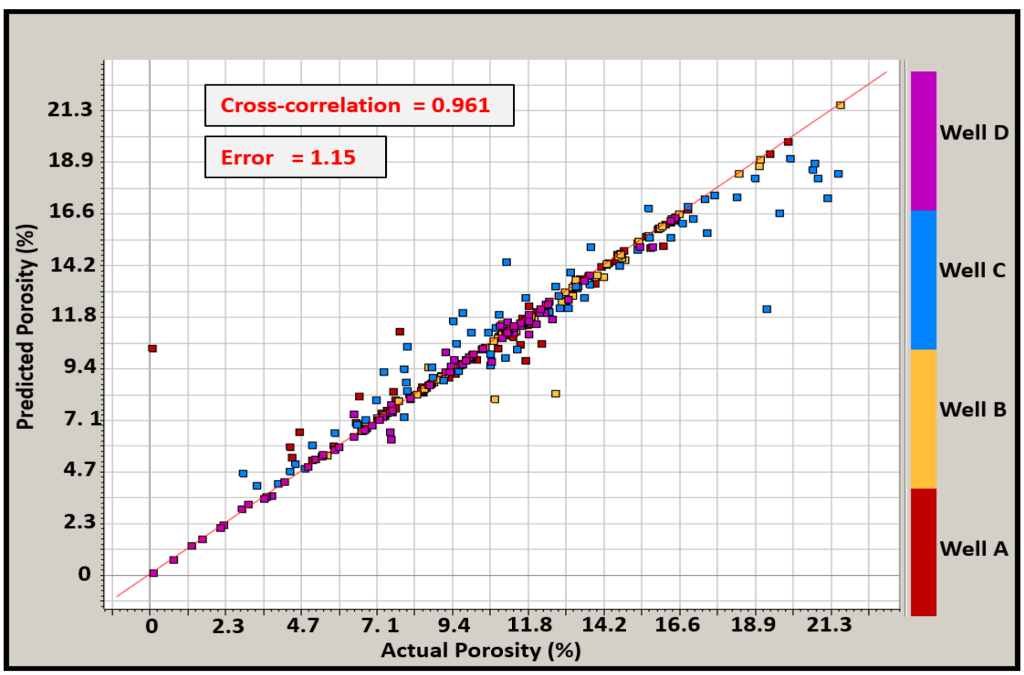

Figure 8.11: Predicted porosity versus measured porosity crossplot at the four wells using a probabilistic neural network.

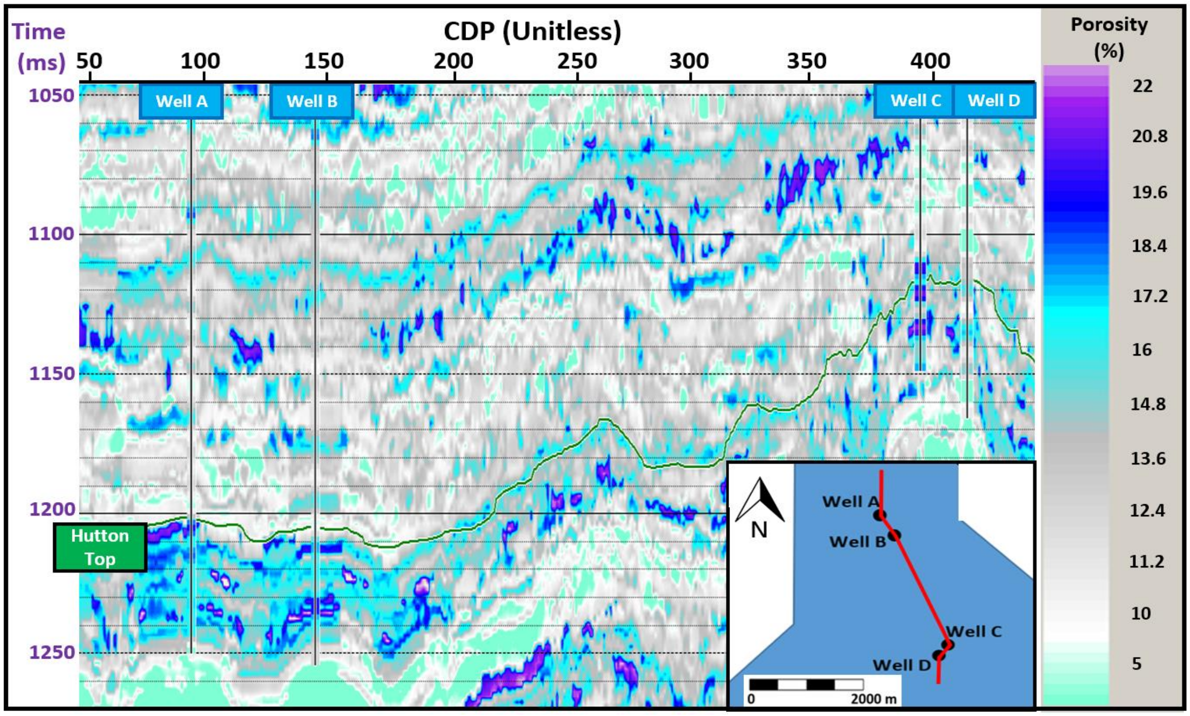

Figure 8.12: Arbitrary line passing through the four wells shows porosity estimated from neural network analysis to conventional seismic data.

Estimated F-test after conducting multiattribute analysis for conventional seismic data, is 7.297 which increases to 478.5 after incorporating selected seismic attributes in the neural network process.

8.1.1.3. Confusion matrix

Confusion matrices were used to compare between high-frequency seismic data and conventional seismic data in porosity prediction accuracy. First of all, the actual porosity log was subdivided into 3 classes, low porosity sand (less than 13%), medium porosity sand (13% -16%) and high porosity sand (more than 16%). Then, confusion matrices were conducted to compare porosity predictions at Well C with actual porosity of the Well using 247 samples chosen within the Hutton Sandstone Formation and 20 m above and below it. Confusion matrix results are shown in Figure 8.13. High-frequency data has much better accuracy than conventional seismic data. In addition, accuracy decreases with less training data which indicates that multiattribute analysis using neural network needs more training data to reach high accuracy prediction.

Accuracy (73.5%)		Predicted		
		High porosity	Medium porosity	Low porosity
Actual	High porosity	79	25	3
	Medium porosity	3	14	3
	Low porosity	6	24	88

High frequency seismic data
(Training data : 4 wells)

Accuracy (65.1 %)		Predicted		
		High porosity	Medium porosity	Low porosity
Actual	High porosity	72	33	2
	Medium porosity	7	12	2
	Low porosity	8	33	77

Conventional seismic data
(Training data : 4 wells)

Accuracy (44.1%)		Predicted		
		High porosity	Medium porosity	Low porosity
Actual	High porosity	0	1	106
	Medium porosity	0	1	21
	Low porosity	0	10	108

High frequency seismic data
(Training data : 3 wells)

Accuracy (42.9%)		Predicted		
		High porosity	Medium porosity	Low porosity
Actual	High porosity	0	22	85
	Medium porosity	0	8	14
	Low porosity	0	20	98

Conventional seismic data
(Training data : 3 wells)

Figure 8.13: Comparison between high-frequency and original seismic data in predicting porosity. Results quality degrades with decreasing training data.

8.1.2. P-impedance estimation

To conduct a comparison between multiattribute analysis and other previous methods used in this research study, some wells were used as blind validation wells and have not incorporated in the analysis. Result quality degrades with decreasing number of wells used.

8.1.2.1. Broadband seismic data

P-impedance logs at Well B and Well D and fifteen seismic attributes extracted from the high-frequency far-offset stack were used in the multiattribute analysis process. Figure 8.14 shows all seismic attributes used in the analysis. Only eight seismic attributes were selected based on minimum validation error and are shown in Table 8.3. Selected seismic attributes were incorporated in probabilistic neural network analysis. Actual and predicted acoustic impedance are crossploted as illustrated in Figure 8.15 where correlation coefficient is 0.926 and estimated error is 880.7 (ft/s*g/cc).

Table 8.3: Seismic attributes used in multi attribute analysis of broadband seismic data.

No	Seismic attributes	Training error [(ft/s)*(g/cc)]	Validation error [(ft/s)*(g/cc)]
1	Average Frequency	1969.68	2437.55
2	Filter 5/10-15/30	1776.38	2337.23
3	Integrated	1686.33	2254.71
4	Integrated Absolute Amplitude	1627.39	1966.76
5	Apparent Polarity	1574.96	1989.51
6	Second Derivative	1517.48	1944.63
7	Instantaneous Frequency	1472.47	1879.07
8	Derivative Instantaneous Amplitude	1439.40	1914.24

An arbitrary line passing through the four wells shows acoustic impedance estimated from neural network analysis using high-frequency seismic data (Figure 8.16). A 10 ms acoustic impedance horizon slice extracted below the Hutton Formation top is shown in Figure 8.17. Low acoustic impedances are distributed over high structures.

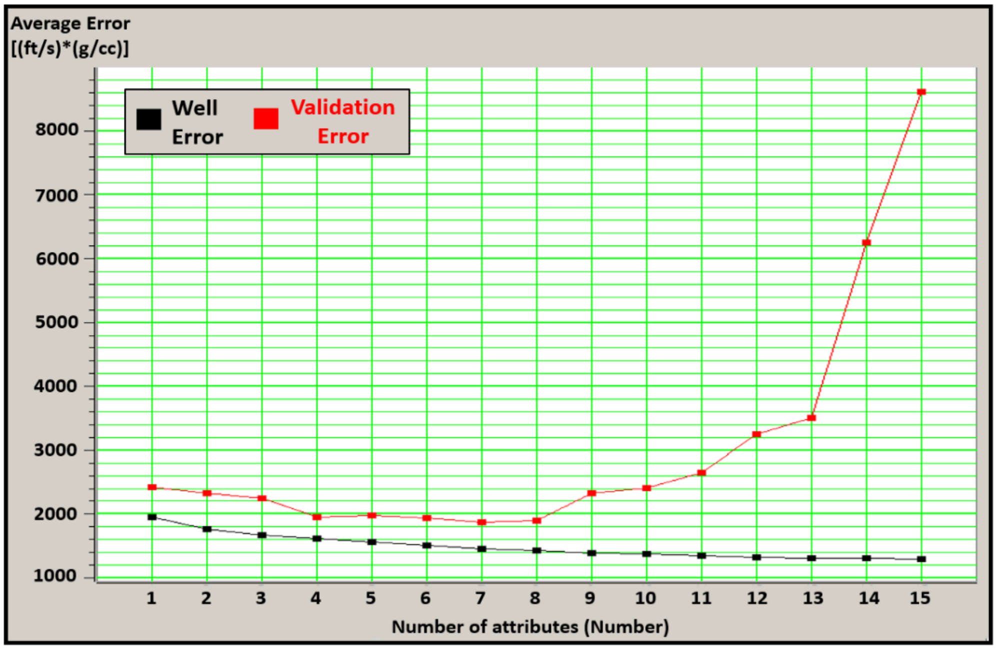

Figure 8.14: Average errors versus number of attributes used for predicting P-impedance.

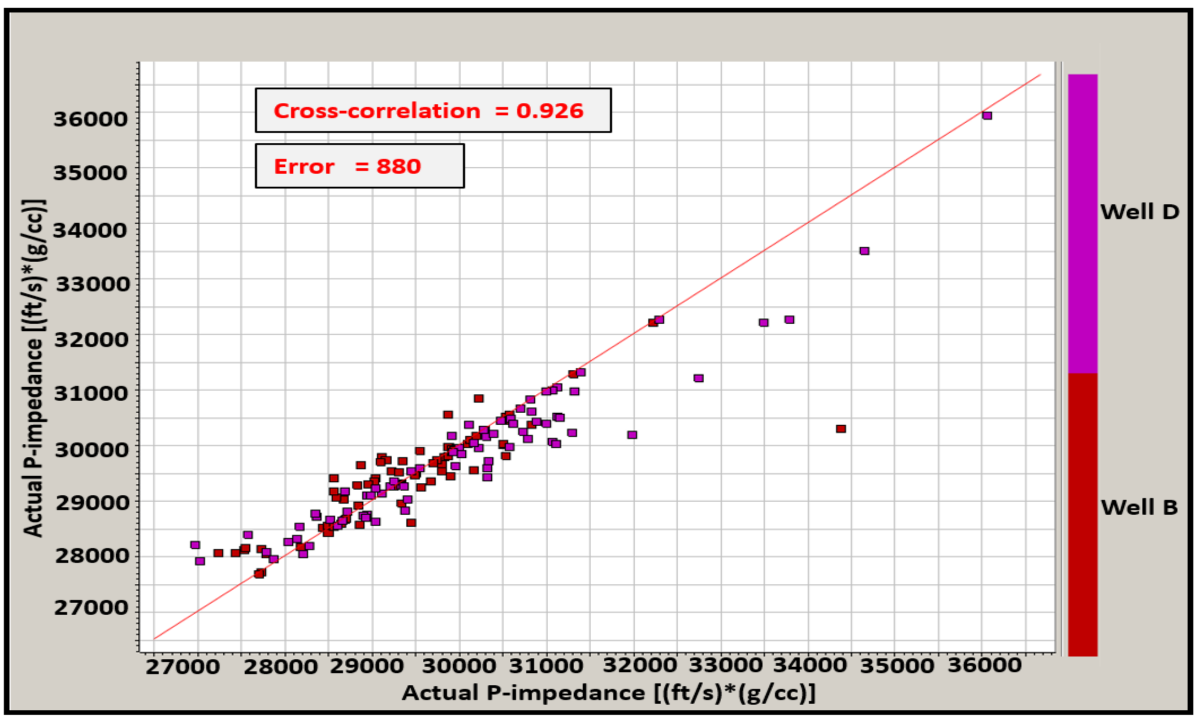

Figure 8.15: Predicted acoustic impedance versus measured acoustic impedance using a probabilistic neural network analysis to broadband seismic data.

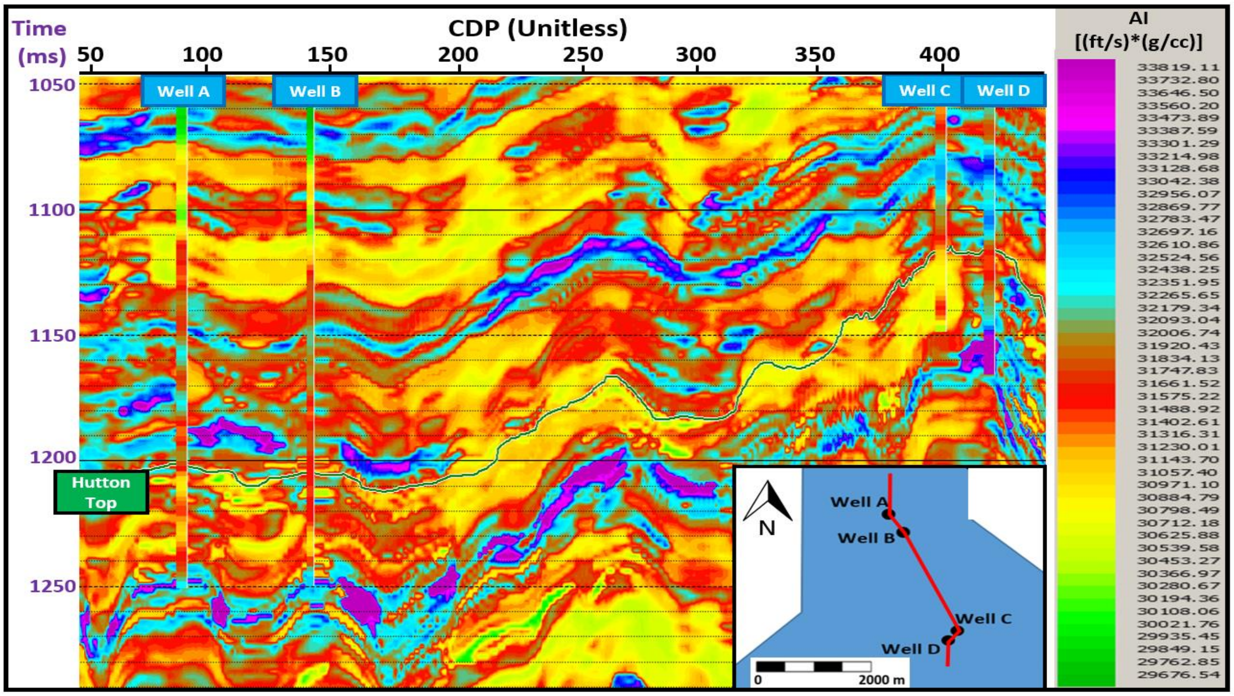

Figure 8.16: Arbitrary line passing through the four wells shows acoustic impedance estimated from neural network analysis to high-frequency seismic data.

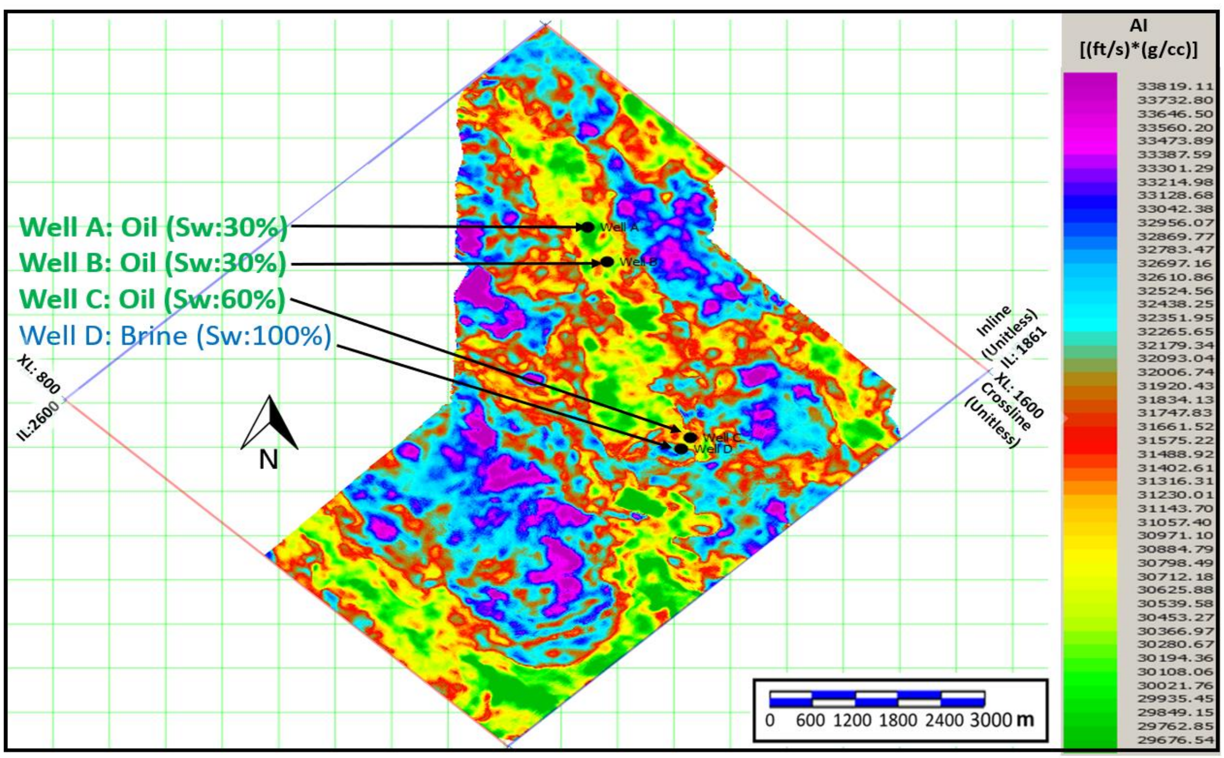

Figure 8.17: Horizon slice shows P-impedance distribution predicted by using high-frequency seismic data.

8.1.2.2. Conventional seismic data

Conventional seismic data is also incorporated in neural network analysis to predict acoustic impedance. Two wells were used in the analysis while the other two wells were kept as test wells. P-impedance logs at Well A and Well B and four seismic attributes extracted from conventional far-offset stack were used in the multiattribute analysis process. Figure 8.18 shows all seismic attributes used in the analysis. Only seven seismic attributes were selected based on minimum validation error and are shown in Table 8.4. Actual and predicted acoustic impedance are crossploted as illustrated in Figure 8.19 where correlation coefficient decreases to 0.789 and estimated error increases to be 941.4 (ft/s*g/cc) when compared with analysis of high-frequency seismic data. An arbitrary line passing through the four wells shows P-impedance estimated from neural network analysis applied to conventional seismic data is shown in Figure 8.20. The result quality degrades which is probably attributed to using insufficient training data or possibly possibly inadequate resolution of the original seismic data.

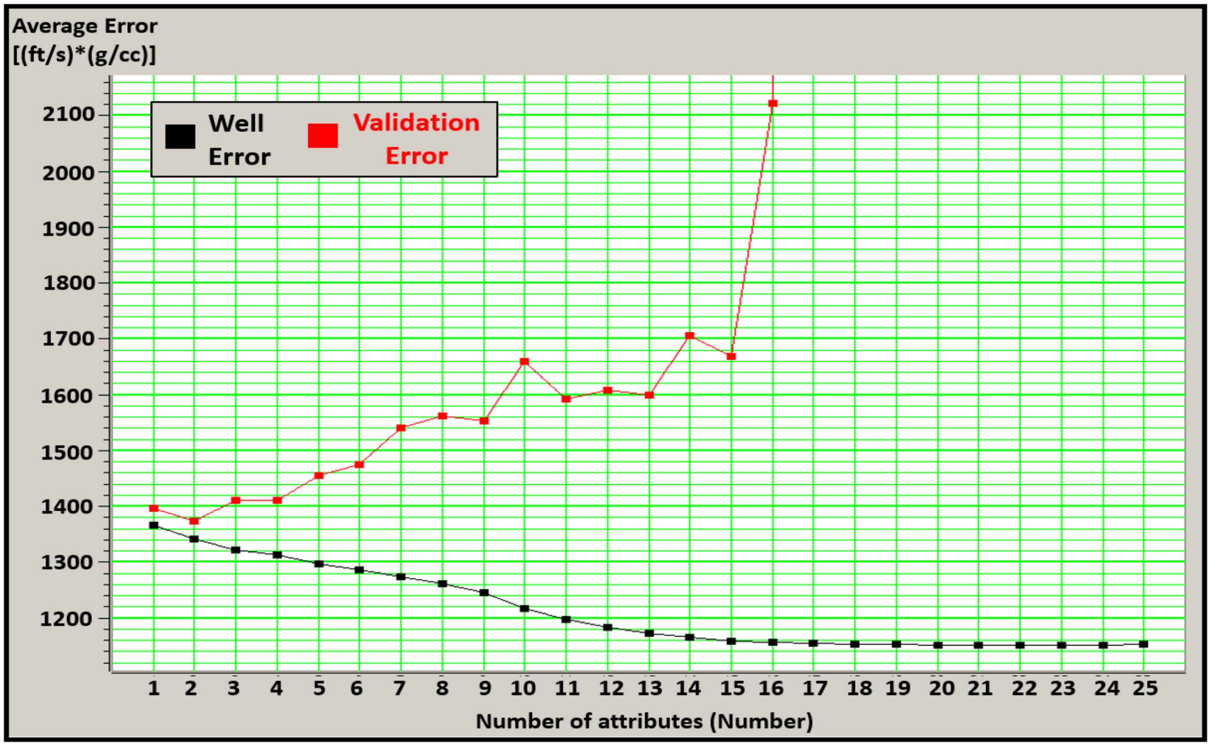

Figure 8.18: Average errors versus number of attributes used for predicting acoustic impedance.

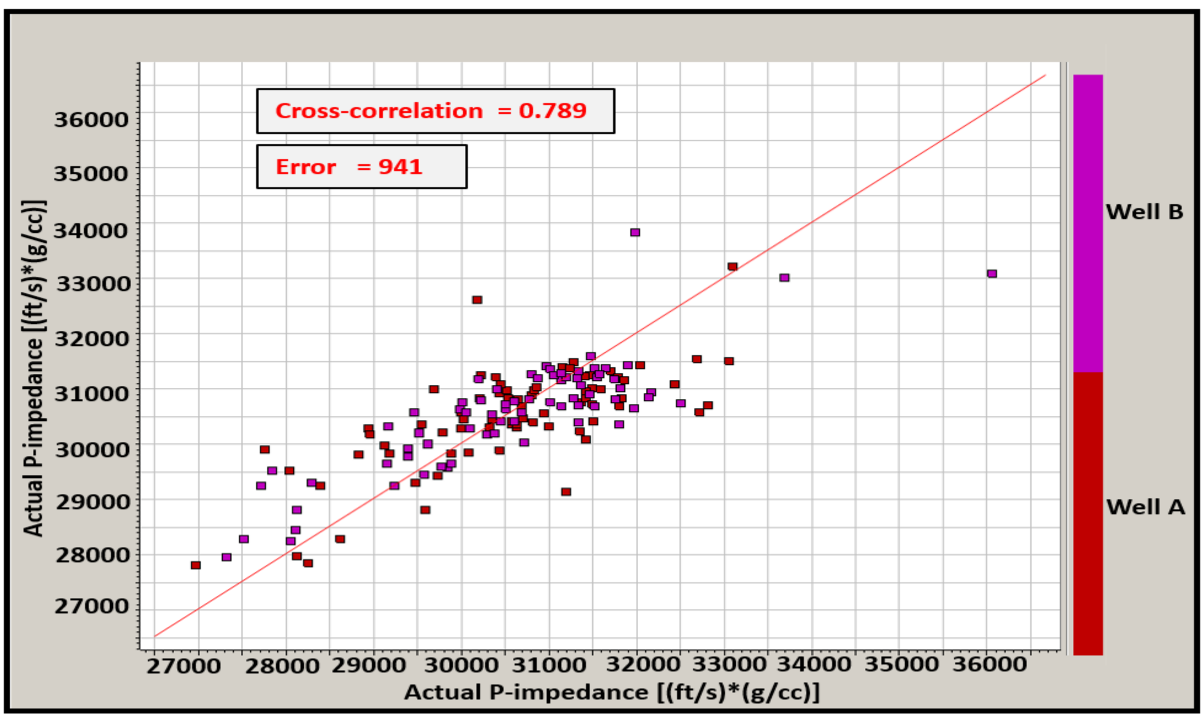

Figure 8.19: Predicted acoustic impedance versus measured acoustic impedance after applying the probabilistic neural network to broadband seismic data.

Table 8.4: Seismic attributes used in multi attribute analysis of conventional seismic data.

No	Seismic attributes	Training error **[(ft/s)*(g/cc)]**	Validation error **[(ft/s)*(g/cc)]**
1	Integrate	1368	1396
2	Cos instantaneous phase	1344	1372
3	Filter 35/40-45/50	1324	1400
4	Filter 5/20-25/30	1318	1417
5	Amplitude Envelope	1309	1430
6	Apparent Polarity	1299	1438
7	Filter 5/10-15/20	1290	1463

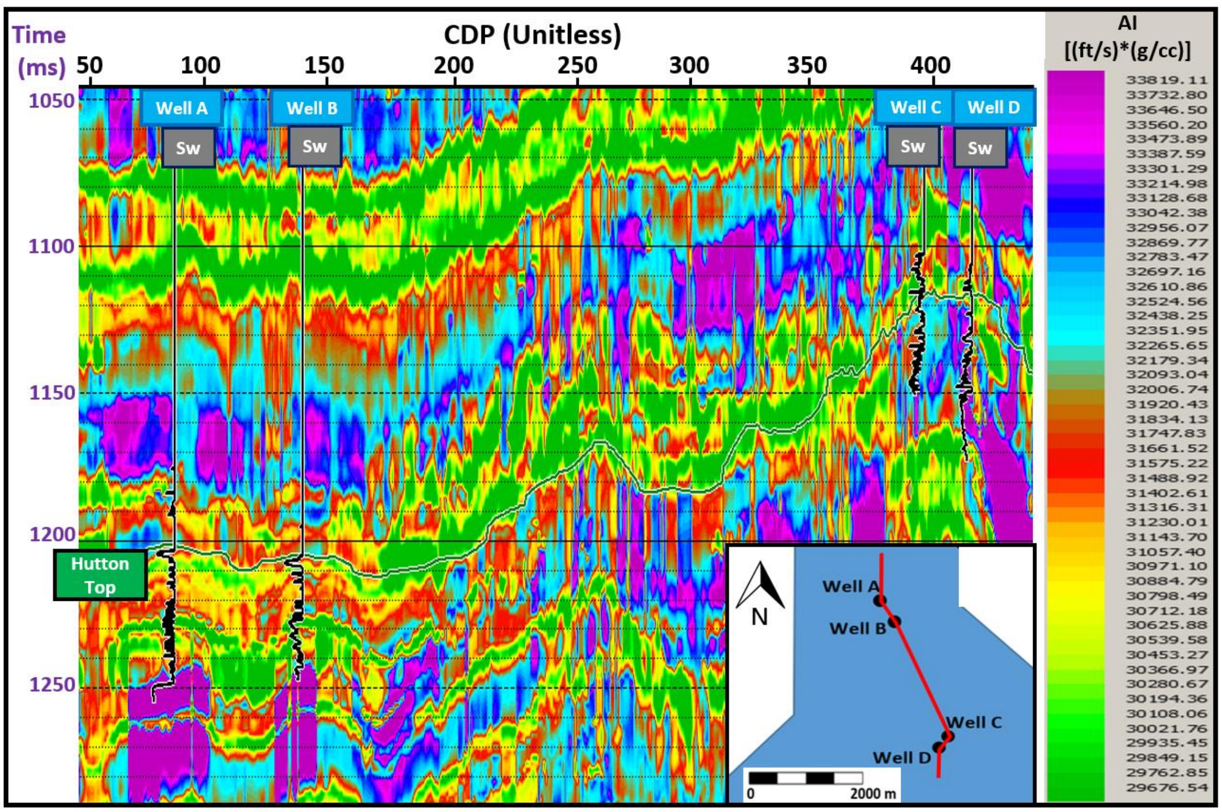

Figure 8.20: Arbitrary line passing through the four wells shows P-impedance estimated from neural network application to conventional seismic data. Result quality degrades due to insufficient training data.

8.2. Unsupervised machine learning

Unlike supervised machine learning that needs well log data to be incorporated in the process, unsupervised machine learning classifies seismic data without using well logs. In this research study, Principal Component Analysis (PCA) and Self-Organizing Map (SOM) algorithms were used as unsupervised machine learning for facies classification (Roden et al., 2015). Principal Component Analysis (PCA) is a mathematical technique that arranges seismic attributes in descending order according to their contribution in each eigenvector component. Hence, Principal Component Analysis (PCA) helps the interpreter to select appropriate seismic attributes and detect the most useful attributes within a large dataset by its ability to reduce data dimensionality. These meaningful attributes are identified based on their contribution in producing the large variability in seismic data that probably represents geologic variations. PCA is conducted by calculating eigenvalues and eigenvectors for the covariance matrix. At each principle component estimated from PCA, the interpreter can select seismic attributes that contribute a high percentage of variance for the multiattribute dataset. The selected meaningful seismic attributes will be then employed in Self-Organizing Maps. On the other hand, unselected seismic attributes that have less contribution will be eliminated.

Seismic attribute selection depends mainly on research study purpose. Geometric (multi-trace) attributes such as curvature and similarity, are very helpful to identify structure and stratigraphic geological features, but instantaneous attributes like instantaneous frequency and amplitude (envelope) of single traces are linked to pore-fluid and rock physical properties (Paradise, 2017). Because seismic attributes have different scales, normalization was applied before conducting PCA to make sure that attributes are equally treated. This normalization was conducted using the mean and standard deviation of each seismic attribute (Roden et al., 2015).

In this study, focus is mainly on identification of oil-sand facies. Based on this purpose, instantaneous seismic attributes were carefully selected. Geometric attributes such as curvature attributes, were ignored. Selected instantaneous seismic attributes were incorporated in the PCA. This analysis was only applied to small subarea around Well B that has an anomalous bright spot and AVO class 3. The first principal component calculated at each inline, is shown in Figure 8.21. The Principal Component Analysis (PCA) at Well B is shown in Figure 8.22. The eigenvalue, which represents spread of data, was calculated for each eigenvector. Seismic attributes that have large contribution percentage at each eigenvector, were selected as shown in Figure 8.23. For the first principal component, envelope, sweetness and attenuation attributes were selected. For the second principal component, Hilbert, instantaneous phase and amplitude attributes were selected.

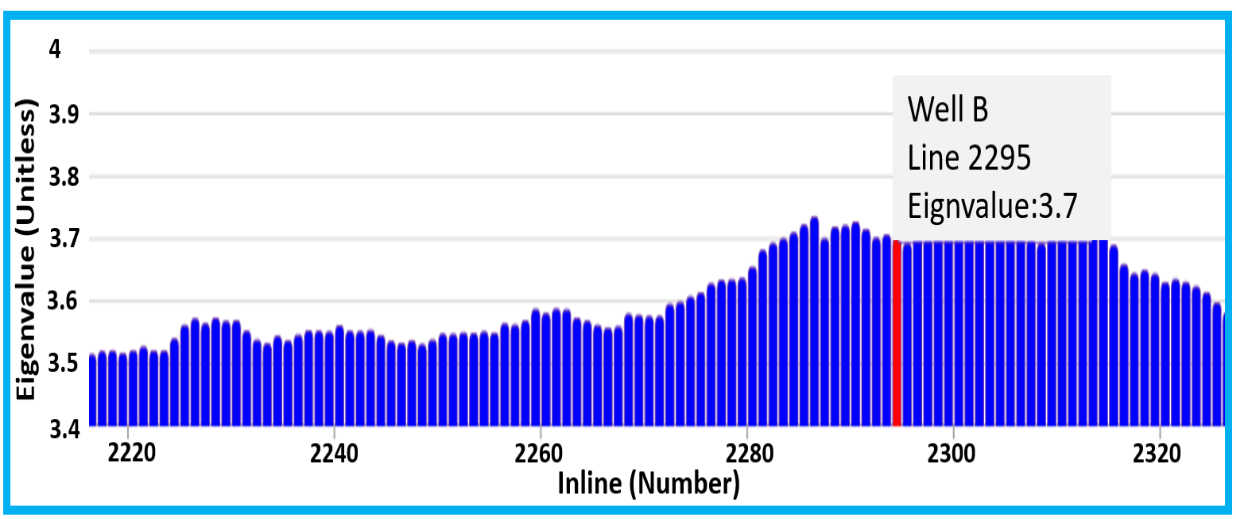

Figure 8.21: Calculated eigenvalues of first principal component at each inline. The red bar represents the eigenvalue at Well B.

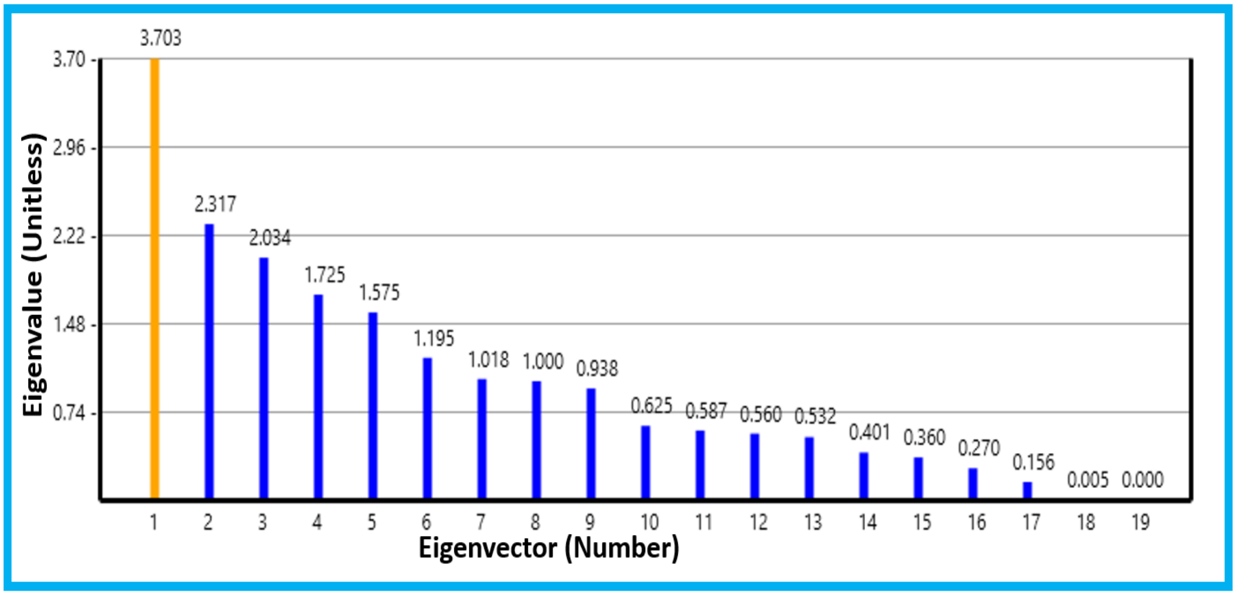

Figure 8.22: The Principal Component Analysis (PCA) at Well B.

Attributes contribution to 1st principal component	
ATTRIBUTE NAME	PERCENTAGE
Envelope	25.30
Sweetness	25.11
Attenuation	10.02
Similarity_Total_Energy	4.27
Similarity_Energy_Ratio	3.61
DipGST_GST_Similarity	2.18
Smoothed Frequency(	1.87
Bandwidth	1.48
Relative Acoustic Impedance	0.37
Seismic_Conditioned_1200_1800_SBLA_	0.10
Thin Bed	0.10
Hilbert	0.09

Attributes contribution to 2nd principal component	
ATTRIBUTE NAME	PERCENTAGE
Hilbert	25.53
Instantaneous Phase	17.06
Seismic_Conditioned_1200_1800_SBLA_	12.29
Normalized Amplitude	10.27
Attenuation	0.49
Thin Bed	0.36
Acceleration of Phase(	0.34
Similarity_Total_Energy	0.16
Attenuation Bands on Phase Breaks(	0.11
DipGST_GST_Similarity	0.08
Sweetness	0.08
Envelope	0.07
Smoothed Frequency	0.06

Figure 8.23: Attributes contribution to first and second principal components.

A Self-Organizing Map (SOM) is a type of unsupervised machine learning that is applied to multiattributes. This algorithm learns to classify seismic data without any external supervision represented by well logs. It uses an unsupervised neural network to reduce data dimensions

(Roden et al., 2017). SOM was first developed by Kohonen (1982) to classify world countries according to personal traits.

A SOM produces neurons (prototypes) which classify seismic data into clusters based on their properties (Paradise, 2019). A lattice of neurons represented by nodes responds to the input set of seismic attributes. Each neuron identifies a natural cluster of attributes (Roden et al., 2017). During construction of the SOM, neurons have two learning behaviors (cooperative and competitive learning behaviors). In cooperative learning, neurons start to move toward data clusters in a way that neurons depend on each other. In other words, they move toward the clusters and toward themselves. Then, neurons behavior switches to competitive learning, in which, neurons move independent to each other toward the data cluster. Neurons continue to move in epochs until being attached to a data cluster (Paradise, 2019).

Because productive hydrocarbon areas are small compared to the entire seismic dataset, they are hardly captured by these neurons (Marfurt, 2018). The data points that are not attached to neurons, are called low probability points which may be regarded as direct hydrocarbon indicators. Since noises may be small compared with signal, low probability points could be noises. Furthermore, by practice, investigating low probability points as a direct hydrocarbon indicator sometimes does not work and is not conformable with blind validation wells with oil pore fluid.

After conducting PCA, selected attributes were incorporated in constructing Self-Organizing Maps (SOM). Dimensions (8 by 8) were used as a topology for the constructed Self-

Organizing Map. Thus, the number of used neurons is sixty-four as shown in Figure 8.24. Each neuron has its own color and represents a cluster of datapoints in the 3D space.

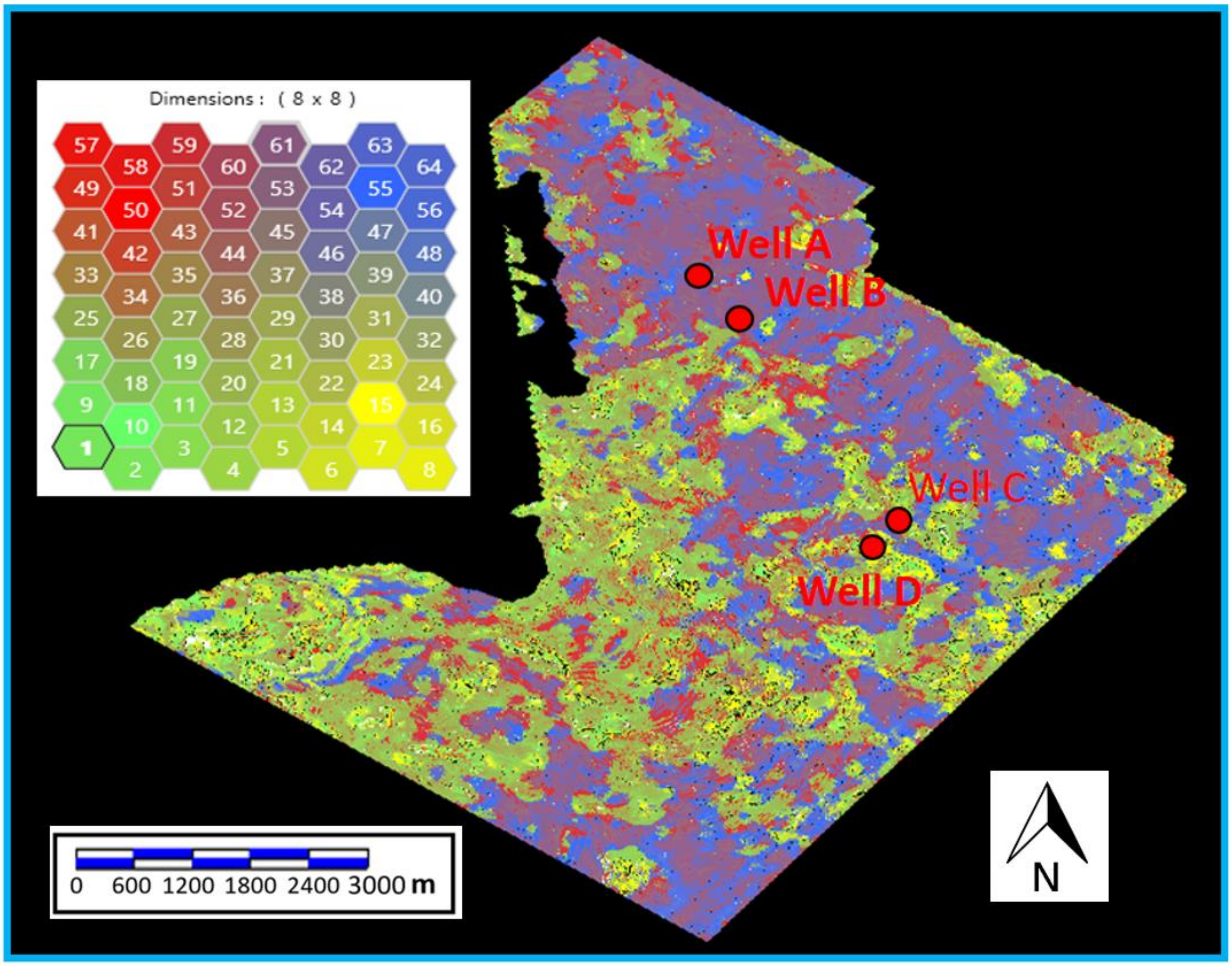

Figure 8.24: High-frequency seismic data SOM created by using 64 neurons represented by different colors.

To address the cluster of oil-sand facies, color that passed through Well B was highlighted, and other neuron colors were switched off as illustrated in Figure 8.25. Well A, Well C and Well D are used as blind validation wells. Well A that has oil pore fluid passes through the cluster and Well D that is a dry hole, does not cut across the highlighted cluster. Thus, Well A and Well D blind validation wells show a good pore-fluid prediction match. However, the oil-sand cluster does not pass through Well C that has 60% water saturation. The small layer thickness and 60% water saturation at Well C could cause that response to cluster differently from the pay responses at Wells A and B. The channel feature is identified between well C and Well D as shown in Figure 8.26 suggesting reservoir quality similar to wells A and B. This channel feature is like that identified previously with inversion.

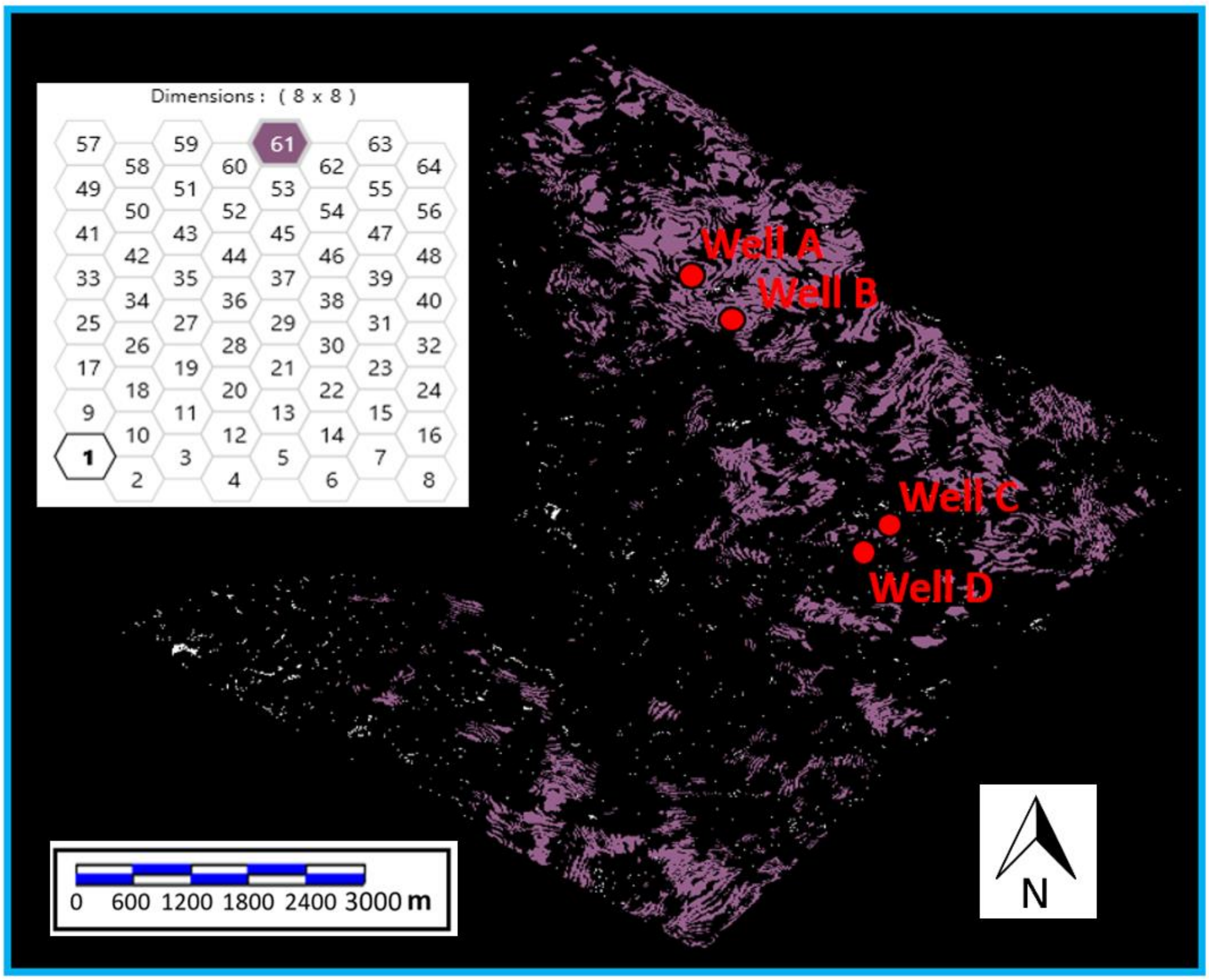

Figure 8.25: High-frequency seismic data SOM after highlighting neuron number 61.

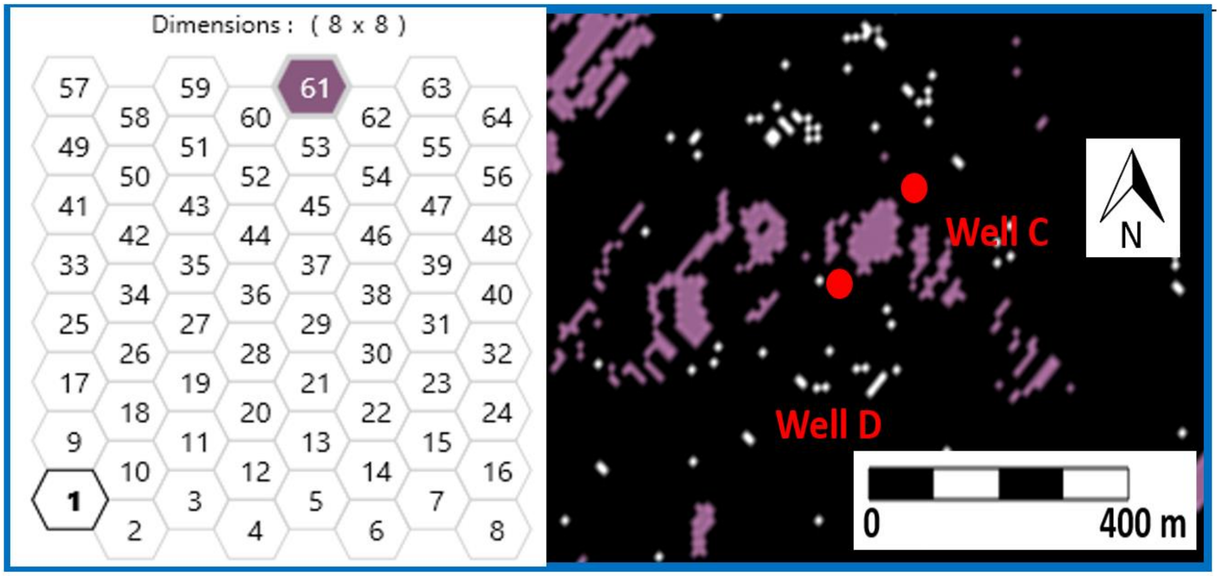

Figure 8.26: High-frequency seismic data SOM around Well C and Well D area.

The previous SOM was established using the high-frequency far-angle stack as input. The unsupervised machine learning process was repeated with full-stack seismic data. The low probability points distribution is highlighted by white after deactivating all neuron colors as shown in Figure 8.27. To address result reliability in this case, all wells are regarded as blind validation wells. The low probability points' distribution, which may represent hydrocarbon facies, passes through Well B and Well C, and does not pass through Well D. However, Well A that has oil pore fluid does exhibit the low probability points at the pay zone. Facies passing through Well A can be highlighted by one neuron activation. The colored zone plus low probability data point distribution represents the entire oil-sand facies distribution.

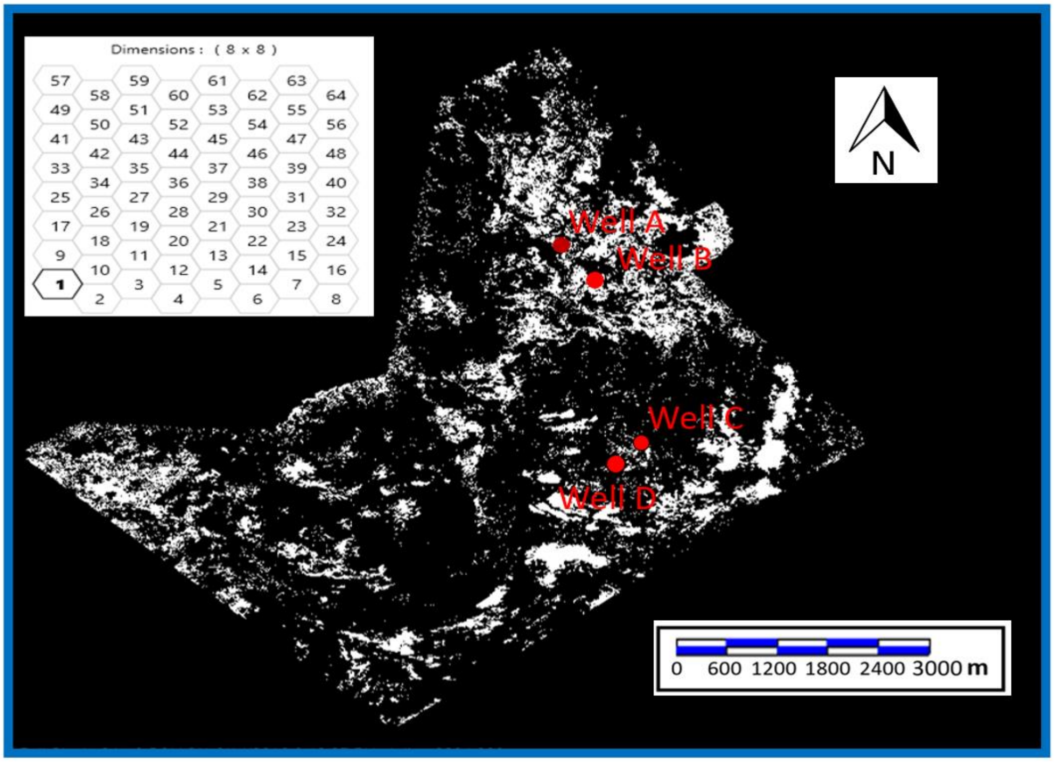

Figure 8.27: Conventional far-offset stack SOM shows distribution of low probability data points.

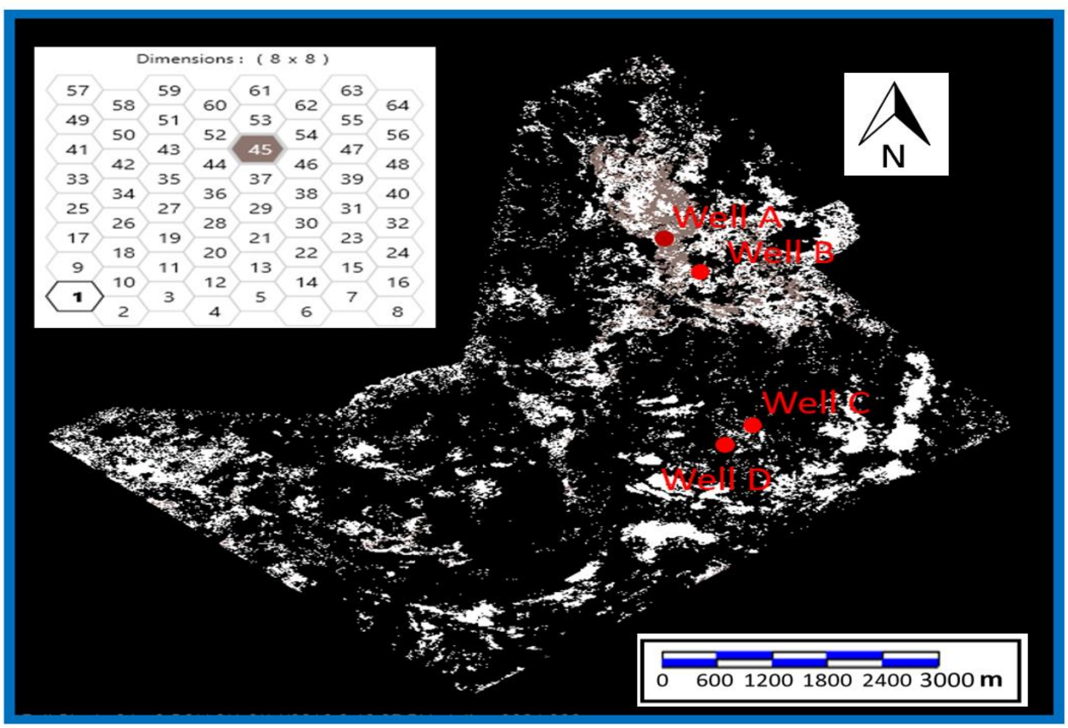

Figure 8.28: Conventional far-offset stack SOM shows distribution of low probability data points and neuron 45.

Chapter 9

Discussion and Conclusion

9.1 Discussion

Although the Hutton Formation in the Eromanga Basin is a mature play, many prospects remain. Drilling is very risky since many wells drilled high on structure are water charged. Because hydrocarbon chemical properties approach heavy oil properties (API=32), there is little discrimination between oil and brine physical properties. To reduce drilling risk the area, reservoir quality and lithology discrimination is badly needed. In this case study, I compared seismic responses at four wells. Wells A and B had commercial hydrocarbons. Well C and Well D, though being higher on structure, were not successful. Well C had a thin 2 m thick layer with oil, but with high water-saturation and lower porosity. Well D was a dry hole.

Seismic amplitudes, amplitude-variation-with-offset, detailed comparisons of seismic data to synthetic seismograms, simultaneous inversion, and crossplotting of various parameters do not yield an unambiguous seismic direct hydrocarbon indicator in this location. These studies were hampered by the lack of shear-wave velocity logs in Wells B, C, and D, and it is possible with more calibration that a more definitive indicator could have been identified.

To robustly identify minute structural details that are not readily apparent on the seismic data, seismic reflection attributes were constructed. Depositional and structural features were robustly identified from curvedness, dip of maximum similarity, most-positive curvature and most-negative curvature attributes. These features include faults that cut across basement and the overlying sedimentary section as well as meandering and forked features that belong to ancient fluvial depositional systems. High structural locations that possibly are hydrocarbon charged, due to updip migration of hydrocarbons, are revealed by positive curvature attributes. These attributes are co-rendered with most negative structure attributes to robustly discriminate between high structure locations that are probably hydrocarbon charged and low structural locations that are probably water charged. However, hydrocarbon charged locations are not precisely identified based only on seismic reflection attributes and the problem still exists since high structure may be water charged as facies changes may localize hydrocarbon occurrence. That this occurs is obvious from Well D that has no pay but is higher on structure than wells with hydrocarbons. Thus, qualitative seismic interpretation needs to be integrated with quantitative analysis to reasonably estimate pore fluids and lithology distribution over the study area.

Physical properties away from the wells were estimated from post-stack inversion, pre-stack simultaneous inversion and multiattribute analysis performed on conventional and high-frequency seismic data obtained from bandwidth extension methods. Estimated rock properties were converted into facies delineated over the 3D seismic volume. Sand facies distribution is observed below the Hutton Formation top overlain by shale facies. In addition, sand facies are discriminated into low- and high-porosity sands or high-probability oil and brine sands. Thus, the facies discrimination problem encountered in qualitative interpretation is tackled by quantitative analysis. A comparison between compressional-to-shear-wave velocity ratio, acoustic impedance, RMS amplitude, high-probability oil distribution, scaled Poisson's ratio and anomalous hydrocarbons, identified from AVO intercept and gradient horizon slices extracted from the same time window, are shown in Figure 9.1. There are great similarities between horizon slices which imply that anomalous behavior may result from the interplay between reservoir quality and hydrocarbon pore-fluid effects. For example, capillary pressure effects may result in higher oil saturation in high porosity rocks, and higher water saturation in lower porosity rocks. This would produce a correlation between acoustic impedance and the Vp/Vs ratio with oil saturation, even if oil and brine had the same acoustic properties. This effect could then be accentuated when oil and brine properties are different; further lowering the impedance and Vp/Vs ratio of oil-bearing porous reservoir rock. There may be additional interplay, such as a correspondence between layer thickness and reservoir quality. As thinner layers produce weaker responses, this would again favor a higher amplitude for the thicker zones, further accentuating the amplitude difference.

After facies discrimination using quantitative analysis methods, delineated facies should have a geological interpretation. Thus, data integration can be achieved by co-rendering geological features identified from qualitative interpretation with rock properties and facies identified from quantitative analysis, and hence, extracting more information from seismic data that leads, in turn, to a geological model with a robustly identified geological scenario uncertainty.

Before data integration, reliability of predicted facies results was first addressed. Some wells were used as blind validation wells for evaluating the performance of applied techniques for lithology and pore-fluid discrimination. Table 9.1 summarizes blind well predictions using different methods and datasets. Inaccurate results are highlighted by orange shading that are dominantly observed at Well C and Well D test wells. In addition, a comparison was conducted between applied quantitative analysis methods in this research study as well as data incorporated in these methods including conventional and high-frequency seismic data. The aim of this comparison is to evaluate method performance and to detect which quantitative analysis is the best for deciphering the available data.

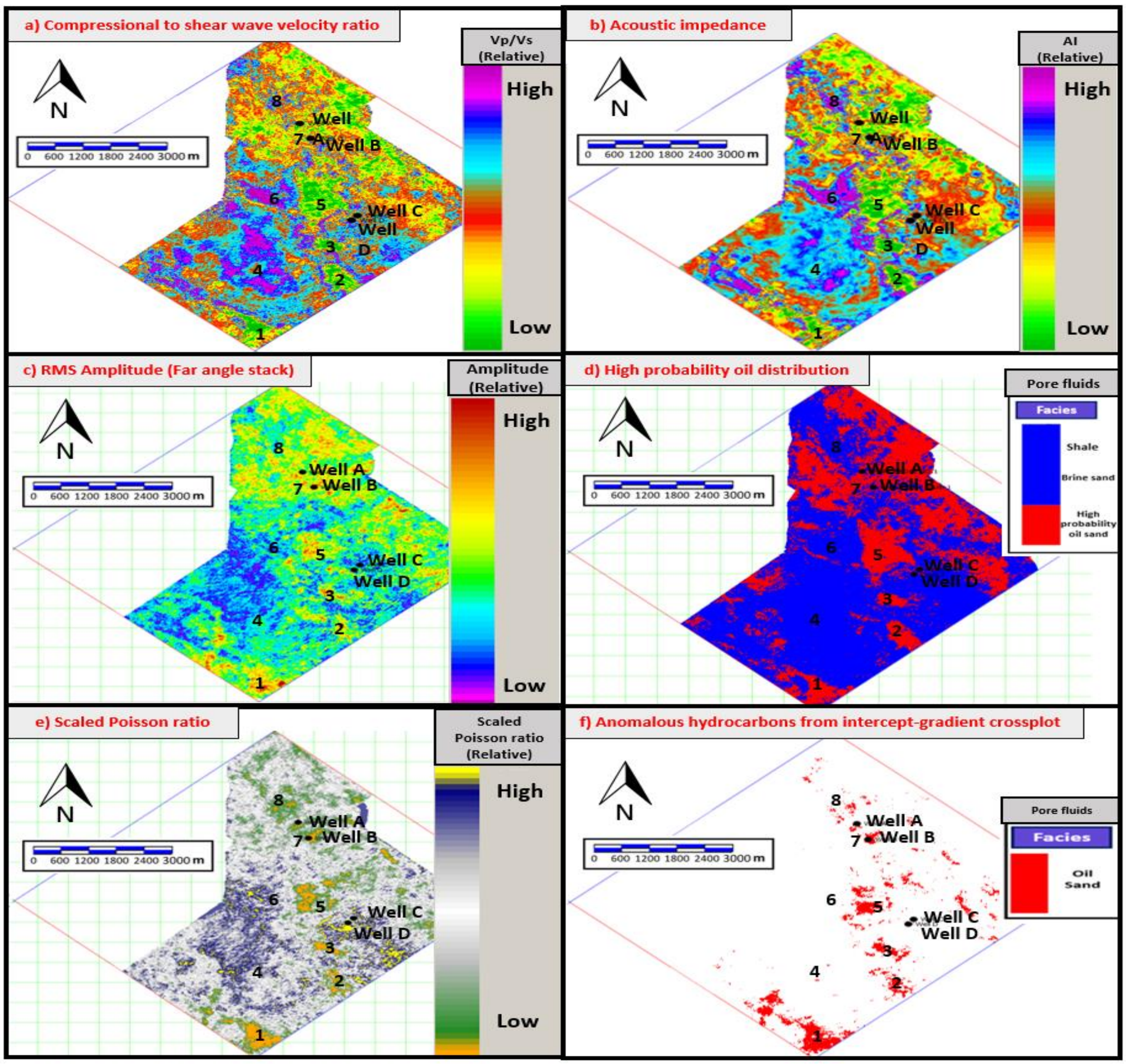

Figure 9.1: Comparing between different 10 ms horizon slices below the Hutton Formation top. a) Vp/Vs, b) Acoustic impedance, c) RMS amplitude, d) High-probability oil distribution. e) scaled Poisson's ratio and f) Anomalous hydrocarbons from intercept-gradient crossplot.

Table 9.1: Summary of results at the four wells. Inaccurate results are highlighted by orange.

Techniques		Attributes		Well A (Sw=30%)	Well B (Sw=30%)	Well C (Sw=60%)	Well D (Sw=100%)
Qualitative seismic interpretation		Structure contour map		High	High	High	High
		Positive curvature		+ve	+ve	+ve	+ve
		Isochron map		+ve	+ve	-ve	+ve
		DHI analysis (Far-offset amplitude)		High	High	Low	Low
AVO attributes		AVO		Large increase	Large increase	Small decrease	Small increase
		Far (Far-near)		+ve	+ve	-ve	-ve
		A*B		+ve	+ve	+ve	+ve
		Scaled Poisson ratio		Large negative	Large negative	Small positive	Large positive
		Polar magnitude		+ve	+ve	-ve	-ve
Seismic Inversion	Post-stack inversion	Far-angle stack	AI	Low	Low	Low	Low
		Broadband far angle stack	AI	Low	Low	Low	High
	Pre-stack simultaneous inversion	Vp/Vs		Low	Low	Moderate	High
		AI		Low	Low	Moderate	High
Machine Learning		Supervised	AI	Low	Low	Moderate	High
		Unsupervised		+ve	+ve	-ve	+ve

Because acoustic impedance can be estimated using most used methods and it can be used to discriminate different facies, this physical property was investigated to measure how well its estimation by different methods can predict pore fluids. Well C was used as a blind validation well to assess different methods since confusion matrices were calculated by different methods and data to measure acoustic impedance prediction accuracy when it is compared with well log impedance at Well C. Since the pay zone depth range at Well C is precisely estimated from a drill stem test, a cut off value (AI= 30000 (ft/sec*g/cc)) estimated from filtered acoustic impedance was used to separate pore fluids (oil and brine). Confusion matrices were constructed to evaluate different methods and datasets are shown in Figure 9.2. Post stack inversion of high-frequency seismic data shows the highest prediction accuracy (94.5%). Figure 9.3 shows predicted pore fluids using different methods and datasets and their comparison with the pay interval at Well C.

Accuracy (94.5 %)	Predicted oil	Predicted brine
Actual oil	10	3
Actual brine	4	112

Post-stack inversion (High-frequency seismic data)

Accuracy (74.4%)	Predicted oil	Predicted brine
Actual oil	0	13
Actual brine	20	96

Post-stack inversion (Original seismic data)

Accuracy (89.9%)	Predicted oil	Predicted brine
Actual oil	0	13
Actual brine	0	116

Pre-stack inversion (Original seismic data)

Accuracy (46.5%)	Predicted oil	Predicted brine
Actual oil	13	0
Actual brine	69	47

Neural network (High-frequency seismic data)

Accuracy (89.9%)	Predicted oil	Predicted brine
Actual oil	0	13
Actual brine	0	116

Neural network (Original seismic data)

Figure 9.2: Confusion matrices estimated from comparing Well C actual values of acoustic impedance with predicted one using different methods and datasets.

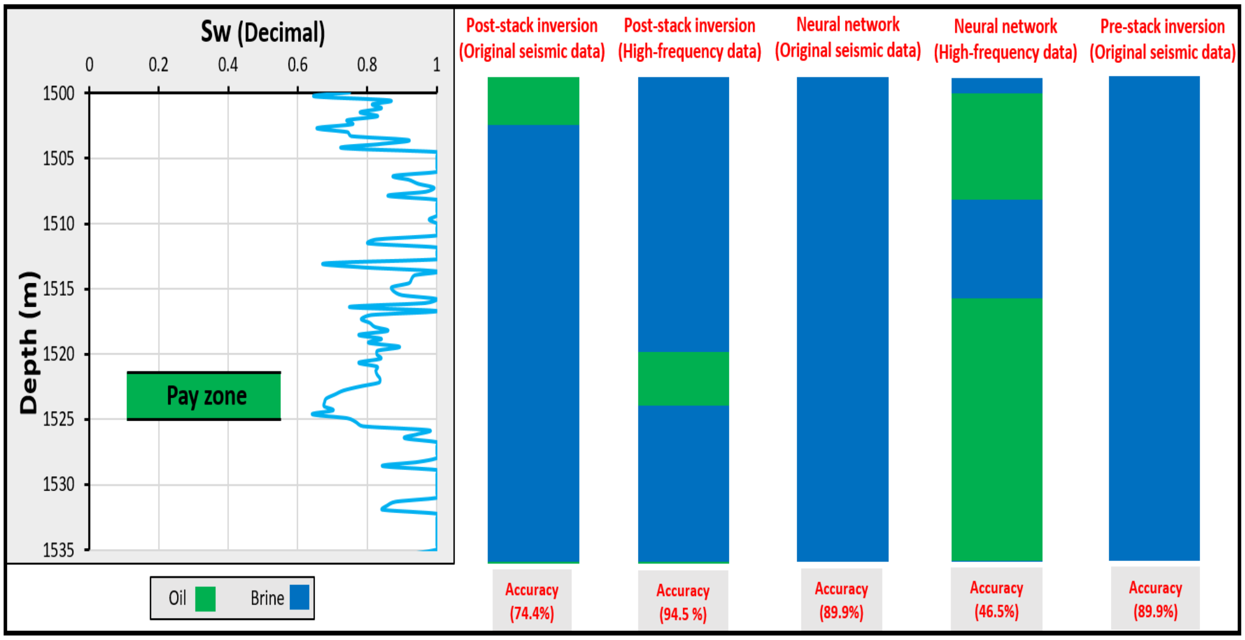

Figure 9.3: Predicted pore fluids using different methods and datasets.

After addressing results reliability of different quantitative analysis methods using conventional and high-frequency seismic data, quantitative analysis methods of high prediction accuracy are incorporated into data integration with qualitative seismic interpretation. Seismic refection attributes are co-rendered with rock properties estimated from inversion results and facies delineated from rock-physics templates. Figures 9.4 and 9.5 show acoustic impedance (AI) and compressional-to-shear-wave-velocity (Vp/Vs) horizon slices co-rendered with dip of maximum similarity and curvedness seismic attributes, respectively. High acoustic impedance and Vp/Vs ratio are observed along meandering features which are probably brine sands and shale facies. On the other hand, low acoustic impedance and Vp/Vs ratio are observed for other subareas which are probably sand facies with high probability of oil occurrence.

Furthermore, a lithofacies slice is co-rendered with most-positive curvature as shown in Figure 9.6. Shale facies are distributed along meandering features located on positive structures. From this observation, not all positive structures are hydrocarbon charged sand. This hypothesis casts doubt on previous thoughts that relate high values of most-positive curvature to hydrocarbon distribution since shale and brine sands can occur high on structure. This is possibly attributed to stratigraphic interferences preventing hydrocarbon updip migration.

All the above-mentioned results show compartmentalization of the Hutton Formation reservoir described by (Hamilton et al.,1998) which is attributed to the overlaying Birkhead Formation incision evidenced by truncation of reflections at some locations and shale facies distribution along meandering features. Birkhead Formation incision in the Hutton Sandstone Formation results from incised valley filling by the Birkhead formation deposition. The upper surface of the Hutton formation is regarded as a sequence boundary which is subjected to erosion after base level falling. This erosion formed a paleo-valley system in which the low stand systems tract of the Birkhead Formation was deposited (Boult et al., 1998). Unlike well-known incised valleys initially filled by sand facies, the Birkhead Formation incision is clay rich (Lanzilli, 1999) since its lithofacies are fine to medium grain sandstone, siltstone and shale. Incision caused by the paleo-valley system removes all or upper part of the Hutton Formation. Thus, when it comes to risk addressing, these meandering features should not be drilled if the upper unit of the Hutton Formation is the target. A conceptual model shown in Figure 9.7 illustrates the geological scenario for the Hutton Formation upper surface over the study area before the Birkhead deposition.

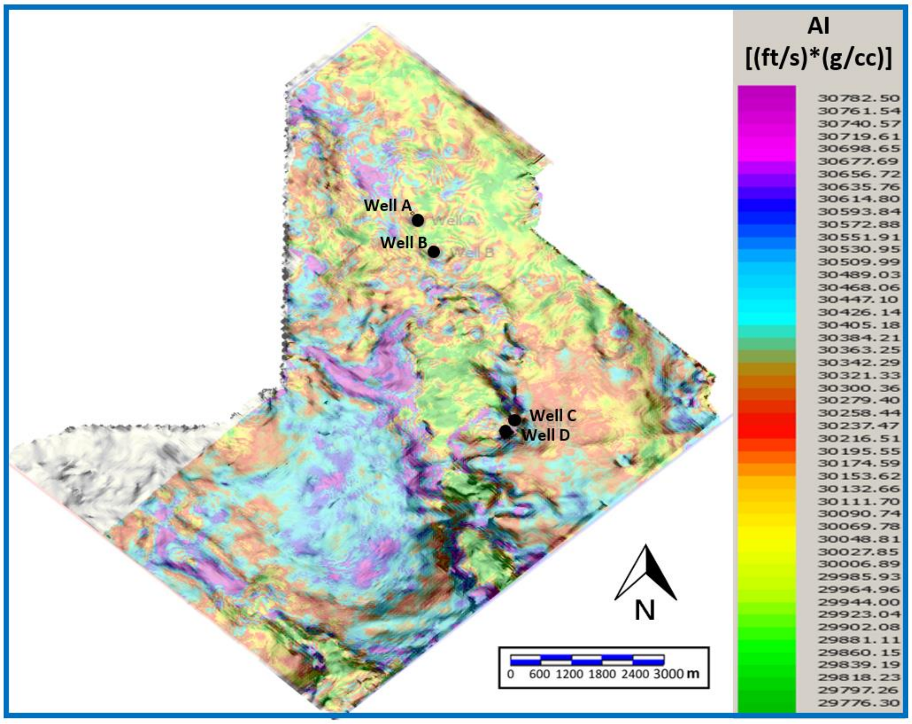

Figure 9.4: Paleogeographic meandering features shown in maximum similarity seismic attribute matches with high acoustic impedance.

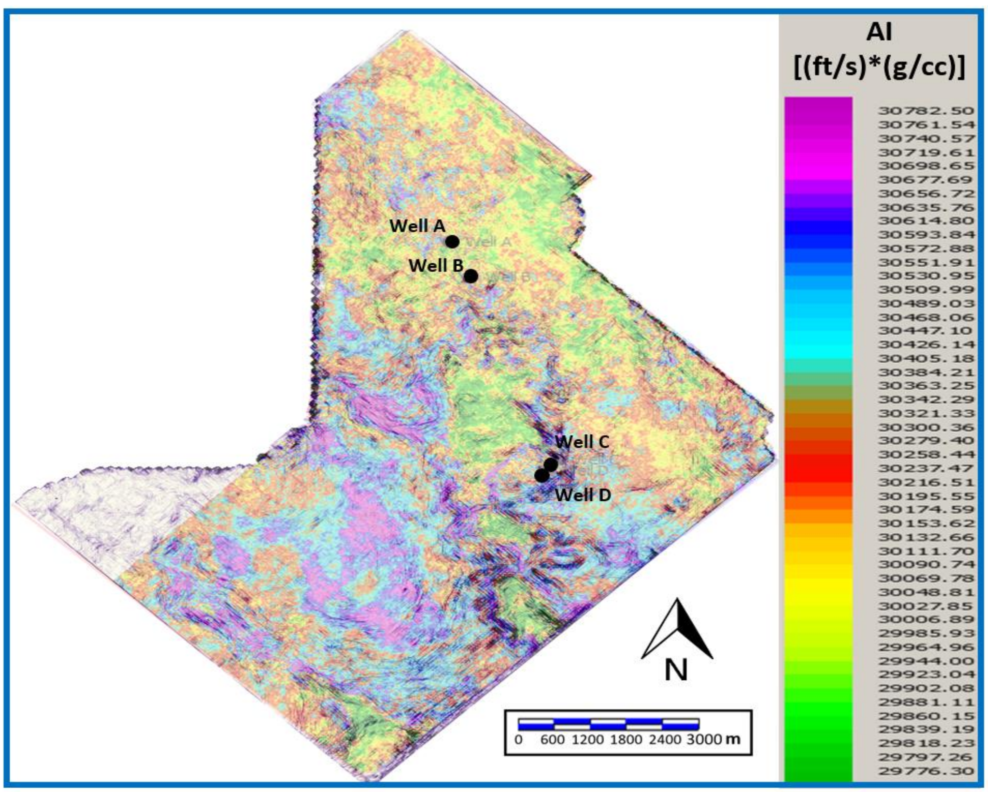

Figure 9.5: Paleogeographic meandering features shown in curvedness seismic attribute matches with high Vp/Vs ratio.

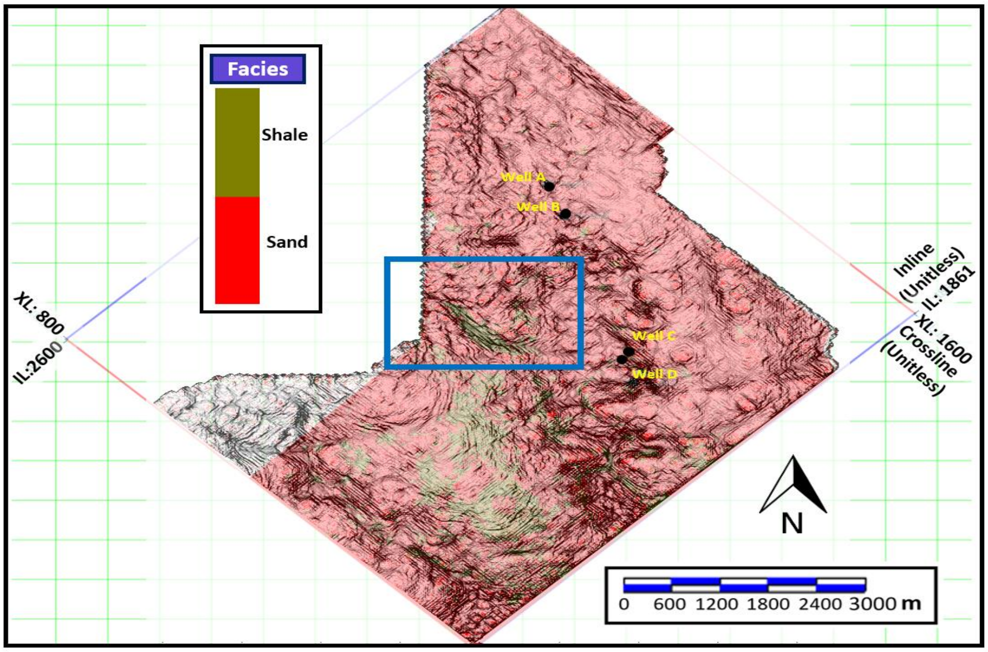

Figure 9.6: Shale facies are distributed along paleogeographic meandering features observed on the most-positive curvature attribute.

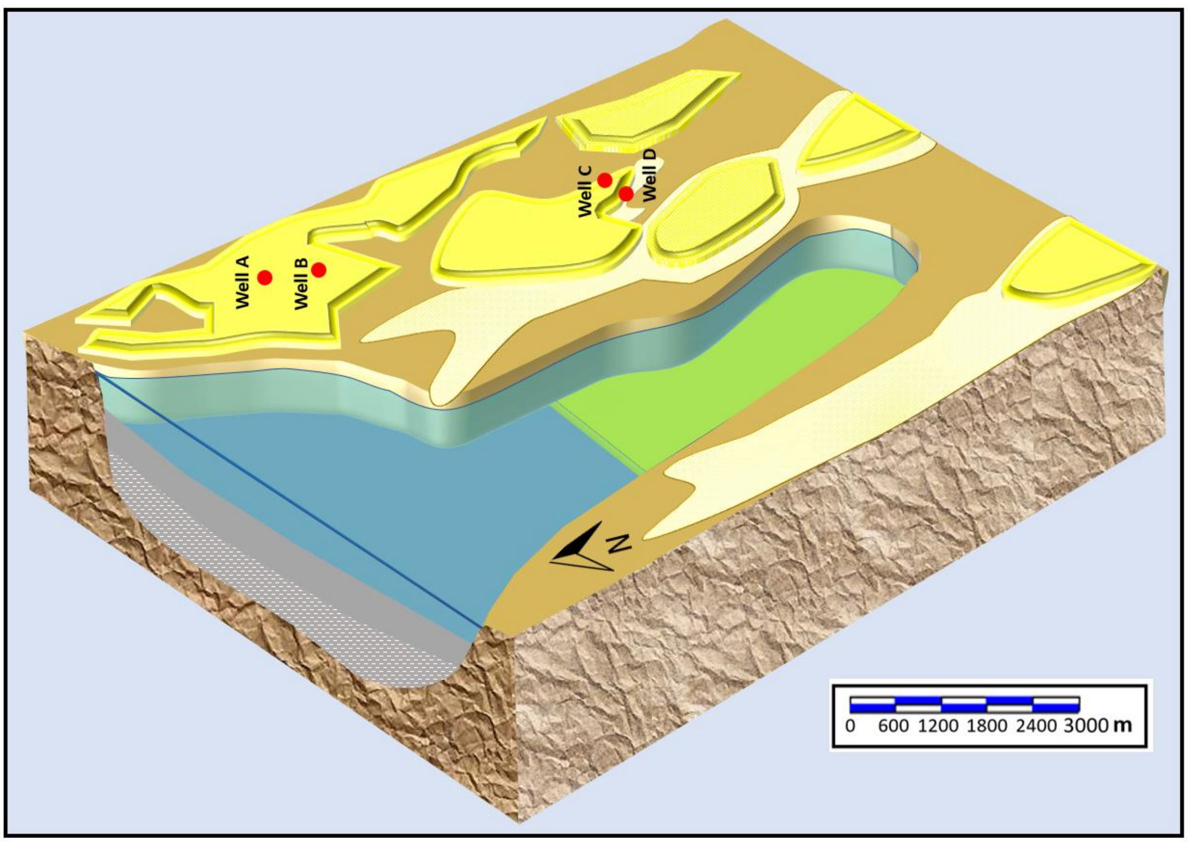

Figure 9.7: Conceptual model for the Hutton Formation distribution over the study area before Birkhead formation deposition.

To address the poor results in the Well C and Well D area, seismic attributes were first investigated. Faults are noticed around Well C from the curvedness attribute created from the mid-angle stack. These faults are separating Well C from Well D. A channel feature near the pay zone of Well C is also seen. By tracking the AVO response of the area around Well C, a class 4 AVO anomaly occurs at the same location of the channel. AVO analysis of this channel shows AVO response different from the response of the Hutton Formation at Well D.

While investigating a 10 ms acoustic impedance horizon slice, constructed from post stack inversion of the high-frequency far-angle stack, at the proposed channel location around Well C, a gradual decrease in acoustic impedance was observed from Well C to the zone of interest and vicinity. This is confirmed with an arbitrary line passing through Well C and the channel exhibiting low acoustic impedance that ties perfectly with the pay zone at Well C. Well D exhibits high acoustic impedance that is not continuous with the acoustic impedance at well C.

After integrating the acoustic impedance result with seismic data as shown in Figure 9.8, faults between the channel and Well C and Well D can be seen. There is high fault displacement between the channel and Well D. However, there is a small fault displacement between the channel and Well C. This observation provides a plausible conclusion for oil accumulation at Well C and its absence at Well D. When fault displacement is small, there is no seal between fault blocks and oil can find pathways to cross between fault blocks. Thus, oil has probably migrated from the channel to Well C. On the other hand, large fault displacement observed between the channel and Well D probably produces a seal and this provides a plausible reason for oil absence at Well D.

After investigating many arbitrary lines crossing Well C and Well D from different directions and horizon slices above and below the Hutton Formation top, facies change along Well D not only at the Hutton Formation but also at the overlying Birkhead Formation. There is an increase of shale intercalations within the Hutton Formation along Well D. When it comes to the Birkhead Formation, facies change from shale to sandy shale is observed at Well D. This result matches with facies change observed in the Birkhead Formation from well log correlation. Facies change in the seal very close to Well D can provide pathways for upward oil migration. Facies change is also confirmed by porosity prediction using both inversion and machine learning since a porosity decrease was predicted at Well D.

After discriminating facies using a rock physics template, sand facies are observed along the Hutton Formation at Well C and the channel. A siltstone or low porosity sand layer occurs between the two upper units of the Hutton Formation providing a reason for oil absence for the first upper unit of the Hutton Formation since the siltstone may provide a seal for oil upward migration. On the other hand, Birkhead incision was observed at Well D on gamma-ray logs and inverted seismic data. This incision probably removes the upper part of the Hutton Formation at Well D. High-probability oil-sand facies are observed at Well C and the channel in the second upper unit of the Hutton Formation but not observed at Well D.

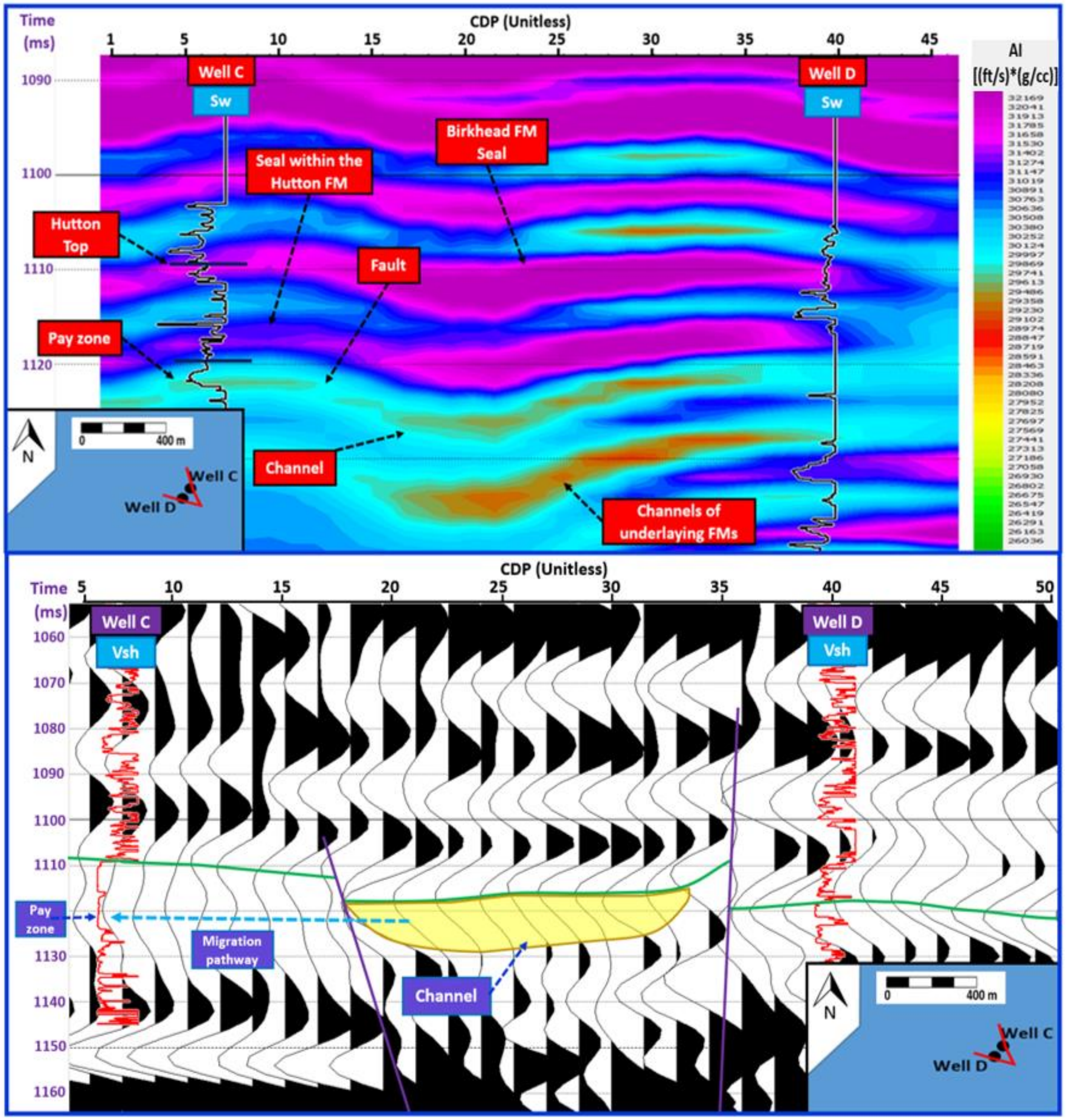

Figure 9.8: Integration between qualitative interpretation of mid-angle stack and acoustic impedance result from quantitative analysis.

Based on data integration between well logs correlation, inversion and facies discrimination using rock physics template and Bayesian classification, a cartoon section was constructed along arbitrary line passing through Well C, the channel and Well D as shown in Figure 9.9.

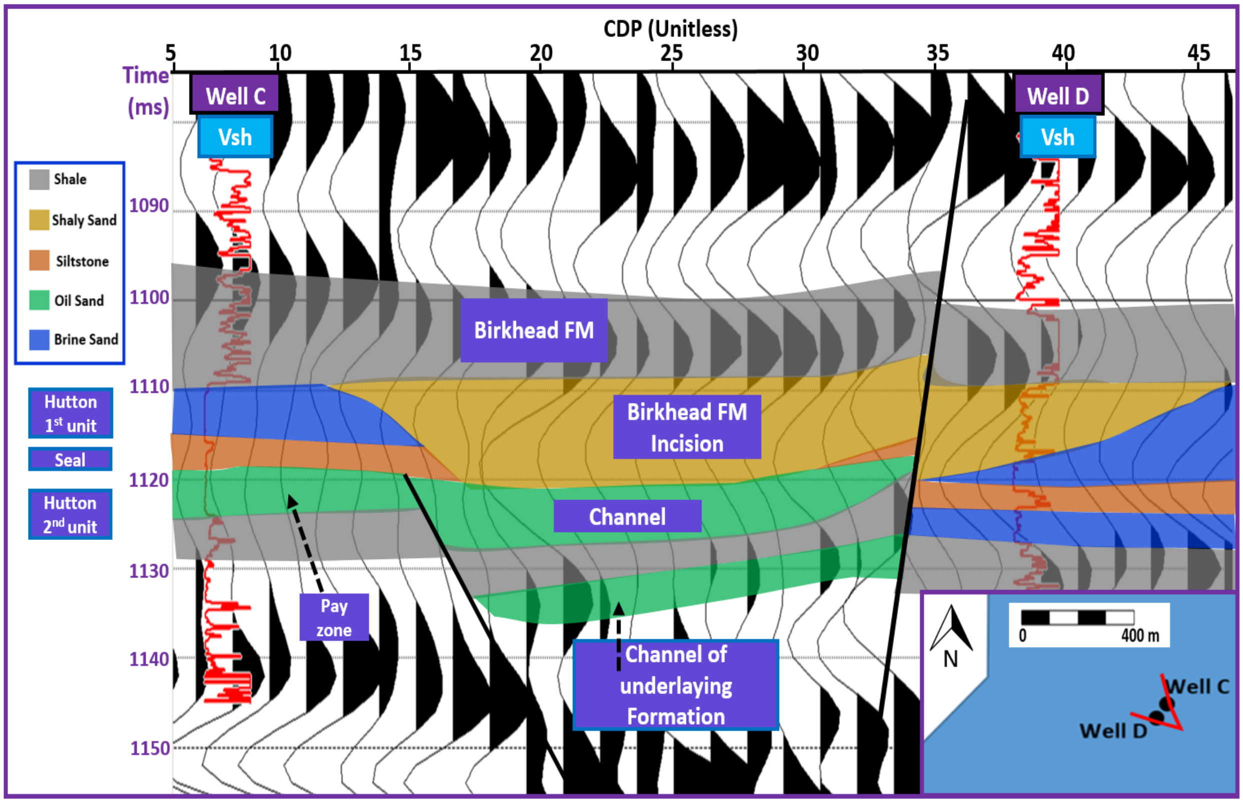

Figure 9.9: Facies distribution along arbitrary line passing through Well C, Channel and Well D.

9.2. Conclusion

In conclusion, this study resulted in the findings summarized below.

- Integration between data using different methods and analyses enhances extracting information from seismic data.
- A channel occurrence near Well C is probably the reason for oil occurrence at the well since oil can find migration pathways from the channel to the well. On the other hand, oil absence at well D is probably attributed to large fault displacement around it that produces a seal preventing oil migration from the channel to the well. Facies change from

sand to shale at some zones of the Hutton formation at Well D and seal absence along its surrounding area also provide a plausible conclusion for oil absence at Well D.

- Not all positive structures identified from most-positive curvature, are hydrocarbon charged. Most-positive curvature should be integrated with facies distribution for enhancing interpretation.
- Pore fluids and lithology are more robustly discriminated using high-frequency broadband seismic data than by conventional seismic data using different techniques.
- Unlike inversion methods that can be conducted using one well, quality of supervised machine learning using neural network degrades with fewer wells since this method needs more training data.
- A lot of blind validation wells are needed to address reliability of supervised and unsupervised machine learning results.
- Acoustic impedance inversion produced by performing post-stack inversion on high-frequency seismic data, is the best result in this research study with the highest accuracy of confusion matrix prediction-success percentage among other results.
- Confusion matrices should be used for prediction evaluation. For example, the neural network predicted oil occurrence at well C correctly, but with low prediction accuracy in the confusion matrix because this method also predicted brine zones as pay zones.
- Lithology and hydrocarbon prediction are enhanced by using probabilistic Bayesian classification since high probability oil of 30% water saturation was robustly addressed using this statistical approach.

- The full-stack volume should not be used for direct hydrocarbon detection here as it did not prove useful in predicting commercial pay.
- Sparse-layer inversion shows geological details that are hidden in original seismic data and hence, is a robust method for quantitative seismic interpretation.

The methods investigated here suggest there are additional drilling locations such as the channel near Well C. Bandwidth extension using sparse-layer inversion was invaluable in producing the high-frequency seismic data exploited so well by seismic inversion and machine learning.

Bibliography

Aki, K., & Richards, P. G. (1980). Chapt. 13 Seismic waves in three-dimensionally inhomogeneous media. Quantitative seismology theory and methods, 2, 721-797.

Al-Dossary, S., & Marfurt, K. J. (2006). 3D volumetric multispectral estimates of reflector curvature and rotation. Geophysics, 71(5), P41-P51.

Archie, G. E. (1942). The electrical resistivity log as an aid in determining some reservoir characteristics. Transactions of the AIME, 146(01), 54-62.

Avseth, P., & Veggeland, T. (2015). Seismic screening of rock stiffness and fluid softening using rock-physics attributes. Interpretation, 3(4), SAE85-SAE93.

Avseth, P. A., & Odegaard, E. (2004). Well log and seismic data analysis using rock physics templates. First break, 22(10), 37-43.

Avseth, P., Mukerji, T., & Mavko, G. (2005). Quantitative seismic interpretation: Applying rock physics tools to reduce interpretation risk. Cambridge university press.

Avseth, P. A., & Odegaard, E. (2004). Well log and seismic data analysis using rock physics templates. First break, 22(10), 37-43.

Batzle, M., & Wang, Z. (1992). Seismic properties of pore fluids. Geophysics, 57(11), 1396-1408.

Bergbauer, S., Mukerji, T., & Hennings, P. (2003). Improving curvature analyses of deformed horizons using scale-dependent filtering techniques. AAPG bulletin, 87(8), 1255-1272.

Bioregional Assessment Programme (2018) National Geoscience Mapping Accord (NGMA) Cooper Eromanga Basins Basement. Bioregional Assessment Derived Dataset. Viewed 20 November 2018, https://www.bioregionalassessments.gov.au/assessments/23-conceptual-modelling-cooper-subregion/2322-geology-and-hydrogeology

Boult, P. J., Lanzilli, E., Michaelsen, B. H., McKirdy, D. M., & Ryan, M. J. (1998). A new model for the Hutton/Birkhead reservoir/seal couplet and the associated Birkhead-Hutton petroleum system. The APPEA Journal, 38(1), 724-744.

Buick, G. (2015). The Bauer Field, Cooper/Eromanga Basin: Case study of a low relief, high productivity, oil field. Search and Discovery article #110225: AAPG International Convention and Exhibition, Melbourne, 2015.

Buland, A., & Omre, H. (2003). Bayesian linearized AVO inversion. Geophysics, 68(1), 185-198.

Castana, J.P., (1993), AVO analysis, Tutorial and reveiew: in Castagna, J.P. and Backus, M.M. eds., Offset-dependent reflectivity – Theory and practice of AVO anomalies, SEG, Investigaations in Geophysics, No. 8, 3-36.

Castagna, J. P., Batzle, M. L., & Eastwood, R. L. (1985). Relationships between compressional-wave and shear-wave velocities in clastic silicate rocks. Geophysics, 50(4), 571-581.

Castagna, J. P., & Swan, H. W. (1997). Principles of AVO crossplotting. The leading edge, 16(4), 337-344.

Castagna, J. P., Swan, H. W., & Foster, D. J. (1998). Framework for AVO gradient and intercept interpretation. Geophysics, 63(3), 948-956.

CGG, 2017, CGG GeoSoftware training catalog.

Chaveste, A., & Hilterman, F. (2007). Well-log inversion and modeling—A tool for understanding ambiguity and sensitivity of seismic data to changes in petrophysical properties. The leading edge, 26(7), 812-817.

Chopra, S., & Castagna, J. P. (2014). AVO. Society of Exploration Geophysicists.

Chopra, S., Castagna, J., & Portniaguine, O. (2006). Thin-bed reflectivity inversion. In SEG Technical Program Expanded Abstracts 2006 (pp. 2057-2061). Society of Exploration Geophysicists.

(DEM) Department for Energy and Mining (2018). Technical information [Online]. Available at http://www.energymining.sa.gov.au/petroleum/prospectivity/eromanga_basin (Verified June 25, 2019)

Dillinger, A., Huddlestone-Holmes, C. R., Zwingmann, H., Ricard, L., & Esteban, L. (2014, February). Impacts of diagenesis on reservoir quality in a sedimentary geothermal play. In Proceedings, thirty-ninth workshop on geothermal reservoir engineering, Stanford University, Stanford, California.

Dodman, A. P., & Rodrigues, J. T. (1989). The Jackson oil field development.

Draper, N. R., & Smith, H. (1966). Applied linear regression.

Dvorkin, J., & Nur, A. (1996). Elasticity of high-porosity sandstones: Theory for two North Sea data sets. Geophysics, 61(5), 1363-1370.

Fatti, J. L., Smith, G. C., Vail, P. J., Strauss, P. J., & Levitt, P. R. (1994). Detection of gas in sandstone reservoirs using AVO analysis: A 3-D seismic case history using the Geostack technique. Geophysics, 59(9), 1362-1376.

Foster, D. J., Keys, R. G., & Lane, F. D. (2010). Interpretation of AVO anomalies. Geophysics, 75(5), 75A3-75A13.

Gardner, G. H. F., Gardner, L. W., & Gregory, A. R. (1974). Formation velocity and density The diagnostic basics for stratigraphic traps. Geophysics, 39(6), 770-780.

Gassmann, F. (1951). Elastic waves through a packing of spheres. Geophysics, 16(4), 673-685.

Goodway, B., Chen, T., & Downton, J. (1997). Improved AVO fluid detection and lithology discrimination using Lamé petrophysical parameters; “λρ”, “μρ”, & “λ/μ fluid stack”, from P and S inversions. In SEG Technical Program Expanded Abstracts 1997 (pp. 183-186). Society of Exploration Geophysicists.

Greenberg, M. L., & Castagna, J. P. (1992). Shear wave velocity estimation in porous rocks: Theoretical formulation, preliminary verification and application. Geophysical prospecting, 40(2), 195-209.

(GSA) Government of South Australia (2012). Technical Information [Online]. Available at http://eromangabasin.com/category/eromanga-basin-australia/ (Verified June 25, 2019).

Hamilton, D. S., Holtz, M. H., Ryles, P., Lonergan, T., & Hillyer, M. (1998). Approaches to identifying reservoir heterogeneity and reserve growth opportunities in a continental-scale bed-load fluvial system: Hutton Sandstone, Jackson field, Australia. AAPG bulletin, 82(12), 2192-2219.

Hampson, D. P., Russell, B. H., & Bankhead, B. (2005). Simultaneous inversion of pre-stack seismic data. In SEG Technical Program Expanded Abstracts 2005 (pp. 1633-1637). Society of Exploration Geophysicists.

Hampson, D. P., Schuelke, J. S., & Quirein, J. A. (2001). Use of multiattribute transforms to predict log properties from seismic data. Geophysics, 66(1), 220-236.

Han, D. H., Nur, A., & Morgan, D. (1986). Effects of porosity and clay content on wave velocities in sandstones. Geophysics, 51(11), 2093-2107.

Hendrickson, J. S., 1999, Stacked: Geophysical Prospecting, 47, 663–706.

Hill, R. (1952). The elastic behaviour of a crystalline aggregate. Proceedings of the Physical Society. Section A, 65(5), 349.

Hilterman, F. J. (2001). Seismic amplitude interpretation. Society of Exploration Geophysicists and European Association of Geoscientists and Engineers.

Izarra Dial, L. A. 2011, Enhancement of geological features in the Fort Worth Basin by the application of spectral decomposition and spectral inversion, Shackleford County, TX, USA: M.S. thesis, University of Houston.

Johnson, J. 2017. Applications of Geostatistical Seismic Inversion to the Vaca Muerta, Neuquen Basin, Argentina. MS thesis, Colorado School of Mines, Golden, Colorado.

Kabaca, E. (2018). Seismic stratigraphic analysis using multiple attributes-an application to the f3 block, offshore Netherlands (Doctoral dissertation, University of Alabama Libraries).

Keho, T., Lemanski, S., Ripple, R., & Tambunan, B. R. (2001). The AVO hodogram: Using polarization to identify anomalies. The Leading Edge, 20(11), 1214-1224.

Kohonen, T. (1982). Self-organized formation of topologically correct feature maps. Biological cybernetics, 43(1), 59-69.

Lanzilli, E. (1999). The Birkhead Formation: reservoir characterisation of the Gidgealpa south dome and sequence stratigraphy of the Eromanga Basin, Australia (Doctoral dissertation).

Mahob, P. N., & Castagna, J. P. (2003). AVO polarization and hodograms: AVO strength and polarization product. Geophysics, 68(3), 849-862.

Mathworks (2019). Technical Information [Online]. Available at https://www.mathworks.com/help/stats/machine-learning-in-matlab.html (Verified June 25, 2019).

Marfurt, K. J. (2018). Seismic attributes as the framework for data integration throughout the oilfield life cycle. Society of Exploration Geophysicists.

Masters, T. (1995). Advanced algorithms for neural networks: a C++ sourcebook (Vol. 97). New York: Wiley.

Mukerji, T., Avseth, P., Mavko, G., Takahashi, I., & González, E. F. (2001). Statistical rock physics: Combining rock physics, information theory, and geostatistics to reduce uncertainty in seismic reservoir characterization. The Leading Edge, 20(3), 313-319.

Ostrander, W. (1984). Plane-wave reflection coefficients for gas sands at non normal angles of incidence. Geophysics, 49(10), 1637-1648.

Okonkwo, O. S. (2014). Improved interpretation of an incised valley system, channel delineation and thickness estimation using spectral inversion, Blackfoot field, Alberta, Canada: M.S. thesis, University of Houston.

Paradise, 2017, Geophysical Insights Training videos Available at https://geoinsights.freshdesk.com/support/solutions/articles/27000040092-resources (verified Oct 25, 2019)

Paradise, 2019, Geophysical Insights Training Videos. Available at https://geoinsights.freshdesk.com/support/solutions/articles/27000040091-new-training-material (verified Oct 25, 2019)

Partyka, G., Gridley, J., & Lopez, J. (1999). Interpretational applications of spectral decomposition in reservoir characterization. The leading edge, 18(3), 353-360.

Pickett, G. R. (1963). Acoustic character logs and their applications in formation evaluation. Journal of Petroleum technology, 15(06), 659-667.

(PIRSA) Primary Industries and Resources South Australia (2000). Available at www.energymining.sa.gov.au/petroleum/prospectivity/eromanga_basin (verified June 25, 2019)

Puryear, C. I., & Castagna, J. P. (2008). Layer-thickness determination and stratigraphic interpretation using spectral inversion: Theory and application. Geophysics, 73(2), R37-R48.

Radke, B. M. (2009). Hydrocarbon and geothermal prospectivity of sedimentary basins in central Australia: Warburton, Cooper, Pedirka, Galilee, Simpson and Eromanga basins. Geoscience Australia.

Raymer, L. L., Hunt, E. R., & Gardner, J. S. (1980, January). An improved sonic transit time-to-porosity transform. In SPWLA 21st annual logging symposium. Society of Petrophysicists and Well-Log Analysts.

Roberts, A. (2001). Curvature attributes and their application to 3D interpreted horizons. First break, 19(2), 85-100.

Roden, R., & Chen, C. W. (2017). Interpretation of DHI characteristics with machine learning. First Break, 35(5), 55-63.

Roden, R., Smith, T., & Sacrey, D. (2015). Geologic pattern recognition from seismic attributes: Principal component analysis and self-organizing maps. Interpretation, 3(4), SAE59-SAE83.

Ross, C. P. (2002). Comparison of popular AVO attributes, AVO inversion, and calibrated AVO predictions. The Leading Edge, 21(3), 244-252.

Ruess, A. (1929). Berechnung der Fleissgrenze von Mischkristallen auf Grund der Plastizitats bedingung fur Einkrisalle. Zeitschrift für Angewandte Mathematics aus Mechanik, 9, 49-58.

Russell, B. H. (1988). Introduction to seismic inversion methods. Society of Exploration Geophysicists.

Russell, B. H., K.Hedlin, and F. J. Hilterman, 2003, Fluid-property discrimination with AVO: A Biot-Gassmann perspective: Geophysics, 68, 29–39.

Rutherford, S. R., & Williams, R. H. (1989). Amplitude-versus-offset variations in gas sands. Geophysics, 54(6), 680-688.

Simmons Jr, J. L., & Backus, M. M. (1996). Waveform-based AVO inversion and AVO prediction-error. Geophysics, 61(6), 1575-1588.

Specht, D. F. (1991). A general regression neural network. IEEE transactions on neural networks, 2(6), 568-576.

Specht, D. F. (1990). Probabilistic neural networks. Neural networks, 3(1), 109-118.

Stieber, S. J. (1970, January). Pulsed neutron capture log evaluation-louisiana gulf coast. In Fall Meeting of the Society of Petroleum Engineers of AIME. Society of Petroleum Engineers.

Trappe, H., & Hellmich, C. (2000). Using neural networks to predict porosity thickness from 3D seismic data. First Break, 18(9), 377-384.

Voigt, W. (1928). Textbook of crystal physics. BB Teubner, Leipzig, 2.

Whitcombe, D. N., and J. G. Fletcher, 2001, TheAIGI cross plot as an aid to AVO analysis and calibration: 71st Annual International Meeting, SEG, ExpandedAbstracts, 219–222.

Widess, M. B. (1973). How thin is a thin bed?. Geophysics, 38(6), 1176-1180.

Wood, A. B. (1955). A textbook of sound: being an account of the physics of vibrations with special reference to recent theoretical and technical developments. G. Bell.

Wyllie, M. R. J., Gregory, A. R., & Gardner, L. W. (1956). Elastic wave velocities in heterogeneous and porous media. Geophysics, 21(1), 41-70.

Yao, X., & Liu, Y. (1998). Towards designing artificial neural networks by evolution. Applied Mathematics and Computation, 91(1), 83-90.

Zoeppritz, K. (1919). On the reflection and propagation of seismic waves. Gottinger Nachrichten, 1(5), 66-84.